X-RAY PHOTOELECTRON SPECTROSCOPY (XPS), X-RAY DIFFRACTION (XRD), DIFFERENTIAL SCANNING CALORIMETRY (DSC) AND DENSITY STUDY OF TERNARY CHALCOGENIDE GLASSES BASED ON Ge-Se AND Ge-S.

A thesis submitted for the degree of Doctor of Philosophy

by

Ghassan Saffarini

Brunel University

Physics Departement

Kingston Lane

Uxbridge, Middlesex UB8 3PH

September 1991

Abstract

Glasses of the systems Ge-Se-X (X = Ga, Sn, Bi, Sb), Ge-S-Y (Y = Ag, Ga, Sn, Bi) and Se-S have been examined using X-ray photoelectron spectroscopy (XPS), X-ray diffraction (XRD), density and differential scanning calorimetry (DSC). Two of the compositions, $GeSe_2$ and $(GeSe_2)_{92}Ga_8$, have also been examined by extended X-ray absorption fine structure (EXAFS) and X-ray absorption near edge structure (XANES). The emphasis of the XPS measurements was on the changes in the binding energies with composition of the core peaks of the glasses, and on the plasmon energy losses from the $L_3M_{4,5}M_{4,5}$ Auger lines of Se and Ge. It was found that there were small shifts in the binding energies of the core peaks on substitution but the plasmon energy changed markedly with composition. For the XRD measurements, the focus was on two features : (a) to ensure that the samples prepared were truely amorphous and (b) to confirm the presence of the first sharp diffraction peak (FSDP) on the interference functions. The density measurements showed that the addition of the third element (X or Y) to the binary resulted in an increase in the relative density except for one system, Ge-Se-Sn, which showed the opposite behaviour. The DSC measurements showed that the addition of the third element to the binary resulted in a decrease in the glass transition temperatures. The EXAFS and XANES measurements of $GeSe_2$ and $(GeSe_2)_{92}Ga_8$ glasses showed that there was very little change in the local order around the Ge atom in $GeSe_2$ glass with

increase in temperature and that the local order around the Ge atom changes on alloying $GeSe_2$ with Ga. Correlations between parameters and measured properties of the ternary alloys have been investigated. It has been found that the parameter < m >, the average coordination number, correlates well with certain structural properties but badly with others. Suggestions are made for an alternative to < m >.

ACKNOWLEDGEMENTS

I would like to express my deep appreciation and gratitude to my supervisor, Dr B.R.Orton for his supervision, guidance, encouragement, and kind attitude throughout the course of this work. I would also like to express appreciation to the technical staff of the physics department at Brunel University for their technical assistance and to the staff of the Experimental Technique Centre who provided the necessary time for XPS measurements. I also wish to thank the British Council for financial support which enabled me to carry out this work.

Finally, I would like to thank my wife for her understanding, encouragement and patience throughout the course of this work.

Contents Page

List of tables

List of Figures

CHAPTER 1

Introduction

1.1 Historical introduction of glass

The word "glass" is derived from Indo-European root meaning "shiny". The history of glass is summarised in articles in the Encyclopaedia Britannica (1985) and in the book by Morey (1954). Glass is one of the oldest substances used by the earliest human civilizations and knowledge of it has been acquired gradually over many centuries.

The invention of glass-blowing by Syrian glass makers in about the first century B.C. greatly increased the use of glass for practical purposes in Roman times, mainly for vessels but later for windows. The important techniques like blowing, drawing, moulding and casting of glass were well established by the third century. After the fall of the Roman Empire, glass manufacturing dispersed to the West and to the Middle East. The preparation of coloured glasses started in the 6th century (Maloney 1967). Egyptian and Alexandrian workers made specific coloured glasses by mixing metallic oxides to the basic raw materials for the first time. Venice became the most famous glass making centre in the

West from about 1300 onward and Venetians made mirrors by coating plates of glass with tin and mercury (Person 1969). Most glasses made before the 17th century were of alkali/lime/silica. A lead crystal glass was first produced in England by George Ravenscroft in 1793 and by the end of the 18th century England and Wales were the main countries for the production of the so-called lead crystal glasses.

Faraday (1830) was among the first to study glass in a more basic way. His work on the optical properties of glasses in the early part of the 19th century could be considered as the first "classical" research on glass. He described a glass as a solution of different substances, one in the other, rather than a strong chemical compound. Faraday also studied the electrolysis and conductivity of melts of various glasses. In the late 19th century, the first systematic study of the relationship between the physical and chemical properties of glass and its composition was started in Germany by the work of Winkelmann and Schott (Weyl and Marobe 1962). Goldschmidt (1926) made one of the earliest attempts to discover characteristics common to glass-forming oxide. Zachariasen (1932) and Warren (1934) described the structure of glass in terms of chemical bonding. The understanding of the structure of glass was enlarged by the papers of Warren (1935, 1936, 1937, 1938). In the 1950's and 1960's a true revolution came in the glass science after finding that glass could be formed from many known materials, including polymers, salts,

simple organics, chalcogenides, and even metals. Glass has optical, electrical, mechanical, thermal and chemical properties which make it a highly practical and versatile material. In the field of telecommunications, glass fibers can be made to carry messages better than copper wires. Much of the information about the technical glasses can be found in a number of monographs (Kohal 1967, Espe 1968) and in a recent review (Rawson 1988). The relative ease of manufacture of glasses compared with analogous crystalline materials, encouraged researchers all over the world to study their different properties.

1.2 Definition of glass

There is no universally accepted definition of the glassy state found in the literature. There are, however, many definitions, each reflecting different aspects or characteristics of this state. Thus, according to Tammann (1935), a substance in the glassy state is a supercooled liquid at a temperature so low that the growth rate of the crystal seeds, and the rate of formation of crystallisation centres, is practically equal to zero. Morey (1954) defined a glass as "an inorganic substance in a condition which is continuous with, and analogous to, the liquid state but which, as the result of having been cooled from a fused condition, has attained so high a degree of viscosity as to be for all practical purposes rigid". Cohen (Borisova 1981), a specialist on electronic phenomena in semiconductors, gave an interesting definition, namely," an ideal glass is characterised by short-range order, complete absence of

long-range order, and also by total local saturation of all the valences". Jones (1971) described glass, or a substance in the glassy or vitreous state, as a material which has been formed by cooling from the normal liquid state and which has shown no discontinuous change in the first order thermodynamic properties, such as volume, heat content or entropy, but has become rigid through a progressive increase in its viscosity. Discontinuities are observed however, in the second order thermodynamic properties such as specific heat capacity and thermal expansion. Mackenzie (1960), a noted authority on the modern aspects of glass, has expressed his views as "Any isotropic material, whether it be inorganic or organic, in which three-dimensional periodicity is absent and the viscosity of which is greater that about 10^{14} poise may be described as a glass". The fifth All-union Conference on the Glassy state (1971) has adopted the following definition: glass is in the form of amorphous state in which the substance has a dynamic viscosity coefficient larger than 10^{13}-10^{14} poise i.e. it has the mechanical properties of a crystalline solid and differs in its ability to return after melting to the initial state under set cooling conditions.

From the above definition we generally conclude that

(a) glasses are substances which are rigid at low temperatures and plastic at high temperatures.

(b) they are optically isotropic, and

(c) they are amorphous in nature and show lack of periodicity

when examined by X-rays.

1.3 Nature of the glassy state

The volume/temperature diagram is often used to discuss the inter-relationships between the liquid, glassy and crystalline states. This is illustrated in Fig. 1.1 for a simple, imaginary substance which could occur in all three states; viz. crystalline solid, glassy and liquid states (Jones 1956). As the liquid is cooled from high temperature, the volume decreases along the line ab. If the rate of cooling of the liquid is sufficiently slow, and the necessary nuclei are present in the melt, crystallization will take place at the temperature T_f and an abrupt change appears in the volume and in other physical properties along bc. If the cooling continues, the crystalline material will contract along cd. If the liquid is cooled very rapidly, crystallisation will not take place at T_f and as the cooling continues, the volume of the liquid which is now a super-cooled liquid will continue to decrease without any discontinuity along the line be which is a smooth continuation of ab. Upon further cooling, a region of temperature will be reached in which a change of slope appears in the figure. The temperature region over which this change occurs is represented roughly by a "transformation or glass-transition temperature", T_g. The transition from the liquid to glassy state takes place over a range of temperatures. There is no clearly defined glass transition temperature which could be compared with the well-defined melting point of a crystalline solid. The value of T_g depends on the

chemical composition and also on the thermal history of the glass.

If, however, the cooling is halted and the temperature is held constant at T, the glass will slowly contract further until its volume reaches a point on the dotted line which is a continuation of the contraction curve of the supercooled liquid. This process by which the glass reaches a more stable state is known as stabilisation and it demonstrates an important difference between the glass and the supercooled liquid which cannot achieve a stable state without crystallisation. Due to the stabilisation process, the properties of a glass up to a certain degree depend on the rate of cooling, especially near the glass transition temperature. The viscosity of a molten glass is nearly 10^2 poise. As the liquid cools down the viscosity continuously increases and in the glass transition range it is usually about 10^{13} poise. By further cooling the viscosity continues to increase but at a slower rate. At ordinary temperatures, the viscosity of a glass may be as high as 10^{20} poise and it behaves in practice as a solid.

1.4 Conditions of glass formation

The ability of an oxide or multicomponent oxides to form a glass was considered from several different angles. Stanworth (1946) explained glass formation in terms of the electronegativity of various elements found in oxide glasses. Smekal (1951) suggested that the presence of mixed chemical bonds is necessary if the material is to form a glass because the random arrangement of atoms maintained on cooling is incompatible with sharply defined bond lengths and bond angles. The concept of the

relationship between glass formation and bond strength was first put forward by Sun (1947). According to him, the stronger bonds cause the slower re-arrangement process and hence a glass will be formed more readily. Rawson (1967) pointed out that the effect of the melting point of any oxide in its glass-formation ability should be taken into account. He introduced the ratio of single bond strength to the melting temperature, and tabulated this ratio for a number of oxides. Turnbull and Cohen (1958) proposed a kinetic theory of glass formation in which limiting rates for the process of nucleation and crystal growth in liquids are established in order that the glass formation may occur. It has been noted, however, that virtually any liquid will form a glass if cooled sufficiently rapidly, and will form a crystalline or partly crystalline solid if cooled more slowly. On this basis it was suggested by Uhlmann (1972) that the question to be addressed in considering glass formation is not whether a liquid will form a glass, but rather how fast must the liquid be cooled in order that detectable crystallinity be avoided. In conclusion, glass formation depends on many factors and a detailed knowledge of this process is far from complete.

1.5 Structure of glass

The first hypothesis of glass structure was suggested by Lebedev in 1921. The hypothesis established some possibility of a relation between the structure of a glass and its properties and led the physicist and chemist to investigate the vitreous state in a more fundamental manner. Goldschmidt 1926 introduced the idea

of thinking of a glass structure in terms of its atomic arrangement and of the relative sizes and valencies of the atoms or ions concerned. According to him, the glass forming oxides are those for which the ratio of ionic radii R_c/R_a lies in the range of 0.2-0.4 and the tetrahedral configuration of the oxide is a prerequisite of glass formation. Zachariasen (1932) suggested that the ion ratio concept is not a satisfactory criterion because not all oxides having a radius ratio in the specified range are glass formers. He gave the example BeO which would be included in such a group but does not form glasses. He presented a picture of the atomic structure of vitreous silica indicating that since the crystalline form of silica contains SiO_4 tetrahedra joined at their corners then in the same way vitreous silica must also contain SiO_4 tetrahedra joined at their corners. The only difference between the crystalline and glassy form is that in vitreous silica, the relative orientation of adjacent tetrahedra varies, whereas in the crystalline form it is constant throughout the structure. Such a difference is shown in Fig. 1.2 for an imaginary two-dimensional oxide X_2O_3 in both the crystalline and vitreous forms. In both cases the structural units are XO_3 triangles. Therefore glasses have short-range order since the oxygens are arranged in fairly regular polyhedra, but long range order is absent. Zachariasen suggested the following four rules for an X_mO_n to be a glass former:

(1) No oxygen atom is linked to more than two X atoms.

(2) The number of oxygen atoms around an atom X must be small,

4 or less.

(3) The oxygen polyhedra share corners but not edges or faces.

(4) At least three corners in each oxygen polyhedra must be shared.

The oxides of formula XO and X_2O cannot satisfy these requirements for glass formation while oxides of the formula (a) X_2O_3, (b) XO_2, X_2O_5 and (c) XO_3, X_2O_7 and XO_4 where the polyhedra are triangles, tetrahedra and octahedra, respectively, do satisfy Zachariasen's rules and they could in fact exist in the glassy state. Warren (1937) proposed a model for simple silicate glasses (SiO_2, Na_2O-SiO_2) based on the continuous random (CRN) network of SiO_4 tetrahedra with the sodium atoms fitting into large interstices within the network to preserve the local electrical charge neutrality. In fused silica all oxygens are bonded to two silicon atoms, but in sodium silicate glasses extra oxygen atoms are introduced by Na_2O_3, thus increasing the O/Si ratio. Thus some oxygens in sodium silicate glasses are bonded to two silicon atoms and are called "bridging oxygen" while the others are bonded to one silicon atom and called "non-bridging oxygens". The two dimensional picture of the structure of a sodium-silicate glass is shown in Fig. 1.3. The Warren and Zachariasen hypothesis has been criticised by many scientists. Urnes (1960) stated that there is a tendency for the modifying ions to form clusters rather than to be randomly distributed throughout the network. But in spite of these criticisms, the random network theory has been widely accepted

for many years. Recently the limitations of this theory were fully accepted because of the discovery that many oxide glasses can be made which do not obey Zachariasen rules (e.g. elemental glasses). It is now generally agreed that almost any material if cooled sufficiently fast could be obtained in the glassy state, although in practice crystallisation intervenes in many substances.

1.6 Glass classification

Various schemes for the classification of non-crystalline materials have been suggested by several writers (Grigorovici 1969, Stevels 1971, Bell 1972). Generally glasses are classified into four groups.

1.6.1 Oxide glasses

Oxide glasses are the main group of glasses with an extensive use in ordinary life. Glass-making oxides have been classified into glass formers, modifiers and intermediates according to their behaviour in glass making. Oxides which form glasses when cooled from the melt are termed glass formers. The glass modifiers are those oxides which are not bonded to the network but whose presence in the glass tends to open up the network by reducing the network bonds. Modifiers tend to reduce the viscosity of the glass as well as giving some useful chemical or physical properties. The intermediates occupy a position between the glass formers and glass modifiers and cannot form glasses on their own, but they can do so when melted with a suitable quantity of a second oxide.

The most important of the oxide glasses are

(a) silicate glasses

(b) borate glasses

(c) germanate glasses

(d) phosphate glasses

and (e) tellurite glasses

1.6.2 Hydrogen-bond glasses

The presence of the hydrogen bond in certain oxides leads to the formation of glasses. The chemical bonds linking the atoms in the oxides are known to be partly ionic and partly covalent. A number of aqueous solutions form glasses far more readily, particulary solutions with HCl, $HClO_4$, NH_4OH, KOH and LiCl.

1.6.3 Elemental glasses

This category of glass contains only one kind of atom. A few elements are found in group VI of the periodic table which can form a glass on their own e.g Se, S, and Te. These elements are known to form a vitreous network when mixed or chemically bonded to each other and are known to be very viscous in the liquid state and to undercool very easily. These glasses are completely covalently bonded and possess only positional disorder.

1.6.4 Chalcogenide glasses

The elements S,Se,Te are the main constituents of the chalcogenides which form glasses over a fairly wide region of compositions when mixed with one or more of the elements Ge, Si, As, P, Sb, Bi and others (Rawson 1967, Pearson 1964, Dembovskii 1969). Of the binary glasses, As_2S_3, As_2Se_3 and As_2Te_3 have been most extensively studied and are often regarded as prototypes of

the chalcogenide glasses. Because of the large variety of ternary and quaternary systems, classification of these materials becomes difficult, particulary in view of the freedom that is allowed in amorphous systems to depart from stoichiometric compositions. However, use of stoichiometric compositions allows useful comparison with the material in its crystalline phase. These materials, generally, obey the so-called "8-N bonding rule", according to which all electrons are taken up in bonds. The structures of most amorphous chalcogenides are not so well characterized. The complication arises from separating contribution from A-A, B-B and A-B bonds in radial distribution studies (RDF) for binary system A_xB_{1-X}. In multicomponent systems identification is even more complicated. In principle, extended X-ray absorption fine structure (EXAFS) studies are capable of making the distinction between bond types. The simplest structural model of binary system is that of a continuous random network (CRN) in which 8-N valence coordination rule is satisfied for both components and at all compositions. The average coordination number $< m >$, for a binary system A_xB_{1-x}, is given by Phillips (1979) as :

$$< m > = x\, N_c(A) + (1-x)\, N_c(B)$$

where $N_c(A)$ and $N_c(B)$ are the atomic coordination numbers of A and B respectively. Phillips (1979) has demonstrated that the glassy structure has maximum stability around $< m > = 2.4$.

The chalcogenide glasses are semiconductors and they are

opaque in the visible region of the spectrum and excited much interest because of their potential application in electronic devices.

In the next section we will discuss the structure of amorphous-Se, amorphous-$GeSe_2$, and amorphous-GeS_2, which form the basic structural units for the ternary glasses studied in this work, along with previous work on the binary system amorphous-Se-S.

1.7 Structure of a-Se, a-$GeSe_2$, a-GeS_2 and a-Se-S systems

1.7.1 a-Selenium

Crystalline selenium occurs commonly in the trigonal form which consists of long spiral chains and in two monoclinic forms designated as alpha and beta which consist of eight-membered puckered rings of atoms (Moody and Himes 1967) (see Fig.1.4). The chain is periodic with three atoms per unit cell and has trigonal symmetry about the chain axis. It is either right-handed or left-handed, depending on the sense of the spiral. Each atom has two near neighbours at distance r and with an angle θ between the bond vectors, and four second neighbours at distance R (see Fig. 1.5). The ratio of second-to first-neighbour distances R/r is a measure of the molecular nature. Both monoclinic and amorphous selenium are seen to be more molecular than trigonal form. The position of all atoms in the chain are fixed by the symmetry and the parameters r and θ. The eight-member puckered ring molecule is shown in Fig. 1.4 from a perspective that shows the similarity to the chain. It is in essence a bent chain in which the sign of the

dihedral angle ψ(the angle between two adjacent bonding planes) alternates. The magnitude of ψ (approximately 102^0 for both the helical chain and eight-membered ring structures) is constrained as a function of bond length r and bond angle θ so that the "bent chain" closes with eight atoms. In both cases the covalently-bonded molecular units are weakly interbonded by van der Waal's interaction. The most difficult question to answer about the structure of amorphous selenium is the extent to which these molecular units (chains and rings) are intermixed. This can be judged by a discussion of the earlier structural work.

Eisenberg and Tobolsky (1960) considered amorphous selenium to be a mixture of Se_8 ring molecules and long chains. Briegleb (1929) argued that the properties of amorphous selenium should be governed by those of long-chain molecules, since the content of the ring molecules in amorphous selenium has been estimated to be only 0.22 Wt% at 230^0 C. The average chain length of liquid selenium was calculated to be 7200 at 230^0 C by the thermodynamic theory developed by Eisenberg and Tobolsky (1960), a result which agreed with that obtained by means of measurements of the viscosity of molten selenium (Shirai and Hamada 1963).

The structural work on amorphous selenium has been carried out by many workers (Henninger et al 1967, Kaplow et al 1968, Richter 1972, Hansen and Knudsen 1975, Bellissent and Tourand 1980) and indicates that the bond length, the coordination number,

and the bond angle are essentially the same as in the crystalline forms up to second neighbours. The details of the structure beyond the second-neighbour distribution have not been established. The first peak at 2.34Å contains two atoms, the average bond length being shorter than in the trigonal crystal, 2.37Å, (Unger and Cherin 1966). The second peak centered on about 3.75Å contains six atoms. Because the bond and dihedral angles are both similar in magnitude in monoclinic and trigonal selenium, their pair distribution function differs significantly only at the fourth neighbour. The possibility of distinguishing between these two species in amorphous selenium by means of an RDF is therefore low. Kaplow et al (1968) also gave a computer fit to the RDF by producing structures which involved small displacements from the atomic positions in trigonal or monoclinic selenium. Grigorovici (1973) has pointed out that this is unlikely to be correct, as the atoms in the network must occupy positions of local minimum energy. Rechtin and Averbach (1973) also made computer simulations of atomic positions and found a high number of incomplete chains and rings, many of order six. Long, Galison, Alben and Connell (1976) have built a network model of a-Se/a-Te from convoluted covalently bonded two-fold coordinated chains of atoms. No rings or broken chains were present in the body of the model, which was energy-relaxed using van der Waal's forces acting between the chains. The resulting configuration gave reasonable agreement with the experimental RDF and exhibited a

random distribution of dihedral angles. A relaxation of the dihedral angle towards the crystalline value resulted in worse agreement with the experimental RDF. Richter (1972) proposed a structure of flat or straight spiralling zig-zag chains to fit the experimental RDF data, thus advocating a constant value for the dihedral angle in the amorphous phase. Corb et al 1982 from their modelling studies of the structure of a-Se gave supporting evidence in favour of a predominantly chain-like structure.

As will be described in detail a complementary technique X-ray photoelectron spectroscopy (XPS) has been used to supplement structural measurements.

Photoemission experiments have been carried on the density of valence states of both trigonal and amorphous forms of selenium (Laude et al 1973, Williams and Polanco 1974, Nielsen 1972, Shevchik et al 1973, Orton and Riviere 1980). The most complete data of Shevchik et al (1973) show that the density of valence states (DOS) of both structural modifications exhibit three important regions as the binding energy is increased. They are the non-bonding or lone pair p states, the bonding p states, which had two maxima, and the s-states. The only major difference in the (DOS) of the two modifications is the reversal of the intensity of the two peaks in the bonding p band (see Fig. 1.6). As the s-states were not observed in UPS measurements of Nielsen (1972) and were not found in the calculation of Chen (1973), there has been some controversy concerning this (Joannopoulos and Kastner 1975, Davis

1974). It is generally recognized that these s-states were not observed in Nielsen's measurements because of the low matrix elements for the transition from s-bands at UPS energies and also from the lack of conduction band states for an incident photon of 21.1 eV, the maximum photon energy used in Nielsen's study. Better agreement between theory and experiment was obtained when an error in Chen's calculation was pointed out by Robertson (1976). Correction for this error led to the s-states appearing in the calculated density of states. Joannopoulos et al (1975), and Shevchik (1974) have produced conflicting interpretations of the structure of amorphous selenium, based mainly on the DOS in the p bands. Joannopoulos et al (1975) argued that an increase in the interchain separation was responsible for the change in the electronic properties of the amorphous form. They also infer from the form of the s-band, that Se rings may be present. Shevchik (1974) has shown that the change in the shape of the p-band could be explained by a lowering of the dihedral angle from that in trigonal selenium (102^0) to that found in Se_6 rings. Robertson (1976) presented a model, based on tight-binding calculations, of amorphous selenium in which the bond angle and the dihedral angle are kept relatively fixed in magnitude and showed that the change in the sign of the dihedral angle down a chain is sufficient to explain the reversal of intensities of the two peaks in the bonding p-bands. He concluded that a chain like structure in which this alternation occurs, or in which the sign is random behave in the molecular fashion characteristic of amorphous selenium. The

photoemission results of the s band might, in part, be accounted for by the decrease in the interchain bonding (Robertson 1975, Joannopoulos et al 1975), which need not arise solely from an increase in the interchain separation, a contraction of the orbitals will probably also occur. Kramer et al (1973) showed that the removal of the long-range order of trigonal selenium to simulate the amorphous form resulted in a density of states that was essentially a broadened version of that of the trigonal form.

The infrared and Raman spectra of amorphous selenium have been studied and compared with the corresponding spectra of trigonal and α-monoclinic selenium (Schottmiller et al 1970, Lucovsky et al 1967, Pine and Dresselhaus 1971, Axmann and Gissler 1967, Cherin 1969, Lucovsky 1969). On the basis of the comparison, and on the observation that the near-neighbour bonding is similar in all three forms of selenium, the features in the infrared and Raman spectra have been assigned to the ring and chain components of the amorphous form. Raman spectra of thin films of amorphous selenium, deposited by evaporation onto a liquid nitrogen cooled substrate indicate the growth of a peak at about 110 cm^{-1} (Carroll and Lannin 1981). This growth has been attributed to changes in the dihedral angle distribution of the amorphous selenium network and the formation at 300^0K of about 5% of eight-membered rings. Gorman and Solin (1976) claim that the polarization behaviour of a Raman mode at 112 cm^{-1} clearly indicates the presence of rings but could not estimate the ring-

chain fraction. This was because in an independent chain or ring the Raman modes are identical, and also have the same frequency as the principal structure in the Raman spectrum of amorphous selenium, so it is not possible to differentiate between a ring or chain structure using these spectra. This line of argument casts some doubt on the conclusions concerning the existence of ring-molecules in amorphous selenium. The vibrational spectra of disordered two-fold coordinated chains of atoms were calculated using bond stretching and bending intra-molecular forces only (Meek 1976). He interpreted his results as suggesting a prefered magnitude for the dihedral angle along the chain-molecular units composing amorphous selenium. He also indicated that the sign of the dihedral angle is constant or random and may be distributed about the crystalline value with a standard deviation up to a maximum of about $\pm 10^0$. Lucovsky and Galeener (1980) proposed a structural model of amorphous selenium based on chains. Their model assumes a fixed dihedral angle, equal to that of the rings and the chains in the crystalline structures (102^0), but allows for a variation in the relative phase of this dihedral angle, thereby leading to local regions which are either ring-like in the sense of Se_8 molecule or chain-like in the sense of trigonal selenium. Suzuki and Misawa (1977, 1978) studied the structure of liquid and amorphous selenium by pulsed neutron diffraction. Based on their observations of the structure factor in the high-scattering-wave-vector regime, they concluded that the structure was best

described by a model based on long chains.

From the above discussion, the model that will be used for the structure of amorphous selenuim in the present work is that which is based on chains.

1.7.2 a-$GeSe_2$

The crystalline structure of β-$GeSe_2$ was reported to be isotypic with high temperature GeS_2 which is monoclinic (Dittmar and Shaffer 1976a). This structure forms the basis of the outrigger raft model for amorphous $GeSe_2$ (Phillips 1980, 1981) which will be discussed later.

The Ge-Se phase diagram was investigated over the whole composition range by (Liu et al 1962) and in the composition range 0-66.67 at % Se by Ross and Bourgon (1969). Figure (1.7) shows complete phase diagram of the Ge-Se system compiled from several sources and taken from Borisova (1981). The system is characterised by two compounds, the monoselenide GeSe and the diselenide $GeSe_2$ with melting points of 670^0 C and 740^0 C respectively. The glass forming region extends from 0 to 42 at % Ge (Feltz and Lippmann 1973, Tronc et al 1973) but $GeSe_2$ itself and samples near that composition are more difficult to obtain in the glassy form without microcrystallities of $GeSe_2$ embeded in the bulk material.

The viscosity isotherms of Ge-Se melts were investigated by Galzov and Situlina (1969) and the results indicate that $GeSe_2$ is stable in liquid phase while GeSe dissociates in the liquid phase.

A study of the physical properties of amorphous bulk and thin film samples in the Ge-Se system (Loehman et al 1972) did not show gross phase separation while annealing above the glass transition temperature (Feltz et al 1972) of amorphous samples in Ge-Se system resulted in gross phase separation which was followed by recrystallisation.

X-ray (Satow et al 1973), neutron (Uemura et al 1975), and electron (Fawcett et al 1972, Uemura et al 1974) diffraction have been employed to obtain the radial distribution function (RDF) of amorphous $GeSe_2$ by Fourier transformation of the scattered intensity data. The results of these studies on amorphous $GeSe_2$ have shown that $GeSe_2$ essentially has the same short-range order in both the crystalline and amorphous state.

The density of Ge-Se glasses in the composition range 4-16.7 at % Ge was investigated for the temperature range 20-360^0 C (Avetikyan and Baidakov 1972). The authors concluded from the slight change in the density that the structure of the short-range order and the character of the chemical bond change little in the glass when the temperature is raised.

The change of short-range order with temperature and composition in liquid Ge_xSe_{1-x} system, as shown by density measurements, was monitored by (Ruska and Thurn 1976). Within the compositon range $0 \leq x \leq 1/3$ the short-range order at lower temperature is determined mainly by $GeSe_4$ tetrahedra linked directly corner-to-corner or via Se atoms. At higher temperatures

$p\sigma$ bonds arise more and more. Within the composition range $1/3 \leq x \leq 0.5$ the short-range order is mainly determined by a distorted octahedral configurations even at lower temperatures which leads to difficulties in glass formation near $GeSe_2$ composition. The short-range order of the glasses and their corresponding melts was shown to be similar (Krebs and Ackermann 1972). Very recently, the neutron diffraction study of molten $GeSe_2$ (Penfold and Salmon 1990) showed that Ge correlations contribute to the first sharp diffraction peak (FSDP) of the total structure factor, give a nearest-neighbour distance of 2.40 Å and give a coordination number of 3.7 selenium atoms around the germanium atom.

Density and microhardness measurements of amorphous $Ge_x\ Se_{1-x}$ alloys in the range $0 \leq x \leq 0.33$ and glass transition temperatures in the range $0 \leq x \leq 0.3$ were reported by Azoulay et al (1975). Also the crystallisation process for $0.15 \leq x \leq 0.3$ was investigated in Azoulay et al's work.

Two basic types of continuous network structures have been proposed for covalent amorphous materials. The first model, the random covalent network (RCN) model, allows minimum chemical ordering for all compositions (Betts et al 1970, White 1974). For example, glasses in the $A_x\ B_{1-x}$ system could have A-A, A-B, and B-B bonds. The bond type distribution in this model is completely determined by the atomic coordination numbers and the concentrations and not by the relative bond-energies. The second model, the chemically-ordered covalent network (COCN) model,

emphasises just the relative bond-energies and thereby favours heteropolar A-B bonds (Lucovsky et al 1977).

For glassy Ge_xSe_{1-x}, the (RCN) model results in a connected matrix of tetrahedra which have the following types of coordination, a Ge atom at the centre surrounded by (a) four Se atoms, (b) three Se and one Ge, (c) two Se and two Ge, (d) one Se and three Ge, or (e) four Ge atoms. The (COCN) model maximises the probability of a Ge atom at the centre being totally surrounded by Se atoms. In both cases the tetrahedra are bridged by linear Se-Se chains, crosslinked chains, or directly connected. In the (COCN) model, the basic structural unit for stoichiometric composition can only be the $GeSe_4$ tetrahedra interconnected by Se-Se chains and can be derived by substituting the four-fold, tetrahedrally coordinated Ge atoms into amorphous Se thus resulting in cross-linking of the Se chains. The (COCN) model gives a short-range order to stoichiometric compounds similar to that in their crystalline counterparts.

The results of the electron diffraction study of amorphous Ge_xSe_{1-x} films (Fawcett et al 1972) were considered in terms of both network models. The 32 at % Ge alloy results (closest composition in this study to $GeSe_2$) agree well with both models. The 56 and 73 at % Ge results agree in general with (RCN) model. The authors concluded from their results that the (RCN) model gives a better representation of the structure of GeSe alloys.

Optical absorption edge and Raman scattering measurements

for Ge_xSe_{1-x} glasses were reported for the range $0 \leq x \leq 0.4$ (Tronc et al 1973). Their results showed that, except for compositions near pure Se, crystallisation tended towards $GeSe_2$ suggesting that there are no appreciable amounts of Ge-Ge bonds for $x \leq 0.33$ and that the glass structure is locally similar to either crystalline Se (for compositions near Se) or to crystalline $GeSe_2$. This was supported by observation of lines in the Raman spectrum of the glasses corresponding to those found in crystalline $GeSe_2$ or Se. As a result of this study, a structural model for Ge_xSe_{1-x} glasses with $x \leq 1/3$ has been proposed, in which Ge and Se atoms have coordination numbers of 4 and 2 respectively and the Ge-Ge bonds being statistically forbidden. Moreover, Ge-Se-Ge sequences remain scarce as long as the Ge concentration of the mixture make it possible.

Infrared absorption and Raman scattering studies were also reported for Ge_xSe_{1-x} system by (Lucovsky et al 1975, Nemanich et al 1977). The results of these studies are essentially similar to those of Tronc et al (1973) but Nemanich et al (1977) argues that Tronc assignment of the 219 cm^{-1} line cannot be explained in terms of composition dependence and instead proposed the existence of large rings containing five to eight Ge atoms interconnected by Se atoms with a Ge-Se-Ge angle of 123.8^0 and a Se-Ge-Se angle of 109.5^0. Nemanich (1977) from his low-frequency light-scattering measurements extracted a structural correlation range for the order existing in the ring structures and obtained a

value of about 8.5 Å for $GeSe_2$ glass which was consistent with the 7.5 Å value obtained from X-ray diffraction and optic-mode Raman spectra.

Tronc et al (1977) dispute the assignment of the 219 cm^{-1} line to Ge_6Se_6 rings for two reasons: firstly they claim that the bond angles used to calculate Raman modes are inconsistent with those obtained from studies on crystalline $GeSe_2$ (Dittmar and Schaffer 1976) and secondly the assignment of highly symmetric mode to large distorted ring structures is suspect. In real terms, the Nemanich (1977) assignment of the 219 cm^{-1} line is essentially the same as Tronc et al (1973) which is due to Ge-Se-Ge sequence. Tronc et al (1977) also deduced that $(GeSe_{1/2})_4$ tetrahedral units are randomly distributed within the glass structure, that is, without cluster formation.

The average band gap and Raman spectra of amorphous Ge_xSe_{1-x} for $0 \leq x \leq 0.7$ were measured by Kawamura et al (1980). Their results for the structure of amorphous $GeSe_2$ agree with those of Tronc et al (1973) but both band gap and Raman spectra showed a discontinuous and drastic change between $x = 0.45$ and 0.5. These changes were explained in terms of three-fold coordinated bonds for both Se and Ge atoms with a transfer of valence electrons from Ge to Se at composition of $Ge > 0.5$. They also concluded that with high intensity laser irradiation, the structure is transformed into the one based on 4-2 coordination.

Cohesive energy calculations of Ge_xSe_{1-x} glasses in the range

$0 \leq x \leq 0.33$ were performed in the tight binding approximation with a self-consistent Hartree model (Tronc 1987). The results showed that the main contribution to the cohesive energy was due to the transfer of electronic charges from Ge atoms to Se atoms and that the calculation of cohesive energy versus local structure confirmed Tronc's Raman results (1973).

X-ray spectroscopic studies of glassy $Ge_x Se_{1-x}$ system with $x = 0.1, 0.15, 0.22$ and 0.3 were reported by Agnihotri et al (1988). They found that the Ge K-absorption edge always shifts towards higher energies with respect to pure amorphous Ge whereas the Se K-absorption edge shifts towards lower energies with respect to amorphous Se. In both cases, the shift was found to be a minimum for $x=0.22$ which indicated some modifications in the structure at this composition.

The structure of evaporated $GeSe_2$ film and the influence of annealing at the glass transition temperature were studied by extended X-ray absorption fine structure (EXAFS) and by Raman spectroscopy (Nemanich et al 1978). Both measurements showed that the evaporated film exhibited significant homopolar bonding in contrast to the almost totally heteropolar bonding of the corresponding bulk glass, which was mostly eliminated upon film annealing. The data suggested that evaporated $GeSe_2$ film did not contain well-defined molecular structures. These results mean that the (RCN) model cannot be excluded for $GeSe_2$.

Malaurent and Diximer (1980) observed a first sharp

diffraction peak (FSDP) on their interference functions. The interference functions were obtained from X-ray diffraction studies on Ge_xSe_{1-x} glasses in the composition range $0 < x < 0.4$. Experimental results were consistent with a model which assumes Ge to be fourfold coordinated and Se to be two-fold coordinated. The FSDP was produced when Ge-Ge bonds were forbidden but Ge-Se-Ge sequences were allowed but remain scarce. These results are in agreement with Tronc et at (1973).

From recent Raman scattering measurements of $GeSe_2$ glass, Nemanich et al (1982) re-iterated support for the (COCN) model stating that the 219 cm^{-1} line in the Raman spectrum of $GeSe_2$ glass implies larger structural units than those assigned by Tronc et al (1977) to this mode and also pointed out that there is no evidence of sharp modes in the low-frequency Raman spectrum indicative of a layer structure. It was also suggested that $GeSe_2$ glass could contain edge-sharing tetrahedra because of the similarity between the short-range order of crystalline and amorphous states.

Marcus et al (1983) applied the (COCN) model to study the effects of ion-beam damage on X-ray diffraction and Raman spectra of amorphous $GeSe_2$ films. They observed that large changes in the X-ray diffraction pattern occur after damage but the Raman spectra remain relatively unchanged. They suggested that the as-prepared material consists of clusters with centres separated by about 6Å, and concluded that the excess free volume between the clusters could be squeezed out bringing the clusters

closer together. As a result the FSDP is shifted in the direction of the higher wavevectors, as observed, but the Raman spectra, which represent intracluster vibrations, remained unchanged.

The outrigger raft model mentioned previously and proposed by Phillips (1980, 1981) provides and alternative to the network models for chalcogenide amorphous materials. It was first given by Bridenbaugh et al (1979). The development of the raft model as given by Phillips will be outlined.

The main problem over the structure of the chalcogenide amorphous materials arises from the prominence of medium-range order which shows up as a distinctive first sharp diffraction peak (FSDP) in diffraction patterns from these materials (Phillips 1980).

The interpretation is not yet agreed upon but one view (Phillips 1980) is that the FSDP corresponds to molecular clusters with a centre-to-centre spacing S_c of 5Å and a correlation length R of about 15-20Å. As the FSDP persists at temperatures in excess of the melting point for $GeSe_2$ (Uemura et al 1978), it cannot be attributed to microcrystallities. Phillips concluded from the composition dependence that each cluster must contain at least five $GeSe_2$ units and that the clusters are responsible for the 219 cm^{-1} Raman mode observed by Tronc et al (1977). In order to construct clusters within the bonding constraints Phillips turned to the layer-crystal structure of high temperature GeS_2 (β-GeS_2). The cluster layer is extracted from the crystal by terminating the unit cells with a chalcogenide element bonded to a-axis Ge atoms. The

Ge atoms are removed from the left-and-right hand edges of the layer and replaced by the chalcogenide element rebonded as edge dimers (see Fig. 1.8). The rafts then form stacks with an interlayer distance of about 6 Å giving rise to the first sharp diffraction peak (FSDP). The 219 cm^{-1} mode, in the Raman spectrum of amorphous $GeSe_2$ is attributed to the in phase motion of the edge dimers.

A study of the electronic structure and optical spectra of evaporated $GeSe_2$ film (Aspnes et al 1981) indicated the existence of medium range order in $GeSe_2$ i.e. the presence of 4-atom $GeSe_2$ rings. These data support the assignment of the 219 cm^{-1} Raman mode by Nemanich et al (1977). Bridenbaugh et al (1979) disputed the assignment of this mode to ring formation.

Mossbauer emission spectroscopy on ^{129}Te doped $GeSe_2$ glass (Bresser et al 1981) and on ^{119}Sn doped $GeSe_2$ glass (Boolchand et al 1982) provided direct evidence for intrinsically broken chemical order in these network glasses. The origin of this broken chemical order derives from the presence of characteristic large clusters in the network.

Experiments in which photons are absorbed at low laser power levels below the band gap (in the Urbach tail region) reversibly altered the molecular structure of glassy $GeSe_2$ (Griffiths et al 1982) and the results were explained in relation to the outrigger raft model. The energy was considered to break homopolar bonds, an intrinsic feature of the glass, in favour of forming heteropolar bonds. Continued laser pumping produced a

structure in the glass which contained many crystalline features in its Raman spectrum but which reverted to the original glassy structure upon elimination of the laser flux. The authors named this phenomenon "quasicrystallisation" which appears to be athermal and with the structure lying somewhere between the glass and the crystal. Eventually, at high laser power levels crystallisation does occur but it cannot be described as microcrystallities because not all the Raman lines for crystalline $GeSe_2$ appear.

Finally, in our discussion of the structure, a transmission electron microscopy (TEM) study of amorphous $GeSe_2$ films revealed columnar growth (Chen 1981) which is believed to be due to the stacking of layered molecular clusters which will grow more rapidly in the column centre due to preferential centering by van der Waal's interaction.

From the work presented in the present section, it seems that the outrigger raft model is gaining popularity at the expense of network models.

1.7.3 a-GeS_2

The Ge-S phase diagram was investigated by (Liu et al 1963) and is shown in Fig. 1.9. The system is characterised by two compounds, the monosulphide GeS and the disulphide GeS_2 with melting points of 665^0 C and 840^0 C respectively.

There are two crystalline structures of GeS_2 : a low-temperature (L-T) form (Dittmar and Schaffer 1976 b) and a high-

temperature (H-T) form (Dittmar and Schaffer 1975). The L-T form is 3-dimensional (3D) in which the $GeS_{4/2}$ tetrahedra share corners whereas the (H-T) form is a layer structure (2D) in which the tetrahedra share corners as well as edges.

Glass-forming regions in the Ge-S system were investigated by (Kawamoto and Tsuchihashi 1969, Cervinka and Hruby 1973). Two glass-forming regions in Ge-S system were obtained (Kawamoto et al 1969). The first was relatively large and contained compositions from GeS_2 to GeS_9. The second glass-forming region was much smaller from $GeS_{1.31}$ to $GeS_{1.5}$. Three glass-forming regions were established (Cervinka et al 1973) : (1) compositions from GeS to $GeS_{1.1}$ have a very low glass-forming tendency; (2) compositions from $GeS_{1.1}$ to GeS_2 have a very high ability to form glass; (3) composition from GeS_2 upward are easiest to form.

Various physical properties in the two glass-forming regions of Ge-S system were reported (Kawamoto and Tsuchihashi 1971). The authors concluded from the analysis of their experimental data that the structure of the glasses in the two regions was different. In the first region, the GeS_2 tetrahedral units in glasses of compositions < GeS_{4-5} are distributed among sulphur chains while in compositions > GeS_{4-5} ringlike S_8 molecules are also present. As the sulphur content increases the structure of the glass approaches that of plastic sulphur. In the second glass-forming region the structure of the glasses is made up of a combination of GeS_2 and GeS (of GeS_4 tetrahedra and GeS_6 octahedra).

The crystallisation processes of $Ge_x S_{1-x}$ glasses in the composition range $0.33 \leq x \leq 0.4$ (Malek et al 1989) and in the composition range $0.322 \leq x \leq 0.44$ (Malek 1989) were studied by differential scanning calorimetry (DSC). It was shown that two crystalline compounds GeS and GeS_2 crystallise in these glasses.

The short range order of glassy GeS_2 was obtained from X-ray diffraction measurements (Rowland et al 1972, Cervinka and Hruby 1973, Feltz et al 1985). The results of these studies established the tetrahedral structure of GeS_2 glass. The most recent study (Felts et al 1985) reported the presence of a remarkable number (one fourth) of edge-sharing $GeS_{4/2}$ units in the three dimensionally connected network by modelling the glass structure of GeS_2 in order to interpret the experimental RDF.

Lin et al (1984) measured the temperature dependence of the first two peaks in the structure factor of glassy GeS_2. They found that the first peak showed an increase in intensity between 300 and 523^0 K while the second peak intensity was practically independent of temperature. They stated that this anomalous behaviour of the first peak support a short range order corresponding to layers for the structure of GeS_2 glass.

From the analysis of their data obtained by X-ray diffraction, ESR, and density measurements of Ge_xS_{1-x} glasses in the composition range $0.1 \leq x \leq 0.44$ (Zhilinskaya et al 1990), the authors concluded that agreement with experiment for GeS_2 is achieved if a basis circular structural unit is a six-member $Ge_6S_{16/2}$

ring which includes the edge connections of tetrahedra.

X-ray Ge K-absorption band and extended X-ray absorption fine structure (EXAFS) measurements of a-GeS_x with $1 \leq x \leq 2$ was reported by (Drahokoupil et al 1986). It was concluded that the short range order in a-GeS_2 is essentially similar to that in c-GeS_2 but appears to be more chemically ordered than the random covalent network model (RCN) and less ordered in comparison with the chemically ordered covalent network model (COCN).

Mossbauer emission spectroscopy on ^{129}Te doped GeS_2 (Bresser et al 1981) provided direct evidence for intrinsically broken chemical order which derives from the existence of characteristic large clusters.

Infrared and Raman spectra of bulk glasses of Ge_xS_{1-x} in the composition range $0.1 \leq x \leq 0.45$ (Lucovsky et al 1974 b) and for $Ge_{0.3}\ S_{0.7}$ glass (Lucousky et al 1974 a) were interpreted in terms of models based on covalent bonding in which the 8-N rule is satisfied and that heteropolar bonds are always favoured. The spectrum of GeS_2 glass was interpreted in terms of COCN in which the element of local order is a tetrahedral arrangement of S atoms about a central Ge atom.

Nemanich (1977) from his low-frequency light-scattering measurements extracted a structural correlation range for GeS_2 glass and obtained a value which was consistent with that obtained from X-ray diffraction and optic-mode Raman spectra.

The observation of "the companion A_1 Raman line" in the spectra of $Ge(S,Se)_2$ glasses was interpreted as an indication of

tetrahedra which are linked by corners and partially be edges (Bridenbaugh et al 1979, Nemanich 1977).

Weinstein et al (1982) carried experiments to study the effect of pressure on the optical properties of a-GeS_2, 2D-GeS_2 (H-T crystalline form), and 3D-GeS_2 (L-T crystalline form). Analysis of their data led them to conclude that a-GeS_2 is a 2D- network.

Finally, Arai (1983) from his Raman study suggested the existence of H-T GeS_2-like 2D-cluster on the basis of the resemblance of the Raman spectra between the glass and the H-T crystal.

1.7.4 a-Se-S

Very little data have been published on Se-S glasses. An equilibrium copolymerisation theory (Tobolsky and Owen 1962) was developed for the liquid structure in which copolymer molecules are in dynamic equilibria with S_8 and Se_8 monomer molecules and in which the relative monomer-polymer concentrations depend not only on temperature but also on the relative S and Se concentrations. The copolymerisation is demonstrated experimentally by the temperature dependence of the viscosity and by the compositional dependence of the glass transition temperatures of the various copolymer compositions (Schenk 1957). The compositional dependence of the glass transition temperatures for a-Se-S was measured by differential thermal analysis (DTA) and showed a linear decrease with increasing S content (Myers and Felty 1967). Berkes (1977)

developed a simple analytical model to calculate the variation of glass transition temperatures with composition for different binary selenide systems including Se-S and a good agreement between the model and experiment was obtained. Recently, the structure and optical properties of glassy thick films in Se-S system were investigated (Jecu et al 1987). From the analysis of their structural results, the authors concluded that the elements form mixed configurations as opposed to separated phases. Their optical results indicated that the absorption edge shifts nearly linearly towards lower values with Se content.

1.8 The ternary glasses

The binary glasses have been extensively studied except for Se-S whereas relatively little work has been carried out on the ternary glasses.

An important property investigated for possible applications was the ability of the chalcogenides to transmit light into the far infra-red 8-12 μm range compared to other glasses. Chalcogenides including the selenides and the sulphides have been investigated to assess their suitability as optical components (Savage 1985). Their infra-red properties make them good candidates as infra-red transmitting media suitable for use with high-energy CO_2 lasers emitting at 10.6 μm. However, their high optical losses do not make these materials practical for long range telecommunication fibers. A selenide glass studied here with 28 at % Ge, 12 at %Sb, 60 at % Se was found to give good transmission in the far infra-red range

(Hilton et al 1975).

Another important property investigated was photodoping or photodiffusion of group I metals - silver and copper - in chalcogenide vitreous semiconductors (Kostyshine et al 1966, Kokado et al 1976, Goldschmidt and Rudman 1976). The metal can be induced to dissolve in chalcogenides in large concentrations. Undoped chalcogenides are known to be soluble in dilute alkali solution but insoluble in acid solution whereas chalcogenides doped with only few at % Ag are insoluble in alkali. The metal doped chalcogenides are opaque and have much slower plasma etch rate which make them very useful for practical applications such as photolithography (Yoshikawa et al 1976).

Some of the glasses in the Ge-S-Ag system studied here have the same composition as those which must be obtained in the photodoping of Ge-S system with Ag. It is possible to see changes with composition because of the large glass-forming regions for this system (Feltz and Thieme 1974) and the large atomic number of Ag.

Furthermore, the ternary alloys germanium-selenium-bismuth and germanium-sulphur-bismuth studied also in this work were known to have special electrical properties. The electrical conductivity for Ge-Se-Bi system changes from p- to n-type in the vicinity of 7-9 at % Bi (Tohge et al 1979, Tohge et al 1980 a, Tohge et al 1980 b, and Nagels et al 1981) whereas the Ge-S-Bi exhibits the same phenomenon in the vicinity of 11 at % Bi

(Nagels et al 1983, Vikhrov and Ampilgov 1987, Tichy et al 1990).

These ternaries and others will be discussed in more detail in due course.

1.9 Sample preparation, glass transition temperature and density measurement

As stated in section 1.4, virtually any liquid will form a glass if cooled sufficiently rapidly. In the present work the method given in the following section was used for all samples.

The bulk glasses were prepared by the conventional melt quenching method using high purity elements (99.999%). The method consisted of sealing, under a high vacuum, the weighed amounts of the constituent elements in a carefully outgassed, argon flushed, rectangular-section silica ampoules. The ampoules were then placed in a rocking furnace in which they were heated to temperatures ranging between 800^0 C to 1050^0C, depending on the constituent of the glass, and were agitated to ensure thorough mixing of the melt. After homogenising for periods ranging between one day and three days, the ampoules were quenched to room temperature in a large volume water path. The flat surfaces of the quenched glasses adjacent to the walls of the silica tubes provided a good surface for X-ray examination and provided material for XPS examination. It was always attempted to go to the limit of the glass-forming regions of the ternary glasses studied within the glass preparation technique employed and the sample

sizes prepared in this work. A distinguishing feature of this work is that the "as quenched" virgin surfaces were examined by X-ray diffraction and XPS and not their powders.

A Perkin-Elmer DSC-2C differential scanning calorimeter using a scan rate of 20^0K/min and sample sizes ranging from 15 to 40 mg of the powdered glass was utilised to study the glass transition temperatures. The powdered samples were sealed in aluminium pans and compared to an empty aluminium pan. The measurements were done in dried, oxygen free, nitrogen atmosphere. The glass transition temperature was taken at the midpoint of the step in the thermogram.(Fig. 1.10).

The macroscopic densities at room temperature of the as-prepared glasses were measured by the Archimedes method using ethyl-methyl ketone (C_2H_5-CO-CH_3) as the immersion fluid which has a relative density of 0.803-0.805 gmcm^{-3} at 20^0C. The densities were calculated using the formula

$$\rho_g = (w_0/[w_0-w_L])\ \rho_L$$

where w_0 and w_L represent the weight of the sample in air and in the fluid, respectively, and ρ_L is the relative density of the immersion fluid.

1.10 Objective of the present work

In the previous sections we have shown that the outrigger raft model is a better candidate than the network models to describe the structure of $GeSe_2$ and GeS_2 glasses. There is clearly considerable interest in investigating the changes in topological and electronic structures of these glasses when a ternary alloy is made

using elements from different columns of the periodic table. These changes were investigated, for glasses of the systems Ge-Se-X (X=Ga, Sn, Bi, Sb) and Ge-S-Y (Y=Ag, Ga, Sn, Bi), using X-ray photoelectron spectroscopy (XPS), X-ray diffraction (XRD), differential scanning calorimetry (DSC) and density measurements. Two of the glasses, $GeSe_2$ and $(GeSe_2)_{92}$ Ga_8, were also studied by extended X-ray absorption fine structure (EXAFS) and X-ray absorption near edge structure (XANES) techniques.

Essentially to help with the understanding of the structure of binary glasses an investigation was undertaken on mixtures of Se and S where the elements have an extended polymer-like structure in the glassy phase. Here the problem was to determine if the elements form mixed configurations or was the structure maintained by independent intermingling of the polymer-like structures. The investigation was carried out using the techniques mentioned previously.

CHAPTER 2

X-ray Photoelectron Spectroscopy (XPS)

2.1 Principles of XPS

Surface analysis by X-ray photoelectron spectroscopy (XPS), initially designated as electron spectroscopy for chemical analysis (ESCA), is accomplished by irradiation of a sample under vacuum with monoenergetic soft X-rays and energy-analysing the emitted electrons. The spectrum obtained represents the number of emitted electrons in a fixed small energy interval versus their kinetic energy. The X-rays that are usually used for XPS are derived either from an aluminium or magnesium anode which have photon energies of 1486.6 eV or 1253.6 eV, respectively. These photons interact with atoms on the surface region of the sample by the photoelectric effect. An electron excited by the incident radiation may escape from the sample, provided it has sufficient energy to overcome the work function barrier. The emitted electrons have kinetic energies given by:

$$E_k = h\nu - E_B - \Phi \qquad (2.1)$$

where $h\nu$ is the energy of the incident photon, E_B is the binding energy of the atomic orbital from which the electron originates,

and Φ is the work function of the material. It is clear from equation (2.1) that only electrons with binding energy smaller than the photon energy can be emitted. Photoelectrons emitted within the sample may reach the surface of the sample without suffering any collisions or being elastically scattered. These photoelectrons form the well-defined core-peaks in the spectra and are most useful. Other photoelectrons suffer inelastic collissions and loss of energy may occur by the creation of electron-hole pairs or by the generation of collective electrons or plasmon oscillations. Inelastically scattered electrons form the raised background (on which the photoelectron peaks ride) at binding energies higher than the peaks (see Fig. 2.1). The background is continuous because the energy loss processes are random and multiple.

An ionised atom can relax back to its equilibrium state by either X-ray fluorescence or Auger emission (Fig. 2.2). X-ray fluorescence results in the emission of a characteristic photon from the atom as an electron from a higher level fills the hole left by the photoelectron. This process is a minor one in this energy range (below 2keV), occurring less than one percent of the time. Auger emission occurs when an outer electron is emitted, carrying off the excess energy. The Auger electron possesses kinetic energy equal to the difference between the energy of the initial ion and the doubly-charged final ion and is independent of the X-ray photon energy that is used for its excitation (see equation 2.11). If the extra energy is given to an electron in the same energy level as the

first electron i.e. having the same principal quantum number (n), this is called a Coster-Kronig transition. This process is heavily favoured for the initial decay of holes in core levels with low angular momentum quantum numbers (e.g. 2s, 3s and 3p, 4s and 4p, etc.) and is faster than the normal Auger process. These core levels, therefore, are broader than those which decay by normal Auger processes.

The sampling depth from which photoelectrons can escape without being inelastically scattered is of the order of 10-50 Å, therefore, XPS is a surface-sensitive technique. The sampling depth is determined by the electron mean free path λ, which is defined as the average distance electrons may travel before being inelastically scattered, and the angle of emission to the surface normal, α It is simply given as $\lambda \cos \alpha$. Experimental values of λ as a function of the electron kinetic energy for a number of elements have been compiled by Seah and Dench (1979) and shown in Fig. 2.3. It is worth noting that this has a minimum for an energy of approximately 100 eV which corresponds to a sampling depth of the order of a single atomic layer. In the range of energies used in XPS (500-1500 eV) λ varies between two and eight atomic layers.

A consequence of the surface-sensitive nature of XPS is that a relatively small quantity of surface contaminants can have a significant effect on the recorded spectra. Therefore it is imperative that experiments take place under UHV conditions after an atomically clean surface has been prepared. The sample to be

examined must also be vacuum compatible which means that it must neither decompose nor give large quantities of gas when exposed to a vacuum. The degree of vacuum determines the rate of growth of surface contaminants, the better the vacuum the slower will be the growth.

The simplest theoretical model to explain photoemission from solids is the three step model, originally put forward by Spicer (1958). This model is based on a semi-phenomenological explanation of events occurring during photoemission. According to this model photoemission is divided into three independent processes

(i) The interaction of the X-ray photon of energy $h\omega$ with an atom and the release of a photoelectron.

(ii) The transit of the electron of energy E through the material on the way to the material-vacuum interface.

(iii) The escape of the electron through the material-vacuum interface into the vacuum and on to the electron detector.

The energy distribution of the photoemitted current $I(E,\omega)$ is given by

$$I(E,\omega) = I_p(E,\omega) + I_s(E,\omega) \qquad (2.2)$$

where $I_p(E,\omega)$ is the primary distribution of electrons that have not suffered any energy loss and $I_s(E,\omega)$ is the secondary distribution of electrons which have suffered inelastic energy losses in one or more collisions. The primary distribution according to the three-step model is given by

$$I_p(E,\omega) = P(E,\omega)\, T(E)\, D(E) \qquad (2.3)$$

where $P(E,\omega)$ is the distribution of photoelectrons, $T(E)$ is the propagation factor and $D(E)$ is the escape factor. Although equation 2.3 can be used for many purposes it is often useful to write down an equation which incorporates a number of other important factors e.g that given by Hercules (1982).

The measured signal depends on many factors. Equation (2.4) describes the intensity of the XPS signal originating from the surface layers (Hercules 1982)

$$I_i = F\, S\, N_i\, \sigma_i\, \lambda_i\, T_i\, (1-e^{-d/\lambda_i}) \qquad (2.4)$$

where

I_i is the intensity of ith photoelectron of a given energy

F is the X-ray photon flux

S is the fraction of electrons detected by spectrometer

N_i is the number of atoms per cubic centimetre emitting "i" photoelectrons

σ_i is the atomic cross sections of i-level ionisation

λ_i is the mean free path of ith electrons

T_i is the transmission factor of i photoelectrons

d is the sample thickness.

In order to obtain absolute quantitative analysis, all the parameters must be known very accurately. In general this has not been accomplished because of difficulties involved in evaluating the parameters. Workers have either used calibration standards or have measured empirical atomic sensitivity factors to obtain

relative concentrations of the surface species (Shwartz and Hercules 1971, Wagner 1972). This can be done to within ±10% of the relative proportions of the chemical elements present on a sample surface. For this purpose the areas under the equivalent peaks of the elements of interest are measured above a linear background. After making allowance for the respective atomic sensitivity factors of the lines, then comparing the areas gives the relative proportions of the elements present.

Finally it is interesting to compare the time scales of the various processes derived from energy considerations, as given by Gadzuk (1978) (table 2.1). These time values give a quantitative feel for the physics of the processes. Thus the plasmon effects are clearly linked with screening response of bonding electrons.

The following sections describe in greater detail the various spectral features that are likely to be observed in an XPS spectrum.

2.2 Core-lines

Core lines are usually the most intense and the narrowest lines observed in the XPS spectrum. The basic parameters which governs the intensity of the core-lines are the atomic photo-emission cross-section, the escape depth and the photon flux. The atomic photo-emission cross-section is defined as the total transition probability per unit time divided by the resolution of the analyser. Values of the cross-sections for many useful core-lines have been calculated for AlK_{α} radiation in terms of the C1s cross-section (Scofield 1976).

The peak width, defined as the full width at half-maximum (FWHM) ΔE, is determined by several contributions :

$$\Delta E = (\Delta E^2_n + \Delta E^2_p + \Delta E^2_a)^{1/2} \qquad (2.5)$$

where ΔE_n is the natural or inherent width of the core-line, ΔE_p is the width of the X-ray photon source and ΔE_a is the analyser resolution. Equation (2.5) assumes that all components have a Gaussian line shape. The analyser contribution is the same for all peaks in the spectrum when the analyser is operated in the fixed analyser transmission (FAT) mode, but varies across the spectrum when the analyser is operated in the fixed retarded ratio (FRR) mode in which the relative resolution is constant. The natural line width of the core-line is dependent on the lifetime of the core hole remaining after photoemission. From Heisenberg uncertainty principle we obtain the line width

$$\Gamma = h/\tau \qquad (2.6)$$

with Planck's constant expressed in eV-s and the liftime τ expressed in seconds. Core-hole lifetimes are governed by the processes which follow photoemission, viz. emission of an X-ray photon (X-ray fluorescence), or emission of an electron either in an Auger process or in a Coster-Kronig process. An increase in the valence electron density enhances the probability of the relevant Auger process, decreasing the lifetime of the core-hole and thus increasing the line width. The widths of characteristic soft X-ray lines for magnesium and aluminium which are universally used in XPS machines are 0.7 eV and 0.85 eV respectively. The line shape of core-level lines in XPS spectrum is further discussed by Doniach and Sunjic (1970) and Wertheim and Citrin (1978).

The binding energies of core electrons are often referenced to the Fermi level (E_f) which is taken as the uppermost occupied state in the valence band. The true zero point of the electron energy scale is the vacuum level (E_v) and,

$$E_f - E_v = \Phi \qquad (2.7)$$

where Φ is the work function of the material (see Fig. 2.2). On an XPS spectrum of the valence band E_f is usually taken at the point of inflection on the rising part of electron density curve (EDC). The binding energies of the emitted photoelectrons are characteristic of the elements irradiated and often contain information on the chemical states of the elements. No two elements have the same set of electronic binding energy, thus making elemental identification possible. When different elements interact to form compounds bonding takes place and the electronic structure of the elements involved changes. It is possible to see shifts in the binding energies, due to bonding with other elements, on an XPS trace. This shift in the binding energies due to a change in the chemical enviroment of an atom e.g. a change in oxidation state, molecular enviroment or lattice site is known as the "chemical shift".

A change in the chemical enviroment of a particular atom involves a spatial rearrangement of the valence charges on that atom and a different potential created by the nuclear and electronic charges on all other atoms in the compound. Chemical shifts can vary from few tenth of eV to several eV.

The physical basis of the chemical shift effect is interpreted by

a simple model - the charge potential model (Siegbahn 1969)

$$E_i = E^0_i + kq_i + \Sigma_{i \neq j}\ q_j/r_{ij} \qquad (2.8)$$

where E_i is the binding energy of a particular core-line on atom i, E^0_i is a reference energy, q_i is the charge on atom i and the last term is a summation of the potential at atom i from point charges on surrounding atoms j. If the atom is considered to be an essentially hollow sphere and the valence charge q_i is distributed on the surface of the sphere, then the potential inside the sphere is the same for all points and given by q_i/r_v, where r_v is the average valence orbital radius. A change in the valence electron charge of Δq_i changes the potential inside the sphere by $\Delta q_i/r_v$. Subsequently, the binding energy of all core electrons will be modified by this amount. It follows that as r_v increases, the binding energy shift for a given Δq_i will decrease. Classically the q's are treated as screening charges that give rise to a screening potential and the summation can be abbreviated as V_i. Then the shift in binding energy for a given core line of atom i in two different enviroments A and B is

$$E_i^A - E_i^B = k(q_i^A - q_i^B) + (V_i^A - V_i^B) \qquad (2.9)$$

The first term $k\Delta q_i$ takes into account the difference in the electron-electron interaction between the core orbital and the valence charges q_A and q_B, respectively. The second term V is often referred to as Madelung potential because it is closely related to the Madelung energy of the solid. V has an opposite sign to that of Δq_i. The model described above is a simple model and does not

take into account the relaxation effects i.e. no account is taken of the polarising effect of the core hole on the surrounding electrons, both intra-atomic (on atom i) and extra-atomic (on atoms j). When a core-hole is created in the photoemission process, there is a flow of negative charge to screen the positive hole which suddenly appears. This screening has the effect of lowering the measured binding energy. The total relaxation energy $E_R(j)$ accompanying the photoemission from an orbital j is

$$E_R(j) = E_R^{in}(j) + E_R^{ex}(j) \qquad (2.10)$$

where $E_R^{in}(j)$ is the intra-atomic relaxation energy present in both free atoms and condensed phases and represents the binding energy difference between the isolated atom and the atom in the condensed phase, and $E_R^{ex}(j)$ is the extra-atomic relaxation energy present in condensed phases and occurs because of the sudden creation of a positive hole and the subsequent flow of negative charges to screen it. The extra atomic term is large in materials which have highly polarisable atoms. A difference in extra-atomic relaxation arises due to the difference in the response of a solid or a liquid or glass to the creation of the positive core hole. The screening mechanism differs from ionic through to covalent to metallic materials.

2.3 Valence levels

Valence levels are those occupied by electrons of low binding energy between the Fermi level and about 20 eV binding energy. The spectrum in this region consists of many closely spaced levels

giving rise to a band structure which closely relates to the occupied density of states structure. Figure 2.4 illustrates the density of electron states (per unit energy in unit volume) for (a) an insulator and (b) a conductor (Orchard 1977). In the case of an insulator the occupied valence band is separated from the empty conduction band, whilst in the conductor these bands overlap and the uppermost occupied state is termed the Fermi level.

Cross-sections for photoelectron emission from valence levels are much lower than for core levels, giving rise to low intensities in general.

2.4 Auger lines

As explained in section 2.1, the Auger process takes place in an ionised atom and is independent of the method of ionisation, so that it may be observed as a result of excitation by electrons, photons or ions. Since no radiation is emitted during the Auger process it is termed a radiationless transition. The kinetic energy of the electron ejected as a result of the Auger process ABC in an atom of atomic number Z can be expressed in its simplest form in the way given originally by Pierre Auger (1925), i.e.

$$E_{ABC}(Z) = E_A(Z) - E_B(Z) - E_C(Z) \qquad (2.11)$$

where E_A, E_B and E_C are the binding energies of electrons in the various respective shells. It is obvious that the Auger energy E_{ABC} expressed by equation (2.11) is a function only of atomic orbital energies, and that each atom will have a characteristic spectrum of Auger energies since no two atoms have the same set of atomic binding energies. Thus analysis of Auger energies provides an

additional means for elemental identification. The difficulty with equation (2.11) was that it did not take into account that the second electron ejected from level C is from an atom which is already ionised. The first attempt to improve the original Auger equation (2.11) was by Burhop (1952), who proposed the following empirical approximation to the Auger energy :-

$$E_{ABC}(Z) = E_A(Z) - E_B(Z) - E_C(Z+1) \qquad (2.12)$$

where $E_C(Z+1)$ is the binding energy of level C in the element of atomic number Z+1. Burhop's relation did not give very good agreement with experimental measurements of KLL transition energies, even allowing for spin-orbit effects and relativistic corrections. Another approximation to the Auger energy E_{ABC} that has proved sufficiently accurate for most practical purposes, is the one obtained, empirically, by Chung and Jenkins (1970). It is

$$E_{ABC}(Z) = E_A(Z) - [E_B(Z) + E_B(Z+1)]/2 - [E_C(Z) + E_C(Z+1)]/2 \qquad (2.13)$$

where $E_i(Z)$ are the binding energies of the ith levels in the elements of atomic numbers Z and $E_i(Z+1)$ are the binding energies of the same levels in the elements of atomic number (Z+1).

A more physically acceptable expression for the Auger energy (Hoogewijs 1977) is given as :

$$E_{ABC}(Z) = E_A - E_B - E_C - F(BC:x) + R_x \qquad (2.14)$$

where F(BC:x) is the energy of interaction between the holes in B and C in the final atomic state x and R_x is the relaxation energy. The relaxation energy R_x is split into two terms

$$R_x = R_x^{in} + R_x^{ex} \qquad (2.15)$$

where Rx^{in} is the intra-atomic relaxation energy and Rx^{ex} is the extra-atomic relaxation energy.The magnitudes of the F and R terms are often a number of electron volts.. In the calculation of Auger energies using equation (2.14) it is customary to use experimentally determined binding energies E_i and calculated values for the other terms, so that the approach is semi-empirical.

A change in the chemical state giving rise to a chemical shift in the photoelectron spectrum will also produce chemical shifts in the Auger spectrum. However, the magnitude of the Auger shifts is often significantly greater than that of the photoelectron chemical shifts (see for example Wagner and Biloen (1973)).

The term scheme used to describe Auger transitions for elements of atomic number in the range $20 \leq Z \leq 75$ is the intermediate coupling (IC) scheme where neither of the j-j nor L-S coupling schemes adequately describe the transitions observed. In this coupling scheme the nomenclature is that of term symbols of the form $^{(2S+1)}L_J$ with each L-S term split into the multiplets of the different J values. The intermediate coupling scheme predicts ten possible states in the KLL series, shown in table 2.2, but one of these ($^3P_1$) is forbidden through the principle of conservation of parity. As can be seen from table 2.2, it is common to use a mixed notation, so that the KLL transitions would be $KL_1L_1(^1S_0)$, $KL_1L_2(^1P_1)$, $KL_1L_2(^3P_0)$, $KL_2L_2(^1S_0)$, $KL_1L_3(^3P_1)$, $KL_1L_3(^3P_2)$, $KL_2L_3(^1D_2)$, $KL_2L_3(^3P_1)$(forbidden)), $KL_2L_3(^3P_0)$ and $KL_3L_3(^3P_2)$.

2.5 Plasmon loss features

As mentioned in section 2.1 any electron of sufficient energy passing through a solid can excite collective oscillations of conduction electrons. These plasmons result in the appearance of peaks at lower kinetic energies of the primary peak representing energy losses (Powell 1968, March and Parrinello 1982). Energy loss to the conduction electron occurs in well-defined quanta characteristic of the material of the solid. An electron that has given up an amount of energy equal to one of these characteristic energies, in the course of excitation, is said to have suffered a plasmon loss. Many of the features of collective plasmon loss oscillation can be described by the "Jellium model" of Pines (1964). This model views the metal as consisting of a system of positive ions immersed in a sea of valence electrons. At equilibrium there are equal quantities of positive and negative charges at any point. If an imbalance occurs, i.e in the course of photoemission, then the valence electrons will try to maintain charge neutrality by screening the variation in the charge density but will be pulled back in the positive region by Coulombic attraction and proceed to oscillate with simple harmonic motion. Because of the long range of Coulomb interaction this oscillation is only part of the correlated oscillation of all the free electrons. The so-called "bulk" plasmons (which are the more prominent of these lines) correspond to the losses which occur within the solid. The fundamental characteristic frequency of the bulk plasmon ω_b is given by (Mahan 1978, Kittel

1986) :

$$\omega_b = (ne^2/\varepsilon_0 m)^{1/2} \qquad (2.16)$$

where n is the valence electron density, e is the electronic charge, m is the electronic mass, and ε_0 is the permittivity of free space. The bulk plasmon energy is given by the energy interval between the primary peak and the loss peak,

$$\Delta E = \hbar\omega_b = \hbar (ne^2/\varepsilon_0 m)^{1/2} \qquad (2.17)$$

From equation (2.17), the plasmon energy is dependent on the electron density so a change in electron density with composition should result in a measurable change in plasmon energy. Since electrons that have suffered plasmon loss in energy can themselves suffer further losses of this kind in a sequential fashion, then a series of losses, all equally spaced by $\hbar\omega_b$ but of decreasing intensity will occur (Ritchie 1957).

At a surface the regular atomic lattice of the solid terminates and a different type of collective oscillations can be excited. These correspond to the surface plasmons with fundamental frequency ω_s which can be shown to be equal to $\omega_b/(1+\varepsilon)^{1/2}$, with ε being the dielectric constant (Stern and Ferrel 1960). For a free electron metal ω_s can be shown theoretically to be equal to $\omega_b/\sqrt{2}$ (Ritchie 1957). Plasmon loss peaks are observed in XPS spectra at lower kinetic energies of the elastic peak. The fundamental or "first" plasmon loss will always be observable for most materials and several multiple plasmon losses of decreasing intensity may also be observable depending on the material and experimental conditions.

Surface plasmon loss peaks may be found but will always be of lower intensity than the adjacent bulk plasmon peak.

The excitation of plasmons in photoelectron spectroscopy is often described in two ways : (1) an intrinsic process due to the collective response of valence electrons to the creation of a core hole as a consequence of photoelectron emission; (2) an extrinsic process due to the collective excitation of valence electrons as photoelectrons are transmitted to the material vacuum interface and is manifested most clearly in the free electron metals, for example Al or Mg (van Attekum and Trooster 1978, 1979). The relative intensity and origins of the two types of plasmons in photoemission has not been clearly resolved (Pardee, Mahan, Eastman, Pollack, Ley, McFeely, Kowalyczyk and Shirley 1975; Cardona and Ley 1978), but the intrinsic process is believed to contribute a minor part of the total intensity (van Attekum and Trooster 1978, 1979) who state that intrinsic processes contribute 25% of the total plasmon loss intensity from Al metal and 22% of the total loss intensity from Mg metal. It must be pointed that for the transition and noble elements and those elements, such as Au, Ag etc., which have d states close to the Fermi level, strong plasmon peaks are not observed. An alternative to plasmon excitation is interband transition. In the present work the measurement of plasmon energies is very important because of their relationship to the electronic structure of glasses under investigation (Orton et al 1990).

Recently, a simple model based on plasma frequency formalism has been developed for the calculation of the average energy gap and other associated parameters for various crystal structures (Srivastava 1984a, 1984b, 1986, 1987). The average energy gap of the X-Y bond is given by

$$E^2_g = C^2_{XY} + E^2_{h,XY} \qquad (2.18)$$

where C is the ionic part and E_h is the covalent part. It was shown by Srivastava (1987) that the ionic and covalent energy gaps for the B-C bond in $A^{II}B^{IV}C_2^{V}$ semiconductors can be written in terms of plasmon energy as

$$E_{h,BC} = 0.04158\ (\hbar\omega_{p,BC})^{\nu} \quad eV \qquad (2.19)$$

$$C_{BC} = 1.81\ b_{BC}(\hbar\omega_{p,BC})^{\mu}\exp\{-6.4930\ (\hbar\omega_{p,BC})^{-\mu/2}\}\ eV \qquad (2.20)$$

where ν=1.6533, μ=2/3 and the average value of the prescreening constant b_{BC} = 2.4516.

In this work we make use of the above equations to calculate the average energy gaps E_g of Ge-Se bonds from our experimentally determined plasmon energies from the $L_3M_{4,5}M_{4,5}$ Auger lines of Se. It is assumed that the ternary additive can take on the role of a group-II element and that selenium takes on the role of a group-V element and that it can be ionic, as demonstrated by the ability to form valence-alternation pairs (VAP) (Kastner 1980) and single-bonded charged ions.

2.6 X-ray satellites

Standard X-ray sources are not monochromatic, therefore the X-ray emission spectra used for irradiation exhibits not only the principal $K\alpha_{1,2}$ line (the transitions giving rise to $K\alpha_{1,2}$ are

$2p_{3/2,1/2}$ -> 1s) but also a series of low intensity lines at higher photon energies referred to as X-ray satellites. Satellites arise from less probable transitions (e.g. K_β; valence band-> 1s) or transitions in a multiply ionised atom (e.g. $K\alpha_{3,4}$). The intensity and spacing of these lines are characteristic of the X-ray anode material. The patterns of such satellites for Mg and Al anodes are shown in table 2.3.

2.7 X-ray ghosts

X-ray ghosts are due to excitations arising from an element other than the X-ray source anode material which produce on impinging upon the sample small peaks corresponding to the most intense spectral peaks but displaced by a characteristic energy interval. The most common of these lines are due to the generation of X-ray photons in the aluminum foil X-ray window which will produce ghost peaks 233.0 eV to the higher kinetic energy of those excited by the dominant Mg $K\alpha_{1,2}$ .These lines can also be due to Mg impurity in the Al anode , or vice versa , or could be excited by Cu L_α radiation from the anode base structure which will produce ghost peaks 323.9 eV(556 eV) to lower kinetic energies of Mg $K\alpha_{1,2}$ ($AlK\alpha_{1,2}$) excited peaks. The appearance of ghost lines is a rare occurrence.

2.8 Shake-up/off satellites

Not all photoelectronic processes are simple ones, leading to the formation of ions in the ground state. On occasions, there is a finite probability that the ion will be left in an excited state, a few

eV above the ground state. In this case, the kinetic energy of the emitted photoelectron is reduced, with the difference corresponding to the energy difference between the ground state and the excited state. This results in the formation of a satellite peak a few eV lower in kinetic energy than the main peak. These peaks are referred to as shake-up satellites.

Valence electrons can be excited to an unbound continuum state, i.e. completely ionised. This process which leaves an ion with vacancies in both a core level and a valence level is referred to as shake-off. However, discrete shake-off satellites are rarely discerned in the solid-state because firstly the energy separation from the primary photoelectron peak is greater than for shake-up satellites, which means that the satellites tend to fall within the region of the broad inelastic tail, and secondly transitions from discrete levels to a continuum produce onsets of broad shoulders rather than discrete peaks (Briggs and Seah 1983).

2.9 Instrumentation

2.9.1 The spectrometer

The basis of electron spectroscopy is the measurement of the kinetic energies of electrons emitted from a sample under vacuum following ionisation by incident photons or electrons.

The X-ray photoelectron spectrometer used in this study, shown schematically in Fig. 2.5, was a type ES300 manufactured by Kratos. The essential components of this spectrometer are (1) sample analysis chamber (2) X-ray excitation sources (3) electron

energy analyser and detector. Additional features to the basic spectrometer included an argon ion etching gun, a sample insertion probe with heating and cooling facilities, a pumped sample treatment chamber, and a quadrupole mass spectrometer for residual gas analysis.

2.9.2 Vacuum system

As mentioned in section 2.1, XPS is a surface sensitive technique sampling a number of monolayers, which requires a clean sample enviroment, hence ultrahigh vacuum (UHV) conditions are essential. For studies of clean samples an ultrahigh vacuum of 10^{-9} torr or less is needed, since at about 10^{-6} torr a monolayer of gas typically forms in about 1-5 seconds at room temperatures, while at 10^{-9} torr a monolayer forms in about 30 minutes. Surface contamination obscures the signal from the surface one wishes to study. For most surface sensitive materials the best possible vacuum must be used. However, for the present work the vacuum conditions were relaxed to values better than 10^{-7} torr.

The pumping system used on ES300 consisted of two liquid nitrogen cold trapped diffusion pumps and two rotary pumps. The rotary pumps evacuate down to 10^{-3} torr from atmosphere. One of them was used for general roughing of the insertion lock, the other provided the backing for the main UHV diffusion pumps. The diffusion pumps produce a vacuum over the range 10^{-3} to 10^{-9} torr or better with the use of liquid nitrogen cold traps. The

analysis chamber was evacuated by one diffusion pump, while the other diffusion pump was used to reduce the pressure in the sample treatment chamber. The spectrometer analysis chamber was constructed from stainless steel. This allows the whole spectrometer to be heated up to about 200^0 C using a "bake out" hood or shield around the spectrometer to facilitate the attainment of UHV by the removal of residual gas from the spectrometer inner walls. Stainless steel is also a good material for making "knife-edge" flanges which provide a good seal between one part of the spectrometer and another, by the use of soft copper gaskets.

2.9.3 Operation of sample insertion lock and probe

Vacuum compatible samples were introduced into the spectrometer by attachment to the end of a long, very highly polished probe, which has cooling and heating facilities. The sample probe was introduced into the evacuated analysis chamber via a sample insertion lock (Fig. 2.6). It was inserted until it sealed on the first "Viton" O ring, the insertion lock was then pumped out using a rotary pump to about 10^{-3} torr. The probe was then pushed in until it sealed on the second O ring. The insertion ball valve was then slowly opened, maintaining the spectrometer pressure below 10^{-5} torr, the sample probe was then inserted further to align the sample surface with the argon ion etching gun for cleaning the surface. After ion etching, the sample was aligned with the X-ray gun for analysis. The sample probe had the provision for rotation so that angular dependence analysis could be

carried out.

2.9.4 The X-ray source

The X-ray source used in the Kratos ES300 was a dual anode AlK_{α} or MgK_{α} X-ray gun (Fig. 2.7). The filament was at near earth potential, while the anode was at a few KV positive potential. The impinging electron from the filament strike the anode, emitting X-radiation characteristic of the anode material. The Al window, through which the X-rays pass to enter the sample chamber, filters out much of the continuous Bremsstrahlung radiation and most of the unwanted characteristic lines superimposed on it. It also acts as a barrier to elecrons stopping them from passing directly into the analysis chamber.

The X-ray source was separately pumped from the spectrometer by an ion triode pump, this avoids contamination of samples by outgassing products from the X-ray gun as well as keeping the X-ray source clean from contamination by pump hydrocarbons and volatile samples. The anode material was coated onto a copper base through which copper tubing provided water cooling, to prevent anode evaporation.

2.9.5 The electron energy analyser

The analyser used was a 127 mm radius, 180^0 deflection concentric hemispherical electrostatic analyser with a retarding lens (Fig. 2.8). The analyser measures the energy distribution of photoelectrons emitted from the irradiated sample by dispersing the electron energies in a deflecting electrostatic field so that only those electrons in a narrow energy band are collected at one time.

The photoelectrons enter the analyser through a slit and travel along equipotential lines in a circular path in a field set up by a potential difference between the inner and outer hemispheres (Fig. 2.9). This field provides two dimensional point to point focussing after 180^0 deflection. The field was shielded from stray magnetic field by a mu-metal screen. At the exit slit the field was terminated by biased electrodes. The source and collector slit widths (W_S and W_C respectively), could be varied in size to change spectral resolution, (thus decreasing the slit widths increases resolution but decreases sensitivity and vice versa). The analyser could be operated in two different modes, fixed analyser transmission (FAT) mode and fixed retarding ratio (FRR) mode. In FAT mode the analyser voltage is kept constant while the retarding ratio is varied. The sensitivity in FAT mode is inversely proportional to kinetic energy. In FRR mode the retarding ratio is kept constant while the analyser voltage is varied and the sensitivity is proportional to kinetic energy. The present study made use of the FAT mode.

2.9.6 Peak widths

The full width at half maximum (FWHM) is given by equation 2.5. The analyser resolution, which is dependent on the emission energy and the choice of the slit widths is given by Kratos as:

$$\Delta E_a = E\ W/230 \qquad (2.21)$$

where W is the width in inches of the source slit or the collector slit whichever is the largest, and E is the energy of the electrons being

investigated. The slits width is changed from outside the vacuum system by operating the knurled nut on the adjustment mechanism which is mounted on the body of the collector. Four postions are available :

position 1 0.20 inch

2 0.12 inch

3 0.07 inch

4 0.04 inch

For the present work, source and collector slits were put on position 2.

2.9.7 Resolving power and resolution

Resolving power is defined as the ratio :

$$p = E/\Delta E \qquad (2.22)$$

where E is the kinetic energy of the photoelectron being studied. Relative resolution is defined (Briggs and Seah 1983) as the reciprocal of p, i.e :

$$R = 1/p = \Delta E/E \qquad (2.23)$$

For Kratos ES300, R is given by

$$\Delta E/E = W/230 \sim 5 \times 10^{-4} \qquad (2.24)$$

2.9.8 The detector

The collector slit current (which is about 10^{-13} to 10^{-19} A) was detected by an electron multiplier called a " channeltron ". A channeltron consists of a coiled tube of semiconducting glass, the inside of which has a high secondary electron emission coefficient. The incident electrons strike the tube walls, producing a shower of

secondary electrons, these produce a cascade of subsequent electron showers along the tube giving an overall gain of about 10^8. Output of the detector passes through an amplifier, ratemeter system to a digital data storage system, where the output of the electron counts versus electron kinetic energy is displayed.

2.9.9 The ion gun

The ion gun used in the ES300 spectrometer was a rastered ion tech B21 gun (Fig. 2.10). The ion gun was used for sample cleaning in situ. The B21 ion gun produced a beam of positive argon ions (Ar^+) of energies from 0 to 5 keV. The beam was rastered mechanically across the sample surface, the ions bombard the sample surface, first cleaning contaminant atoms from the surface and then removing actual sample atoms. The B21 is a discharge source, in it there is an electrostatic field which has the configuration shown in Fig. 2.10. Because of the shape of the field configuration this type of source is referred to as the "saddle field" source. Fast moving electrons ionise argon (fed into the gun at a pressure of about 10^{-4} torr) and a steam of Ar^+ ions is extracted through a slit lying along the saddle field's axis giving a diverging ion beam which impinges on the sample and etches it. Care has to be exercised in interpreting data obtainable after ion etching because it can introduce many artefacts such as chemical state, topographical (islanding or surface roughening), or elemental composition changes due to varying sputtering yields for different elements.

2.9.10 Spectrometer conditions

AlK_{α} was used as the exciting radiation for all the measurements reported with an excitation voltage of 14 kV and an excitation current of 15 mA. These values are recommended by the manufacturer as giving the best signal to background ratio. The sample was positioned at 30^0 to the X-ray beam giving approximate maximum signal intensity. The Ar^+ ion beam used for etching was directed close to the normal to the surface to prevent shadowing effects (Seah and Lea 1981). Rastering of the gun ensured that the whole surface of the sample was etched. Samples were etched using 4-5 kV, 2mA Ar^+ ions for 30 minutes.

2.9.11 Determination of peak positions

The procedures followed in determining peak positions are those recommended by Wagner (1978), Anthony and Seah (1984), Bird and Swift (1980) and the ASTM (1987). A typical photoelectron peak is shown in Fig. 2.11. The peak position is determined by bisecting a number of chords near the top of the peak and drawing the best straight line through the midpoints to intersect the peak. In the case of the overlapping of two peaks, only those upper parts of the peak which do not overlap are used to draw chords for bisecting.

2.9.12 Calibration of photoelectron spectrometer

The calibration procedure followed was based on the method described in the Kratos ES300 instruction manual. To check the

agreement with Anthony and Seah's reference binding energy values, spectroscopically clean thin foils of Au, Ag, and Ni were firmly screwed to a 4 sided Cu sample holder leaving one face exposed for Cu measurements. After achieving the best vacuum conditions, surfaces were Ar^+ etched (5kV,2mA) to reduce surface contaminants (mainly carbon and oxygen). The intense d band of the conduction electrons in Ni metal provides a Fermi edge for use as a zero reference. The peaks were recorded in FAT mode in the following order : Cu $2p_{3/2}$, Cu LMM, $Cu2p_{3/2}$, Ag MNN , $Cu2p_{3/2}$, $Ag3d_{5/2}$, $Cu2p_{3/2}$, $Au4f_{7/2}$, $Cu2p_{3/2}$, Ni Fermi level, and $Cu2p_{3/2}$. The determination of $Cu2p_{3/2}$ value between measurements allowed the instrument drift and the repeatability of the results to be assessed. The electronics were left on overnight to reduce drift mobilities. Twenty minutes were allowed for stabilisation of the X-ray source before taking measurements. The binding energies were measured with respect to the Fermi level of Ni. The results of the calibration are summarised in table 2.4. The errors were assessed by considering the difference D in binding energies between the values obtained by this calibration and those obtained by Anthony and Seah (1984) at National Physical Laboratory (NPL). The difference D was plotted as a function of measured binding energies for the reference peaks (Fig. 2.12), and a least square fit was made. The gradient of the least square fit showed an inaccuracy in the voltage measurement indicating a voltage scaling error of 366.8 ppm. It also indicated that the zero was offset by 97.8 meV. These measurements were used to check on the general

performance of the spectrometer and were not used to normalise any of the observed data.

CHAPTER 3

X-ray diffraction from a disordered structure

3.1 Introduction

As described earlier in section 2.9.4, the output of an X-ray tube contains intense radiation of well-defined wavelength characteristic of the target element, superimposed on the relatively low intensity continuous spectrum. If the output from such an X-ray tube is incident on a material, the intensity of the scattered radiation from an atom will depend on the scattering angle 2θ, which is the angle between the incident and scattered beams. The scattered radiation will be partly coherent and partly incoherent.

Coherent scattering occurs when the incident X-rays are elastically scattered by the electrons within the atom. According to classical electrodynamics the electron is forced to oscillate at the same frequency as the incident X-rays, resulting in the re-emission of this frequency in all directions. The intensity scattered by the nucleus is negligible because the mass of the nucleus is very much greater than that of the electron. Assuming that the electrons are distributed throughout the atomic volume and the wavelength of incident X-rays is comparable to the atomic size, interference

effects between waves scattered by different electrons in the atom will occur. In the forward direction ($2\theta = 0$), waves scattered by different electrons in the atom are in phase. At all other scattering angles, waves scattered by different electrons will be out of phase by an amount depending on the scattering angle, thus resulting in a reduction in intensity compared to that in the forward direction. The ratio of the amplitude of scattered radiation by the atom to that scattered by a free electron is defined by the atomic scattering factor f, given by

$$f = \frac{\text{Amplitude of wave scattered by the atom}}{\text{Amplitude scattered by a free electron}} \qquad (3.1)$$

which is usually given as a function of $s = \sin\theta / \lambda$, where λ is the wavelength of the incident radiation. The amplitude of the radiation scattered by a free electron is given by Thomson's equation (Compton and Allison 1935). Therefore f^2 is a measure of the intensity scattered by an atom to that scattered by an electron often defined in electron units. In the forward direction where no interference occurs, the amplitude scattered by an atom will be simply the sum of the amplitudes independently scattered by its electrons and hence for s=0, f=Z. If there were no interference effects between the coherent scattering from the individual atoms the coherent intensity from N atoms would be given by Nf^2. In crystals there are strong interference effects between the coherent scattering from different atoms, due to the regular atomic arrangement, and very intense coherent scattering occurs in sharply defined directions. In disordered structures (gases, liquids,

amorphous solids) where the atomic order is considerably less (short range order), interference effects are much less marked.

Incoherent scattering occurs when the incident X-rays are inelastically scattered by the electrons within the atom. The scattered X-rays have wavelengths longer than the incident wavelength. The increase $\Delta\lambda$ in the wavelength of the scattered X-rays over that of the incident is given by

$$\Delta\lambda = \lambda_c - \lambda = h(1 - \cos 2\theta)/(m_0 c) \qquad (3.2)$$

where h is Planck's constant, m_0 is the rest mass of the electron and c is the speed of light. The scattered Compton radiation covers a band of modified wavelengths centred on λ_c. Due to the variation of λ_c with θ, the possibility of interference between modified waves from different atoms is very small. The intensity of Compton incoherent scattering is large for low mass atoms, where the electrons are loosely bound. The amount of Compton scattering from a given atom will thus be determined by the photon energy of the incident X-rays, so the shorter the incident wavelengths the greater is the Compton intensity. Tabulated values for Compton intensity are given by Compton and Allison (1935). An approximate formula for the incoherent intensity is given by James (1950),

$$I_{inc} = Z - f^2/Z \qquad (3.3)$$

where Z is the atomic number. For low angles I_{inc} tends to zero since f tends to Z. The total incoherent scattering for a mixture of atomic types is the sum from all the individual atoms and is

independent of the state of the specimen. However, if it is crystalline, the total incoherent scattering is very small compared with coherent scattering and may be neglected. In the case of a disordered material the incoherent scattering may be an appreciable fraction of the total scattering especially at high angles. Incoherent scattering can, however, be reduced to negligible proportions by the use of post-diffraction monochromatisation, as in the present work.

Apart from coherent and incoherent scattering, the atom may emit fluorescent radiation which results from the atom de-exciting by emitting radiation of characteristic frequencies in all directions with equal intensity. This can occur if the incident radiation has sufficient energy to eject inner shell electrons from the atoms of the specimen. Outer shell electrons will subsequently fall into the vacancies with the emission of fluorescent radiation characteristic of the atom. The fluorescent wavelength is always longer than that of the incident radiation and provided that the wavelength of the incident radiation is not close to an absorption edge, fluorescent radiation may be neglected.

The theory of diffraction applies only to the coherently scattered radiation, thus precautions must be taken to ensure that experimental intensities are free from any other components. This can be achieved mainly by the proper choice of incident wavelength and the use of post-diffraction monochromatisation.

The scattering of X-rays by an arbitrary structure is

considered in detail in Guinier (1963) and a brief description of the theory is given here.

3.2 Calculation of the diffracted amplitude from a small object

Consider a monochromatic parallel beam of X-rays incident on an atomic scattering centre at point 0 (Fig. 3.1). If the amplitude of the incident wave at point 0 is $A_0 \cos \omega t$, then the amplitude of scattered wave at the distance r from 0 is given by

$$A = f A_0 \cos [\omega(t - r/c) - \Psi] \qquad (3.4)$$

where f is the atomic scattering factor and Ψ is the scattering phase shift which is generally equal to π. If two scattering centres O and M (Fig. 3.1) are considered, then the resultant scattered radiation in a given direction is due to the interference of the waves scattered by O and M. Let us assume that the phase shift Ψ due to scattering is the same for both centres. The phase difference between the emitted waves depends on the respective positions of the two scattering centres O and M. The path length for the ray going through M is greater by $\delta = mM + Mn$, m and n being the projections of O on the rays through M. If we define the directions on the incident and scattered rays by the unit vectors $\underline{S_0}$ and $\underline{S}$, then

$$\begin{aligned} mM &= \underline{S_0}.\underline{OM} \\ Mn &= - \underline{S}.\underline{OM} \\ \delta &= - \underline{OM}.(\underline{S} - \underline{S_0}) \end{aligned} \qquad (3.5)$$

the phase difference is therefore

$$\Phi = (2\pi\delta)/\lambda = -2\pi \underline{OM}.(\underline{S} - \underline{S_0})/\lambda \qquad (3.6)$$

Here we introduce the scattering vector $\underline{s}$ which is equal to $(\underline{S} - \underline{S_0})/\lambda$ and plays a fundamental role in scattering theory and will be used throughout all scattering calculations. It should be noted that since phase differences depend only on the vector $\underline{s}$, interference calculations do not depend explicitly on the three parameters $\underline{S}$, $\underline{S_0}$ and λ but only on $\underline{s}$. As shown in Fig. 3.2, the direction of $\underline{s}$ is that of ON which bisects the angle formed between $\underline{S}$ and $-\underline{S_0}$, and its magnitude is

$$s = 2 \sin\theta/\lambda \, . \qquad (3.7)$$

All scattering experiments can be reduced to the determination of the value of the scattered intensity for as many s values as can be measured.

We now need to calculate the amplitude resulting from the addition of the waves scattered by the individual atoms. Using the Fresnel geometrical method, the amplitude resulting from the interference of several waves will be represented by the vector sum of the component amplitudes (Fig. 3.3). For any number of scattering centers with scattering factors $f_0, f_1, f_2, \ldots, f_n$ and corresponding phase differences $0, \Phi_1, \Phi_2, \ldots, \Phi_N$, the resultant amplitude is

$$A = A_0 \left[\left(\sum_0^n f_i \cos\Phi_i \right)^2 + \left(\sum_0^n f_i \sin\Phi_i \right)^2 \right]^{1/2} \qquad (3.8)$$

The observable quantity in any system is the intensity of X-rays

which is given by the square of the modulus of the amplitude. It is also the product of the complex amplitude and its complex conjugate, so it is useful to write Eq. (3.8) in complex notation as

$$A = A_0 \sum_{0}^{n} f_i \exp(i\Phi_i) \tag{3.9}$$

Let us consider a group of N atoms with atomic scattering factors $f_1, f_2, \ldots, f_n$ and their positions with respect to an arbitrary origin to be given by the vectors $\underline{x}_1, \underline{x}_2, \ldots, \underline{x}_n$. The amplitude of the scattered wave of the n-th atom being f_n times larger than if it were replaced by an isolated electron. It is assumed that the object is small enough that absorption can be neglected. The incident beam is then of the same intensity for all the atoms. The amplitude $A(\underline{s})$ of the diffracted wave is given by

$$A(\underline{s}) = \sum_{1}^{n} f_n \exp(-2\pi i \underline{s}.\underline{x}_n) \tag{3.10}$$

and if the individual atoms are replaced by a function representing the electron density, $\rho(\underline{x})$, then Eq. (3.10) for $A(\underline{s})$ is replaced by

$$A(\underline{s}) = \int \rho(\underline{x}) \exp(-2\pi i \underline{s}.\underline{x}) dv_x \tag{3.11}$$

This integral is evaluated over all of the object space and it is easily interpreted in terms of a Fourier transformation pair $\rho(\underline{x})$

and $A(\underline{s})$. $\rho(\underline{x})$ can be deduced from $A(\underline{s})$ using an inverse transformation

$$\rho(\underline{x}) = \int A(\underline{s}) \exp(2\pi i \underline{s}.\underline{x}) dv_s \qquad (3.12)$$

The integral for $\rho(\underline{x})$ is extended to all of reciprocal space. Because it is not possible to measure the amplitude of scattered X-rays the equations given above cannot be used directly.

3.3 Calculation of the diffracted intensity from a small object

Let us consider an object which is small enough that absorption is negligible, and then let us replace the object by a single free electron, all other experimental conditions remaining unchanged. The scattering power of the object $I_N(\underline{s})$ is defined as the ratio of the measured intensity from the object and an isolated electron. The scattering power per atom (or per atomic group if the object is composed of N such groups) is given by

$$I(\underline{s}) = I_N(\underline{s})/N \qquad (3.13)$$

The interference function is defined as

$$J(\underline{s}) = I(\underline{s})/F^2 = I_N(\underline{s})/NF^2 \qquad (3.14)$$

where $F(\underline{s})$ is the structure factor of the atomic group. The interference between the scattered waves determines the value of the interference function and it would be equal to unity for any value of $\underline{s}$ if the atomic groups scattered incoherently. Considering the relationship between the amplitude of the scattered wave and its intensity and using Eq.(3.10) we can write

$$I_N(\underline{s}) = |A(\underline{s})|^2 = A(\underline{s})\, A^*(\underline{s})$$

$$= \sum_{1}^{n} f_n \exp(-2\pi i \underline{s}.\underline{x}_n) \sum_{1}^{n'} f_{n'} \exp(2\pi i \underline{s}.\underline{x}_{n'}) \qquad (3.15)$$

$$= \sum_{1}^{n}\sum_{1}^{n'} f_n f_{n'} \exp(-2\pi i \underline{s}.(\underline{x}_n - \underline{x}_{n'}))$$

Setting $\underline{x}_{nn'}$ as the vector from atom n to atom n', the intensity becomes

$$I_N(\underline{s}) = \sum_{1}^{N} f_n^2 + \sum_{n}\sum_{n'} f_n f_{n'} \cos(2\pi \underline{s}.\underline{x}_{nn'}) \qquad (3.16)$$

For identical atoms or atomic groups with structure factor F, the unit scattering power is

$$I(\underline{s}) = \frac{I_N(\underline{s})}{N} = F^2 + \frac{F^2}{N}\sum_{n}\sum_{n'} \cos(2\pi \underline{s}.\underline{x}_{nn'}) \qquad (3.17)$$

and the interference function is

$$J(\underline{s}) = \frac{I(\underline{s})}{F^2} = \frac{I_N(\underline{s})}{NF^2} = 1 + \frac{1}{N}\sum_{n}\sum_{n'} \cos(2\pi \underline{s}.\underline{x}_{nn'}) \qquad (3.18)$$

We can now average over all possible orientations and it can be shown that the final expression for the interference function is

$$J(s) = 1 + \frac{1}{N}\sum_{n}\sum_{n'}\frac{\sin(2\pi s x_{nn'})}{2\pi s x_{nn'}} \qquad (3.19)$$

This is known as the Debye equation and from this equation the interference function can be calculated provided that the positions of all the atoms are known.

3.4 Scattering from a homogeneous, isotropic, finite disordered structure.

Let us consider matter which is homogeneous, in which the distribution of the atoms with respect to one of them is statistically independent of the atom which is chosen to be at the origin. It is also assumed that the matter under consideration is made up of a single type of atom or atomic group. It can be shown (Guinier 1963) that the intensity measured experimentally can finally be written as

$$J(\underline{s}) = 1 + (1/v_1)\int [P(\underline{x}) - 1] \exp(-2\pi i\, \underline{s}.\underline{x})\, dv_x \qquad (3.20)$$

where v_1 is the average volume available for each atom, and $P(\underline{x})$ is the distribution function which defines the statistical configuration of the atoms. $J(\underline{s})$ is independent of the volume and shape of the object. It depends exclusively on the statistical distribution of the atoms in homogeneous and infinite matter. If this distribution is statistically uniform, $P(\underline{x})=1$, then the interference function is constant and equal to unity in reciprocal space. The variations of this function about the average value show the variations in the

atomic distribution. The inverse Fourier transform of Eq. (3.20) leads to the determination of the distribution of the atoms in the object, as defined by the function $P(\underline{x})$:

$$P(\underline{x}) = 1 + v_1 \int [J(\underline{s}) - 1] \exp(2\pi i\, \underline{s}.\underline{x})\, dv_s \qquad (3.21)$$

This is the most complete result which X-ray diffraction can provide about the structure of an object formed of identical atoms or group of atoms when it is statistically homogeneous.

If we now further assume that the matter under consideration is isotropic then $P(\underline{x})$ depends only on the modulus of $\underline{x}$ and not on its direction. These conditions are found in gases, in most liquids and also in glasses discussed in the present work. It can be shown that

$$\int [P(\underline{x})-1]\exp(-2\pi i \underline{s}.\underline{x}) dv_x = 2\int_0^\infty [P(x)-1]\frac{\sin(2\pi s x)}{s} x\, dx \qquad (3.22)$$

Then Eq. (3.20) is replaced by

$$J(s) = 1+\frac{2}{v_1 s}\int_0^\infty [P(x)-1]\sin(2\pi s x)\, x\, dx \qquad (3.23)$$

and the distribution function P(x) can be obtained by inverse Fourier transform of Eq.(3.23) to give

$$P(x) = 1+\frac{2v_1}{x}\int_0^\infty [J(s)-1]\sin(2\pi s x)\, s\, ds \qquad (3.24)$$

The interference function Eq. (3.23) can also be written differently as

$$J(s) = 1+ \int_0^{\infty} 4\pi x^2 [\rho(x)-\rho_0] \frac{\sin(2\pi sx)}{2\pi sx} dx \qquad (3.25)$$

where $\rho(x)$ is the atomic density at a distance x from an origin atom and tends towards the average density ρ_0 when x becomes large. The radial distribution function $4\pi x^2\rho(x)$, has a useful physical interpretation, which represents the number of atoms in a spherical shell of thickness dx and with radius x from the origin atom. The number of atoms surrounding another atom up to some distance R is therefore

$$N = \int_0^R 4\pi x^2 \rho(x) dx \qquad (3.26)$$

X-ray diffraction by a homogeneous and isotropic body therefore gives the average number of neighbouring atoms as a function of the distance to the atom chosen to be at the origin.

Until now we have assumed that all the atomic scattering centres were identical. The case of a random mixture of several different types of atoms or group of atoms is very complex.

Consider a set of different types of atoms for which we can define both the positions of the atoms and the nature of the atom occupying a given position, the two distributions being completely independent. The intensity is the average of equation (3.16) evaluated over all possible configurations :

$$\overline{I_N(\underline{s})} = N\overline{f_n^2} + \sum_n \sum_{n'} \overline{f_n f_{n'} \cos(2\pi \underline{s}.\underline{x}_{nn'})} \qquad (3.27)$$

or

$$\overline{I_N(\underline{s})} = N\overline{f_n^2} + \sum_n \sum_{n'} \bar{f}_n \bar{f}_{n'} \overline{\cos(2\pi \underline{s}.\underline{x}_{nn'})}$$

which can be written as

$$\overline{I_N(\underline{s})} = N[\overline{f_n^2} - \overline{(f_n)}^2] + \overline{(f_n)}^2 [N + \sum_n \sum_{n'} \overline{\cos(2\pi \underline{s}.\underline{x}_{nn'})}] \qquad (3.28)$$

where $\overline{f}^2 = c_A f^2_A + c_B f^2_B$ and $\bar{f} = c_A f_A + c_B f_B$ with c_A and c_B being the atomic concentrations of A and B respectively in the binary alloy AB. The intensity is thus decomposed into two terms, the second of which is the diffracted intensity for a set of N identical atoms with scattering factors $\bar{f}_n$. The interference function for different types of atoms can be written from equation (3.28) as

$$J(\underline{s}) = \frac{I_N(\underline{s})}{N\overline{(f_n)}^2} = \frac{\overline{f_n^2} - \overline{(f_n)}^2}{\overline{(f_n)}^2} + \left[1 + \frac{1}{N} \sum_n \sum \overline{\cos(2\pi\, \underline{s}.\underline{x}_{nn'})}\right] \qquad (3.29)$$

The additional scattering term (first term in equation 3.29) results from the differences between the scattering factors of the various atomic scattering centres. Since, in general, $\overline{f^2}_n$ and $\bar{f}_n$ vary slowly with $\underline{s}$ in the case of atoms or small molecules, this term gives a general scattering of low intensity with no pronounced maxima but

varying slowly with diffraction angle and it is superimposed over the scattering pattern produced by average identical atoms.

The total interference function $J_t(s)$ for a binary alloy AB can be written as the sum of partial interference functions $J_{AA}(s)$, $J_{BB}(s)$ and $J_{AB}(s)$ (Wagner and Halder 1967) :

$$J_t(s) = \alpha J_{AA}(s) + \beta J_{BB}(s) + \gamma J_{AB}(s) \qquad (3.30)$$

where $\alpha = (c^2_A f^2_A)/(f)^2$, $\beta = (c^2_B f^2_B)/(f)^2$, $\gamma = 2c_A c_B f_A f_B/(f)^2$ and $f = c_A f_A + c_B f_B$, with c_A and c_B being the atomic concentrations of A and B respectively.

Three radiation experiments are needed to determine the individual partial interference functions which were not available for this work. The situation for a ternary alloy is more complex where six radiation experiments are needed to determine the individual partial interference functions.

3.5 Experimental X-ray diffraction

3.5.1 The Bragg-Brentano Para-focusing geometry

The Bragg-Brentano para-focusing geometry (shown in Fig. 3.4) was employed in this work. The main advantage of using this geometry is that the absorption of the beam in the sample is independent of θ (Klug and Alexander 1974). Therefore no absorption correction need be applied to the measured intensities and errors in the estimation of an absorption correction can be avoided. Another advantage is that the recorded intensity is considerably greater for a focusing diffractometer than for a parallel beam arrangement of the same angular resolution.

The geometry of a focusing diffractometer is shown in Fig. 3.4. A rectangular area of the sample is irradiated and the error introduced by the sample surface being flat as opposed to being curved to the radius of the focusing circle is small provided the divergence of the beam is small. With a free horizontal sample surface the Bragg-Brentano geometry can only be achieved by moving both the X-ray tube and the detector about a stationary sample in such a way that the angle of incident beam to the sample surface is equal to the angle of the diffracted beam to the surface.

3.5.2 The diffractometer

The axis of the diffractometer was designed to be horizontal. This is the only orientation of the axis that can be used to examine a free sample surface using the Bragg-Brentano Para-focusing geometry. It is possible to view along the diffractometer axis by means of a telescope and the surface can be clearly seen if the field of view is illuminated from the opposite end of the axis.

The X-ray tube is attached to one of the diffractometer arms (known as the source arm) via a plate, which enables the tube to be raised or lowered in order to adjust its height when setting the beam to pass through the axis. In front of the tube window was the support for the first Soller slit sl_1 and the divergence slit s_1. These were firmly attached to the height adjustment plate so that the Soller slits always maintained the same relative vertical position to the tube window. All the Soller slits could, however, be rotated about a vertical axis and all the divergence slits could be adjusted in

the vertical direction.

The other diffractometer arm (known as the detector arm) carried the monochromator and the detector and formed the support for the Soller slits sl_2 and the divergence slit s_2. Since post diffractometer monochromatisation was to be used, a slider with a rotatable mounting for a monochromator was attached to this arm. A further slider (known as the subsidiary detector arm) was attached to the monochromator mounting which was capable of rotation about the centre of the monochromator mount. To this slider was attached the divergence slit s_3 and the scintillation counter tube. Thus the distance (s_2-monochromator) and (monochromator-s_3) could be varied. These distances could be accurately adjusted by means of vernier scales attached to the arms.

The two arms could be driven about the horizontal axis in variable sized steps down to a minimum of $2X10^{-6}$ of a revolution (1^0=1388.9 steps). The angular positions of both arms are read by four verniers on a circular scale. The arms could be driven in unison, so that a constant beam geometry could be maintained, or they can be driven independently. The Soller slits sl_1 and sl_2 consisted of side cheeks machined from graphite with fine slots into which individual plates slide. A small open ended box held the cheeks in position, and the divergence could be adjusted by removing plates from the system. Divergence slits of different fixed widths can be inserted and are made so that their mid-points will

come at the same height. The size of the slit could be altered by interchanging slits of different sizes without any further adjustments in slit positions being necessary.

Lead shielding was used to prevent radiation reaching the detector direct from the X-ray tube.

3.5.3 The X-ray tube

The X-ray tube was a standard Philips type, 2.7 kW sealed tube with molybdenum target. The X-ray tube was supplied from a Philips PW 1140 generator with full-wave rectified and smoothed output voltage which had a maximum variation of ± 0.03% on the kilovolt and milliamp settings for mains fluctuation of ±10%. The line focus of the X-ray tube was parallel to the diffractometer axis.

3.5.4 Monochromator and detector

The X-rays diffracted from the sample were monochromatised by a bent pyrolytic graphite crystal which was set to reflect the Mo K_α characteristic wavelength (K_α = 0.71069Å). A filtering system was not employed on the source side since the maximum possible intensity was required to improve the counting statistics. The detector was a scintillation counter with an end window of beryllium and consisting of a thallium-activated sodium iodide crystal with an EMI 9524s type photomultiplier.

3.5.5 Controlling unit for diffractometer

Standard Harwell 6000 series units were assembled with microprocessor control to give the X-ray spectrometer 36409. This was linked to the X-ray diffractometer and the two units controlled

by an Apple// + computer (see Fig. 3.5). The "Harwell disk" which was run on the Apple // + computer contained the programs required for communication between the microprocessor and Harwell 6000 series units. Each of the diffractometer arms had its own motor controller which could drive stepping motors linked to the arms in either direction about the horizontal axis. A rate meter output was available so that quick visual checks on the intensity could be made.

3.5.6 Diffractometer alignment

The diffractometer was periodically aligned and the configuration of the components changed. So following such a procedure the alignment had to be checked.

The alignment procedure followed was described elsewhere (Causer et al 1971) and hence need not be repeated here. The major steps of the procedure are outlined below which are:

1.Making the diffractometer axis horizontal.

2.Determining the zero angle of the diffractometer arm carrying the X-ray tube.

3.Introducing the crystal monochromator and setting it to its correct position to reflect the characteristic K_{α} Mo line.

4.Determining the zero angle of the diffractometer arm carrying the detector.

The correct alignment to obtain accurate diffraction patterns and maximum intensity is shown in Fig. 3.4. When the apparatus was correctly aligned the radiation from the line source of the X-ray tube (X) passed through the first Soller slit sl_1 and divergence slit s_1

and was incident on the glass sample placed at the diffractometer axis. The diffracted beam then passed through the second Soller slit sl_2 and divergence slit s_2 and was incident on the bent graphite monochromator (M) so that the K_α characteristic wavelength was reflected from the crystal. The diffracted beam passed finally through the third divergence slit s_3 on to the detector. Mis-alignment of the diffractometer or sample can cause reduction in measured peak intensities, asymmetrical broadening of the peaks and errors in peak positions. Distortion of the diffraction pattern is also caused by unavoidable deviations from exact focusing geometry due to the finite width of the X-ray line source, the width of the receiving slit, use of a flat rather than a curved sample, and horizontal divergence of the beam (Klug and Alexander 1974). Although these geometrical conditions have very little effect on the broad diffraction peaks obtained from disordered samples, it is desirable to minimise their effect, especially the greatest effect caused by horizontal divergence. Therefore, the experimental arrangement employed in this work included Soller slits to limit the horizontal divergence to 2^0. The combined effect of flat sample, absorption and horizontal divergence is to shift the diffraction peaks to lower angles and this effect is greatest at small angles θ.

A systematic error in the recorded Bragg angles can also be due to errors in the diffractometer zero angles and a non-systematic error result from the limited accuracy to which the vernier scale can be read, which was ± 1 minute of arc.

3.5.7 Test of alignment

The accuracy of the diffractometer alignment was determined by comparing the positions of the observed diffraction lines from a LiF crystal with the calculated values (i.e with those given by the A.S.T.M index). The LiF crystal was correctly aligned on the diffractometer axis and counting was carried in small angular intervals over the diffraction peaks. The results for n=1, n=2, and n=3 diffraction orders are given in table 3.1. As can be seen from the table the observed peak positions were 3' of arc lower than the the calculated values. This error was found to be always negative and was attributed to an incorrect alignment of the LiF crystal on the diffractometer axis. To correct for this systematic error a 3' of arc was added to the starting angle at which measurements were made.

3.5.8 Elimination of unwanted radiation

For the best possible structural measurements monochromatic radiation must be used. This is achieved by the use of crystal reflection which gives the best monochromatisation. Very early measurements by Gregg and Gingrich (1940) showed that spurious peaks can be produced in intensity patterns from disordered materials if poorly monochromatised radiation is used. A crystal monochromator, when set to reflect the characteristic K_α line of the X-ray tube spectrum, may also reflect harmonics of this wavelength.

Curved crystal monochromators give about ten times the reflected intensity of plane crystals, so that the crystal subtends the

Bragg angle with all the rays in an incident divergent beam, and focuses the reflected beam. It is convenient to place a crystal monochromator in the diffracted beam so that it can reduce the intensity of unwanted scattering from the sample. The monochromator cannot completely eliminate the Compton incoherent radiation, but will reduce it to negligible proportions, depending on the resolution of the crystal. The monochromator will be most effective in reducing the incoherent intensity which is at its maximum for large angles. The amount of fluorescent radiation produced by the sample will be small provided the incident characteristic radiation is not strongly absorbed. There will be a small amount of fluorescence due to certain wavelengths in the "white" radiation. Detection of the fluorescent radiation can be avoided by positioning the monochromator in the diffracted beam which was the arrangement used in the present work.

Scattering from other parts of the diffractometer must be prevented from reaching the detector by the use of suitable shielding. Care is also necessary to prevent radiation from entering the detector direct from the X-ray tube.

3.5.9 Operation of the diffractometer during diffraction runs

The sample surface was aligned to the diffractometer axis. The axis of the diffractometer was defined by an axial bar (in the field of view of the telescope) which fitted tightly into a hole along the diffractometer axis with the end of the bar protruding to intercept

the X-ray beam. The end of the bar has been specially machined to give an accurate flat surface which contained the diffractometer axis. The flat surface of the bar was made to coincide with a convenient marking on the graticule of the viewing telescope. The bar was removed and the sample placed on an adjustable, levelled stand. By viewing the sample through the alignment telescope and altering the height and level of the sample , its surface was made to coincide with the same marking on the graticule as the flat surface of the bar. Once this was done , the surface of the sample was positioned on the axis of the diffractometer.

The X-ray tube and detector arms were set to the starting angle. Both arms were moved through an angular interval of 250 steps and stopped for 300 sec while counting of the diffracted intensity took place. The step count reading and the intensity were stored on a computer disk and the arms moved a further 250 steps. This procedure was repeated until the arms had reached 43^0 to the horizontal. The total time to obtain one diffraction pattern was 21 hr 30 min for a counting time of 300 sec. At least two to three diffraction patterns were taken for the same sample and the analysis was carried on the summed data.

It must be emphasised that the diffraction data was collected from virgin , flat sample surfaces.

3.6 Analysis of Intensity results

3.6.1 Corrections

The recorded counts obtained during the experimental runs

were first corrected for background counts and polarisation and then scaled to electron units. The incident beam was assumed to be unpolarised but became partially polarised on diffraction by the sample and the crystal monochromator. Therefore the recorded counts after being corrected for background, had to be divided by the polarisation factor (Klug and Alexander 1974) which is given by

$$P = (1+\cos^2 2\theta \cos^2 2\alpha)/(1+\cos^2 2\theta) \qquad (3.31)$$

where θ is the Bragg angle for the reflecting planes of the monochromator crystal and α is the Bragg angle of the specimen.

3.6.2 Curve matching

The atomic scattering factor is given by

$$f = f_0 + \delta f \qquad (3.32)$$

where f_0 is the atomic scattering factor for incident wavelengths short in comparison with any atomic absorption edge, and is independent of the incident wavelength. For wavelengths slightly less than the absorption edge, strong absorption occurs and the scattering factor is reduced. δf is called the anomalous dispersion correction which allows for these absorption effects and is a function of λ/λ_a, where λ is the incident wavelength and λ_a is the absorption edge (James 1950). The real and imaginary parts of δf are $\delta f'$ and $\delta f''$ so that equation 3.32 becomes

$$f = f_0 + \delta f' + i\delta f'' \qquad (3.33)$$

f_0 was obtained from the analytical expression given by Cromer and Waber(1965),

$$f_0^{Ds}(s) = \Sigma a_i \exp(-b_i s^2) + C \qquad (3.34)$$

where a_i, b_i and C being tabulated. Values of $\delta f'$ and $\delta f''$ were

obtained from Ramaseshan and Abrahams (1974) but their variation with angle was slight and thus was neglected.

The intensity scattered coherently by N independent atoms of scattering factor f is Nf^2 in electron units. The experimental intensity tends to the independent coherent intensity at large angles where interference effects are neglected. Thus the experimental intensities were converted to electron units by curve matching the intensities at the 10 largest θ values to the weighted sum of atomic scattering factor f^2 for the sample under consideration. A scaling factor Q is given by equation 3.35

$$Q = (1/10)\Sigma f_i^2/N_c \qquad (3.35)$$

where N_c is the corrected counts and f^2 is the weighted scattering factor of the sample. This scaling factor was used to convert the corrected intensities at all scattering angles to electron units.

3.6.3 Accuracy of intensity results

3.6.3.1 Angular accuracy

The uncertainty in the the angular position was found to be $\pm 1'$, representing an error of $\pm$ 0.005Å^{-1} in K, where $K=4\pi\sin\theta/\lambda$. However, when the angular accuracy of the first peak position of the interference function was assessed, the diffuse nature of the peak made it impossible to determine its position with an accuracy better than ± 0.03Å^{-1} in K. Therefore, the angular accuracy of the diffractometer was not a limiting factor. Higher order peaks being even more diffuse had corresponding lower accuracies.

3.6.3.2 Accuracy of corrected counts and curve matching

The accuracy of I_{eu} was determined by the accuracy of the corrected counts (N_c) and errors introduced by the curve-matching procedure described in section 3.6.2. The accuracy of each value of the corrected counts was limited by the statistical error and the instability of the X-ray source. In the work on disordered samples the final value of the corrected counts was an average value obtained from several experiments. The probable error in corrected counts may be taken as ±5% at all θ and attributed to the statistical error and X-ray source instabilities.

The values of $f_0^{Ds}(s)$ given by equation 3.34 were calculated by Cromer and Waber (1965) from Dirac-Slater wavefunctions but no estimate of the error in these calculated values was given. The accuracy of f depends on the accuracy of f_0 and the anomalous dispersion correction δf. There are appreciable differences between the values of δf' and δf'' calculated by various workers. Therefore, it was not possible to give an estimate of the accuracy of f.

CHAPTER 4

Extended X-ray absorption fine structure (EXAFS)

4.1 Introduction

In XPS and X-ray diffraction measurements, constant photon energies were used and these were of the order of 1.5 keV and 17.4 keV respectively. In EXAFS the photon energies are varied and we are concerned with the oscillations which occur and extend up to ~1 keV beyond an absorption edge of an atom.

The absorption of X-rays by atoms varies smoothly with photon energy except at some discrete energies where abrupt increases occur called absorption edges. The absorption of X-rays on the high energy side of absorption edges does not vary monotonically in condensed matter but has a complicated behaviour which extends past the edges by an amount approximately of the order of 1 keV. This non-monotonic behaviour is known as extended X-ray absorption fine structure and it only occurs when the atoms are present in condensed matter. Isolated atoms do not show this fine structure so that this is an effect caused by the presence of surrounding atoms. EXAFS has been widely successfully used to probe the local structural

enviroment of a particular atomic type within solids and in particular disordered solids. The theoretical background, explanation and applications of EXAFS has been the subject of many articles (Sayers et al 1972, Stern 1974, Lytle et al 1975, Stern et al 1975, Sayers et al 1975, Stern 1976, Stern 1978, Winick and Doniach 1980, Lengeler and Eisenberger 1980, Teo and Noy 1981, Lee et al 1981, Hayes 1984) and the basic ideas will be introduced here.

A typical absorption spectrum indicating the pre-edge, absorption edge and EXAFS region is shown in Fig. 4.1. The spectrum can be analysed into two different regions :

a- the threshold region, or pre-edge and near edge regions, which contains information about the binding energies, quantum numbers, and multiplicities of low-lying bound electronic excited states of the ionised absorbing atom and of low-lying resonant electronic states in the continuum of the absorbing atom. It is known that the position of the edge and the qualitative features of the absorption peaks in the near-edge region are sensitive to the chemical valency of the absorbing atom, and the symmetry of the surrounding near-neighbour atoms.

b- the EXAFS region, in this region the observed series of gentle oscillations in the X-ray absorption coefficient may be interpreted in terms of the scattering of the excited photoelectrons by the surrounding (neighbouring) atoms and the resulting interference of this reflected electron wave with the outgoing photoelectrons'

waves, leading to the observed modulation of the absorption coefficient. Therefore EXAFS can be simply described as a final state interference effect.

This technique is useful because it opens up the possibility of making studies which are not possible by the conventional diffraction methods. The characteristics of structure determination by EXAFS are :

1- The local atomic envirnoment around each kind of atom is determined by tuning the X-rays to the absorption edge energy of a particular atom. Since EXAFS measures only short range order there is no fundamental distinction between crystals with long range order and samples without, such as amorphous solids and liquids.

2- In principle, the kinds of surrounding atoms can be distinguished by the energy dependence of their contribution to EXAFS.

3- The number of atoms at a given average distance and the disorder in their location about the average position can be quantified by EXAFS .

4- In unoriented samples (disordered solids) only the radial distance between the centre atom and its neighbouring atoms is determined, but in oriented samples (molecular solids and crystals) angular positions are discernable.

5- Determination of the chemical state of the atom is possible by determining absorption edge shift and near edge structure.

4.2 EXAFS mechanism

The basic mechanism of EXAFS is described in this section. To understand the mechanism that gives rise to EXAFS we consider the K-edge fine structure (Stern 1974). In the dipole approximation (Bethe and Salpeter 1957), where the wavelength of the classical EM field representing the photon is always large compared to the dimensions of the core state that is excited (so that the field can be treated as uniform in its overlap with the core state) the probability of X-ray absorption is given by

$$P = (2\pi^2 e^2/\omega c^2 m) |M_{fs}|^2 \rho(E_f) \qquad (4.1)$$

where $M_{fs} = \langle f|\underline{p}.\underline{\varepsilon}|s\rangle$, $|s\rangle$ is the K-shell s-state , $|f\rangle$ is the final unoccupied state , $\rho(E_f)$ is the density of final states per unit energy at the energy E_f , $\underline{p}$ is the momentum operator, $\underline{\varepsilon}$ is the electric field vector of the X-ray, ω is the radial frequency of the X-ray photon whose energy is $\hbar\omega$ and e, m, and c have their usual meanings. The contribution to EXAFS comes from the matrix element and/or $\rho(E_f)$ in equation (4.1). For X-ray energies sufficiently above the edge, $\rho(E_f)$ gives a monotonic contribution because it can be closely approximated by the free electron value and any corrections are small and can be easily treated. With this assumption for $\rho(E_f)$ the only remaining factor that can contribute to the EXAFS is M_{fs}. Since the initial state $|s\rangle$ is fixed and does not vary with ω then the contribution to the fine structure (EXAFS) is from the variation of $|f\rangle$ with ω. The wavefunction $|f\rangle$ is a sum of two contributions. If the atom is isolated, the excited photoelectron

would be in a solely outgoing state from the centre atom, as shown schematically in Fig. 4.2 by the outgoing solid rings. In this case, M_{fs} exhibits no fine structure and the X-ray absorption coefficient would vary monotonically with ω. If now the excited atom is in the condensed phase so that it is surrounded by other atoms within the order of angstroms, the outgoing wave is scattered by surrounding atoms producing ingoing waves depicted by the dotted lines in Fig. 4.2. These ingoing waves can constructively or destructively interfere with the outgoing wave near the origin where |s> exists. This interference gives rise to an oscillatory variation in M_{fs} as ω is varied, changing the electron wavelength and thus the phase between ingoing and outgoing waves. Constructive interference corresponding to peaks in the interference pattern increases M_{fs} while destructive interference corresponding to valleys decreases M_{fs} from the isolated atom value. It is from the frequency and amplitude of these oscillations that the interatomic distances from the excited atoms to its neighbours can be determined, as can, in principle, the number of atoms within a coordination sphere and the identity of these atoms.

4.3 Basic equations

The EXAFS is defined as the normalised oscillatory part of μ and is given (Sayers et al 1972, Stern 1974) by

$$\chi(E) = [\mu(E) - \mu_0(E)]/\mu_0(E) \qquad (4.2)$$

where μ_0 is the smoothly varying portion of μ past the edge and physically corresponds to the absorption of an isolated atom.

Assuming a Gaussian distribution of distances around the absorbing atom, neglecting multiple scattering and the curvature of the photoelectron wavefront at the backscattering atom, and using single scattering, small atom and short wavelength approximations, respectively, at sufficiently high k ($>3\text{Å}^{-1}$), the normalised EXAFS $\chi(k)$ can be expressed as :

$$\chi(k) = \frac{1}{k} \sum_j \frac{N_j}{r_j^2} S_j(k) F_j(k) e^{-2\sigma_j^2 k^2} e^{-2 r_j/\lambda(k)} \sin[2kr_j + \Phi_j(k)], \qquad (4.3)$$

where k is the wavevector of the ejected photoelectron and the summation is taken over the neighbouring shells of the absorber. F_j is the backscattering amplitude of the photoelectron from each of the N_j neighbouring atoms of the jth type in a shell of mean radius r_j around the absorbing atom. The Debye-Waller factor $\exp(-2\sigma^2k^2)$ takes account of the thermal vibration and static disorders about their average shell distance of r_j. This disorder can be separated into two components which may be thermally-induced and/or structural in origin but in EXAFS and diffraction studies it is the combined effect which is measured. $S_j(k)$ is the amplitude reduction factor due to many-body effects such as shake-off/up processes at the absorbing atom (Wuilleumier 1976). The damping factor $\exp(-2r_j/\lambda(k))$, including the mean free path λ, accounts for losses by inelastic and multielectron excitations. The amplitude of $\chi(k)$ is attenuated also by the r^{-2} term which reflects the product of the amplitudes of the outgoing and backscattered waves both of

which drop off as r_j^{-1} because of their spherical nature. The argument of the sine gives the phase difference between the outgoing and backscattered portions of the photoelectron wavefunction. The term $2kr_j$ is the phase shift as a free electron of wavenumber k traverses the distance $2r_j$ and the additional phase shift $\Phi_j(k)$ experienced by the ejected photoelectron is introduced because of the fact that the electron is in the presence of other potentials. The phase shift $\Phi_j(k)$ has two contributions, one from the centre atom and the other from the backscattering atom, since the scattering is, in general, complex. $\Phi_j(k)$ is characteristic of a particular emitter-scatterer species pair but insensitive to the chemical nature of the pair. This means that accurate comparisons between known and unknown structural combinations of r_j are possible.

4.4 Limitations on the theory

Several of the approximations mentioned in section 4.3 used to derive equation 4.3 are inadequate under certain conditions. Yet in spite of these inadequacies equation 4.3 can still be used to give accurate structural information if comparisons are made between the unknown and a good standard. A good standard is one which is sufficiently similar to the unknown that the limitations on the theory are avoided (see the following section). The approximations inherent in the simple formula, equation 4.3, will be considered in this section

1- Near edge structure and chemical effects

The approximations of EXAFS are not valid near the absorption edge and the EXAFS data can be distorted by the near edge effect. This usually limits the lower value of the k range ,k_{min}, to a value of $k < 4Å^{-1}$, below which multiple scattering effects become important and where equation 4.3 fails.

2- Disorder

When the disorder cannot be adequately described by a Gaussian, the Debye-Waller factor has to be replaced by more accurate expressions. This disorder restricts the use of EXAFS to structures which have $\sigma < 0.2Å$.

3- Small atom approximation

Equation 4.3 assumes that the size of the atom involved is small compared to the distance from the centre atom so that the incoming electron wave can be treated as a plane wave. This approximation is worst for the first neighbour atoms at low k and improves at higher k values as the effective size of the atom involved in the backscatter becomes smaller.

4- Multiple scattering

It is assumed that the photoelectron is only backscattered once to the origin. This is correct for the first coordination shell but becomes a poor approximation the further the shell is from the origin.

5- Many-electron effects

The photoelectron loses coherence with itself due to the finite

life time of its excited state. The decay of this state occurs through various multi-electron processes, the effect of which can be approximated by the mean free path λ, which is k-dependent. The effect of $\lambda(k)$ is not important for first neighbour atoms but becomes more important for more distant neighbours. The absorption of the X-ray by the atom involves all the electrons in the atom. The X-ray photon interacts with only one electron but due to long range Coulomb interaction between this electron and the rest of the electrons in the atom, it causes a modification to the transition probability. The main effect for EXAFS is a reduction in the probability of single electron transitions.

4.5 Use of a standard for data analysis

An ideal standard would be exactly like the unknown in all respects. The EXAFS spectra for both would be identical and the structure of the unknown could be determined to the same precision as that of the standard. In practice, such an ideal is rarely available. Good standards for practical EXAFS purposes are ones that calibrate out, to a good approximation, the inadequacies of equation 4.3. A good standard would have the same central atom as the unknown, which would compensate for the passive electron effect, while multiple scattering is not a problem for the first neighbour. The first neighbour atom should be approximately the same size and distance from the centre atom as the unknown. By this choice, the small atom approximation is compensated for and the mean free path effect, which is very small in the first shell,

would be accurately eliminated.

Therefore a good standard for an unknown is one with the same central atom, with similar numbers of first neighbours which are approximately the same distance away, and are composed of atoms with approximately the same atomic number.

4.6 X-ray absorption near edge structures (XANES)

The near edge region of the X-ray absorption spectra (XAS) exhibit a low kinetic energy of photoelectrons since the photon energy is small. For low kinetic energies, the photoelectron has a long mean free path (see Fig. 2.3), so the interpretation of the structures found at the near edge region are more complex than EXAFS oscillations and this region is known as the X-ray absorption near edge structures (XANES). The XANES appear as strong, asymmetric, and broad structures which extend up to the energy threshold E_c of EXAFS oscillations and are shown for a calcium complex in Fig.4.3 (Bianconi 1981). E_c is defined as the energy where the wavelength of the initially excited photoelectron is equal to the shortest interatomic distance within the cluster of atoms determining the XANES. Below E_c, the plane wave approximation of the final state and the single scattering approximation are not appropriate and the EXAFS theory breaks down. XANES is actually a new tool for local structure studies and from which it is possible to extract information on unknown local structures which cannot be obtained from EXAFS (Bianconi 1981) :

1. Coordination geometry

2. Symmetry of unoccupied electronic states and

3. Effective atomic charges on the absorbing atom.

The main features of XANES arise from multiple scattering resonances (MSR) as illustrated in Fig. 4.4.

4.7 Experimental technique

In this section the experimental arrangement and procedure for the EXAFS measurement for glassy powdered $GeSe_2$ with temperature are described.

EXAFS measurements were carried out using the synchrotron radiation source (SRS) at Daresbury in the transmission mode and their Lytle cell for high temperature work. The experimental arrangement for measuring EXAFS in the transmission mode is shown in Fig. 4.5 where the sample absorption is measured directly by monitoring the incident and absorbed flux. The Lytle cell used for the high temperature work is shown in Fig. 4.6

Synchrotron radiation from the storage ring passes through a double monochromator. Rotation of the crystals gives various wavelengths. According to Bragg's law, the central wavelength λ of the output beam will be given by

$$n\lambda = 2d \sin\theta \qquad (4.4)$$

where n is the order of diffraction, d is the lattice spacing and θ is the Bragg angle. This angle was controlled by a stepping motor driver. The most successful monochromator design is shown in Fig. 4.7. The first crystal C_1 serves as the primary monochromator, and the second crystal C_2, when correctly adjusted, filters out

harmonics and unwanted reflections, as well as rendering the output beam parallel to the input beam, displaced by a distance $2D\cos\theta$, where D is the distance between crystal faces.

Incident and transmitted X-ray intensities I_0 and I_t were measured by the first and second ion chambers called the beam monitor and transmission monitor. The ion chambers were filled with pure or a mixture of noble gases, depending on the wavelength range employed. In the case of Ge K-edge absorption used in this work the energy was in the region of 11 keV and the ion chambers were filled with argon gas.

The bulk glass samples were finely powdered and weighed amounts were thoroughly mixed with boron nitride (BN) to optimise the Ge K-edge absorption and provide a large volume of powder for sample homogeneity. The powdered sample was held between two thin plates of boron nitride which was selected for the sample cell as it had low X-ray absorption coefficient in the energy range of interest, and is easily machinable. The weight of the powdered sample was choosen so as to give a suitable ratio of the transmitted and incident intensity. To minimise the absorption of X-rays by the boron nitride a very thin window (0.5 mm) was milled where the beam was to be located. The temperature of the sample was measured by a chromel-alumel thermocouple embedded in the boron nitride support. The boron nitride support was attached to a heater, which had an automatic temperature controller. The Lytle cell was evacuated to a pressure of approximately 10^{-3} torr and was aligned with the X-ray beam,

without the sample cell, before commencing data acquisition. The X-ray beam had an estimated intensity of 10^{11} photons/sec.

The EXAFS spectrum was scanned by varying the wavelength of the incident X-rays over the required energy range at two temperatures 22 and 350^0 C. Vacuum atmosphere was replaced by a helium atmosphere for all measurements. Examination of the sample after the experiment indicated that there was no appreciable loss of the sample. The EXAFS of the sample at room temperature(22^0 C) were also measured using Se K-edge, therefore a comparison between the experimental Ge and Se K-edge EXAFS from glassy $GeSe_2$ at at room temperature (22^0C) was possible.

4.8 Data analysis

There are three computer programs that have to be run on Daresbury Convex computer to be used in the data analysis

1-EXCALIB

Starting from the experimental data file, this program produces the normalised absorption spectra versus electron energy in eV.

2-EXBACK

Takes absorption from EXCALIB, defines X-ray absorption edge E_0 and subtracts the background to extract the fine structure function $\chi(k)$ multiplied by k^3 to enhance the higher k values.

3-EXCURV90

Fourier transforms the processed data where the resulting main peak is associated with nearest neighbour distance.

The data processing operation on the raw experimental data using the above mentioned programs are shown in Fig. 4.8.

4.9 Results and discussion

4.9.1 EXAFS results for $GeSe_2$ and $(GeSe_2)_{92}Ga_8$ glasses

The experimental Ge K edge EXAFS results for $GeSe_2$ glass at room temperature (22^0C) and at the high temperature (350^0C) are shown in Fig. 4.9. It is clearly seen from the figure that the EXAFS from $GeSe_2$ for both temperatures agree indicating that the local structure around the Ge atom alters very little with temperature. The experimental Ge and Se K edge EXAFS from $GeSe_2$ are shown in Fig. 4.10. The EXAFS from both edges agree reasonably up to a K value of 9 $Å^{-1}$. The Fourier transform of the EXAFS oscillations is also shown in Fig. 4.10. The nearest interatomic distance R_1 is found to be 2.34±0.05 Å and the number of Se atoms in the first coordination shell is found to be 4. A comparison of the experimental Ge K edge EXAFS taken at room temperature for both $GeSe_2$ and $(GeSe_2)_{92}Ga_8$ (Fig. 4.11) indicates that the EXAFS oscillations are different reflecting that the local structure around the Ge atom is different.

4.9.2 XANES results for $GeSe_2$ and $(GeSe_2)_{92}Ga_8$ glasses

The XANES results from $GeSe_2$ at room temperature (22^0C) and at the high temperature (350^0C) are shown in Fig. 4.12 and table 4.1. It is seen from the figure and the table that the XANES change very little as a function of temperature. The XANES results from $GeSe_2$ and $(GeSe_2)_{92}Ga_8$ taken at room temperature (Fig. 4.13 and

table 4.1) clearly shows that the XANES change on alloying $GeSe_2$ with Ga.

4.10 Conclusions

The preliminary analysis of the EXAFS and XANES results for $GeSe_2$ and $(GeSe_2)_{92}Ga_8$ indicate that there is very little change in the local structure around the Ge atom in $GeSe_2$ glass as a function of temperature and that there is a change in the local structure around the Ge atom on alloying $GeSe_2$ with Ga. This change is illustrated in the shift of the energy of the X-ray absorption edge and the alteration of the second "resonance" which changes from 10 eV for $GeSe_2$ to 13 eV.for $(GeSe_2)_{92}Ga_8$. The EXAFS results for $GeSe_2$ also indicate that only interference from the first coordination shell contributed to the absorption spectrum and that an interatomic distance of 2.34±0.05 Å was found to be consistent for both low and high temperatures.

CHAPTER 5

Results and Discussion

5.1 Results

The results are presented separately and in the following order : Se-S glasses, Ge-Se-X (X = Ga, Sn, Bi, Sb) glasses and Ge-S-Y (Y =Ag, Ga, Sn, Bi) glasses ,where X,Y are changed with increasing valency. Comments on any special points of note are also given.

5.1.1 Se-S glasses

The measured X-ray interference functions for $Se_{1-x}S_x$ glasses with x= 10, 15, 20, 25, 40, and 50 at % S show a first sharp diffraction peak (FSDP) (Fig. 5.1). In order to bring together all the essential properties of the diffraction pattern certain characteristic parameters have been chosen. These are called the peak fit parameters for the FSDP. Clearly the position is important but so also is the width which is related to the 'coherence length' of the medium range order (as defined later in this section). An additional property is the ratio of the first to second peak height since this may be taken as a relative measure of the amount of medium to short range order. An increase in this ratio can be taken as an increase in the amount of medium range order. The peak fit

parameters for the FSDP in these glasses are given in table 5.1. The position of the FSDP in reciprocal space changes from 1.24 $Å^{-1}$ for $Se_{90}S_{10}$ to 1.13 $Å^{-1}$ for $Se_{80}S_{20}$. The full width at half-maximum (FWHM) remain the same (0.17 $Å^{-1}$) for all the compositions examined. The 'coherence length (L)' can be related via an approximate relation to the FWHM (ΔK) by the expression $L \cong 2\pi/\Delta K$ (Susman et al 1988) which gives a value of 37 Å for all the compositions examined. The ratio of the intensity of the FSDP to the second peak in the interference function increases from 0.40 for $Se_{90}S_{10}$ to 0.88 for $Se_{50}S_{50}$.

The measured plasmon energy losses from the $L_3M_{4,5}M_{4,5}$ Auger lines of Se for Se and $Se_{90}S_{10}$ are shown in Fig. 5.2. The value of the plasmon energy changes from 19.3 eV for Se to 18.3 eV for $Se_{90}S_{10}$. The averaged values of the measured plasmon energies from the $L_3M_{4,5}M_{4,5}$ Auger lines of Se and the values calculated from equation 2.17, using the measured relative densities of the alloys, are given in table 5.2. The change of the measured plasmon energy with Se content in the alloy is shown in Fig. 5.3. The change of the calculated values of the plasmon energies with Se content is also shown in Fig. 5.3. The binding energies in eV of the peaks of the valence bands referenced to the Fermi level are given in table 5.3. The non-bonding and bonding p-type peaks remain at binding energies of approximately 1.4 and 4.1 eV, respectively, for all the compositions examined. The s-type peak splits into two peaks at 15 at % S and merge into a single

peak at 40 and 50 at % S. The corrected valence band spectra, measured and generated (a superposition of the traces of Se and S weighted by the respective atomic proportions), for two compositions, $Se_{75}S_{25}$ and $Se_{50}S_{50}$, are shown in Fig. 5.4. The core level binding energies in eV for the glasses with respect to the Fermi level are given table 5.4. The binding energies of the core peaks change little with composition. The variation of glass transition temperature with Se content in the alloy is shown in Fig. 5.5. The observed decrease in the glass transition temperature with decreasing Se concentration in the alloy is consistent with the earlier results of Myers and Felty (1967). The glass transition temperature decreases from 317^0K for Se to 293^0K for $Se_{60}S_{40}$ (see table 5.2). The variation of the measured relative density with Se content in the alloy is shown in Fig. 5.6. The density decreases from 4.31 gm cm^{-3} for Se to 3.19 gm cm^{-3} for $Se_{50}S_{50}$ (see table 5.2).

5.1.2 Ge-Se-Ga glasses

The binding energies in eV of the core peaks in the alloys referenced to the Fermi level are given in table 5.5. The Ge(3d) binding energy changes from 30.1 eV for $GeSe_2$ to 30.2 eV for $(GeSe_2)_{92}Ga_8$ while that of the Se(3d) changes from 54.2 eV for $GeSe_2$ to 54.0 eV for $(GeSe_2)_{96}Ga_4$. The Ga(3d) binding energy remain the same (19.4 eV) for $(GeSe_2)_{96}Ga_4$ and $(GeSe_2)_{92}Ga_8$. The binding energies of the other core levels also change little when Ga is added to $GeSe_2$. The Ga(3d) level in $(GeSe_2)_{92}Ga_8$ together with Ge(3d) level in $GeSe_2$ and $(GeSe_2)_{92}Ga_8$ are shown in Fig. 5.7. The

small peak at a binding energy of ~ 25.8 eV is attributed to a "shake-up" satellite of Ga(3d). The binding energies in eV of the peaks of the valence bands referenced to the Fermi level are given in table 5.6. The p-type peak shifts towards the Fermi level when Ga is added to $GeSe_2$ and its binding energy changes from 2.5 eV for $GeSe_2$ to 2.0 eV for $(GeSe_2)_{96}Ga_4$. The s-type peak binding energy changes from 13.6 eV for $GeSe_2$ to 13.0 eV for $(GeSe_2)_{96}Ga_4$. The corrected valence band spectra for two compositions, $GeSe_2$ and $(GeSe_2)_{96}Ga_4$, are shown in Fig. 5.8. The weak additional peak sometimes referred to as 'three-fold peak (TFP)' (Orton et al 1982) remain at a binding energy ~ 8 eV for the two compositions.

The averaged values of the measured plasmon energies from the $L_3M_{4,5}M_{4,5}$ Auger lines of Se and Ge and the values calculated from equation 2.17, using the measured relative densities of the alloys, are given in table 5.7. The table shows that the values of the plasmon-loss energy for Se and Ge for the compositions examined are different. A similar observation for $GeSe_2$ have been reported previously (Gorgol 1989). It is worth noting that the values of the measured plasmon energies from the $L_3M_{4,5}M_{4,5}$ Auger lines of Ge and the calculated values agree, which may be taken as an indication that the local electron density around the Ge atom is very close to the average electron density. The measured plasmon energy losses from the $L_3M_{4,5}M_{4,5}$ Auger lines of Se for two compositions, $(GeSe_2)_{96}Ga_4$ and $(GeSe_2)_{92}Ga_8$ are shown in Fig. 5.9. The value of the plasmon energy changes from 17.5 eV for

$(GeSe_2)_{96}Ga_4$ to 16.6 eV for $(GeSe_2)_{92}Ga_8$. The variation of the measured plasmon energies from the $L_3M_{4,5}M_{4,5}$ Auger lines of Se with Se content in the alloys is shown in Fig. 5.10. The change of the calculated values of the plasmon energies with Se content in the alloys is also shown in Fig. 5.10. The values of the average energy gaps of the Ge-Se bonds, calculated from the measured plasmon energies of the $L_3M_{4,5}M_{4,5}$ Auger lines of Se (see section 2.5), are listed in table 5.7. The value of the average energy gap changes from 5.42 eV for $GeSe_2$ to 4.88 eV for $(GeSe_2)_{92}Ga_8$.

The measured X-ray interference functions show a FSDP (Fig. 5.11). The peak fit parameters for the FSDP in these glasses are given in table 5.8. The position of the FSDP in reciprocal space changes little from 1.14 $Å^{-1}$ for $GeSe_2$ to 1.16 $Å^{-1}$ for $(GeSe_2)_{92}Ga_8$. The 'coherence length' changes from 39 Å for $GeSe_2$ to 29 Å for both $(GeSe_2)_{96}Ga_4$ and $(GeSe_2)_{92}Ga_8$. The variation in measured relative density with Ga content in the alloy is shown in Fig. 5.12. The density increases from 4.45 gm cm^{-3} for $GeSe_2$ to 4.61 gm cm^{-3} for $(GeSe_2)_{92}Ga_8$ (see table 5.7). The variation of measured glass transition temperatures with Ga content in the alloy is shown in Fig. 5.13. The value of T_g decreases from 687^0K for $GeSe_2$ to 614^0K for $(GeSe_2)_{92}Ga_8$ (see table 5.7).

5.1.3 Ge-Se-Sn glasses

The substitution of Sn for Ge in the ternary mixture alters a number of measured properties of this system. The density and the ratio of medium to short range order decrease. The compositional

dependence on Sn content in the alloys of the measured relative densities is shown in Fig. 5.14. The density decreases from 4.45 gm cm^{-3} for $GeSe_2$ to 3.52 gm cm^{-3} for $Ge_{0.4}Sn_{0.6}Se_2$ (see table 5.9).

The variation of the measured glass transition temperature with Sn content in the alloy is shown in Fig. 5.15. The observed monotonic decrease in the glass transition temperature with increasing Sn concentration is consistent with the results of Mikrut and McNeil. The value of T_g decreases from 687^0K for $GeSe_2$ to 588^0K for $Ge_{0.4}Sn_{0.6}Se_2$ (see table 5.9). Table 5.9 records the averaged values of plasmon energies from the $L_3M_{4,5}M_{4,5}$ Auger lines of Se and Ge and the values calculated from equation 2.17, using the measured relative densities of the alloys, which are given in the same table. There are large differences between the plasmon energies for Se and Ge in this alloy system. Although the Auger lines for Ge were of low intensity it was possible to observe clear plasmon peaks. The measured plasmon energy losses from the $L_3M_{4,5}M_{4,5}$ Auger lines of Se for the two compositions $Ge_{0.7}Sn_{0.3}Se_2$ and $Ge_{0.5}Sn_{0.5}Se_2$ are shown in Fig. 5.16. The value of the plasmon energy changes from 17.5 eV for $Ge_{0.7}Sn_{0.3}Se_2$ to 16.6 eV for $Ge_{0.5}Sn_{0.5}Se_2$. The change of the measured plasmon energy of the $L_3M_{4,5}M_{4,5}$ Auger lines of Se with Sn content in the alloys is shown in Fig. 5.17. The change of the calculated values of the plasmon energies with Sn content is also shown in Fig. 5.17. The calculated average energy gaps of the Ge-Se bonds from the measured plasmon energies of the $L_3M_{4,5}M_{4,5}$ Auger lines of Se (see section 2.5) are listed in table 5.9. The value of the average energy gap

changes from 5.42 eV for $GeSe_2$ to 4.84 eV for $Ge_{0.4}Sn_{0.6}Se_2$. The variation of the calculated average energy gap with Sn content in the alloys is shown in Fig. 5.18. The measured values of the optical energy gaps (Martin et al 1990) normalised to the value of the average energy gap of $GeSe_2$ are also shown in Fig. 5.18. The calculated average energy gaps and the measured optical energy gaps seem to reflect each other inspite the difference in the way they have been obtained.

The measured X-ray interference functions for $Ge_{1-x}Sn_xSe_2$ with x=0.1, 0.2, 0.3, 0.4, and 0.5 show a FSDP (Fig. 5.19). The peak fit parameters for the FSDP in these glasses are given in table 5.10. The position of the FSDP in reciprocal space changes from 1.14 $Å^{-1}$ for $GeSe_2$ to 1.0 $Å^{-1}$ for $Ge_{0.9}Sn_{0.1}Se_2$. The 'coherence length' changes from 39 Å for $GeSe_2$ to 17 Å for $Ge_{0.5}Sn_{0.5}Se_2$. With this reduction of the 'coherence length' there is a decline in the intensity ratio of the FSDP to the second peak in the interference function indicating a reduction of the amount of medium range order.

The core level binding energies in eV in the glasses examined referenced to the Fermi level are given in table 5.11. The value of Ge(3d) binding energy changes from 30.1 eV for $GeSe_2$ to 29.9 eV for $Ge_{0.6}Sn_{0.4}Se_2$ while the value of Se(3d) binding energy changes from 54.2 eV for $GeSe_2$ to 53.9 eV for $Ge_{0.5}Sn_{0.5}Se_2$. The binding energies of the other core levels also change little on substitution. The binding energies in eV of the peaks of the valence bands

referenced to the Fermi level are given in table 5.12. The p-type peaks shift towards the Fermi level on substitution. The binding energy of the s-type peak changes from 13.6 eV for $GeSe_2$ to 13.1 eV for $Ge_{0.7}Sn_{0.3}Se_2$ while that of the weak additional peak changes from 7.9 eV for $GeSe_2$ to 7.1 eV for $Ge_{0.5}Sn_{0.5}Se_2$.

5.1.4 Ge-Se-Bi glasses

In this alloy system the base glass was changed from $GeSe_2$ to $GeSe_{3.5}$. Although this does not influence strongly many of the properties of the base glass it is important to note that Se plasmon energy increases from 17.7 eV for $GeSe_2$ to 18.0 eV for $GeSe_{3.5}$ while Ge plasmon energy decreases from 15.7 eV for $GeSe_2$ to 15.1 eV for $GeSe_{3.5}$. It is also important to note that the position of the FSDP decreases from 1.14 $Å^{-1}$ for $GeSe_2$ to 1.01 $Å^{-1}$ for $GeSe_{3.5}$ and the 'coherence length' decreases from 39 Å for $GeSe_2$ to 20 Å for $GeSe_{3.5}$.

The averaged values of the plasmon energies from the $L_3M_{4,5}M_{4,5}$ Auger lines of Se and Ge and the values calculated from equation 2.17, using the measured relative densities of the alloys, are given in table 5.13. The change in the measured plasmon energies of the $L_3M_{4,5}M_{4,5}$ Auger lines of Se with Se content in the alloy is shown in Fig. 5.20. The change of the calculated values of the plasmon energies with Se content is also shown in Fig. 5.20. The value of the plasmon energy changes from 18.0 eV for $GeSe_{3.5}$ to 17.5 eV for $(GeSe_{3.5})_{90}Bi_{10}$. The measured plasmon energy losses of the $L_3M_{4,5}M_{4,5}$ Auger lines of Se for $GeSe_{3.5}$ and $(GeSe_{3.5})_{90}Bi_{10}$ are

shown in Fig. 5.21.

The measured X-ray interference functions for the glasses examined are all very similar and show a FSDP (Fig. 5.22). The peak fit parameters of the FSDP in these glasses are given in table 5.14. The position of the FSDP changes from 1.01 $Å^{-1}$ for $GeSe_{3.5}$ to 0.93 $Å^{-1}$ for $(GeSe_{3.5})_{90}Bi_{10}$. The 'coherence length' changes from 20 Å for $GeSe_{3.5}$ to 16 Å for $(GeSe_{3.5})_{90}Bi_{10}$ while the ratio of the intensity of the FSDP to the second peak in the interference function remain effectively constant. The variation of the measured relative density with Bi content in the alloy is shown in Fig. 5.23. The density increases from 4.43 gm cm^{-3} for $GeSe_{3.5}$ to 4.93 gm cm^{-3} for $(GeSe_{3.5})_{90}Bi_{10}$ (see table 5.13).

The binding energies of the core peaks referenced to the Fermi level are given in table 5.15. The binding energy of Ge(3d) changes from 30.1 eV for $GeSe_{3.5}$ to 30.2 eV for $(GeSe_{3.5})_{90}Bi_{10}$ while that of Se(3d) changes from 54.2 eV for $GeSe_{3.5}$ to 54.0 eV for $(GeSe_{3.5})_{90}Bi_{10}$. The binding energies in eV of the peaks of the valence bands referenced to the Fermi level are given in table 5.16. The binding energy of the p-type peak changes from 1.7 eV for $GeSe_{3.5}$ to 2.0 eV for $(GeSe_{3.5})_{90}Bi_{10}$ while that of the s-type peak changes from 13.0 eV for $GeSe_{3.5}$ to 13.9 eV for $(GeSe_{3.5})_{90}Bi_{10}$. The weak additional peak remain at a binding energy of ~ 8.0 eV.

5.1.5 Ge-Se-Sb glasses

For this ternary alloy system, three base glasses were used which were $GeSe_2$, $GeSe_3$ and $GeSe_{3.5}$. The measured plasmon

energy losses from the $L_3M_{4,5}M_{4,5}$ Auger lines of Se for $GeSe_2$ and $(GeSe_3)_{80}Sb_{20}$ are shown in Fig. 5.24. The averaged values of the measured plasmon energies from the $L_3M_{4,5}M_{4,5}$ Auger lines of Se and Ge and the values obtained from equation 2.17, using the measured relative densities of the alloys, are given in table 5.17. The measured plasmon energy from the $L_3M_{4,5}M_{4,5}$ Auger lines of Se changes from 17.7 eV for $GeSe_2$ to 17.0 eV for $(GeSe_2)_{94}Sb_6$. The change of the measured plasmon energies from the $L_3M_{4,5}M_{4,5}$ Auger lines of Se with Se content in the alloy is shown in Fig. 5.25. The change of the calculated values of the plasmon energies with Se content is also shown in Fig 5.25. The variation of the glass transition temperature with Sb concentration in the alloy is shown in Fig. 5.26. The value of T_g decreases from 687^0K for $GeSe_2$ to 568^0K for $(GeSe_2)_{88}Sb_{12}$ (see table 5.17). The change in the relative density with Sb concentration in the alloy is shown in Fig. 5.27. The density increases from 4.45 gm cm^{-3} for $GeSe_2$ to 5.18 gm cm^{-3} for $(GeSe_3)_{80}Sb_{20}$ (see table 5.17).

The binding energies in eV of the core peaks of Ge-Se-Sb glasses with respect to the Fermi level are given in table 5.18. The Ge(3d) binding energy changes little from 30.1 eV for $GeSe_2$ to 30.2 eV for $(GeSe_2)_{88}Sb_{12}$. The binding energy of Se(3d) also changes little from 54.2 eV for $GeSe_2$ to 53.9 eV for $(GeSe_3)_{80}Sb_{20}$. Small shifts in the binding energies of the other core peaks are observed on substitution. The binding energies of the peaks of the valence bands referenced to the Fermi level are given in table 5.19. The p-

type and s-type peaks of the valence bands shift toward the Fermi level when Sb is added to $GeSe_2$. The weak additional peak remain at a binding energy of ~8.0 eV. It is unfortunate that we are unable to obtain good interference functions for this system because of the quality of the sample surfaces.

It can be seen from the results of the ternary glasses based on Ge-Se that the addition of Ga, Sn, Bi, and Sb, of valencies 3, 4, 5, and 5 respectively, results in a decrease in the local electron density about the Se atom. It is also worth noting that the ratio of medium to short range order increases for Ga addition, decreases for Sn addition and remains essentially the same for Bi addition.

5.1.6 Ge-S-Ag glasses

The chalcogenide element was changed from Se to S to investigate parallels between the glasses. However, the first system examined was based on Ag as a ternary component.

The binding energies in eV of the levels of the Ge-S-Ag glasses with respect to the Fermi level are given in table 5.20. The binding energy of Ag(4d) is centered about 4.5 eV. The core peak binding energies change little with composition.

The measured X-ray interference functions of the alloys examined are shown in Fig. 5.28. The FSDP totally disappears from the interference functions for Ag concentrations equal or more than 20 at % Ag. The peak fit parameters for the FSDP in $Ge_{39.9}S_{55.1}Ag_5$, $Ge_{36}S_{54}Ag_{10}$, and $Ge_{30}S_{55}Ag_{15}$ are given in table 5.21. The position of the FSDP remain at 1.03 $Å^{-1}$ and the 'coherence length' assumes the value of 15 Å. The ratio of the

intensity of the FSDP to the second peak in the interference function decreases from 0.34 for $Ge_{36}S_{54}Ag_{10}$ to 0.14 for $Ge_{30}S_{55}Ag_{15}$.

The compositional dependence on Ag content in the alloys of the measured glass transition temperatures and relative densities are shown in Fig. 5.29 and 5.30 respectively. The T_g value decreases from 566^0K for $Ge_{39.9}S_{55.1}Ag_5$ to 525^0K for $Ge_{20}S_{50}Ag_{30}$ (see table 5.22). The density increases from 3.69 gm cm^{-3} for $Ge_{39.9}S_{55.1}Ag_5$ to 5.01 gm cm^{-3} for $Ge_{20}S_{50}Ag_{30}$ (see table 5.22).

5.1.7 Ge-S-Ga glasses

The Ge-S-Ga system has direct parallel with Ge-Se-Ga system. The base glass for the ternary was GeS_2.

The binding energies (eV) of the core peaks, of the alloys examined, with respect to the Fermi level are given in table 5.23. The binding energies of Ge(3d) (30.2 eV) and S(2p) (160.8 eV) remain the same in GeS_2 and $(GeS_2)_{90}Ga_{10}$ glasses. The measured plasmon energy losses from the $L_3M_{4,5}M_{4,5}$ Auger lines of Ge for the two compositions GeS_2 and $(GeS_2)_{90}Ga_{10}$ are shown in Fig. 5.31. The value of the plasmon energy changes from 18.4 eV for GeS_2 to 17.6 eV for $(GeS_2)_{90}Ga_{10}$. The averaged values of the measured plasmon energies from the $L_3M_{4,5}M_{4,5}$ Auger lines of Ge and the values obtained from equation 2.17, using the measured relative densities, are given in table 5.24. The variation of the measured plasmon energy from the $L_3M_{4,5}M_{4,5}$ Auger lines of Ge with Ge content in the alloy is shown in Fig. 5.32. The variation of the

calculated values of the plasmon energies with Ge content in the alloy is also shown in Fig. 5.32. The variation of glass transition temperature with Ge content in the alloy is shown in Fig. 5.33. The value of T_g decreases from 624^0K for GeS_2 to 614^0K for $(GeS_2)_{90}Ga_{10}$ (see table 5.24). The binding energies (eV) of the peaks of the valence bands referenced to the Fermi level are given in table 5.25. The p-type peak remain at a binding energy of ~ 3.0 eV for all the compositions while the s-type peak binding energy changes from 12.6 eV for $Ge_{20}S_{80}$ to 13.3 eV for GeS_2.

The measured X-ray interference functions for GeS_2 and $(GeS_2)_{90}Ga_{10}$ show a FSDP (Fig. 5.34). The peak fit parameters for the FSDP in these glasses are given in table 5.26. The position of the FSDP in reciprocal space changes from 1.04 $Å^{-1}$ for GeS_2 to 1.16 $Å^{-1}$ for $(GeS_2)_{90}Ga_{10}$ while the 'coherence length' changes from 17 Å for GeS_2 to 14 Å for $(GeS_2)_{90}Ga_{10}$. The ratio of the intensity of the FSDP to the second peak in the interference function decreases from 0.94 for GeS_2 to 0.61 for $(GeS_2)_{90}Ga_{10}$.

5.1.8 Ge-S-Sn glasses

The base glass for this ternary system was GeS_3 therefore it was found convenient to represent the compositions as $Ge_{1-x}Sn_xS_3$ with x=0.1, 0.2, 0.3 and 0.4.

The variation in measured glass transition temperature with Sn content in the alloy is shown in Fig. 5.35. The glass transition temperature decreases from 603^0K for $Ge_{0.9}Sn_{0.1}S_3$ to 595^0K for $Ge_{0.6}Sn_{0.4}S_3$ (see table 5.27). The measured X-ray interference

functions for the two compositions $Ge_{0.9}Sn_{0.1}S_3$ and $Ge_{0.8}Sn_{0.2}S_3$ show a FSDP (Fig. 5.36). The peak fit parameters for the FSDP in these glasses are given in table 5.28. The position of the FSDP in reciprocal space, the 'coherence length', and the ratio of the intensity of the FSDP to the second peak in the interference function change very little for the two compositions. The variation of the relative density with Sn content in the alloys is shown in Fig. 5.37. The density increases from 2.64 gm cm^{-3} for $Ge_{0.9}Sn_{0.1}S_3$ to 2.94 gm cm^{-3} for $Ge_{0.6}Sn_{0.4}S_3$ (see table 5.27).

The averaged values of the measured plasmon energies from the $L_3M_{4,5}M_{4,5}$ Auger lines of Ge and the values calculated from equation 2.17, using the measured relative densities of the alloys, are given in table 5.27. The measured plasmon energy losses for the $L_3M_{4,5}M_{4,5}$ Auger lines of Ge for $Ge_{0.9}Sn_{0.1}S_3$ and $Ge_{0.8}Sn_{0.2}S_3$ are shown in Fig. 5.38. The value of the plasmon energy changes from 17.9 eV for $Ge_{0.9}Sn_{0.1}S_3$ to 18.8 eV for $Ge_{0.8}Sn_{0.2}S_3$. The variation of the plasmon energy from the $L_3M_{4,5}M_{4,5}$ Auger lines of Ge with Ge content in the alloy is shown in Fig. 5.39. The value of the Ge plasmon energy is a maximum for $Ge_{0.8}Sn_{0.2}S_3$ composition suggesting that the local electron density about Ge has a maximum value at this composition. The variation of the calculated values of plasmon energies with Ge content is also shown in Fig. 5.39. The binding energies in eV of the core peaks of the glasses with respect to the Fermi level are given in table 5.29. The core peak binding energies change little with composition. The binding energies in eV

of the peaks of the valence bands referenced to the Fermi level are given in table 5.30. The p-type and s-type peaks of the valence bands remain at binding energies of approximately 2.0 eV and 13.0 eV respectively.

5.1.9 Ge-S-Bi glasses

For this alloy system the Ge concentration was kept constant, therefore it was found convenient to represent the compositions by $Ge_{20}S_{80-x}Bi_x$ with x = 0, 5, 10 and 15 at % Bi.

The averaged values of the measured plasmon energies from the $L_3M_{4,5}M_{4,5}$ Auger lines of Ge and the values obtained from equation 2.17, using the measured relative densities, are given in table 5.31. The value of the plasmon energy changes from 18.2 eV for $Ge_{20}S_{80}$ to 17.8 for $Ge_{20}S_{65}Bi_{15}$. The change in the measured plasmon energies from the $L_3M_{4,5}M_{4,5}$ Auger lines of Ge with the amount of Bi in the alloy is shown in Fig. 5.40. The change in the calculated values of the plasmon energies is also shown in Fig. 5.40. The binding energies (eV) of the core peaks of the glasses with respect to the Fermi level are given in table 5.32. Small shifts in the core peak binding energies are observed on substitution. The binding energies of the peaks of the valence bands referenced to the Fermi level are given in table 5.33. The p-type peak binding energy changes from 2.0 eV for $Ge_{20}S_{75}Bi_5$ to 1.4 eV for $Ge_{20}S_{65}Bi_{15}$ while the s-type binding energy remain effectively at a binding energy of 12.7 eV for all compositions. The variation of the measured relative density with Bi concentration in the alloy is

shown in Fig. 5.41. The density increases from 2.56 gm cm^{-3} for $Ge_{20}S_{80}$ to 3.84 gm cm^{-3} for $Ge_{20}S_{65}Bi_{15}$ (see table 5.31).

For the Ge-S based glasses, a 'model' base glass (GeS_2) is used to compare the changes in the local electron density around the Ge atom and the changes in the ratio of medium to short range order, when the ternary element is added. It can be seen from the results that the addition of the ternary results in the decrease of the local electron density around Ge except for $Ge_{0.8}Sn_{0.2}S_3$ composition where it showed an increase. The ratio of medium to short range order decreases for Ag and Ga addition and increases for Sn addition.

5.2 Discussion

5.2.1 Se-S glasses

The generally accepted structural model of amorphous Se is believed to be based on chains (Robertson 1976, Meek 1976). Our measured X-ray interference functions of the glassy alloys (see Fig. 5.1) show a first sharp diffraction peak (FSDP). This FSDP, whose intensity increases with the amount of S in the alloy (see table 5.1), is considered to be a signature of the medium range ordering (MRO) occurring in these glassy alloys and it is the first time that it has been identified in this system. Since the value of the 'coherence length' in real space remains the same (37 Å) for all the compositions examined, it is concluded that the structural element at the intermediate-range length scale that gives rise to the FSDP is

the same for all the compositions. The ratio of medium to short range order increases with the amount of S added to the alloy, as is evident from the increase in the intensity ratio of the FSDP to the second peak in the interference function (see table 5.1). As a starting point for a more detailed model, we propose that the addition of S to Se introduces eight-membered mixed rings. These rings are associated with the MRO in this system. This view of eight-membered mixed ring formation has support from published Raman spectra (Schottmiller et al 1970). It is expected that the MRO connected with these structural units (rings) will influence the electronic structure of the amorphous Se network. This change in the electronic structure is exhibited in both the change in measured plasmon energies (see table 5.2 and Figs. 5.2 and 5.3) and valence bands (see table 5.3 and Fig. 5.4). To understand the significance of this change in plasmon energy it is necessary to look at the process of plasmon emission in a little more detail.

In the X-ray (Al K_α) photoelectron spectroscopy of the chalcogenide glasses the most intense features are provided by the LMM series Auger lines. The kinetic energies of the lines of Se are very well known through the work of Weightman et al 1975. A vital property of selenium Auger transitions is that the kinetic energies of the Auger electrons are sufficiently large, about 1300 eV, for which the mean free path in the material will be several atomic layers from the surface (Seah and Dench 1978). So only those selenium atoms within about 30 Å of the material vacuum-interface will contribute to the Auger line, and assuming only

extrinsic plasmons are excited, will sample the local electron density. Thus, the plasmon energy obtained from electron spectroscopy becomes a local probe of the Se electron density in the various glass compositions (Orton et al 1990). Since accurate electron density values were not available for the inclusion in equation 2.17, an exact comparison between simple theory and experiment was not possible and the measured values can be looked upon as a guide to the correct order of magnitude. It should be noted that all the experimental values of the plasmon energies are larger than those obtained from the use of equation 2.17 (see table 5.2). In general, the change in plasmon energy with Se content imply that the local electron density of the Se atom is changing. The change in local electron density of Se atom is reflected in the valence band spectra (see table 5.3) where the s-type peak splits into two peaks at 15 at % S and merge into a single peak at 40 and 50 at % S. In order to have some criterion of comparison for the experimental valence bands of the alloys it was decided to compare them with a superposition of the traces of Se and S weighted by the respective atomic proportions. A close agreement between the generated valence bands and the experimental was obtained especially over the p-type peak region (see Fig 5.4).

As mentioned above, the addition of S to Se will increase the ring concentration which is predicted by the copolymerisation theory (see section 1.7.4) and thereby the system is becoming

more "plasticised" which produces a less rigid structure with the corresponding decrease in both the glass transition temperature and the macroscopic densities as observed (see Figs. 5.5 and 5.6 respectively). The rapid decrease of the glass transition temperatures when S is added to Se is also taken as an indication that the structure of the host amorphous Se network has changed.

5.2.2 Ge-Se-Ga glasses

The measured binding energies of Ga(3d) levels in $(GeSe_2)_{96}Ga_4$ (19.4 eV) and in $(GeSe_2)_{92}Ga_8$ (19.4 eV) glasses (see table 5.5 and Fig. 5.7) are lower than those measured in its crystalline stoichiometric compounds GaSe (20.3 eV) and Ga_2Se_3 (20.1 eV). From this it can be inferred that the Ga enviroment is not the same in the glasses and its crystalline compounds and hence Ga must not have the tetrahedral coordination it has in its crystalline stoichiometric compounds. A coordination number of 3 for Ga in these ternaries is proposed and that Ga atoms replace Ge sites in these glasses. Furthermore, the observation of a small peak at ~ 8 eV between the two main p-type and s-type peaks of the valence bands (see Fig. 5.8 and table 5.6) supports this assignment of a coordination number of 3 for Ga atoms and possibly for Ge atoms on the surface of these glasses. Orton et al (1982) from their XPS study of bulk glassy $Ge_{1-x}Se_x$ associated a peak observed on the valence band traces between the two main 4p and 4s regions with the change in the density of states of Ge when its coordination changes from 4 to 3 and referred to this peak as the three-fold

peak 'TFP' (section 5.1.2). However, from the similarity of the measured binding energies of Ge(3d) and Se(3d) levels in the ternaries and those measured in the binary (see table 5.5), it can be inferred that the coordination numbers of Ge and Se, 4 and 2, respectively, in $GeSe_2$ glass, are conserved in the ternaries. Because the binding energies of the Ga(3d) levels in the amorphous ternaries shifts to lower value by ~ 1eV as compared to the crystalline compounds, it is concluded that the amorphous alloys are more covalent than the crystalline compounds. This shift seems to be independent of the composition of the ternary glasses but this cannot be assured because of the limited number of the ternaries examined.

A rapid alteration of Se plasmon energy with Ga concentration occurs for these alloys (see table 5.7 and Figs 5.9 and 5.10). It can be seen from table 5.7 that the values of the plasmon-loss energy for Se and Ge in $GeSe_2$ are different. Sueoka (1965), using electron-beam excitations to study grain sizes in metallic alloys has shown that, for the critical range between 100 to 60 Å, two plasmon energies were observed but shifted from the values for the pure material. These values were observed for larger grain size, while a single weighted value was found for grain sizes below 60 Å. These results indicate that a medium-range order may exist in $GeSe_2$ glass, similar, but not identical in size, to that found from X-ray diffraction results (Orton et al 1982) and in agreement with the structure proposed by Phillips 1981. It must be pointed that

Mexiner and Chen 1983 have obtained only single values for the plasmon energy from Ge-Se glasses by electron energy loss spectroscopy (EELS) using 250 keV electrons. However, this could be due to radiation-damage effects reducing the " grain " size. The MRO is also exhibited by the presence of the FSDP on the X-ray interference functions of the alloys (see Fig 5.11). The structural element at the intermediate-range length scale that gives rise to the FSDP is reduced in size when Ga is added to $GeSe_2$, which is evident from the decrease of the 'coherence length' (see table 5.8).

The average coordination numbers < m > of the binary and the ternaries, assuming a coordination number of 3 for Ga, are calculated using the standard procedure (section 1.6.4) and listed in table 5.7. Based on constraints theory, where the number of constraints is equal to the number of degrees of freedom, and structural dimensionality considerations, it has been established that a network glass has two critical topological points or thresholds at < m > values of 2.4 and 2.67 (Phillips 1979, Phillips 1981, Thorpe 1983, Phillips and Thorpe 1985, Tanaka 1986, Tanaka 1987, Tanaka 1988 and Tanaka 1989). At < m > =2.4 the network glass changes from " floppy or spongy " to a rigid type. The Ge-Se-Ga glasses studied here have < m > values larger than 2.67; these glasses are therefore all " rigid " in the Phillips-Thorpe sense.

If the average coordination number is taken as a measure of the rigidity of the glass then it is expected that the density of the

ternaries will be higher than the binary and will increase with the increase of Ga content in the ternaries which is indeed experimentally observed (see Fig.5.12). This picture, however, does not explain the behaviour of the glass transition temperature, which is related to rigidity, where it shows a decrease in T_g as Ga content in the alloy is increased (see Fig 5.13). The behaviour of T_g is also inconsistent with the relative bond energies of Ge-Se and Ga-Se where Ge-Se bond energy is weaker than that of Ga-Se (Pauling 1960). This marked decrease in T_g with Ga content in the alloy corresponds to an increase of the configurational entropy and hence the glasses become less stable. It could also be taken as an indication that the underlying glass structure is changing, possibly transforming from a two dimensional (2-D) molecular cluster network (MCN) for $GeSe_2$ ($< m > = 2.67$) to a three dimensional (3-D) chemically-ordered covalent network (COCN) glasses for the ternaries where $GeSe_2$ and Ga_2Se_3 structural units exist. This is particularly true for Se-containing glasses where it has been indicated that these glasses tend to form polymerised network glasses where homopolar bond formation is qualitatively suppressed, and Se promotes the formation of only heteropolar bonds resulting in $GeSe_2$ and Ga_2Se_3 type structural units. However, it must be made clear that the chemical order and hence the local structure of the glasses is consistent with these structural units and not that the glass necessarily contains phase-separated regions of $GeSe_2$ and Ga_2Se_3 (Elliott and Steel 1987). This is true since it was observed that each glass composition had only one T_g value (see

table 5.7) indicating that the glass is homogenous.

The view of transformation from 2-D to 3-D network has support from the work of Tanaka (1989) who, using the structural dimensionality model, accounted for the topological threshold and proposed that at $< m >$ =2.67, 2-D (layer) structures are fully evolved and this threshold is due to the emergence of 3-D structures due to cross-linking for $< m >$ greater than 2.67.

White (1974) using a relatively small number of tight-binding matrix elements calculated the band structure for GeSe system. His model resulted in a relative maximum in the band gap at the compound composition $GeSe_2$. Tronc et al (1973) from their optical absorption edge and Raman scattering measurements for Ge_xSe_{1-x} glasses support the results of White's model. Kawamura et al (1980) calculated the average energy gap for Ge_xSe_{1-x} in the composition range $0 \leq x \leq 0.7$ from their optical dielectric constant measurements and observed that the average energy gap has a maximum for the $GeSe_2$ composition. The values of the average energy gaps, calculated from our measured plasmon energies from the $L_3M_{4,5}M_{4,5}$ Auger lines of Se (see section 2.5), show a maximum value for $GeSe_2$ (see table 5.7) which is consistent with the results of Kawamura et al (1980).

5.2.3 Ge-Se-Sn glasses

The density results show that there is a decrease in density as Sn is added to $GeSe_2$ and Sn/Ge ratio is increased (see Fig. 5.14).

This type of behaviour observed for the density, indicates that the glass network "raft" is progressively fragmenting with increasing Sn concentration. Moreover, between x=0.2 and x=0.3 there is a sudden drop in density, marking the onset of fragmentation at x=0.2. Apparently as the "raft" break up the free interfacial volume between the fragments increases and the ratio of the surface to volume of the molecular clusters would increase. The observed monotonic decrease in the glass transition temperature with increasing Sn concentration (see Fig. 5.15) is consistent with that of Mikrut and McNeil (1989) and does not show the step-like behaviour between x=0.4 and x=0.5 observed by Stevens et al (1985). This smooth monotonic decrease indicates that the glass is becoming less stable and that the configurational entropy is increasing, and is consistent with an increase in the ratio of the surface to volume of the molecular clusters which would occur as the "rafts" break up and their sizes decrease. The slight decrease in the glass transition temperature could be attributed to the replacement of the stronger bond Ge-Se by the weaker bond Sn-Se (Pauling 1960).

Mikrut and McNeil (1989) proposed a model for the structure of these ternary glasses based on the model of amorphous $GeSe_2$ proposed by Bridenbaugh et al (1979) in which Sn atoms substitute preferentially for Ge sites on the edge of the cluster "outrigger raft". As Sn concentration is increased, the average-size cluster can no longer accommodate all of the Sn atoms substitutionally in the

preferred Ge sites on the edge of the cluster "outrigger sites". The clusters, therefore break up into smaller clusters to create more "outrigger" sites for the Sn atoms to occupy. This fragmentation begins to occur at the value x=0.2 and as x increases, Sn atoms continue to occupy "outrigger" sites until the clusters reduce to the smallest possible unit which retains the bonding of amorphous $GeSe_2$, namely one consisting of two chains. For $x > 0.7$ the structure of crystalline $SnSe_2$ begins to dominate and the sample can no longer form a glass. However, it was not possible to prepare a truely amorphous sample for $x > 0.6$ with the cooling technique employed in this work, in the sense that the X-ray diffraction pattern displays sharp peaks characteristic of crystallisation. This was attributed to the slower cooling rates for the samples because of the larger sample sizes prepared. The density results reported here are consistent with this model proposed by Mikrut and McNeil (1989).

Further information on the glass structure in this composition range x=0 to x=0.6 comes from the value of the average coordination number of the glasses examined which remains constant at $< m > = 2.67$ (see table 5.9). According to Tanaka (1987, 1988, 1989) this value of threshold is associated with two dimensional (2-D) structures. Therefore, the idea proposed by Stevens et al (1985) that there is a transition from molecular cluster network (MCN) to continuous random network (CRN) occurring at x=0.35, is not supported.

It has been suggested by Martin et al 1990 that the electrons beyond the mobility edge become localised in a smaller volume as the cluster size is decreased in the composition range $0.2 \leq x \leq 0.3$. This leads to an increase in the energy of the anti-bonding states and thus in optical band gap and average energy gap. The calculated average energy gaps from the measured plasmon energies from the $L_3M_{4,5}M_{4,5}$ Auger lines of Se (see section 2.5) show an increase at x=0.3 from the otherwise decreasing trend (see table 5.9 and Fig. 5.18) which can be explained on this basis. Thus the behaviour of the average energy gap parallels that of the optical energy gap of Martin et al 1990.

The observed FSDP on the X-ray interference functions for all the glassy compositions examined (see Fig 5.19) indicate the presence of MRO for these alloys and is in accord with the observation of the companion mode (A_1^C) in the Raman spectra of Mikrut and McNeil (1989) for all concentrations up to x=0.7. This companion mode is generally associated with MRO of the glass network (Bridenbaugh et al 1979). The decrease of the 'coherence length' when Sn is added to $GeSe_2$ (see table 5.10) indicates that the average size of the clusters associated with MRO is decreasing, which is consistent with the fragmentation into smaller clusters when Sn is added to $GeSe_2$.

The local electron density of Se atoms decreases when Sn is added to $GeSe_2$ as can be seen from the variation of the measured plasmon energies (see Fig. 5.17).

5.2.4 Ge-Se-Bi glasses

It can be seen from table 5.13 and Fig. 5.20 that, for the glasses containing different concentrations of Bi, the Se plasmon energy does not change with composition while the Ge plasmon energy does and the type of conduction is reported to change from p- to n-type (Tohge et al 1979, Tohge et al 1980 a, Tohge et al 1980 b, Nagles et al 1981). From this it is concluded that any electronic or structural changes must be concentrated on the Ge-Bi bond. This seems reasonable since Bi is incorporated as three-fold coordinated in these glasses (Elliott and Steel 1986, 1987). It is fortuitous that the strongest photoelectron line from Bi, $4f_{7/2}$, is close to Se Auger line (see Fig 5.21). So, although the Bi concentration of the glass is small, changes in separation of this line (i.e. Se($^1G_4$- Bi($4f_{7/2}$)) can be measured easily. It is found that this separation is 20.7 eV in the Bi containing alloys, while the separation obtained from published values of the pure components (Malra 1989, Weightman et al 1975) is 22.7eV. This difference is attributed to the change in the binding energy of Bi ($4f_{7/2}$) on alloying, rather than any alteration of the Auger kinetic energy because of the constant value of the plasmon energy.

The results of X-ray K-absorption edge measurements of Ge and Se in glassy $Ge_{22}Se_{78}$ and $Ge_{22}Se_{68}Bi_{10}$ (Agnihotri et al 1987), which showed that the Ge K-edge shifted while the Se K-edge remained unchanged, confirm our conclusion that Bi makes bonds with Ge in these glasses. Further confirmation comes from the results of infrared transmission spectroscopy, which indicated that

Bi-Ge modes rather than Bi-Se modes were found infrared active in Ge-Se-Bi alloys (Bhatia 1983). Similar conclusions were also drawn in support of the Bi-Ge bond formation in the bulk glass $Ge_{20}Se_{70}Bi_{10}$ from pressure-dependent conductivity measurements (Bhatia et al 1985) and in $Ge_{22}Se_{68}Bi_{10}$ thin film from steady-state and transient photoconductivity measurments (Mathur and Kumar 1986).

The X-ray interference functions (see Fig. 5.22) show a FSDP indicating MRO in these glasses which is consistent with the observation of the companion Raman mode A^1_c in the Raman spectra of amorphous $(GeSe_{3.5})_{1-x}$ Bi_x (x =0,14) (Bhatia 1983). The structural element at the intermediate-range length scale that gives rise to the FSDP is reduced in size when Bi is added to $GeSe_{3.5}$ which is evident from the decrease in the 'coherence length' (see table 5.14). The ratio of medium to short range order remain essentially the same as can be seen from the intensity ratio of the FSDP to the second peak in the interference function.

The average coordination number for the alloys, assuming a coordination number of 3 for Bi in these glasses (Elliott and Steel 1986, 1987), was calculated and listed in table 5.13. The glasses all have an average coordination number larger than 2.4 and hence considered to be "rigid" in the Phillips-Thorpe sense. If the rigidity scales with the average coordination number then the density of the glasses, which is related to rigidity, should increase with the addition of Bi to the binary which is observed (see Fig. 5.23).

5.2.5 Ge-Se-Sb glasses

The value of the Se plasmon energy changes with Sb concentration (see table 5.17 and Figs. 5.24 and 5.25) while that of the Ge plasmon energy remains effectively unchanged (see table 5.17). Therefore, any structural changes (the conductivity is reported to remain p-type for all Sb concentrations (Gosain et al 1987)) must be concentrated on the Sb-Se bond and following Phillips (1981) it is suggested that Sb penetrates into the $(GeSe_{1/2})_4$ tetrahedral structural units possibly substituting for Ge atoms and forming Sb_2Se_3 structural units in addition to $GeSe_2$ units. This seems to be reasonable since Sb is incorporated into three-fold coordinated, covalently bonded sites for all Sb concentrations (Elliott and Steel 1987). Similar conclusions supporting the above statement of Sb-Se bond formation rather than Sb-Ge come from the study of X-ray K-absorption edges of Ge and Se in glassy $Ge_{22}Se_{78}$ and $Ge_{22}Se_{68}Sb_{10}$ where it was found that the Ge K-edge remained unchanged while the Se K-edge shifted (Agnihotri et al 1987) and from infrared spectroscopy results (Gerasimenco 1976) where it was found that Sb-Se interaction was favoured for all Sb concentrations.

The marked decrease in glass transition temperature for these alloys as Sb is added to $GeSe_2$ (see Fig. 5.26) indicates that the glasses are becoming less stable and that the underlying glass structure is changing. This fact, combined with the values of the average coordination number (see table 5.17) is tempting to

assume that the structure of the glass is changing from a two dimensional molecular cluster structure (2-D) in $GeSe_2$ and $(GeSe_2)_{94}Sb_6$ to a three dimensional chemically ordered covalent network structure (3-D) for $(GeSe_2)_{88}Sb_{12}$, where $GeSe_2$ and Sb_2Se_3 structural units exist. But as mentioned before, it must be stressed that the glass does not necessarily contain phase-separated regions of $GeSe_2$ and Sb_2Se_3 because the glasses examined are homogeneous, as is evident from the observation of only one T_g for each composition examined. The decrease in T_g is attributed to the replacement of the strong Ge-Se bonds by the weaker Sb-Se bonds (Pauling 1960) as Sb is added to $GeSe_2$. This speculation about the transformation from a 2-D to a 3-D network is consistent with the structure of Ge-Se-Sb glasses which form into polymeric cross-linked chains in the region of low-cross link density (Ray 1978, Rawson 1967). The cross-linking units provided by either Ge or Sb are responsible for the transformation of the structure from one dimensional into two or into three dimensional structures depending on the degree of cross-linking (Phillips 1979, Adler 1982) which is assumed to scale with the average coordination number (Tanaka 1987). Similar conclusions about the structure of these glasses were drawn by Narasimhan et al 1981 from their electrical conductivity study.

The results of the Ge-Se-Sb glasses combined with the results of Ge-Se-Bi glasses indicate that Sb and Bi when incorporated into the Ge-Se glassy network behave quite differently, though both

elements belong to the same group of the periodic table. In the former glasses Sb-Se bonds are favoured and the conduction is reported to remain p-type for all Sb concentrations while in the latter glasses Bi-Ge bonds are favoured and the conductivity is reported to change from p- to n-type with Bi doping. Therefore, Ge-Bi bond must accompany the change in conduction properties observed in Ge-Se-Bi system.

5.2.6 Ge-S-Ag glasses

The electronic structure of the valence levels of silver metal is dominated by a strong d-band which is ~ 4 to 5 eV below the Fermi level. It is known that the position of this d-band is highly sensitive on alloying with other atoms. Since it is found experimentally that this d-band is centered about 4.5 eV below the Fermi level for the glassy ternaries examined (see table 5.20), it is concluded that these d-band states are strongly spatially localised. The localisation of the d-band may be taken as evidence that the Ag-S bonding is covalent and that the Ag is acting as a network-former rather than a network-modifier. This is because, in network-modifiers there will be a charge transfer from the modifying atoms (Ag) to the chalcogen atoms (S). If this is the case then the 4d-band will be the most affected by this charge transfer and will shift deeper, contrary to what is found experimentally.

The X-ray interference functions for glasses with 5, 10, and 15 at % Ag show a FSDP which totally disappears for Ag concentrations equal to or more than 20 at % Ag (see Fig. 5.28). This change

indicates that Ag above a given concentration destroys the MRO which extends over 15 Å distances (see table 5.21). Qualitatively this change in the structure is reflected in the composition dependence of the glass transition temperature where it shows a sudden decrease in T_g between 15 and 20 at % Ag from the otherwise monotonic decrease (see Fig. 5.29). Thus the T_g graph can be separated into two regions, one with at % Ag $\leq$ 15 where the MRO is present and one with at % Ag $\geq$ 15 where the MRO is absent. In general the decrease in T_g indicates that the glass is becoming less stable with the increase of Ag concentration.

It has been suggested previously that Ag has a significant influence on the MRO when added to Ge-Se glasses and that it enters as three-fold coordinated in the ternary glasses (Dejus et al 1988). Assuming a coordination number of three for Ag in Ge-S-Ag glassy system, which is reasonable because of the similarity between this system and Ge-Se-Ag, the average coordination number for the alloys was calculated and listed in table 5.22. All the glasses examined have $< m >$ values greater than 2.67 characteristic of 2-D layer structures (Tanaka 1989), so the structure of these glasses could be visualised as 3-D COCN which contains Ag_2S_3 structural units in addition to GeS_2 structural units.

5.2.7 Ge-S-Ga glasses

The most important feature of the results for this alloy is that the value of the binding energy of Ga(3d) in the glass (19.3 eV) is lower than those measured either in crystalline GaS (20.5 eV) or in

crystalline Ga_2S_3 (20.0 eV). This suggests that Ga must not have the tetrahedral coordination that it possesses in its crystalline compounds and it is proposed that Ga could have a coordination number of 3. But the measured value of the binding energy of 3d core level for Ge in the ternary glass $(GeS_2)_{90}Ga_{10}$ is similar to that measured in the binary glass GeS_2. Also the measured binding energies of 2p core level of S in the ternary and the binary are similar (see table 5.23). From this it could be inferred that the coordination numbers of Ge and S in the ternary assume the values of 4 and 2 respectively, as in the binary. The amorphous ternary compound is considered to be more covalent than the crystalline compounds because of the lower value of the binding energy of Ga(3d).

The plasmon energy of the $L_3M_{4,5}M_{4,5}$ of Ge atom changes as Ga is added to GeS_2 (see Figs. 5.31 and 5.32), indicating that the local electron density of Ge is changing, possibly due to the replacement of Ge atoms by Ga atoms in the $(GeS_{1/2})_4$ tetrahedral structural units which are the building blocks of the stucture of GeS_2 glass. It is not unreasonable to assume that the addition of Ga to GeS_2 modifies the glassy network and possibly transforming it from 2-D in GeS_2 to 3-D COCN in $(GeS_2)_{90}Ga_{10}$. This assumption is in accord with structural dimensionality considerations (see section 5.2.2) where the average coordination number changes from 2.67 for GeS_2 to 2.70 for $(GeS_2)_{90}Ga_{10}$ alloy (see table 5.24). It also has added support from the marked decrease of T_g of GeS_2 when Ga is added to it (see table 5.24 and Fig. 5.33).

The X-ray interference functions for GeS_2 and $(GeS_2)_{90}Ga_{10}$ show a FSDP indicating the presence of MRO in these glasses (see Fig. 5.34). The average size of the clusters that give rise to the FSDP is reduced in size when Ga is added to GeS_2 which is evident from the decrease of the 'coherence length' (see table 5.26). The ratio of medium to short range order decreases as can be seen from the decrease of the intensity ratio of the FSDP to the second peak in the interference function.

5.2.8 Ge-S-Sn glasses

According to Phillips model (1981) of medium range order of Ge-chalcogenide glasses (section 1.7.2), the structure of the S-rich binary glasses is visualised to be dominated by $(GeS_{1/2})_4$ corner sharing tetrahedra and S_8 monomers and S_n chains. As Sn is added to the binary, it is suggested that it randomly substitutes for Ge sites in the tetrahedral structural units and forming $(SnS_{1/2})_4$ units. The formation of the slightly weaker Sn-S bonds at the expense of the slightly stronger Ge-S bonds (Pauling 1960) presumably explains the compositional dependence of T_g (see Fig. 5.35). Based on structural dimensionality considerations (see section 5.2.2) the ternaries, which all have an $< m >$ value of 2.5 (see table 5.27), could be visualised as 2-D glassy netwoks where $(GeS_{1/2})_4$, $(SnS_{1/2})_4$ tetrahedral units as well as S_8 monomers and S_n chains are present. Similar conclusions supporting the view of replacement of Ge atoms by Sn atoms in chalcogen rich Ge-S-Sn glasses were arrived at by Fukunaga et al 1982 from their Raman

scattering measurements.

The X-ray interference functions for $Ge_{0.9}Sn_{0.1}S_3$ and $Ge_{0.8}Sn_{0.2}S_3$ glasses show a FSDP signifying MRO in these glasses (see Fig. 5.36) which is in accord with the observation of the companion Raman line in the Raman spectra of Murase et al 1983. The structural element at the intermediate-range length scale that gives rise to the FSDP and the ratio of medium to short range order are approximately the same for both compositions as can be seen from the approximately equal values of the 'coherence length' and the intensity ratio of the FSDP to the second peak respectively (see table 5.28).>

The plasmon energy of Ge $L_3M_{4,5}M_{4,5}$ is changing with composition, with the maximum change occurring for x=0.2, indicating, in general, that the Ge atom local electron density is changing (see Figs. 5.38 and 5.39).

5.2.9 Ge-S-Bi glasses

It is established that $Ge_{20}S_{80-x}Bi_x$ glassy system exhibits a transition from p- to n-type conduction for Bi concentration ≥ 11 at % (Nagels et al 1983, Vikhrov and Ampilgov 1987). The observed value of plasmon energy from the $L_3M_{4,5}M_{4,5}$ Auger lines of Ge for p-type semiconductors (x=0, 5, 10 at % Bi) is different from that for n-type semiconductors (x=15 at % Bi) (see table 5.31 and Fig. 5.40). Based on this observation and the similarity between this system and Ge-Se-Bi system which exhibits the same p to n transition but at a lower value of Bi concentration, it is suggested that any

structural or electronic changes must be concentrated on Ge-Bi bond and following Phillips 1981 it is also suggested that Bi becomes a constituent of the clusters forming complex structural units containing all three elements Ge, S, and Bi, thus modifying the host amorphous network $Ge_{20}S_{80}$. This seems reasonable because Bi is three-fold coordinated in these glasses (Elliott and Steel 1986, 1987). Similar conclusions supporting the view of Ge-Bi bond formation in this glassy system were arrived at by Gosain et al (1985) from their pressure-induced structural and electrical measurements.

These ternary glasses all have an $< m >$ value larger than 2.4 (see table 5.31) which increases with Bi concentration and thus considered to be rigid in the Phillips-Thorpe sense and their rigidity increases with the addition of Bi as confirmed from our density measurements (see Fig 5.41) and from the glass transition temperature measurements of Bhatia et al 1986.

5.3 Further discussion

In the results that have been discussed in sections 5.2.2 to 5.2.9, we have been concerned with individual ternary glassy systems. Attention is now turned to these systems as a group, and pairs of parameters are examined for evidence of correlations. From the discussion of the results, it is clear that the average coordination number $< m >$ should correlate with the measured properties. For this purpose the linear correlation coefficient R was calculated. The value of R always lies between -1 and +1. Values of

R close to ±1 indicate a good linear correlation; values close to 0 indicate little or no correlations (Taylor 1982).

A more quantitative measure of the correlation can be obtained by calculating the probability $P_N(|R| \geq |R_0|)$, which is the probability that N measurements of two uncorrelated variables would give a coefficient R at least as large as any particular R_0.Thus if a coefficient R, for which $P_N(|R| \geq |R_0|)$ is small, is obtained, then a correlation between the two variables is indicated. In particular, if $P_N(|R| \geq |R_0|) \leq 5$ percent, the correlation is called "significant". A correlation is sometimes called "highly significant" if the corresponding probability is less than 1 percent. Thus, a definite answer that the data are (or are not) correlated, cannot be obtained; instead , a quantitative measure of how improbable it is that they are uncorrelated is obtained. The values of the percentage probabilities $P_N(|R| \geq |R_0|)$ as a function of N and R_0 are tabulated, and were used to judge the correlations with < m >.

The correlations of the different measured properties with < m > are summarised in table 5.36. It can be seen from the table that only two properties are correlated with < m >. These are, the positions, in reciprocal space, of the second peak and the FSDP, of the X-ray interference functions. The other properties are not correlated with < m >. The variation of the measured properties, with < m >, are shown in Figs. 5.42 to 5.50 inclusive. It is shown, in Fig. 5.42, that the position, in reciprocal space, of the second peak increases with the increase in the average coordination number.

This seems to be reasonable since an increase in the average coordination number results in an increase in the degree of cross-linking (Tanaka 1987). With this increase in cross-linking, there is a corresponding decrease in the average first neighbour distances, which will result in an increase in the position of the second peak in reciprocal space. The position, in reciprocal space, of the FSDP increases with the increase of the value of the average coordination number (see Fig. 5.43). The position of the FSDP in reciprocal space is related to d, the repeat distance between the clusters, via the approximate relation $d \cong 2\pi/K$ (Susman et al 1988). What seems to be happening is that , as $< m >$ increases and hence the degree of cross-linking increases, the repeat distance between the clusters decreases , contrary to what is expected. This is only a tentative explanation, since the nature of the MRO, associated with the FSDP, is not fully understood.

The correlations, of the plasmon energy-losses from the $L_3M_{4,5}M_{4,5}$ Auger lines of Ge and Se with the intensity ratio of the FSDP to the second peak, are given in table 5.37. The variation of these plasmon energy-losses with the intensity ratio are shown in Figs. 5.51 and 5.52, respectively. These figures show that the plasmon energy-losses increase with the increase in the intensity ratio i.e. with the increase in the amount of MRO. The increase in the amount of MRO, corresponding to an increase in the number of atomic groupings responsible for the FSDP, will result in an increase in the local electron densities around Ge and Se atoms. This increase in the local electron densities around Ge and Se atoms

result in an increase in the plasmon energy-losses from Ge and Se Auger lines, respectively.

CHAPTER 6

Conclusions and further work

A simple model for the addition of S to Se is proposed in which eight-membered mixed rings are formed and associated with the MRO observed in these glasses. The addition of S to Se also introduced changes in the electronic structure of the amorphous Se network which is exhibited in the changes in the measured plasmon energies from the $L_3M_{4,5}M_{4,5}$ Auger lines of Se, which may be looked upon as a probe of the local electron density around Se atoms. The change of electronic structure is also reflected in the observed changes in the valence bands.

The XPS results for the ternary glasses show that :

(a) the measured plasmon energy-losses from the $L_3M_{4,5}M_{4,5}$ Auger lines of Se and Ge serve as a probe of the local electron density around Se and Ge atoms respectively.

(b) the measured plasmon energy-losses are always larger than the calculated values from simple electron theory except for Ge-Se-Ga glasses where the values of the measured plasmon energies from the $L_3M_{4,5}M_{4,5}$ Auger lines of Ge agree with the calculated values

(c) small shifts in the binding energies of the core peaks are

observed on the addition of the third element to the binary.

The XRD results for the ternary glasses indicated the presence of MRO. For the Ge-S-Ag glasses the addition of Ag concentrations equal to or more than 20 at % resulted in the loss of the MRO in these glasses.

The density results showed that the density increased on addition of the ternary element except for Ge-Se-Sn glasses which showed the opposite behaviour. The addition of the ternary component also resulted in the decrease of the measured glass transition temperatures for all the base glasses examined.

The EXAFS and XANES results for $GeSe_2$ and $(GeSe_2)_{92}Ga_8$ glasses suggest that there is a very little change in the local structure around the Ge atom in $GeSe_2$ glass as a function of temperature and that the local structure around the Ge atom changes on alloying $GeSe_2$ with Ga.

The results of Ge-Se-Bi and Ge-Se-Sb indicate that Bi and Sb, though both belonging to the same group of the periodic table, behave quite differently when incorporated into the Ge-Se glassy network. In the former glasses Ge-Bi bonds are favoured and the conductivity is reported to change from p- to n-type with Bi doping while in the latter glasses Sb-Se bonds are favoured and the conduction is reported to remain p-type with Sb doping. Therefore Ge-Bi bond must accompany the change in the type of conduction observed for Ge-Se-Bi system.

The results of Ge-Se-Sn and Ge-S-Sn glasses show that Sn

substitutes preferentially for Ge sites on the edge of the cluster while in Ge-S-Sn glasses it substitutes randomly for Ge sites.

According to the results presented in this work, the criteria of the average coordination number does not seem to be a good parameter for the structure of the glasses studied. Prelimenary calculation show that there are correlations with the ionic radii of the glasses studied.

Further work is needed on the EXAFS and XANES data from $GeSe_2$ and $(GeSe_2)_{92}Ga_8$ glasses and the full analysis of the EXAFS data from $(GeSe_2)_{92}Ga_8$ will help to indicate the coordination of Ga atom in these glasses. An EXAFS study from Se K-edge in Se-S glasses will also help to indicate the coordination of Se in these glasses. The measurement of the interference functions for Ge-Se-Sb and Ge-S-Bi systems will indicate if MRO exist in these alloy systems and will also indicate the amount of this MRO if it exists.

This work could be extended to other ternary systems, such as Ge-Se-Te and Ge-Si-S, and to quaternary systems such as Ge-As-Se-Te and As-Se-Te-Bi.

References

Adler, D., J. Solid State Chem., **45** (1982) 40.

Agnihotri, A.K., Kumar, A., and Nigam, A.N., J. Non-Cryst. Solids, **93** (1987) 267.

Agnihotri, A.K., Kumar, A., and Nigam, A.N., Phil. Mag. Lett., **58** (1988) 63.

Anthony, M.T., and Seah, M.P., Surface Interface Anal., **6** (1984), Ibid, **6**(1984) 107.

Arai, K., J. Non-Cryst. Solids, **59 & 60** (1983) 1059.

Aspnes, D.E., Phillips, J.C., Tai, K., and Bridenbaugh, P.M., Phys. Rev. **B, 23** (1981) 816.

ASTM. Standard Practice for Checking the Operating Characteristics of X-ray Photoelectron Spectrometers (E 902-82): Surf. Interface Anal., **10** (1987) 55.

van Attekum, P.M.Th.M., and Trooster, J.M., Phys. Rev. **B, 18** (1978) 3872, Ibid, **20** (1979) 2335.

Auger, P., J. Phys. Rad., **6** (1925) 205.

Avetikyan, G.B., and Baidakov, L.A., Izv. Akad. Nauk, SSSR, Neorg. Mater., **8** (1972) 1489.

Axmann, A., and Gissler, W., Phys. Stat. Sol., **19** (1967) 721.

Azoulay, R., Thibierge, H., and Brenac, A., J. Non-Cryst. Solids, **18** (1975) 33.

Bell, R.J., and Dean, P., Phil. Mag., **25** (1972) 1381.

Berkes, J.S., "The Physics of Non-Crystalline Solids", 4th Int. Conf., ed. by G.H. Frischat, 1977, p 405.

Bethe,H., and Salpeter, E., "Quantum Mechanics of One and Two-Electron Systems" (Springer-Verlag, Berlin) 1957.

Betts, F., Bienenstock, A., and Ovishinsky, S.R., J. Non-Cryst. Solids, 4 (1970) 554.

Bhatia, K.L., J. Non-Cryst. Solids, **54** (1983) 173, Ibid, **58** (1983) 151.

Bhatia, K.L., Gosain, D.P., Parthasarathy, G., and Gopal, E.S.R., J Non-Cryst. Solids, **86** (1986) 65.

Bhatia, K.L., Parthasarathy,G., Gosain, D.P., and Gopal, E.S.R., Phil. Mag., **51** (1985) L63.

Bianconi, A., Proc. of the Daresbury Weekend, 1981, p. 13.

Bird, R.J., and Swift, P., J. Elec. Spectrosc., **21** (1980) 227.

Boolchand, P., Grothaus, J., Bresser, W.J., and Suranyi, P., Phys. Rev. **B, 25** (1982) 2975.

Borisova, Z.U., "Glassy Semiconductors" (Plenum Press, New York), 1981.

Bresser, W.J., Boolchand, P., Suranyi, P., and de-Neufville, J.P., Phys. Rev. Lett., **46** (1981) 1689.

Bridenbaugh, P.M., Espinosa, G.P., Griffiths, J.E., Phillips, J.C., and Remeika, J.P., Phys. Rev. **B, 20** (1979) 4140.

Briegleb, G., Z. Phys. Chem., **A144** (1929) 321.

Briggs, D., and Seah, M.P., (eds) :"Practical Surface Analysis by Auger and X-ray Photoelectron Spectroscopy", John Wiley and Sons Ltd, 1983.

Burhop, E.H.S., "The Auger Effect and Other Radiationless

Transitions", Cambridge Univ. Press, London, 1952.

Cardona, M., and Ley, L., (eds) : "Photoemission in Solids I : General Principles. Topics in Applied Physics", Vol. 26 (Springer-Verlag, Berlin, Heidelberg, New York) 1978.

Carroll, P., and Lannin, J.S., Solid St. Commun., **40** (1981) 81.

Causer, R., Isherwood, S.P., Orton, B.R., and Street, R.L.T., J. Phys. E, **4** (1971) 354.

Cervinka, L., and Hruby, A., "Amorphous and Liquid Semiconductors" ed by J. Stuke and W. Brenig, Taylor & Francis Ltd, London, 1974, p. 431.

Chen, C.H., J. Non-Cryst. Solids, **44** (1981) 391.

Chen, I., Phys. Rev. **B, 7** (1973) 3672.

Chung, M.F., and Jenkins, L.H., Surf. Sci., **21** (1970) 253.

Compton, A.H., and Allison, S.K., "X-rays in Theory and Experiment" (Macmillan) 1935.

Corb, B.W., Wei, W.D., and Averbach, B.L., J. Non-Cryst. Solids, **53** (1982) 29.

Cromer, D.T., and Waber, J.T., Acta Cryst., **18** (1965) 104.

Davis, E.A., "Amorphous and Liquid Semiconductors", eds. J. Stuke and W. Brenig, Taylor & Francis Ltd., London, 1974, p. 519.

Dejus, R.J., Susman, S., Volin, K.J., Price, D.L., and Montague, D.G., J. Non-Cryst. Solids, **106** (1988) 34.

Dembovskii, S., Inorg. Mat., **5** (1969) 385.

Dittmar, G., and Schaffer, H., Acta Cryst. **B, 32** (1976a) 2726.

Dittmar, G., and Schaffer, H., Acta Cryst. **B, 32** (1976b) 1188.

Dittmar, G., and Schaffer, H., Acta Cryst. B, 31 (1975) 2060.

Doniach, S., Sunjic, J., J. Phys. C, 3 (1970) 285.

Drahokoupil, J. , Smotlacha, O., Fendrych, F., Klokocnikova, H., and Kozlov, M.A., J. Non-Cryst. Solids, 88 (1986) 43.

Eisenberg, A., and Tobolsky, A.V., J. Polymer Sci., 46 (1960) 19.

Elliott, S.R., and Steel,A.T., Phys. Rev. Lett., 57 (1986) 1316.

Elliott, S.R., and Steel, A.T., J. Phys. C, 20 (1987) 4335.

EXCALIB, EXBACK, and EXCURV90, available from Daresbury SRC programme library.

Espe, W., "Materials of High Vacuum Technology, Vol. 2, Silicates", Pergamon Press, 1968.

Faraday, M., Trans. Roy. Soc, 1 (1830) 1.

Fawcett, R.W., Wagner, C.N.J., and Cargill, G.S., J. Non-Cryst. Solids, 8-10 (1972) 369.

Feltz, A., Buttner, H.J., Lippmann, F.J., and Maul, W., J. Non-Cryst. Solids, 8-10 (1972) 64.

Feltz, A., Pohle, M., Steil, H., and Herms, G., J. Non-Cryst. Solids, 69 (1985) 271.

Feltz, A., and Lippmann, F.J., Z. Anorg. Allg. Chem., 398 (1973) 157.

Feltz, A., and Thieme, C., Z. Chem., 14 (1974) 32.

Feltz, A., Zickmuller, K. and Pfaff, H., in "Proc. 7th Int. Conf. on Amorphous Liquid Semiconductors", Edinburgh, 1977, ed. W.Spear, p. 125.

Fukunaga, T., Tanaka, Y., and Murase, K., Solid St. Commun., 42 (1982) 513.

Gadzuk, J.W., "Photoemission and the Electronic Properties of Surfaces", (ed.) Feuerbacher, B., Fitton, B., and Willis, R.F., John Wiley & Sons, Chichester, 1978.

Galzov, V.M., and Situlina, O.V., Dokl. Akad. Nauk, **187** (1969) 799.

Gerasimenko, V.S., Gutenev, M.S., Korepanova, N.A., and Pazin, A.V., Fiz. Khim. Steckla, **2** (1976) 275.

Goldschmidt, D., Rudman, P.S., J. Non-Cryst. Solids, **22** (1976) 229.

Goldschmidt, V.M., Trans. Faraday Sos., **25** (1926) 253.

Gorgol, J., An X-ray Photoelectron Spectroscopy Study of Ag Dipped $GeSe_2$ and X-ray Generated Auger Plasmon Losses in $GeSe_2$, M.Phil. Thesis, Brunel University 1989.

Gorman, M., and Solin, S.A., Solid St. Commun., **18** (1976) 1401.

Gosain, D.P., Bhatia, K.L., Parthasarathy, G., and Gopal, E.S.R., J. Appl. Phys., **62** (1987) 2313.

Gosain, D.P., Bhatia, K.L., Parthasarathy, G., and Gopal, E.S.R., Phys. Rev. **B, 32** (1985) 2727.

Grigorovici, R., J. Non-Cryst. Solids, **1**(1969) 303.

Grigorovici, R., "Electronic and Structural Properties of Amorphous Semiconductors", ed. by P.G.Le Comber and J. Mort (Academic press) 1973, p.191.

Griffiths, J.E., Espinosa, G.P., Remeika, J.P., and Phillips, J.C., Phys. Rev. **B, 25** (1982) 1272.

Guinier, A., "X-ray diffraction" (Freeman) 1963.

Hansen, F.Y., and Knudsen, T.S., J. Chem. Phys., **62** (1975) 1556.

Hayes, T.M., Il Nuvo Cimento, 3D, N5, 1984.

Henninger, E.H., Buschart, R.C., and Heaton, L., J. Chem. Phys., **46** (1967) 586.

Hercules, D.M., and Klein, J.C., in "Applied Electron Spectroscopy for Chemical Analysis" (eds) Windawi, H., and Floyd, F., John Wiley & Sons, 1982.

Hitton, A.R., Hayes, D.J., and Rechtin, M.D., J. Non-Cryst. Solids, **17** (1975) 319.

Hoogewijs, R., Fiermans, L., and Vennick, J., Surf. Sci. , **69** (1977) 273.

James, R.W., "The Optical Principles of X-ray Diffraction", Bell, London, 1950.

Jecu, D., Jaklovszky, J., Trutia, A., Apostol, I., Dinescu, M., Mihailescu, I., Aldica, G., Popescu, M., Vlahovici, N., Zamfira, S., and Indera, E., J. Non-Cryst. Solids, **90** (1987) 319.

Joannopoulos, J.D., and Kastner, M., Solid St. Commun., **17** (1975) 221.

Joannopoulos, J.D., Schluter, M., and Cohen, M.L., Phys. Rev. **B**, 11 (1975) 2186.

Jones, G.O., "Glass" (Methuen) 1956.

Jones, G.O., "Glass" 2nd Ed (Revised by S.Parke), (Chapman &Hall) 1971.

Kaplow, R., Rowe, T.A., and Averbach, B.L., Phys. Rev., **168** (1968) 1068.

Kastner, M., J. Non-Cryst. Solids, **35&36** (1980) 807.

Kawamoto,Y., and Tsuchihashi, S., J. Am. Ceram. Soc., **52** (1969) 626.

Kawamoto, Y., and Tsuchihashi, S., J. Am. Ceram. Soc., 54 (1971) 131.

Kawamura, H., Matsumura, M., and Ushioda, S., J. Non-Crysrt. Solids, 35 & 36 (1980) 1215.

Klug, H.P., and Alexander, L.E., "X-ray Diffraction Procedures for Polycrystalline and Amorphous Materials", 2nd ed, New York, Wiley-Interscience, 1974.

Kohal, W.H., " Handbook of Materials and Techniques for Vacuum Devices ", Reinhold, 1967.

Kokado, H., Shimizu, I., and Inoue, E., J. Non-Cryst. Solids, 20 (1976) 131.

Kostyshin, M.T., Mikhailovskya, E.V., and Romanenko, P.F., Sov. Phys. Solid State, 8 (1966) 451.

Kramer, B., Maschke, K., and Laude, L., Phys. Rev. B, 8 (1973) 5781.

Krebs, H., and Ackermann, F., Glastech Ber., 45 (1972) 213.

Laude, L., Kramer, B., and Maschke, K., Phys. Rev. B, 8 (1973) 5794.

Lebedev,A., J. Russ. Phys. Chem. Soc., 50 (1921) 57.

Lee,P.A., Citrin, P.H., Eisenberger, P., and Kincaid, B.M., Rev. Mod. Phys., 53 (1981) 769.

Lengeler, B., and Eisenberger, P., Phys. Rev. B, 21 (1980) 4507.

Lin, C., Busse, L.E., Nagel, S.R., and Faber, J., Phys. Rev. B, 29 (1984) 5060.

Liu, C.-H, Pashinkin, A.S., and Novoselova, A.V., Dokl. Akad. Nauk SSSr, 146 (1962) 1092; Proc. Acad. Sci. USSR, Chem. Sect., 146 (1962) 892.

Liu,C.-H., Pashinkin, A.S., and Novoselova, A.V., Dokl. Akad. Nauk SSSR, **151** (1963) 1335; Dokl. Chem., Proc. Acad. Sci. USSR, **151**(1963) 662.

Loehman, R.E., Armstrong, A.J., Firestone, D.W., and Gould, R.W., J. Non-Cryst. Solids, **8-10** (1972) 72.

Long, M., Galison, P., Alben, R., and Connell, G.A.N., Phys. Rev. **B, 13** (1976) 1821.

Lucovsky, G., Galeener, F.L., Keezer, R.C., Geils, R.H., and Six, H.A., Phys. Rev. **B, 10** (1974) 5134.

Lucovsky, G., de Neufville, J.P., and Galeener, F.L., Phys. Rev. **B, 9** (1974) 1591.

Lucovsky, G., Galeener, F.L., Geils, R.H., and Keezer, R.C., "The Structure of Non-Crystalline Materials", ed by P.H. Gaskell (Taylor & Francis, London) 1977, p.127.

Lucovsky, G., Mooradian, A., Taylor, W., Wright, G.B., and Keezer, R.C., Solid St. Commun., **5** (1967) 113.

Lucovsky, G., "Physics of Selenuim and Tellurium", ed by W.C. Cooper, Pergamon Press, Oxford, 1969, p.255.

Lucovsky, G., and Galeener, L., J. Non-Cryst. Solids, **35&36** (1980) 1209.

Lucovsky, G., Nemanich, R.J., Solin, S.A., and Keezer, R.C., Solid St. Commun., **17** (1975) 1567.

Lytle, F.W., Sayers, D.E., and Stern, E.A., Phys. Rev. **B, 11** (1975) 4825.

Mackenzie, J.D., "Modern Aspects of the Vitreous State" Vol. 1,

(Butterworth, London) 1960.

Macropaedia, Encyclopaedia Britannica, 5 (1985) 296.

Malaurent, J.C., and Diximer, J., J. Non-Cryst. Solids, 35&36 (1980) 1227.

Malek, J., J. Non-Cryst. Solids, 107 (1989) 323.

Malek, J., Tichy, L., and Klikoka, J., J. of Thermal Anal., 33 (1988) 667.

Maloney, F.J., "Glass in Modern World", 1967.

Malra, G.K., X-ray Photoelectron Spectroscopic Studies of Certain Metals and Alloys Through the Solid-Liquid Transition, Ph.D Thesis, Brunel University 1989.

March, N.H., and Parrinello, M., "Collective Effects in Solids and Liquids", Adam Hilger Ltd, Bristol, 1982.

Marcus, M., Dynes, R.C., Griffiths, J.E., and McWahan, D., J. App. Phys., 54 (1983) 1792.

Martin, L.W., McNeil, L.E., and Mikrut, J.M., Phil. Mag., 61 (1990) 957.

Mathur, R., and Kumar, A., Solid St. Commun., 59 (1986) 163.

Meek, P.E., Phil. Mag., 34 (1976) 767.

Meixner, A.E., and Chen, C.H., Phys. Rev. B, 27 (1983) 7489.

Mikrut, J.M., and McNeil, L.E., J. Non-Cryst. Solids, 109 (1989) 237.

Misawa, M., Suzuki, K., J. Phys. Soc. Japan, 44 (1978) 1612.

Moody, J.W., and Himes, R.C., Mat. Res. Bull., 2 (1967) 703.

Morey, G.W., "The Properties of Glass" (Reinhold, New York) 1954, p. 4 & p.591.

Murase, K., Fukunaga, T., Tanaka, Y., Yakushiji, K., and Yunoki, I., Physica, **117&118 B** (1983) 962.

Myers, M.B., and Felty, E.J., Mat. Res. Bull., **2** (1967) 715.

Nagels, P., Rotti, M., and Vikhrov, S., J. de Physique, **42** (1981) C4-907.

Nagels, P., Tichy, L., Triska, A., and Ticha, H., J. Non-Cryst. Solids, **59-60** (1983) 1015.

Narasimhan, P.S.L., Giridha, A., and Mahadevan, S., J. Non-Cryst. Solids, **43** (1981) 365.

Nemanich, R.J., Phys. Rev. **B, 16** (1977) 1655.

Nemanich, R.J., Connell, G.A.N., Hayes, T.M., and Street, R.A., Phys. Rev. **B, 18** (1978) 6900.

Nemanich, R.J., Galeener, F.L., Mikkelsen, J.C., Connell, G.A.N., Etherington, G., Wright, A.C., and Sinclair, R.N., "Proc. Int. Conf. on Physics of Amorphous Semiconductors", Montpellier, France, 1982.

Nemanich, R.J., Solin, S.A., and Lucovsky, G., Solid St. Commun. **21** (1977) 273.

de Neufville, J.P., J. Non. Cryst. Solids, **8-10** (1972) 85.

Nielsen, P., Phys. Rev **B, 6** (1972) 3739.

Orchard, A.F., in "Handbook of X-ray and Ultraviolet Photoelectron Spectroscopy", ed. by D.Briggs, Heyden and Son, London, 1977, p.49.

Orton, B.R., and Riviere, J. Non-Cryst. Solids, **37** (1980) 401.

Orton, B.R., Saffarini, G., Gorgol, J., and Riviere, J.C., Phil. Mag., **62** (1990) 71.

Orton, B.R., Purser, T., Malra, G.K., and Riviere, J.C., "The Structure of

Non-Crystalline Solids", ed. by P.H. Gaskell, J.M. Parker and E.A. Davis (London: Taylor & Francis) 1982, p.181.

Pardee, W.J., Mahan, G.D., Eastman, D.E., Pollack, R.A., Ley, L., McFeely, F.R., Kowalyczyk, S.P., and Shirley, D.A., Phys. Rev., **11** (1975) 3614.

Pauling, L., "The Nature of the Chemical Bond" (Ithaca: Cornell Univ.) 1960, p.85.

Pearson, A., "Modern Aspects of the Vitreous State" ed. by J. Mackenzie, (Butterworth, London) 1964, p.29.

Penfold, I.T., and Salmon, P.S., J. Phys. Condens. Matter, **2** (1990) SA233.

Person, R., "Flat Glass Technology" (Butterworth, London, New York) 1969.

Phillips, J.C., J. Non-Cryst. Solids, **35&36** (1980) 1157.

Phillips, J.C., J. Non-Cryst. Solids, **34** (1979) 153.

Phillips, J.C., J. Non-Cryst. Solids, **43** (1981) 37.

Phillips, J.C., and Thorpe, M.F., Solid St. Commun., **53** (1985) 699.

Pine, A.S., and Dresselhaus, G., Phys. Rev. **B, 4** (1971) 356.

Pines, D., "Elementary Excitations in Solids", Benjamin, New York, 1964.

Powell, C.J., Phys. Rev., **175** (1968) 972.

Powell, B.M., and Martel, P., "Proc. 10th Int. Conf. Phys. Semic.", U.S. Atomic-Energy Comm., 1970, p.851.

Ramaseshan, S., and Abrahams, S.C., eds., "Anomalous Scattering", Proc. of Inter-Congress Conf., Spain, 1974, p.50.

Rawson, H., "Inorganic Glass Forming Systems", (Academic Press,

New York) 1967.

Rawson, H., Proc. IEE A, 135(1988) 325.

Ray, N.H., "Inorganic Polymers" (Academic Press, New York) 1978.

Rechtin, M.D., and Averbach, B.L., Solid St. Commun., 13 (1973) 491.

Richter, H., J. Non-Cryst. Solids, 8-10 (1972) 388.

Ritchie, R.H., Phys. Rev., 106 (1957) 874.

Robertson, J., J. Phys. C, 8 (1975) 3131.

Robertson, J., Phil. Mag., 34 (1976(13.

Ross, L., and Bourgon, M., Can. J. Chem., 47 (1969) 2555.

Rowland, S.C., Narasimhan, S., and Bienenstock, A., J. App. Phys., 43 (1972) 2741.

Ruska, J., and Thurn,H., J. Non-Cryst. Solids, 22 (1976) 277.

Satow, T., Uemura, O., and Sagara, Y., J. Japan Inst. Metals, 37 (1973) 1348.

Savage, J.A., "Infra-red Optical Materials and their Antireflection Coatings", Adam Hilger Ltd., Bristol and Boston, 1985, p. 84.

Sayers, D.E., Lytle, F.W., and Stern, E.A., J. Non-Cryst. Solids, 8-10 (1972) 401.

Sayers, D.E., Stern, E.A., and Lytle, F.W., Phys. Rev. Lett., 35 (1975) 584.

Schenk, J., Physica, 23 (1957) 325.

Schottmiller, J., Tabak, M., Lucovsky, G., and Ward, A., J. Non-Cryst. Solids, 4 (1970) 80.

Scofield, J.H., J. Elec. Spectrosc., 8 (1976) 129.

Seah, M.P., and Dench, W.A., Surf. Interface Anal., 1 (1979) 2.

Seah, M.P., and Lea, C., Thin Solid Films, 81 (1981) 257.

Shevchik, N.J., Cardona, M., and Tejeda, J., Phys. Rev. B, 8 (1973) 2833.

Shevchik, N.J., Phys. Rev. Lett., 33 (1974) 1572.

Shirai, T., and Hamada, S., Nippon Kagakn Zasshi, J. Chem. Soc. Japan, Pure Chem. Sect. , 84 (1963) 968.

Shwartz, W.E., and Hercules, D.M., Anal. Chem., 43 (1971) 1774.

Siegbahn, K., et al, ESCA applied to Free Molecules, North Holland, Amsterdam, 1969.

Smekal, A.G., J. Soc. Glass-Technology, 35 (1951) 411.

Spicer, W.E., Phys. Rev., 112 (1958) 114.

Srivastava, V.K., Phys. Rev. B, 29 (1984a) 6993, Phys. Lett., 102A (1984b) 127, J. Phys. C, 19 (1986) 5689, Phys. Rev. B, 36 (1987) 5044.

Stanworth, J.E., J. Soc. Glass-Technology, 30 (1946) 54.

Stern, E.A., Phys. Rev. B, 10 (1974) 3027.

Stern, E.A., Sayers, D.E., and Lytle, F.W., Phys. Rev. B, 11 (1975) 4836.

Stern, E.A., Sci. Am., 234 (1976) 96.

Stern, E.A., Contemp. Phys., 19 (1978) 289.

Stern, E.A., and Ferrel, R.A., Phys. Rev., 120 (1960) 130.

Stevels, J.M., J. Non-Cryst. Solids, 6 (1971) 307.

Stevens, M., Poolchand, P., and Hernandez, J.G., Phys. Rev. B, 31 (1985) 981.

Stuke, J., "Physics of Selenuim and Tellurium", ed. W.C. Cooper, Pergamon Press, Oxford, 1969, p.3.

Sueoka, O., J. Phys. Soc., Japan, **20** (1965) 2212.

Susman, S., Price, D.L., Volin, K.J., Dejus, R.J., and Montague, D.G., J. Non-Cryst. Solids, **106** (1988) 26.

Sun, K.H., J. Am. Ceram. Soc., **30** (1947) 277.

Suzuki, K., and Misawa, M., in "Proc. 3rd Int. Conf. Liquid Metals", (Inst. Phys. Conf. No.3) 1977, p.531.

Tamman, G., "The Vitreous State", OnTi, Moscow, Leningrad, 1935, p.136.

Tanaka, K., Solid St. Commun., **60** (1986) 295.

Tanaka, K., J. Non-Cryst. Solids, **97&98** (1987) 391.

Tanaka,K., J. Non-Cryst. Solids, **103** (1988) 149.

Tanaka, K., Phys. Rev. **B, 39** (1989) 1270.

Taylor, R.J., "An Introduction to Error Analysis", Oxford University Press, 1982, p. 248.

Teo, B.T., Noy, D.C., eds., "EXAFS Spectroscopy, Techniques and Applications", Plenum Press, New York, 1981.

"The Vitreous State", Naukea, Leningrad, 1971, p.392.

Thorpe, M.F., J. Non-Cryst. Solids, **57** (1983) 355.

Tichy, L., Ticha,H., Benes, L., and Malek,J., J. Non-Cryst. Solids, **116** (1990) 206.

Tobolsky, A., and Owen, G., J.Polymer Sci., **59** (1962) 329.

Tohge, N., Minami, T., Yamamoto, Y., and Tanaka, M., J. App. Phys., **51** (1980a) 1048.

Tohge, N., Minami, T., and Tanaka, M., J. Non-Cryst. Solids, 38-39 (1980b) 283.

Tohge, N., Yamamoto, Y., Minami, T., and Tanaka, M., App. Phys. Lett., 34 (1979) 640.

Tronc, P., Bensoussan, M., Brenac, A., and Sebenne, C., Solid St. Commun., 24 (1977) 77.

Tronc, P., Bensoussan, M., BRenac,A., and Sebenne, C., Phys. Rev. B, 8 (1973) 5947.

Tronc, P., J. Non-Cryst. Solids, 97&98 (1987) 447.

Turnbull, D., and Cohen, M.H., J. Chem. Phys., 29 (1958) 1049.

Uemura, O., Sagara, Y., Muno, D., and Satow, T., J. Non-Cryst. Solids, 30 (1978) 155.

Uemura, O., Sagara, Y., and Satow,T., Phys. Stat. Sol., 32 (1975) K91.

Uemura, O., Sagara, Y., and Satow, T., Phys. Stat. Sol., 26 (1974) 99.

Uhlmann, D.R., J. Non-Cryst. Solids, 7 (1972) 337.

Unger, P., and Cherin, P., "Physics of Selenuim and Tellurium", ed. by W.C. Cooper (Academic Press) 1966.

Unger, P., and Cherin, P., "Physics of Selenuim and Tellurium", ed. by W.C. Cooper, Pergamon Press, Oxford, 1969.

Urnes, S., in "Modern Aspects of the Vitreous State" Vol. 1, ed. by J.Mackenzie (Butterworth, London) 1960, p.10.

Vikhrov, S.P., and Ampilgov, V.N., J.Non-Cryst. Solids, 90 (1987) 441.

Wagner, C.D., and Biloen, P., Surf. Sci., 35 (1973) 82.

Wagner, C.D., Anal.Chem., 441 (1972) 1050.

Wagner, C.D., et al : "Handbook of XPS", Perkin-Elmer Corps, Eden Prairie, MN, 1978.

Wagner, C.N.J., and Halder, N.C., Adv. Phys., **16** (1967) 241.

Warren, B.E., and Biscoe, J., J. Amer. Ceram. Soc., **17** (1934) 249.

Warren, B.E., and Loring, A.D., J. Amer. Ceram. Soc.,**18** (1935) 269.

Warren, B.E., and Krutter, H., J. Amer. Ceram. Soc., **19** (1936) 202.

Warren, B.E., J. App. Phys., **8** (1937) 645.

Warren, B.E., and Biscoe, J., J. Amer. Ceram. Soc., **21** (1938) 259.

Weightman, P., Roberts, E.D., and Johnson, C.E., J. Phys. C, **8** (1975) 550, 2336.

Weinstein,B.A., Zallen, R., Slade, M.L., and Mikkelsen, J.C., Phys. Rev. B, **25** (1982) 781.

Wertheim, G.K., Citrin, P.H., "Photoemision in Solids I", (eds.) Cardona, M., and Ley, L., Springer-Verlag, Berlin 1978.

Weyl, L.W.A., and Marboe, E.C., "The Costitution of Glasses", Vol. 1, Interscience publishers, 1962.

White, R.M., J. Non-Cryst. Solids, **16** (1974) 387.

Williams, R.H., and Polanco, J.I., J. Phys. C, **7** (1974) 2745.

Winick, H., Doniach, S., "Synchrotron Radiation Research", Plenum, New York, 1980.

Wuilleumier, F.J., ed., "Photoemission and Other Probes of Many-Electron Interactions", Plenum Pres, New York, 1976.

Yoshikawa, A., Ochi, O., Nagui,H., and Mizyshima, Y., App. Phys. Lett., **29** (1976) 677.

Zachariasen, W.H., J. Amer. Ceram. Soc., **54** (1932) 3841.

Zhilinskaya, E.A., Lazukin, V.N., Valeev, N.Kh., and Oblasov, A.K., J. Non-Cryst. Solids, **124** (1990) 48.

Appendix 1

Calculation of the plasmon energy using equation 2.17

Appendix 1

Calculation of the plasmon energy using equation 2.17

$\hbar\omega_p = \hbar\,(ne^2/\varepsilon_0 m)^{1/2}$ (Mahan 1978, Kittel 1986)

The valence electron density n is given by

$n = n'\,(N_A\rho/\text{atomic weight})$

where n' is the number of valence electrons i.e. Ga=3, Ge=4, Sn=4, N_A is Avogadro's number and ρ is the measured macroscopic density.

Example : Calculation of the plasmon energy for Se

$n' = 6$

$\rho = 4.31\text{x}10^{3}$ Kg/m^3

Atomic weight = 78.96

$N_A = 6.023\text{x}10^{26}$ atoms/Kmole

$e = 1.60219\text{x}10^{-19}$ C

$m = 9.10953\text{x}10^{-31}$ Kg

$\varepsilon_0 = 8.85419\text{x}10^{-12}$ C^2/Nm^2

$\hbar = 1.0545918\text{x}10^{-34}$ J-s

Using these numerical values in the above equations gives a value of the plasmon energy for Se equal to 16.5 eV.

Values of the plasmon energies calculated in the manner described above are compared with experimentally determined values.

Appendix 2

Determination of the position of the plasmon-loss peak

Appendix 2

Determination of the position of the plasmon-loss peak

The command CU, available on the ESCA data system DS300, allows the user to set up the cursor position. The cursor is placed at the maximum count rate of the peak. When set up, its position is displayed on the 4th line of the display, giving the position of the peak in terms of kinetic energy. Two examples are shown in Figs. A2.1 and A2.2.

It was estimated that the reproducibility of this step was ±0.3 eV. Thus when this position had been determined, the difference in energy from that of the peak position of the $^1G_4$ line of the Se or Ge Auger $L_3M_{4,5}M_{4,5}$ peak was obtained. This energy difference gives the plasmon energy which appears as the experimental value in the tables.

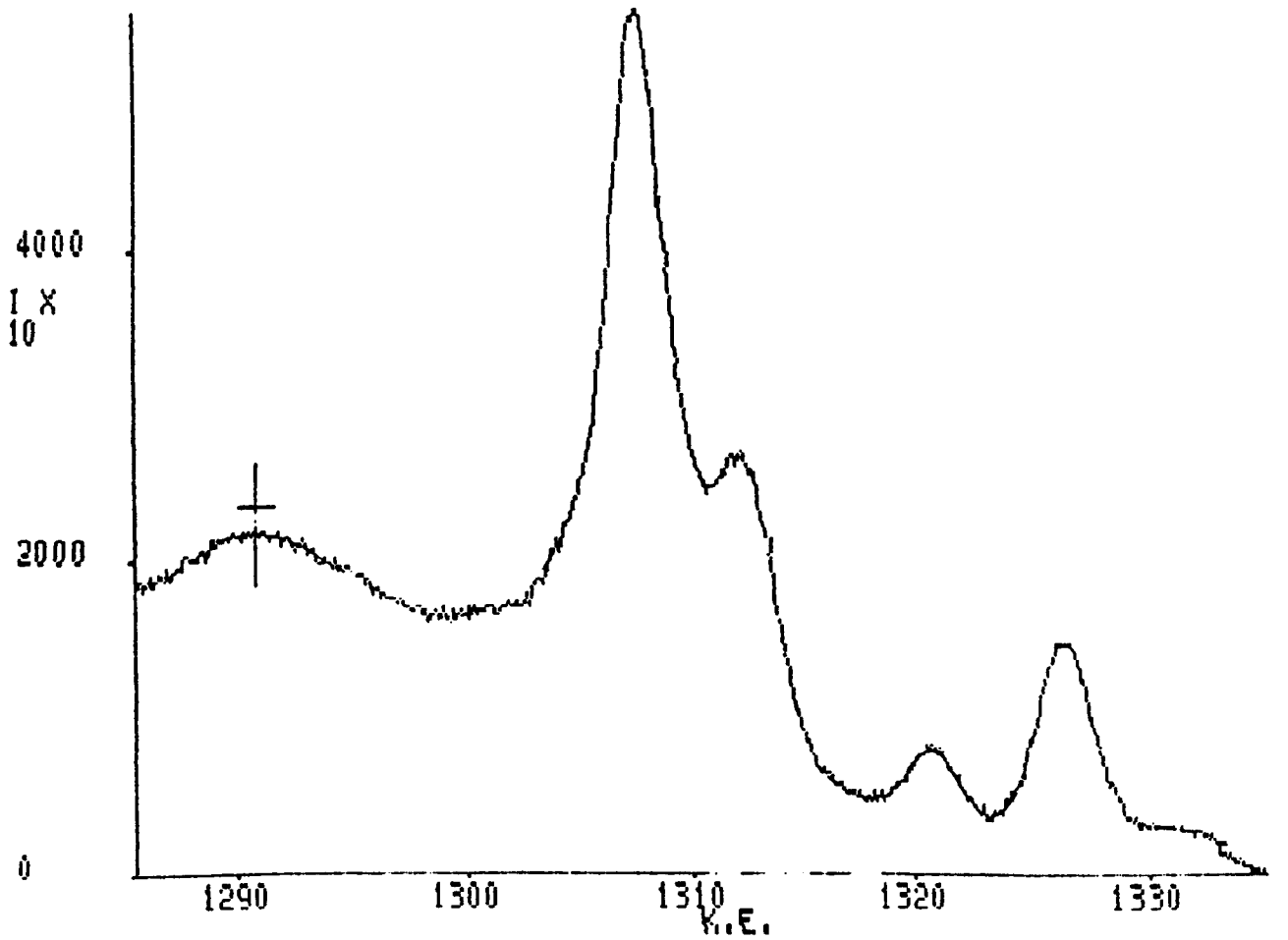

Fig. A2.1 An example of plasmon-loss peak from the $L_3M_{4,5}M_{4,5}$ Auger line of Se in the ternary glass $(GeSe_2)_{92}Ga_8$. The position of the plasmon-loss peak is indicated by the cross.

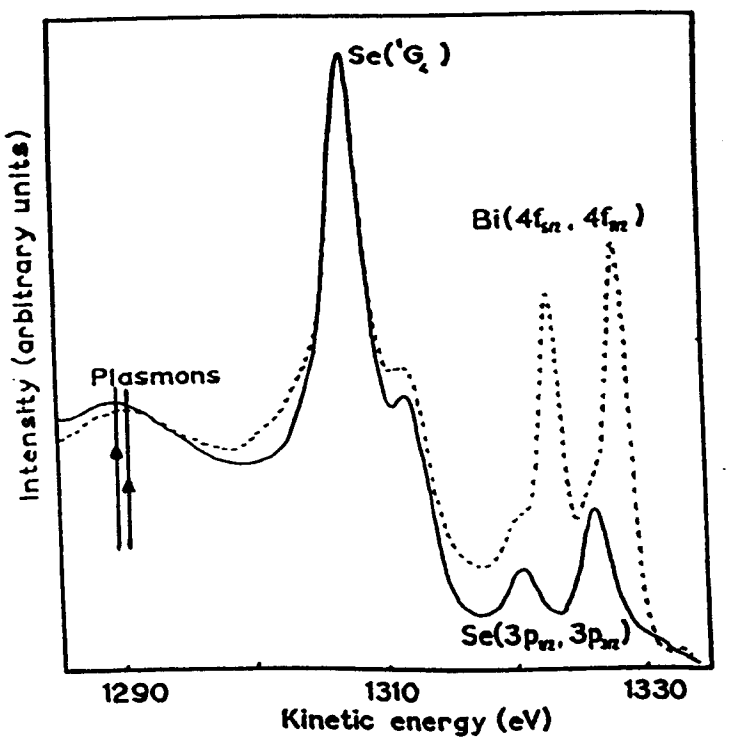

Fig. A2.2 Selenium Auger peaks in $GeSe_{3.5}$ (full curve) and $(GeSe_{3.5})_{90}Bi_{10}$ (broken curve) shifted so that $^1G_4$ peaks coincide. The positions of the plasmon-loss peaks are indicated by the arrows.

Appendix 3

Determination of the full-width at half-maximum (FWHM) of the FSDP

Appendix 3

Determination of the full-width at half-maximum (FWHM) of the FSDP

The background for the first sharp diffraction pattern was obtained as shown in Fig. A3.1. The height of the peak was measured and the FWHM (BD) was determined by projecting BA and DC normals onto the K-axis.

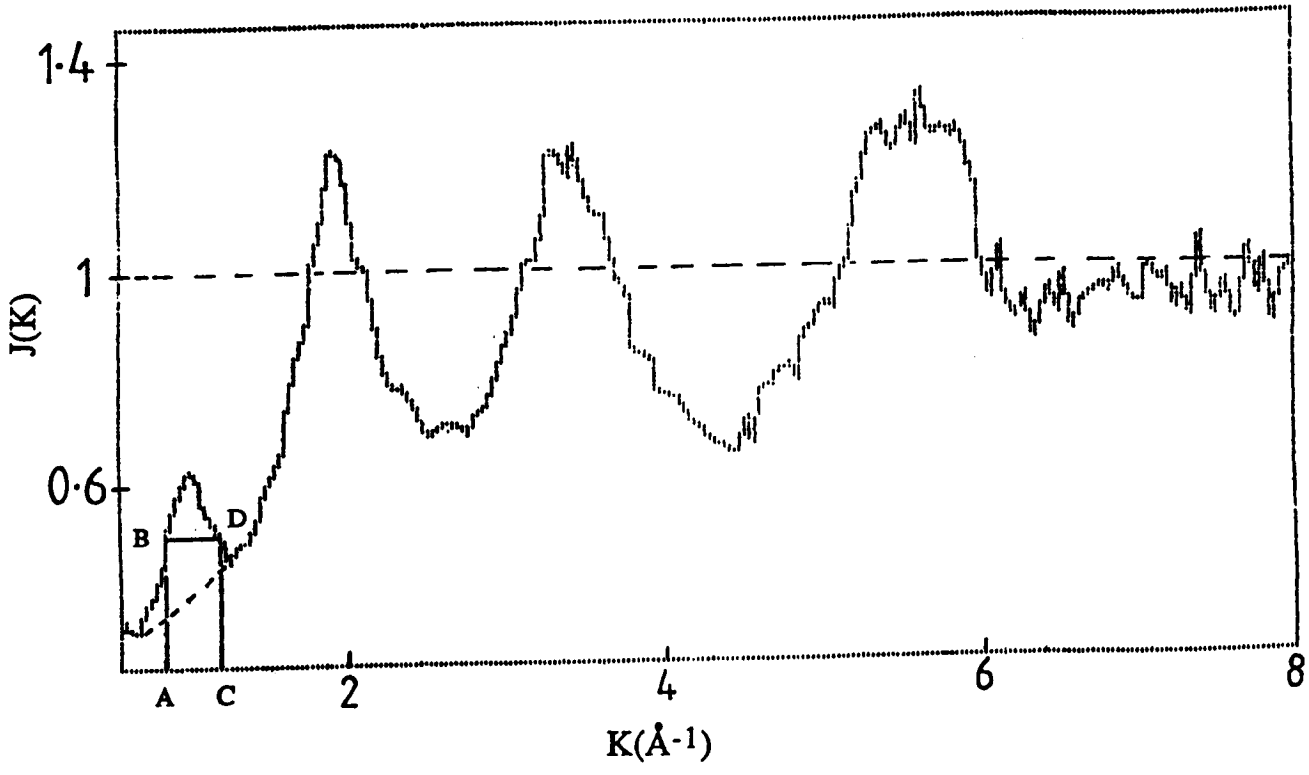

Fig. A3.1 X-ray interference function J(K) for $(GeSe_{3.5})_{95}Bi_5$ glass.

Time(s)	Process	Manifestation	Energy (eV)
$\leq 10^{-17}$	Photon absorption		
10^{-16}	Screening response	Plasmon satellite	1-10
	Coster-Kronig and		
10^{-15}	Core-core-valence	Hole switch-on	
	Auger		
	Pair shake-up	Line asymmetry	~0-1.0
10^{-14}	Intra-molecular	Franck-Condon	0.1-1.0
	vibrations		
10^{-13}	Phonons	Sidebands and broadening	≤ 0.1
	Core-valence-valence	Hole delocalisation	$\leq 10^{-2}$
	Auger		
10^{-12}			
'Forever'			

Table 2.1 Time scales in photoemission.

Transition	Configuration	L–S term	L	S	J	IC term
KL_1L_1	$2s^02p^6$	^1S	0	0	0	$^1S_0$
		^1P	1	0	1	$^1P_1$
$KL_1L_{2,3}$	$2s^12p^5$		1	1	0	$^3P_0$
		^3P	1	1	1	$^3P_1$
			1	1	2	$^3P_2$
$KL_{2,3}L_{2,3}$	$2s^22p^4$	^1S	0	0	0	$^1S_0$
			1	1	0	$^3P_0$
		^3P	[1	1	1	$^3P_1$]*
			1	1	2	$^3P_3$
		^1D	2	0	2	$^1D_2$

*Forbidden.

Table 2.2 Notation in intermediate coupling.

	$\alpha_{1,2}$	α_3	α_4	α_5	α_6	β
displacement,eV	0	8.4	10.2	17.5	20.0	48.5
Mg						
relative height	100	8.0	4.1	0.55	0.45	0.5
displacement,eV	0	9.8	11.8	20.1	23.4	69.7
Al						
relative height	100	6.4	3.2	0.4	0.3	0.55

Table 2.3 X-ray satellite energies and intensities.

Peak	Measured B.E (eV)	NPL B.E (eV)	Difference D(eV)
$Au(4f_{7/2})$	84.1	83.98	0.12
$Ag(3d_{5/2})$	368.5	368.27	0.23
Cu(LMM)	568.3	567.97	0.33
$Cu(2p_{3/2})$	933.1	932.67	0.43
Ag(MNN)	1129.3	1128.79	0.51

Table 2.4 Results of calibration of ES300 spectrometer.

Order of diffraction(n)	Observed		Calculated	
	α_1	α_2	α_1	α_2
n=1	$10^0\ 6'$		$10^0\ 9'$	
n=2	$20^0\ 35'$	$20^0\ 42'$	$20^0\ 38'$	$20^0\ 46'$
n=3	$31^0\ 52'$	$32^0\ 5'$	$31^0\ 54'$	$32^0\ 7'$

Table 3.1 Results of calibration of the diffratometer using LiF crystal.

Composition	P_1 eV	P_2 eV	P_3 eV	P_2-P_1 eV	P_3-P_1 eV	Temp. (^{0}C)
$GeSe_2$	11100	11103	11110	3	10	22
$GeSe_2$	11101	11103	11110	2	9	350
$(GeSe_2)_{92}Ga_8$	11092	11095	11105	3	13	22

Table 4.1 Resonances in the XANES for $GeSe_2$ and $(GeSe_2)_{92}Ga_8$.

P_1: represents the binding energy of the photoelectron where the kinetic energy is almost zero (selected by positioning the point 2/3 up the absorption edge)

P_2: is the maximum point on the absorption edge peak where the kinetic energy is slightly greater than zero

P_3: is the second maximum or "resonance" where the kinetic energy is greater than that for P_2 but still small.

Composition	Peak position $Å^{-1}$(±0.03)	FWHM $Å^{-1}$(±0.03)	Coherence length(Å)	Ratio FSDP/second peak
$Se_{90}S_{10}$	1.24	0.17	37	0.40
$Se_{85}S_{15}$	1.21	0.17	37	0.40
$Se_{80}S_{20}$	1.13	0.17	37	0.43
$Se_{75}S_{25}$	1.17	0.17	37	0.67
$Se_{60}S_{40}$	1.21	0.17	37	0.88
$Se_{50}S_{50}$	1.21	0.17	37	0.88

Table 5.1 Peak fit parameters for the FSDP in Se-S glasses.

Composition	$\hbar\omega_p$ Exp. (±0.3)	$\hbar\omega_p$ Calc.	Density $gmcm^{-3}$ (±1%)	T_g(K) (±0.2%)
Se	19.3	16.5	4.31	317
$Se_{90}S_{10}$	18.3	16.7	4.15	314
$Se_{85}S_{15}$	18.2	16.9	4.10	309
$Se_{80}S_{20}$	18.8	17.0	4.02	308
$Se_{75}S_{25}$	18.8	17.1	3.92	306
$Se_{70}S_{30}$	18.8	17.3	3.87	303
$Se_{60}S_{40}$	19.3	17.2	3.56	293
$Se_{50}S_{50}$	19.3	16.9	3.19	288
Se*	19.3			
Se+	19.3			
S			2.07	

* Shevchick, N.J., Cardona, M., & Tejeda, J., 1973, *Phys.Rev.*B, 8, 2833.

+ Meixner, A.E., & Chen, C.H., 1983, *Phys.Rev.* B, 27, 7489.

Table 5.2 Plasmon energies in eV (measured and calculated), measured relative densities and measured glass transition temperatures.

Composition	p-type		s-type	ΔE_p
	Non-bonding (±0.2)	Bonding	(±0.3)	
Se	1.4	4.1	12.1	2.7
$Se_{90}S_{10}$	1.4	4.0	11.8	2.6
$Se_{85}S_{15}$	1.3	4.0	10.1,13.6	2.7
$Se_{80}S_{20}$	1.3	4.1	11.3,14.6	2.8
$Se_{75}S_{25}$	1.3	4.0	10.5,14.2	2.7
$Se_{70}S_{30}$	1.4	4.1	10.0,14.0	2.7
$Se_{60}S_{40}$	1.4	4.2	10.0	2.8
$Se_{50}S_{50}$	1.4	4.2	11.6	2.8

Table 5.3 Binding energies in eV of the peaks of the valence bands referenced to the Fermi level for Se-S glasses.

Composition	Se(3d) (±0.2)	$Se(3p_{1/2},3p_{3/2})$	Se(3s)	S(2s)
Se	54.0	165.6,159.9	228.7	-
$Se_{90}S_{10}$	54.2	165.8,160.1	228.8	-
$Se_{85}S_{15}$	54.1	165.8,160.1	228.8	-
$Se_{80}S_{20}$	54.1	165.7,160.0	228.7	-
$Se_{75}S_{25}$	54.1	165.7,160.0	228.7	-
$Se_{70}S_{30}$	54.1	165.7,160.0	228.7	-
$Se_{60}S_{40}$	54.1	165.7,160.0	228.7	226.2
$Se_{50}S_{50}$	54.1	165.8,160.1	228.6	226.4

Table 5.4 Binding energies in eV of core peaks referenced to the Fermi level for Se-S glasses.

Composition	Ge($3p_{3/2}$) (±0.2)	Ge(3d)	Se($3p_{1/2}$,$3p_{3/2}$)	Se(3d)	Ga(3d)
$GeSe_2$	122.8	30.1	166.0,160.2	54.2	-
$(GeSe_2)_{96}Ga_4$	122.7	30.1	165.9,160.1	54.0.	19.4
$(GeSe_2)_{92}Ga_8$	122.6	30.2	165.8,160.0	54.1	19.4

Table 5.5 Binding energies in eV of core peaks referenced to the Fermi level for Ge-Se-Ga glasses.

Composition	p-type (±0.2)	s-type (±0.3)	Additional peak 'TFP' (±0.3)
$GeSe_2$	2.5	13.6	7.9
$(GeSe_2)_{96}Ga_4$	2.0	13.0	8.0
$(GeSe_2)_{92}Ga_8$	1.8	13.1	7.0

Table 5.6 Binding energies in eV of the peaks of the valence bands referenced to the Fermi level for Ge-Se-Ga glasses.

Composition	$\hbar\omega_p$(Exp) Se (±0.3)	$\hbar\omega_p$(Exp) Ge (±0.3)	$\hbar\omega_p$(calc.)	Density $gmcm^{-3}$ (±1%)	T_g(K) (±0.2%)	E_g(eV)	<m>
$GeSe_2$	17.7	15.7	16.0	4.45	687	5.42	2.67
$(GeSe_2)_{96}Ga_4$	17.5	16.2	16.1	4.55	650	4.97	2.68
$(GeSe_2)_{92}Ga_8$	16.6	16.1	16.1	4.61	614	4.88	2.69
$GeSe_2$+					692		
$GeSe_2$*					664		

+ de Neufville, J.P., J. Non-Cryst. Solids, 8-10 (1972) 85.

* Feltz, A., Zickmuller, K. and Pfaff, H., in Proc. 7th Int. Conf. on Amorphous Liquid Semiconductors, Edinburgh, 1977, ed. W. Spear, p. 125.

Table 5.7 Plasmon energies in eV (measured and calculated), measured relative densities, measured glass transition temperatures, calculated average energy gaps and calculated average coordination numbers.

Composition	Peak position $Å^{-1}$(±0.03)	FWHM $Å^{-1}$(±0.03)	Coherence length(Å)	Ratio FSDP/second peak
$GeSe_2$	1.14	0.16	39	0.46
$(GeSe_2)_{96}Ga_4$	1.14	0.22	29	0.56
$(GeSe_2)_{92}Ga_8$	1.16	0.22	29	0.60

Table 5.8 Peak fit parameters for the FSDP in Ge-Se-Ga glasses.

Composition	$\hbar\omega_p$(Exp) Se (±0.3)	$\hbar\omega_p$(Calc.) Ge		Density $gmcm^{-3}$ (±1%)	T_g(K) (±0.2%)	E_g(eV)	<m>
$GeSe_2$	17.7	15.7	16.0	4.45	687	5.42	2.67
$Ge_{0.9}Sn_{0.1}Se_2$	17.5	15.8	15.8	4.39	662	5.32	2.67
$Ge_{0.8}Sn_{0.2}Se_2$	17.3	15.8	15.5	4.31	642	5.22	2.67
$Ge_{0.7}Sn_{0.3}Se_2$	17.5	15.8	14.7	3.94	622	5.32	2.67
$Ge_{0.6}Sn_{0.4}Se_2$	16.6	15.5	14.2	3.76	608	4.88	2.67
$Ge_{0.5}Sn_{0.5}Se_2$	16.6	15.5	13.8	3.63	592	4.88	2.67
$Ge_{0.4}Sn_{0.6}Se_2$	16.5	15.5	13.5	3.52	588	4.84	2.67

Table 5.9 Plasmon energies in eV (measured and calculated), measured relative densities, measured glass transition temperatures, calculated average energy gaps and calculated average coordination numbers for Ge-Se-Sn glasses.

Composition	Peak position $Å^{-1}$(±0.03)	FWHM $Å^{-1}$(±0.03)	Coherence length(Å)	Ratio FSDP/second peak
$GeSe_2$	1.14	0.16	39	0.46
$Ge_{0.9}Sn_{0.1}Se_2$	1.00	0.22	29	0.42
$Ge_{0.8}Sn_{0.2}Se_2$	1.00	0.22	29	0.45
$Ge_{0.7}Sn_{0.3}Se_2$	1.03	0.38	17	0.32
$Ge_{0.6}Sn_{0.4}Se_2$	1.05	0.38	17	0.22
$Ge_{0.5}Sn_{0.5}Se_2$	1.05	0.38	17	0.32

Table 5.10 Peak fit parameters for the FSDP in Ge-Se-Sn glasses.

Composition x	Ge($3p_{3/2}$)	Ge(3d)	Se($3p_{1/2,3/2}$)	Se(3d)	Sn($3d_{3/2,5/2}$)	Sn(4d)
0.0	122.8	30.1	166.0,160.2	54.2	-	-
0.1	122.7	29.9	165.9,160.1	54.0	492.3,483.9	24.1
0.2	122.9	30.0	166.0,160.2	54.0	492.6,484.2	24.4
0.3	122.9	29.9	166.0,160.2	54.1	492.5,484.1	24.1
0.4	122.9	29.9	166.0,160.2	54.0	492.5,484.1	24.4
0.5	122.9	30.0	165.9,160.1	53.9	492.6,484.2	24.4
0.6	123.0	29.9	166.0,160.2	54.0	492.6,484.3	24.4

Table 5.11 Core level binding energies in eV referenced to the Fermi level.for $Ge_{1-x}Sn_xSe_2$ glasses.

Composition	p-type (±0.2)	s-type (±0.3)	Additional peak 'TFP' (±0.3)
$GeSe_2$	2.5	13.6	7.9
$Ge_{0.9}Sn_{0.1}Se_2$	1.6	13.1	7.6
$Ge_{0.8}Sn_{0.2}Se_2$	1.5	13.2	7.5
$Ge_{0.7}Sn_{0.3}Se_2$	1.9	13.1	7.0
$Ge_{0.6}Sn_{0.4}Se_2$	1.5	13.4	7.3
$Ge_{0.5}Sn_{0.5}Se_2$	1.4	13.4	7.1
$Ge_{0.6}Sn_{0.4}Se_2$	1.4	13.6	x

Table 5.12 Binding energies in eV of valence band peaks referenced to the Fermi level for Ge-Se-Sn glasses

Composition	$\hbar\omega_p$(Exp.) Se (±0.3)	Ge	$\hbar\omega_p$(calc.)	Density $gmcm^{-3}$ (±1%)	<m>
$GeSe_{3.5}$	18.0	15.1	16.3	4.43	2.44
$(GeSe_{3.5})_{95}Bi_5$	17.5	15.1	16.3	4.83	2.47
$(GeSe_{3.5})_{90}Bi_{10}$	17.5	14.8	15.8	4.93	2.50

Table 5.13 Plasmon energies in eV (measured and calculated), measured relative densities and calculated average coordination numbers for Ge-Se-Bi glasses.

Composition	Peak position $Å^{-1}$(±0.03)	FWHM $Å^{-1}$(±0.03)	Coherence length(Å)	Ratio FSDP/second peak
$GeSe_{3.5}$	1.01	0.32	20	0.36
$(GeSe_{3.5})_{95}Bi_5$	0.93	0.40	16	0.36
$(GeSe_{3.5})_{90}Bi_{10}$	0.93	0.40	16	0.37

Table 5.14 Peak fit parameters for the FSDP in Ge-Se-Bi glasses.

Composition	Ge($3p_{3/2}$) (±0.2)	Ge(3d)	Se($3p_{1/2}3/2$)	Se(3d)	Bi($4f_{5/2}7/2$)	Bi($5d_{5/2}$)
$GeSe_{3.5}$	122.6	30.1	166.0,160.2	54.2	-	-
$(GeSe_{3.5})_{95}Bi_5$	122.8	30.1	-	54.1	163.2,158.0	24.7
$(GeSe_{3.5})_{90}Bi_{10}$	122.8	30.2	-	54.0	163.2,158.0	24.8

Table 5.15 Core level binding energies in eV referenced to the Fermi level.for Ge-Se-Bi glasses.

Composition	p-type (±0.2)	s-type (±0.3)	Additional peak 'TFP' (±0.3)
$GeSe_{3.5}$	1.7	13.0	8.1
$(GeSe_{3.5})_{95}Bi_5$	2.0	13.3	8.1
$(GeSe_{3.5})_{90}Bi_{10}$	1.6	13.9	8.3

Table 5.16 Binding energies in eV of the peaks of the valence bands referenced to the Fermi level for Ge-Se-Bi glasses.

Composition	$\hbar\omega_p$(Exp) Se (±0.3)	Ge	$\hbar\omega_p$(calc.)	Density gmcm-3 (±1%)	T_g(K) (±0.2%)	<m>
$GeSe_2$	17.7	15.7	16.0	4.45	687	2.67
$(GeSe_2)_{94}Sb_6$	17.0	15.8	16.1	4.63	628	2.66
$(GeSe_2)_{88}Sb_{12}$	17.1	15.8	16.2	4.85	568	2.68
$(GeSe_{3.5})_{90}Sb_{10}$	17.2	15.7	16.3	4.77	-	2.50
$(GeSe_3)_{80}Sb_{20}$	16.8	15.7	16.4	5.18	-	2.60
$Ge_{28}Se_{60}Sb_{12}$				4.67	550	

Table 5.17 Plasmon energies in eV (measured and calculated), measured relative densities, measured glass transition temperatures and calculated average coordination numbers for Ge-Se-Sb glasses. Values of the density and glass transition temperature for $Ge_{28}Se_{60}Sb_{12}$ composition are taken from Savage (1985).

Composition	Ge($3p_{3/2}$) (±0.2)	Ge(3d)	Se($3p_{1/2,3/2}$)	Se(3d)	Sb($3d_{3/2,5/2}$)	Sb(4d)
$GeSe_2$	122.8	30.1	166.0,160.2	54.2	_	_
$(GeSe_2)_{94}Sb_6$	122.6	30.1	166.0,160.2	54.0	538.6,529.2	32.6
$(GeSe_2)_{88}Sb_{12}$	122.7	30.2	166.0,160.2	54.1	538.5,529.1	32.8
$(GeSe_{3.5})_{90}Sb_{10}$	122.6	30.2	165.8,160.0	53.9	538.6,529.2	32.8
$(GeSe_3)_{80}Sb_{20}$	122.6	30.1	165.8,160.0	53.9	538.3,528.9	32.7

Table 5.18 Core level binding energies in eV referenced to the Fermi level for Ge-Se-Sb glasses.

Composition	p-type (±0.2)	s-type (±0.3)	Additional peak 'TFP' (±0.3)
$GeSe_2$	2.5	13.6	7.9
$(GeSe_2)_{94}Sb_6$	1.6	13.0	8.0
$(GeSe_2)_{88}Sb_{12}$	1.5	12.9	8.2
$(GeSe_{3.5})_{90}Sb_{10}$	1.7	13.0	8.0
$(GeSe_3)_{80}Sb_{20}$	1.6	12.9	8.0

Table 5.19 Binding energies in eV of the peaks of the valence bands referenced to the Fermi level for Ge-Se-Sb glasses.

Composition	Ag(4d) (±0.2)	Ge(3d)	Ge($3p_{3/2}$)	S(2p)	Ag($3d_{3/2,5/2}$)
$Ge_{39.9}S_{55.1}Ag_5$	4.4	29.8	122.7	160.8	374.3,368.3
$Ge_{36}S_{54}Ag_{10}$	4.6	29.9	122.7	160.9	374.4,368.4
$Ge_{30}S_{55}Ag_{15}$	4.6	29.9	122.9	161.0	374.5,368.5
$Ge_{28}S_{52}Ag_{20}$	4.6	29.9	122.9	160.8	374.5,368.5
$Ge_{25}S_{50}Ag_{25}$	4.5	29.8	122.8	160.8	374.3,368.3
$Ge_{20}S_{50}Ag_{30}$	4.5	30.0	122.9	160.9	374.4,368.4

Table 5.20 Core level binding energies (eV) referenced to the Fermi level for Ge-S-Ag glasses.

Composition	Peak position $Å^{-1}$(±0.03)	FWHM $Å^{-1}$(±0.03)	Coherence length(Å)	Ratio FSDP/second peak
$Ge_{39.9}S_{55.1}Ag_5$	1.03	0.43	15	0.26
$Ge_{36}S_{54}Ag_{10}$	1.03	0.43	15	0.34
$Ge_{30}S_{55}Ag_{15}$	1.03	0.43	15	0.14

Table 5.21 Peak fit parameters for the FSDP in Ge-S-Ag glasses.

Composition	Density $gmcm^{-3}$ (±1%)	T_g(K) (±0.2%)	<m>
$Ge_{39.9}S_{55.1}Ag_5$	3.69	566	2.85
$Ge_{36}S_{54}Ag_{10}$	3.95	544	2.82
$Ge_{30}S_{55}Ag_{15}$	4.21	541	2.75
$Ge_{28}S_{52}Ag_{20}$	4.48	529	2.76
$Ge_{25}S_{50}Ag_{25}$	4.73	526	2.75
$Ge_{20}S_{50}Ag_{30}$	5.01	525	2.70

Table 5.22 Measured relative densities, measured glass transition temperatures and calculated average coordination numbers for Ge-S-Ag glasses.

Composition	Ge($3p_{3/2}$) (±0.2)	Ge(3d)	S(2p)	Ga(3d)
$Ge_{20}S_{80}$	122.8	30.1	160.9	-
GeS_2	122.7	30.2	160.8	-
$(GeS_2)_{90}Ga_{10}$	122.8	30.2	160.8	19.3

Table 5.23 Binding energies in eV of core peaks referenced to the Fermi level for Ge-S-Ga glasses.

Composition	$\hbar\omega_p$(Exp.) Ge (±0.3)	$\hbar\omega_p$(Calc.)	Density $gmcm^{-3}$ (±1%)	T_g(K) (±0.2%)	<m>
$Ge_{20}S_{80}$	18.2	17.2	2.56	561	2.40
GeS_2	18.4	16.4	2.76	624	2.67
$(GeS2)_{90}Ga_{10}$	17.6	16.0	2.90	614	2.70

Table 5.24 Plasmon energies in eV (measured and calculated), measured relative densities, measured glass transition temperatures and calcualted average coordination numbers for Ge-S-Ga glasses.

Composition	p-type (±0.2)	s-type (±0.3)	Additional peak 'TFP' (±0.3)
$Ge_{20}S_{80}$	3.0	12.6	x
GeS_2	2.9	13.3	8.3
$(GeS_2)_{90}Ga_{10}$	3.0	13.3	8.3

Table 5.25 Binding energies in eV of the peaks of the valence bands referenced to the Fermi level for Ge-S-Ga glasses.

Composition	Peak position $Å^{-1}$(±0.03)	FWHM $Å^{-1}$(±0.03)	Coherence length(Å)	Ratio FSDP/second peak
GeS_2	1.04	0.38	17	0.94
$(GeS_2)_{90}Ga_{10}$	1.16	0.45	14	0.61

Table 5.26 Peak fit parameters for the FSDP for GeS_2 and $(GeS_2)_{90}Ga_{10}$ glasses.

Composition	$\hbar\omega_p$(Exp.) Ge (±0.3)	$\hbar\omega_p$(Calc.)	Density $gmcm^{-3}$ (±1%)	T_g(K) (±0.2%)	<m>
$Ge_{0.9}Sn_{0.1}S_3$	17.9	16.7	2.64	603	2.50
$Ge_{0.8}Sn_{0.2}S_3$	18.8	16.8	2.75	598	2.50
$Ge_{0.7}Sn_{0.3}S_3$	17.8	16.9	2.86	596	2.50
$Ge_{0.6}Sn_{0.4}S_3$	17.8	17.1	2.94	595	2.50

Table 5.27 Plasmon energies in eV (measured and calculated), measured relative densities, measured glass transition temperatures and calculated average coordination numbers for Ge-S-Sn glasses.

Composition	Peak position $Å^{-1}$(±0.03)	FWHM $Å^{-1}$(±0.03)	Coherence length(Å)	Ratio FSDP/second peak
$Ge_{0.9}Sn_{0.1}S_3$	0.96	0.42	15	0.98
$Ge_{0.8}Sn_{0.2}S_3$	0.96	0.40	16	0.99

Table 5.28 Peak fit parameters for the FSDP for $Ge_{0.9}Sn_{0.1}S_3$ and $Ge_{0.8}Sn_{0.2}S_3$ glasses.

Composition	Ge($3p_{3/2}$) (±0.2)	Ge(3d)	S(2p)	Sn($3d_{3/2,5/2}$)	Sn(4d)
$Ge_{0.9}Sn_{0.1}S_3$	122.8	29.9	160.9	492.8,484.5	24.2
$Ge_{0.8}Sn_{0.2}S_3$	122.7	30.1	161.2	493.1,484.7	24.5
$Ge_{0.7}Sn_{0.3}S_3$	122.9	29.9	160.8	492.7,484.3	24.3
$Ge_{0.6}Sn_{0.4}S_3$	122.9	29.8	160.8	492.7,484.4	24.4

Table 5.29 Binding energies in eV of core peaks referenced to the Fermi level for Ge-S-Sn glasses.

Composition	p-type (±0.2)	s-type (±0.3)	Additional peak 'TFP' (±0.3)
$Ge_{0.9}Sn_{0.1}S_3$	2.0	12.8	7.0
$Ge_{0.8}Sn_{0.2}S_3$	2.0	13.0	7.7
$Ge_{0.7}Sn_{0.3}S_3$	1.8	13.1	7.0
$Ge_{0.6}Sn_{0.4}S_3$	1.8	13.2	7.0

Table 5.30 Binding energies in eV of the peaks of the valence bands referenced to the Fermi level for Ge-S-Sn glasses.

Composition	$\hbar\omega_p$(Exp.) Ge (±0.3)	$\hbar\omega_p$(Calc.)	Density $gmcm^{-3}$ (±1%)	<m>
$Ge_{20}S_{80}$	18.2	17.2	2.56	2.40
$Ge_{20}S_{75}Bi_5$	18.3	16.8	3.01	2.45
$Ge_{20}S_{70}Bi_{10}$	18.2	16.5	3.43	2.50
$Ge_{20}S_{65}Bi_{15}$	17.8	16.2	3.84	2.55

Table 5.31 Plasmon energies in eV (measured and calculated), measured relative densities and calculated average coordination numbers for Ge-S-Bi glasses.

Composition	Ge($3p_{3/2}$) (±0.2)	Ge(3d)	S(2s)	Bi($4f_{5/2,7/2}$)	Bi(5d)
$Ge_{20}S_{80}$	122.8	30.1	224.9	_	_
$Ge_{20}S_{75}Bi_5$	122.9	29.8	224.8	162.7,157.7	24.9
$Ge_{20}S_{70}Bi_{10}$	122.9	29.9	224.9	162.8,157.7	24.9
$Ge_{20}S_{65}Bi_{15}$	122.8	29.8	224.8	162.5,157.5	24.7

Table 5.32 Binding energies in eV of core peaks referenced to the Fermi level for Ge-S-Bi glasses.

Composition	p-type (±0.2)	s-type (±0.3)	Additional peak 'TFP' (±0.3)
$Ge_{20}S_{80}$	3.0	12.6	x
$Ge_{20}S_{75}Bi_5$	2.0	12.7	7.7
$Ge_{20}S_{70}Bi_{10}$	1.8	12.8	7.7
$Ge_{20}S_{65}Bi_{15}$	1.4	12.5	7.3

Table 5.33 Binding energies in eV of the peaks of the valence bands referenced to the Fermi level for Ge-S-Bi glasses.

Composition	FSDP $Å^{-1}(\pm 0.03)$	second peak $Å^{-1}(\pm 0.03)$
$Se_{90}S_{10}$	1.24	1.92
$Se_{85}S_{15}$	1.21	1.92
$Se_{80}S_{20}$	1.13	1.87
$Se_{75}S_{25}$	1.17	1.90
$Se_{60}S_{40}$	1.21	1.76
$Se_{50}S_{50}$	1.21	1.81
$GeSe_2$	1.14	2.00
$(GeSe_2)_{96}Ga_4$	1.14	2.00
$(GeSe_2)_{92}Ga_8$	1.16	2.03
$Ge_{0.9}Sn_{0.1}Se_2$	1.00	2.00
$Ge_{0.8}Sn_{0.2}Se_2$	1.00	2.03
$Ge_{0.7}Sn_{0.3}Se_2$	1.03	2.03
$Ge_{0.6}Sn_{0.4}Se_2$	1.05	2.08
$Ge_{0.5}Sn_{0.5}Se_2$	1.05	2.08
$GeSe_{3.5}$	1.01	1.89
$(GeSe_{3.5})_{95}Bi_5$	0.93	1.87
$(GeSe_{3.5})_{90}Bi_{10}$	0.93	1.87
$Ge_{39.9}S_{55.1}Ag_5$	1.03	2.16
$Ge_{36}S_{54}Ag_{10}$	1.03	2.16
$Ge_{30}S_{55}Ag_{15}$	1.03	2.16
$Ge_{28}S_{52}Ag_{20}$	x	2.14
$Ge_{25}S_{50}Ag_{25}$	x	2.20
$Ge_{20}S_{50}Ag_{30}$	x	2.20
GeS_2	1.04	2.15
$(GeS_2)_{90}Ga_{10}$	1.16	2.10
$Ge_{0.9}Sn_{0.1}S_3$	0.96	2.10
$Ge_{0.8}Sn_{0.2}S_3$	0.96	2.10

Table 5.34 Summary table of the positions of the FSDP and the second peak in the X-ray interference functions.

Table 5.35 Summary of observation

Change on alloying	T_g	Density	Plasmon energy	Core shifts		Valence p-type		Additional peak 'TFP'	FSDP intensity ratio	Coherence length
				Ge(3d)	Se(3d)	B	NB			
$Se_{90}S_{10}$	0	0	0	(x)	0	0	0	(x)	0	0
$Se_{85}S_{15}$	-	-	-	(x)	-	=	-	(x)	=	=
$Se_{80}S_{20}$	-	-	+	(x)	-	+	-	(x)	+	=
$Se_{75}S_{25}$	-	-	+	(x)	-	=	-	(x)	+	=
$Se_{70}S_{30}$	-	-	+	(x)	-	+	=	(x)	x	x
$Se_{60}S_{40}$	-	-	+	(x)	-	+	=	(x)	+	=
$Se_{50}S_{50}$	-	-	+	(x)	-	+	=	(x)	+	=
$GeSe_2$	0	0	0	0	0		0	*	0	0
$(GeSe_2)_{96}Ga_4$	-	+	-	=	-		-	*	+	-
$(GeSe_2)_{92}Ga_8$	-	+	-	+	-		-	*	+	-
$Ge_{0.9}Sn_{0.1}Se_2$	-	-	-	-	-		-	*	-	-
$Ge_{0.8}Sn_{0.2}Se_2$	-	-	-	-	-		-	*	-	-
$Ge_{0.7}Sn_{0.3}Se_2$	-	-	-	-	-		-	*	-	-
$Ge_{0.6}Sn_{0.4}Se_2$	-	-	-	-	-		-	*	-	-
$Ge_{0.5}Sn_{0.5}Se_2$	-	-	-	-	-		-	*	-	-
$Ge_{0.4}Sn_{0.6}Se_2$	-	-	-	-	-		-	(x)	-	-
$GeSe_{3.5}$	x	0	0	0	0		0	*	0	0
$(GeSe_{3.5})_{95}Bi_5$	x	+	-	=	-		+	*	=	-
$GeSe_{3.5})_{90}Bi_{10}$	x	+	-	+	-		-	*	=	-

$GeSe_2$	0	0	0	0	0	0	*	0	0
$(GeSe_2)_{94}Sb_6$	-	+	-	=	-	-	*	x	x
$(GeSe_2)_{88}Sb_{12}$	-	+	-	+	-	-	*	x	x
$(GeSe_{3.5})_{90}Sb_{10}$	x	+	-	+	-	-	*	x	x
$(GeSe_3)_{80}Sb_{20}$	x	+	-	=	-	-	*	x	x
GeS_2	0	0	0	0	(x)	0	*	0	0
$(GeS_2)Ga_{10}$	-	+	-	=	(x)	+	*	-	-
$Ge_{20}S_{80}$	-	-	-	-	(x)	+	(x)	x	x
$Ge_{39.9}S_{55.1}Ag_5$	-	+	(x)	-	(x)	(x)	(x)	-	-
$Ge_{36}S_{54}Ag_{10}$	-	+	(x)	-	(x)	(x)	(x)	-	-
$Ge_{30}S_{55}Ag_{15}$	-	+	(x)	-	(x)	(x)	(x)	-	-
$Ge_{28}S_{52}Ag_{20}$	-	+	(x)	-	(x)	(x)	(x)	(x)	(x)
$Ge_{25}S_{50}Ag_{25}$	-	+	(x)	-	(x)	(x)	(x)	(x)	(x)
$Ge_{20}S_{50}Ag_{30}$	-	+	(x)	-	(x)	(x)	(x)	(x)	(x)
$Ge_{0.9}Sn_{0.1}S_3$	-	-	-	-	(x)	-	*	+	-
$Ge_{0.8}Sn_{0.2}S_3$	-	-	+	-	(x)	-	*	+	-
$Ge_{0.7}Sn_{0.3}S_3$	-	+	-	-	(x)	-	*	x	x
$Ge_{0.6}Sn_{0.4}S_3$	-	+	-	-	(x)	-	*	x	x
$Ge_{20}S_{80}$	0	0	0	0	(x)	0	(x)	x	x
$Ge_{20}S_{75}Bi_5$	x	+	+	-	(x)	-	*	x	x
$Ge_{20}S_{70}Bi_{10}$	x	+	=	-	(x)	-	*	x	x
$Ge_{20}S_{65}Bi_{15}$	x	+	-	-	(x)	-	*	x	x

Key for the summary table : 0 is the reference value, + increase in measured quantity, - decrease in measured quantity,
= equal to the reference value, x quantity not measured, (x) property not present, * additional peak present on the valence band spectra, 'TFP' three-fold peak, B Bonding p-type peak, NB Non-bonding p-type peak, and FSDP intensity ratio is the ratio of the FSDP to the second peak in the interference function.

	Correlated	Value of correlation coefficient (R)	Percentage probability that R is due to chance	Number of data points (N)
Measured Property (correlations with intensity ratio)	1-plasmon energy-loss from the $L_3M_{4,5}M_{4,5}$ Auger lines of Ge	+0.92	< 0.05	14
	2-plasmon energy-loss from the $L_3M_{4,5}M_{4,5}$ Auger lines of Se	+0.67	0.3	16

Table 5.37 Correlations of the plasmon energy-losses from the $L_3M_{4,5}M_{4,5}$ Auger lines of Ge and Se, with the intensity ratio of the FSDP to the second peak.

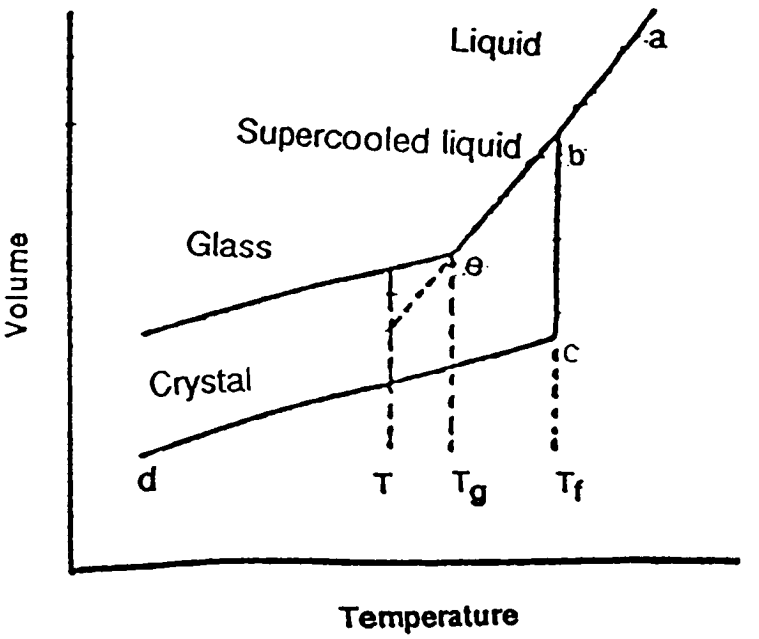

Fig. 1.1 Volume/temperature plot showing the relation between the glassy, liquid and solid states.

PAGE
NUMBERS
CUT OFF
IN THE
ORIGINAL

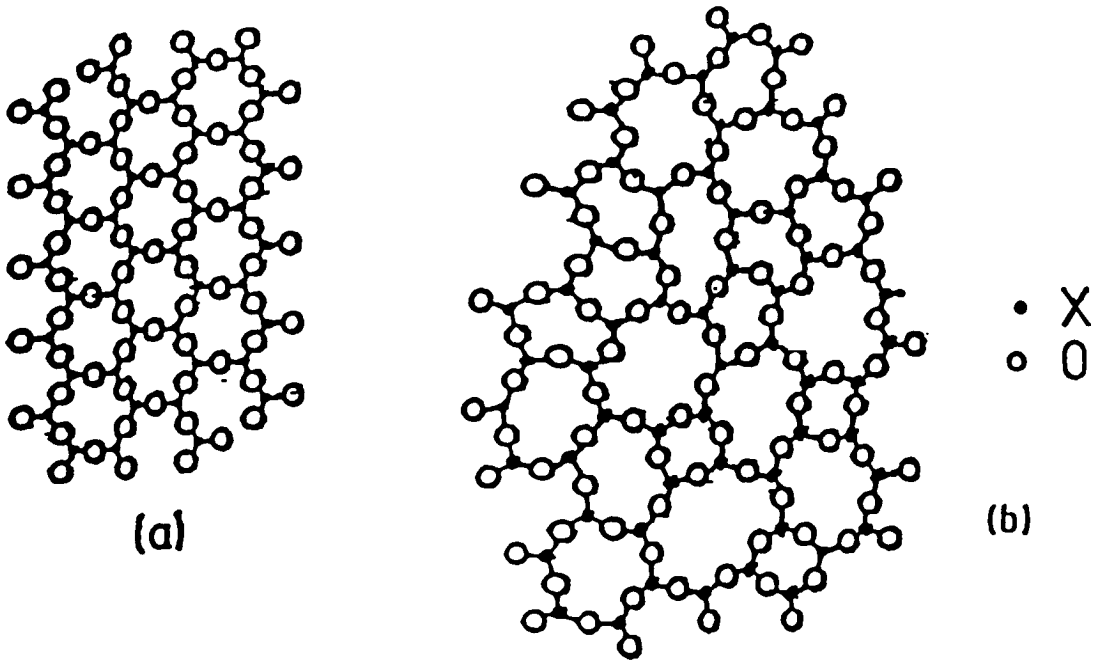

Fig. 1.2 Two dimensional representation of the structure of the hypothetical compound X_2O_3

(a) crystalline form (b) glassy form.

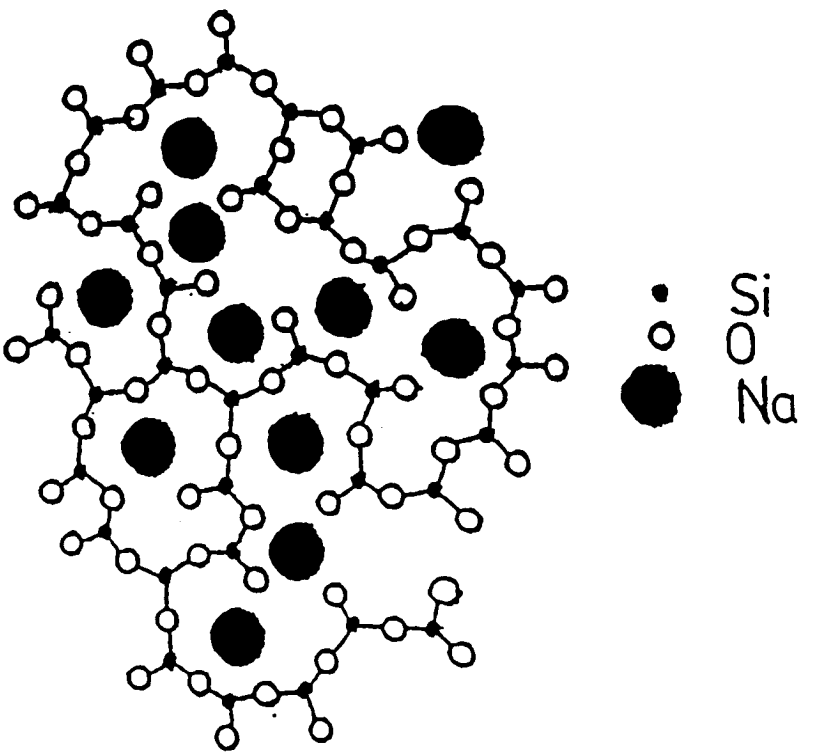

Fig. 1.3 Two dimensional representation of the structure of sodium silicate (Na_2O/SiO_2) glass.

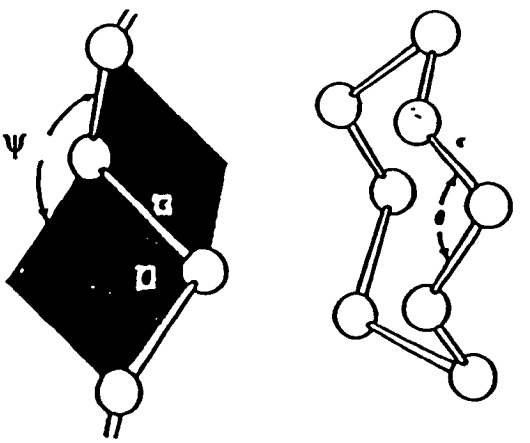

Fig. 1.4 Local coordination of atoms in the chain and ring forms of Se.

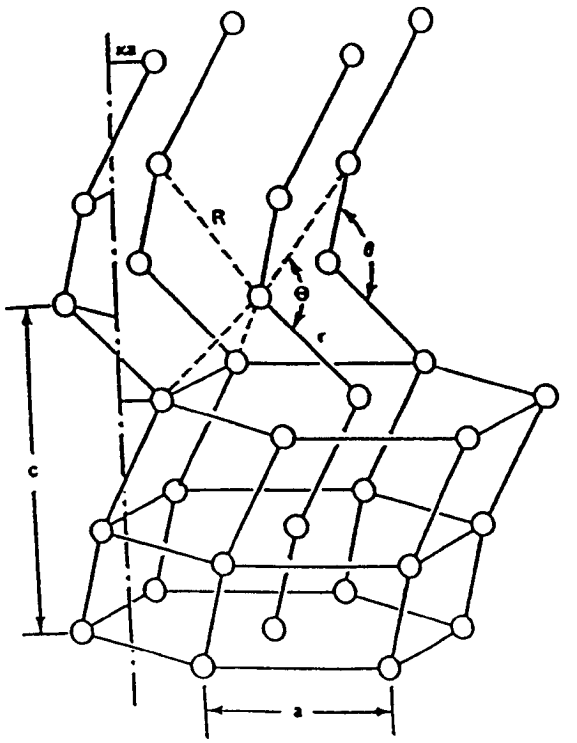

Fig. 1.5 Schematic illustration of the trigonal lattice structure of Se. Solid lines denote the chains which spiral about a vertical axis as shown for the chain at the left.

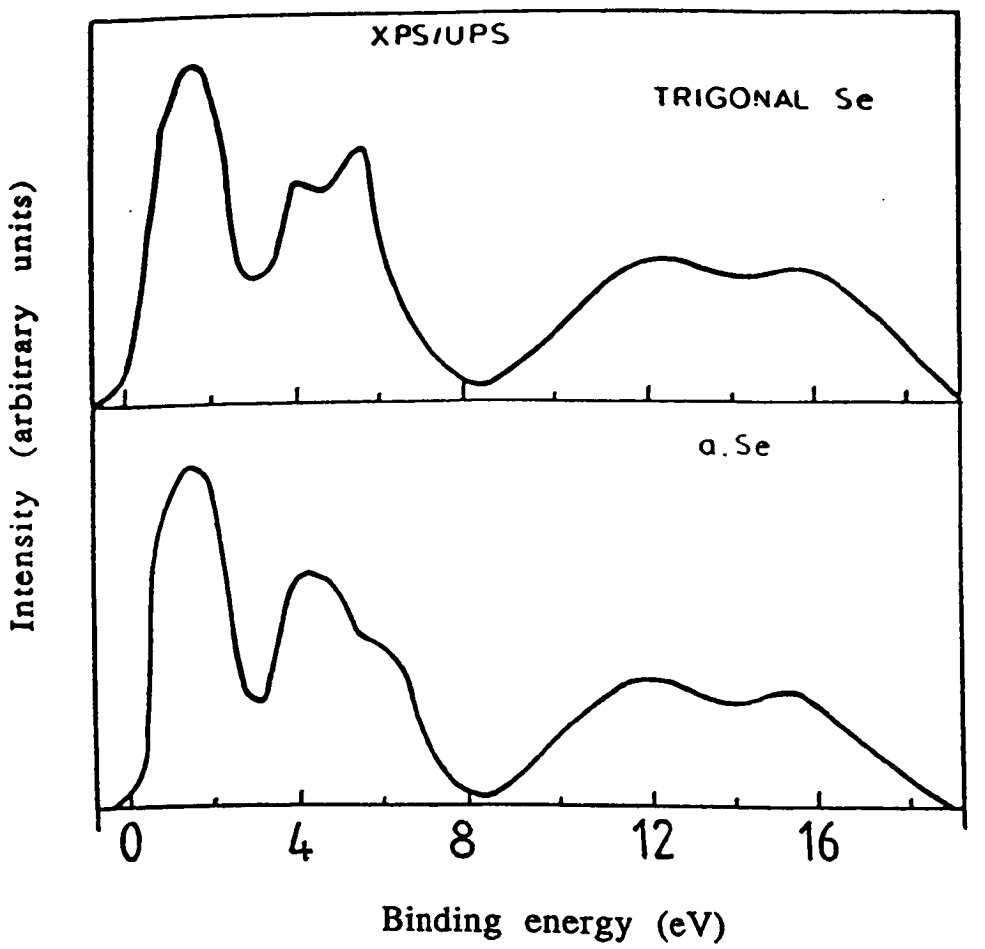

Fig. 1.6 XPS of trigonal and amorphous Se.

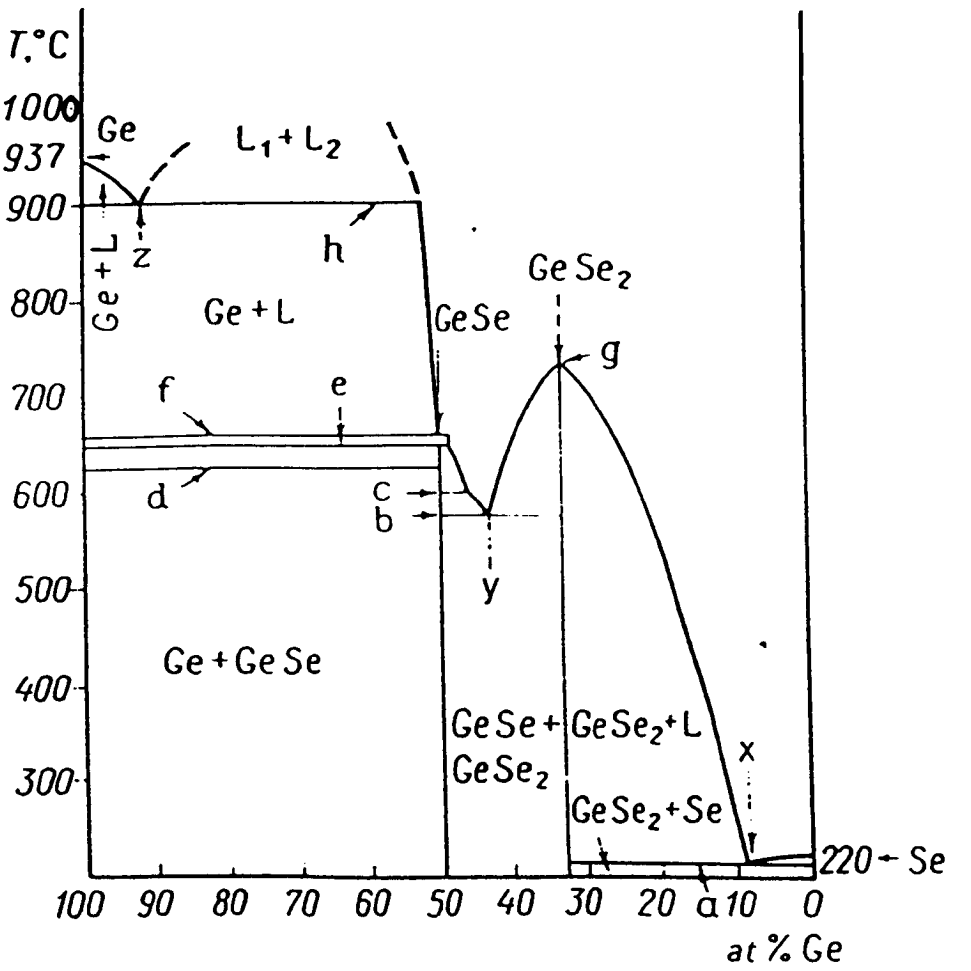

Fig. 1.7 Phase diagram of the Ge-Se system.

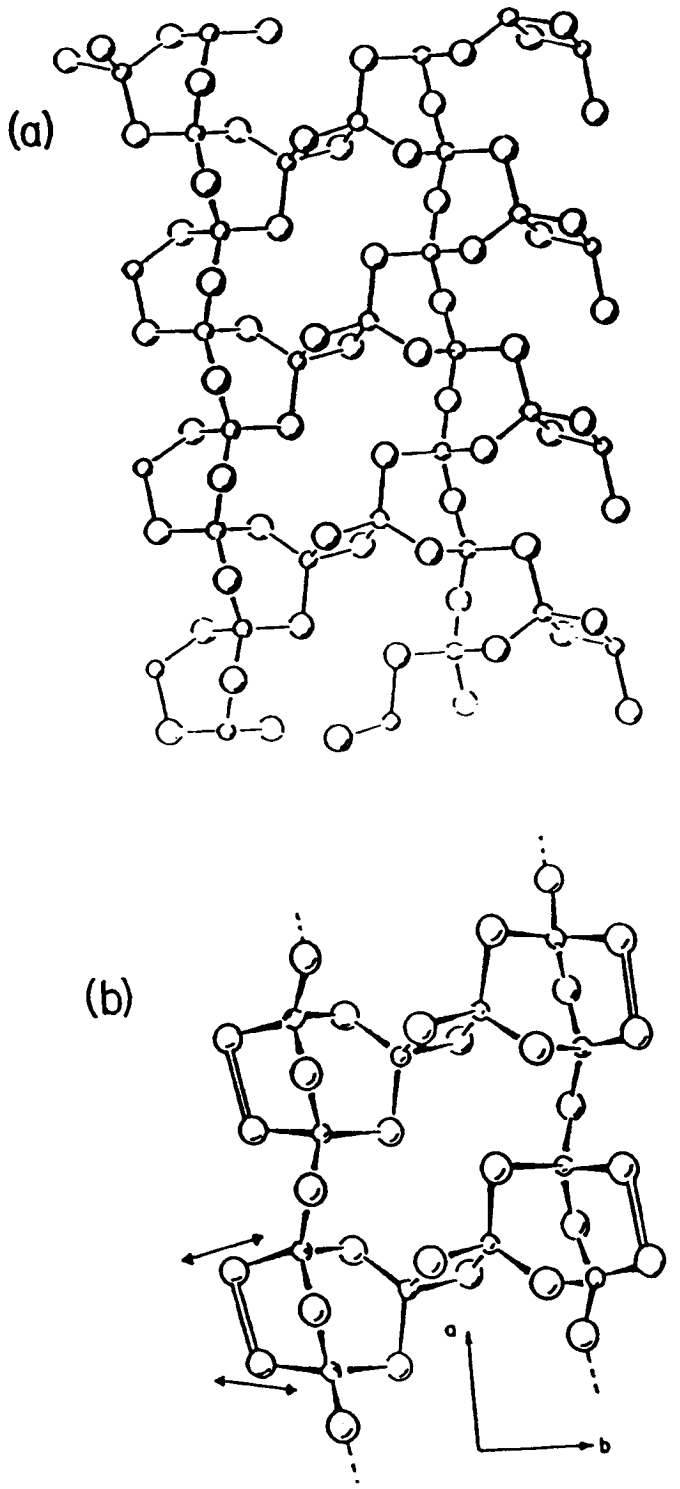

Fig. 1.8 Molecular models of (a) one layer of the high-temperature form of $GeSe_2$ and (b) the smallest unit of a partially polymerised cluster (PPC) in the glass. Germanium atoms are represented by the small balls.

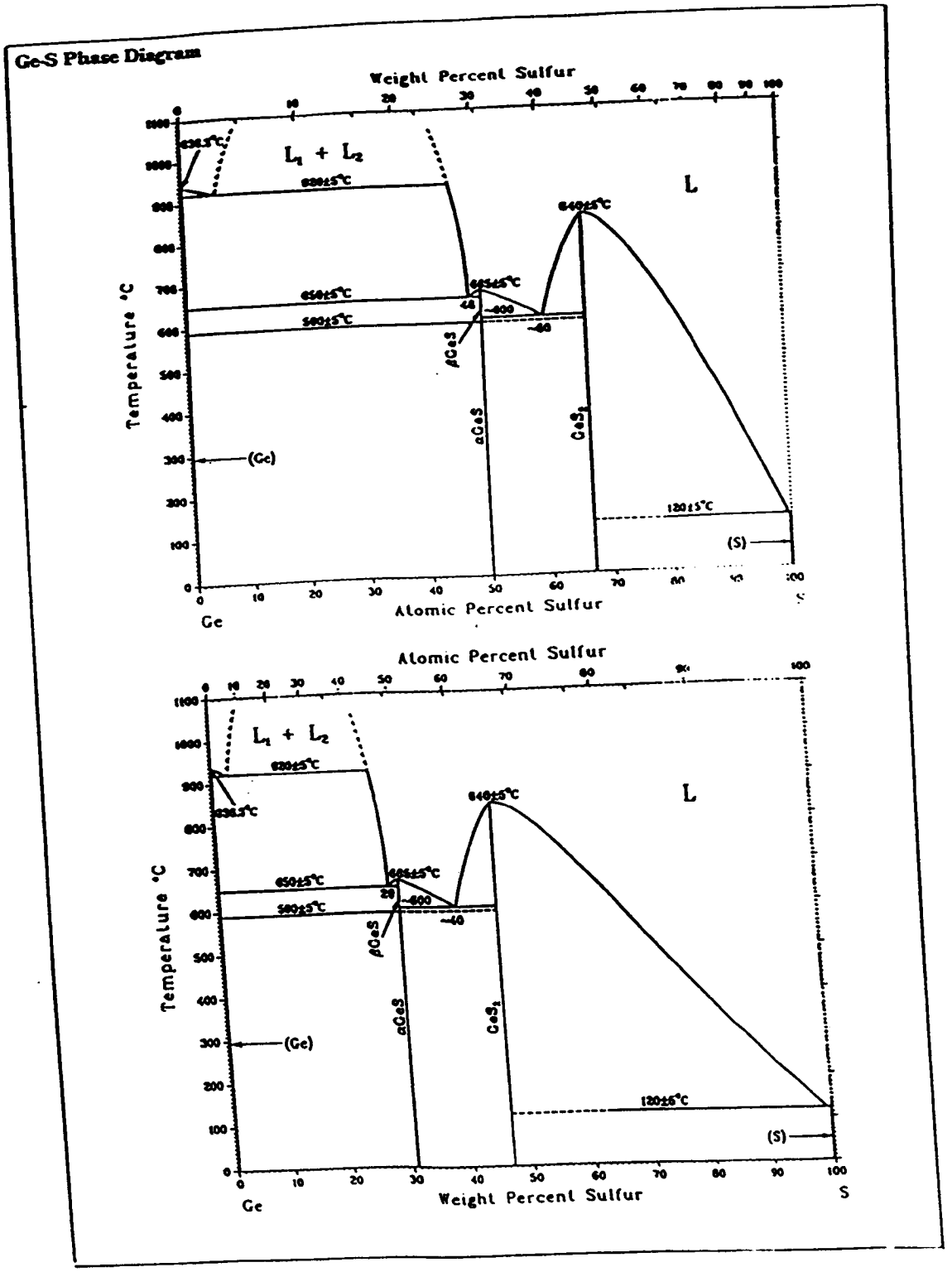

Fig. 1.9 Phase diagram of the Ge-S system.

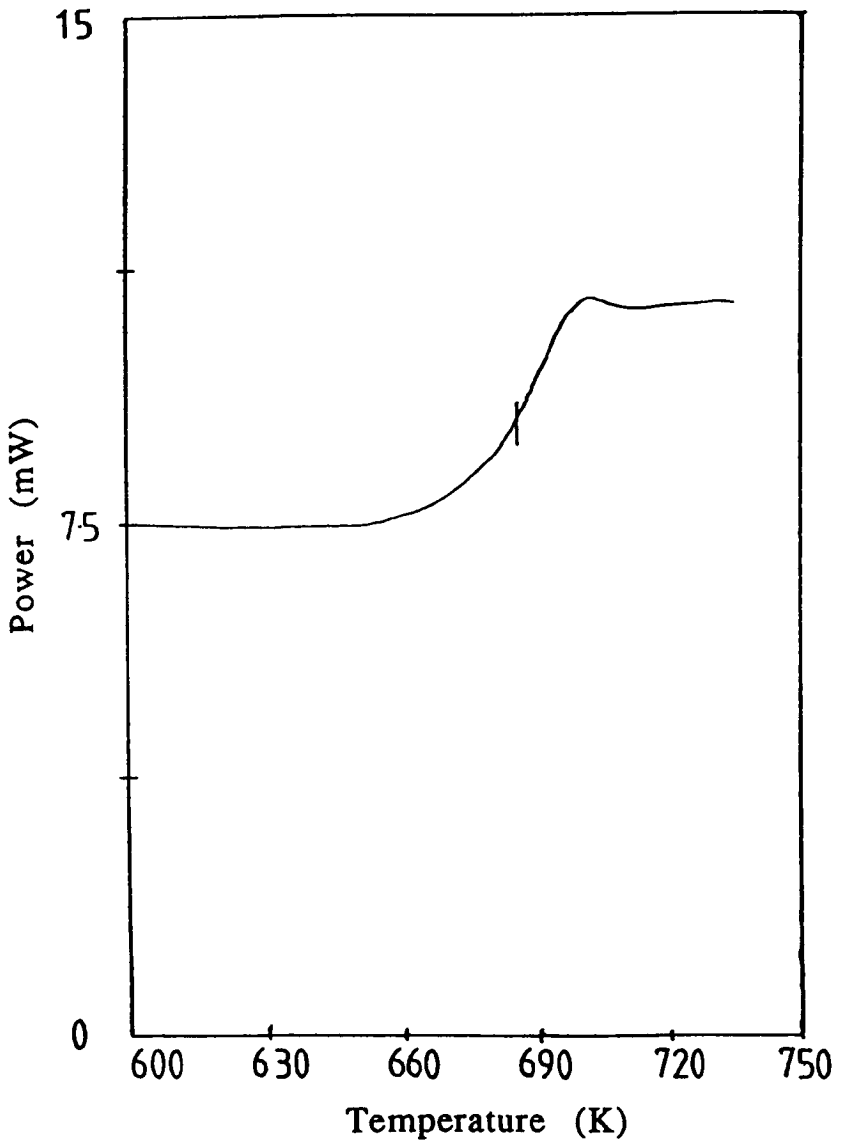

Fig. 1.10 Thermogram for $GeSe_2$ glass.

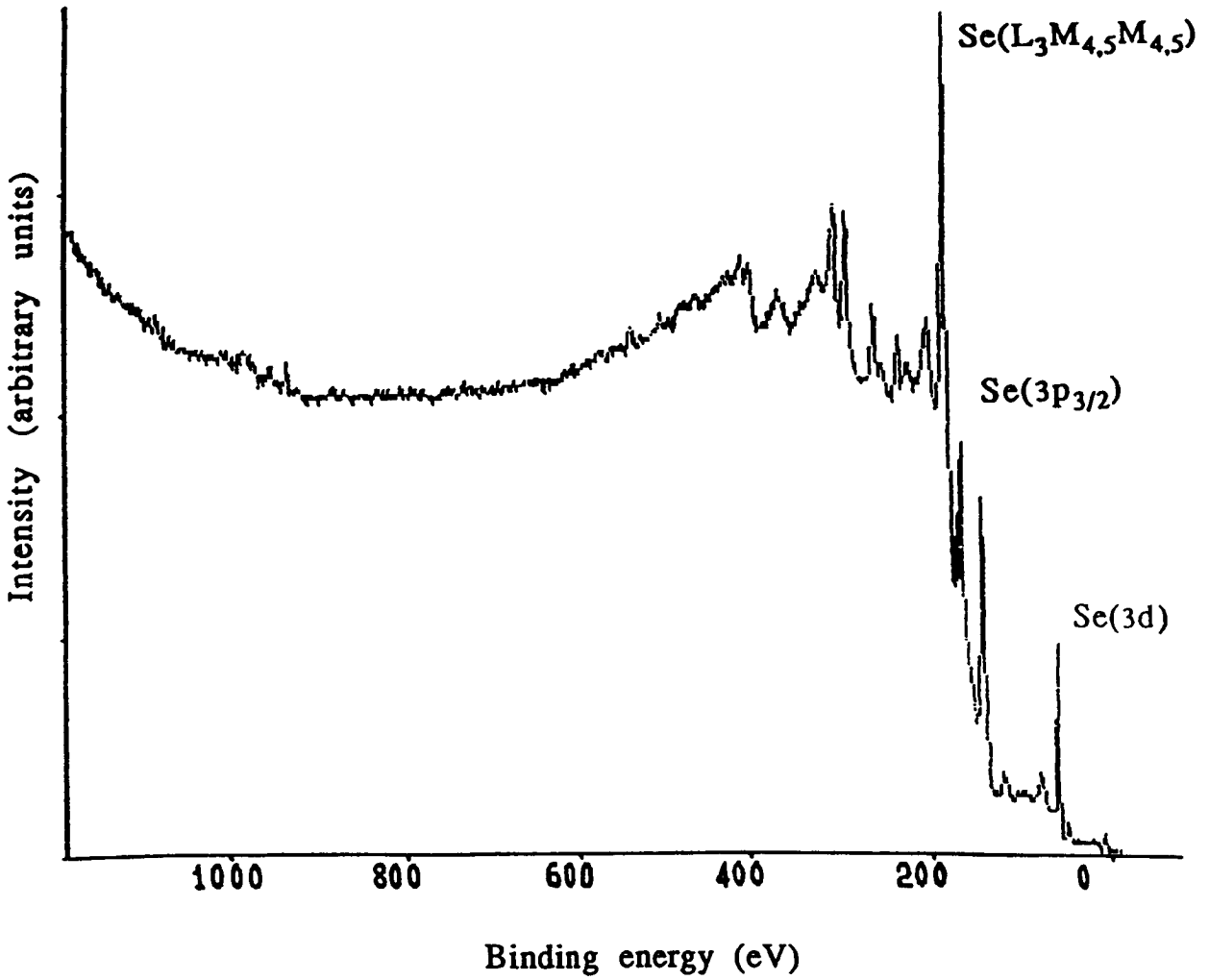

Fig. 2.1 Survey scan for amorphous Se.

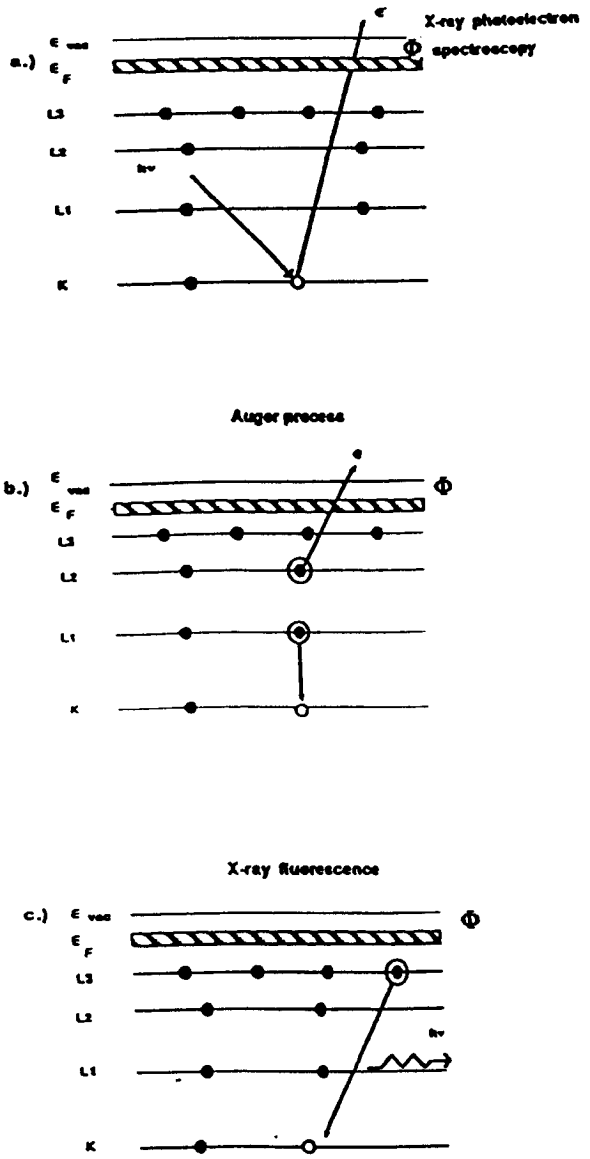

Fig. 2.2 Energy level diagram showing (a) the creation of a core hole, (b) filling of the core hole by Auger emission and (c) filling of the core hole and the emission of a photon as in X-ray fluorescence.

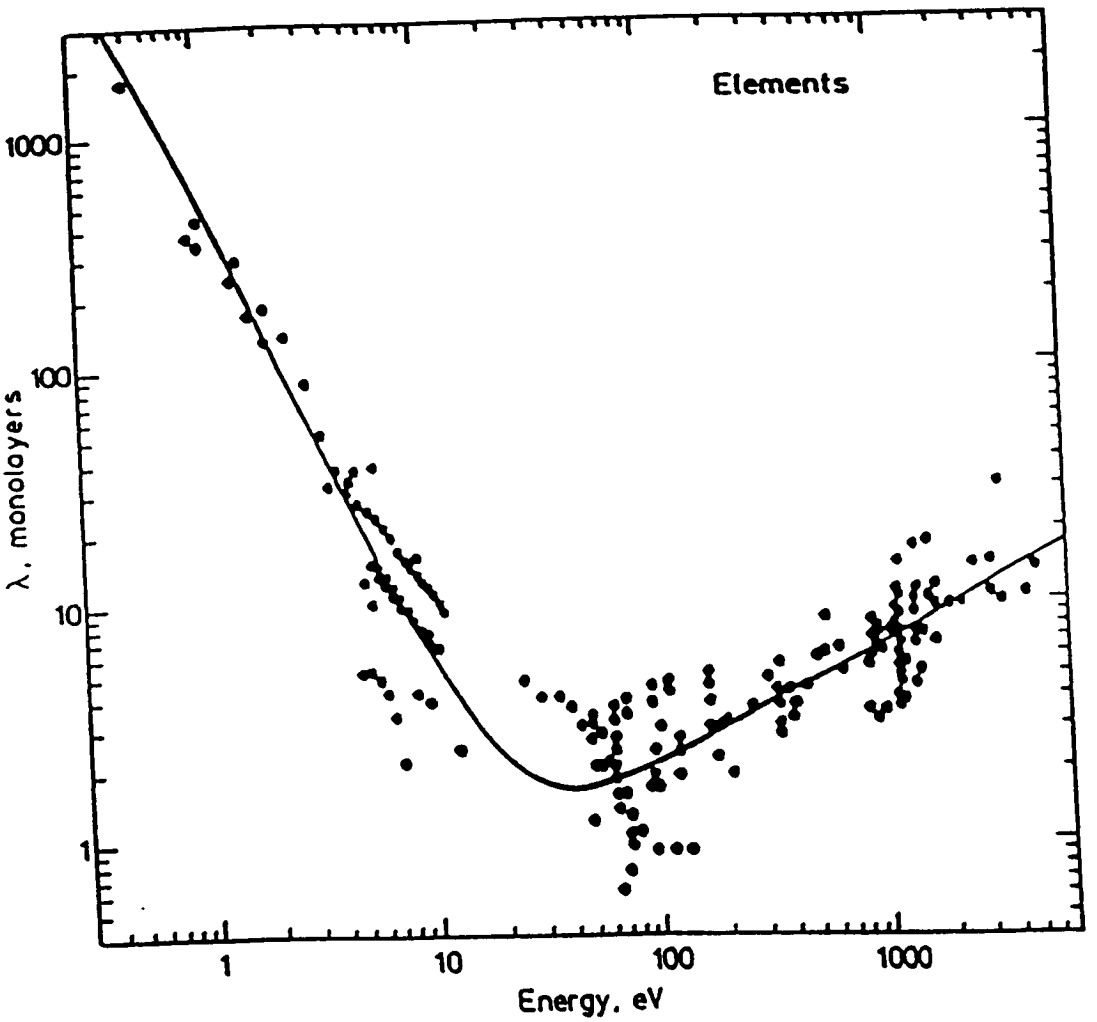

Fig. 2.3 The dependence of λ(imfp) on electron energy.

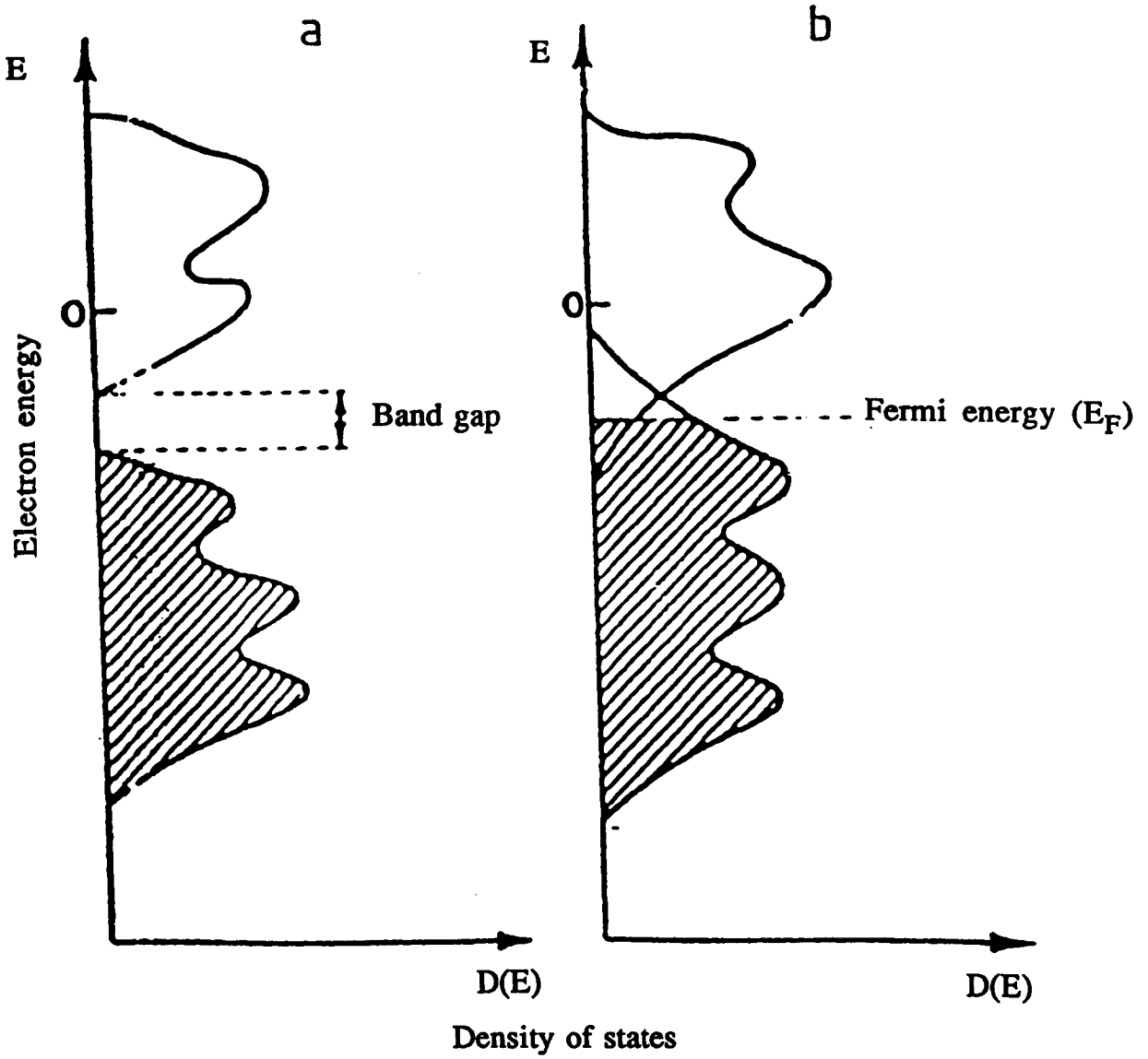

Fig. 2.4 Schematic density of states for (a) an insulator and (b) a metal. The shading indicates the extent to which energy levels are occupied.

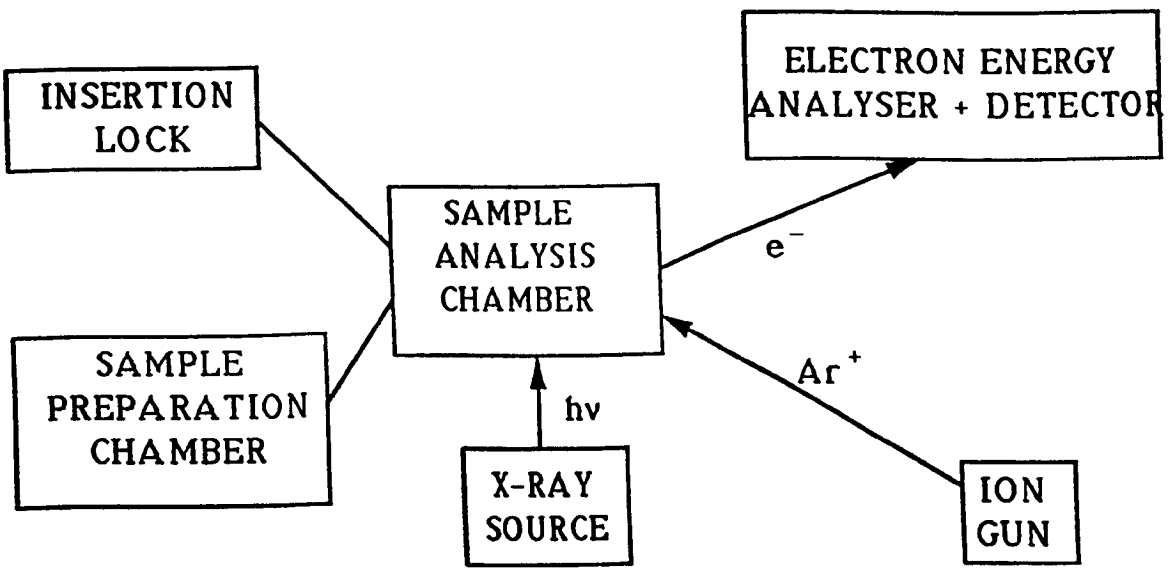

Fig. 2.5 Schematic representation of the spectrometer.

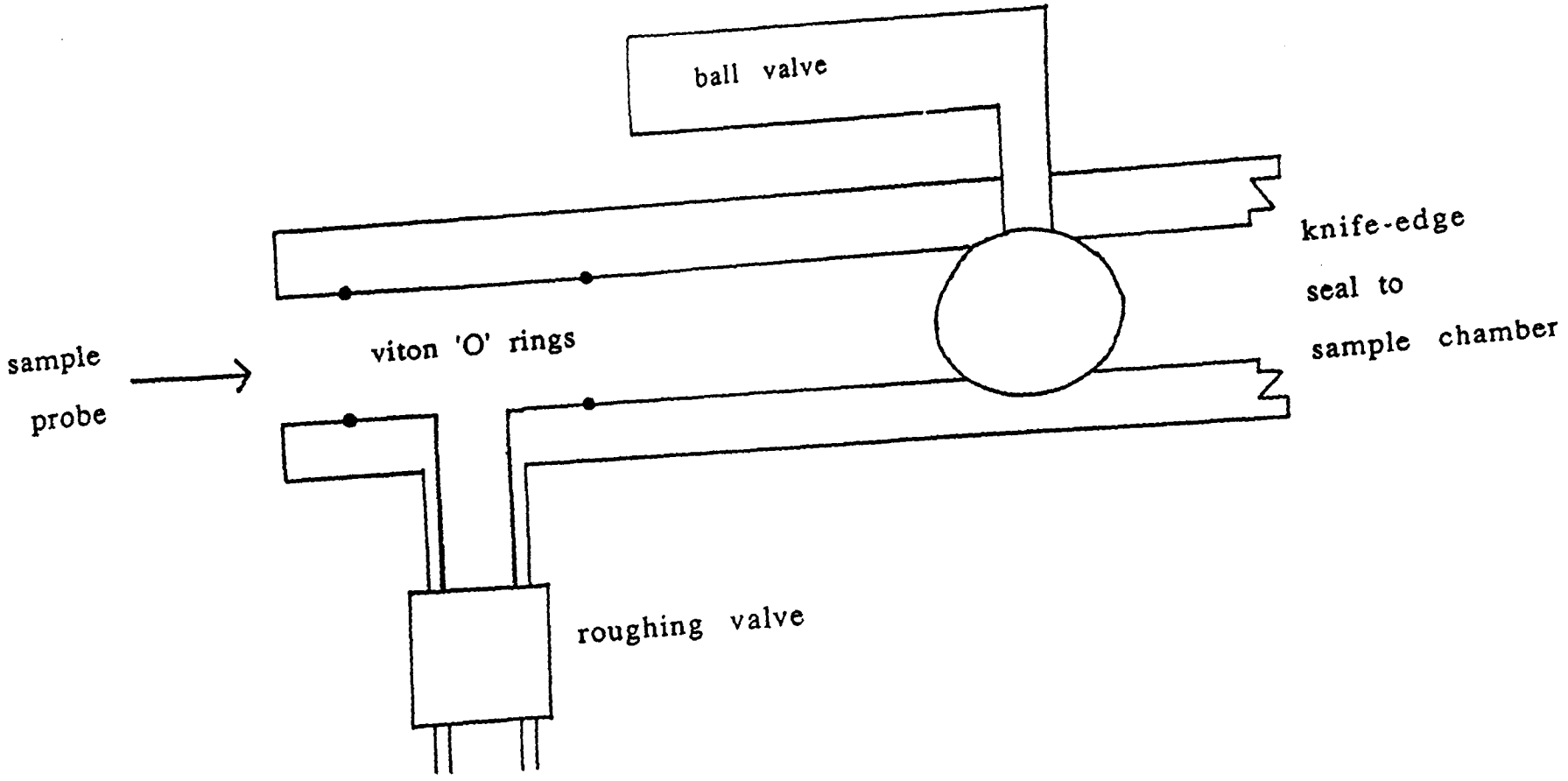

Fig. 2.6 Sample insertion lock.

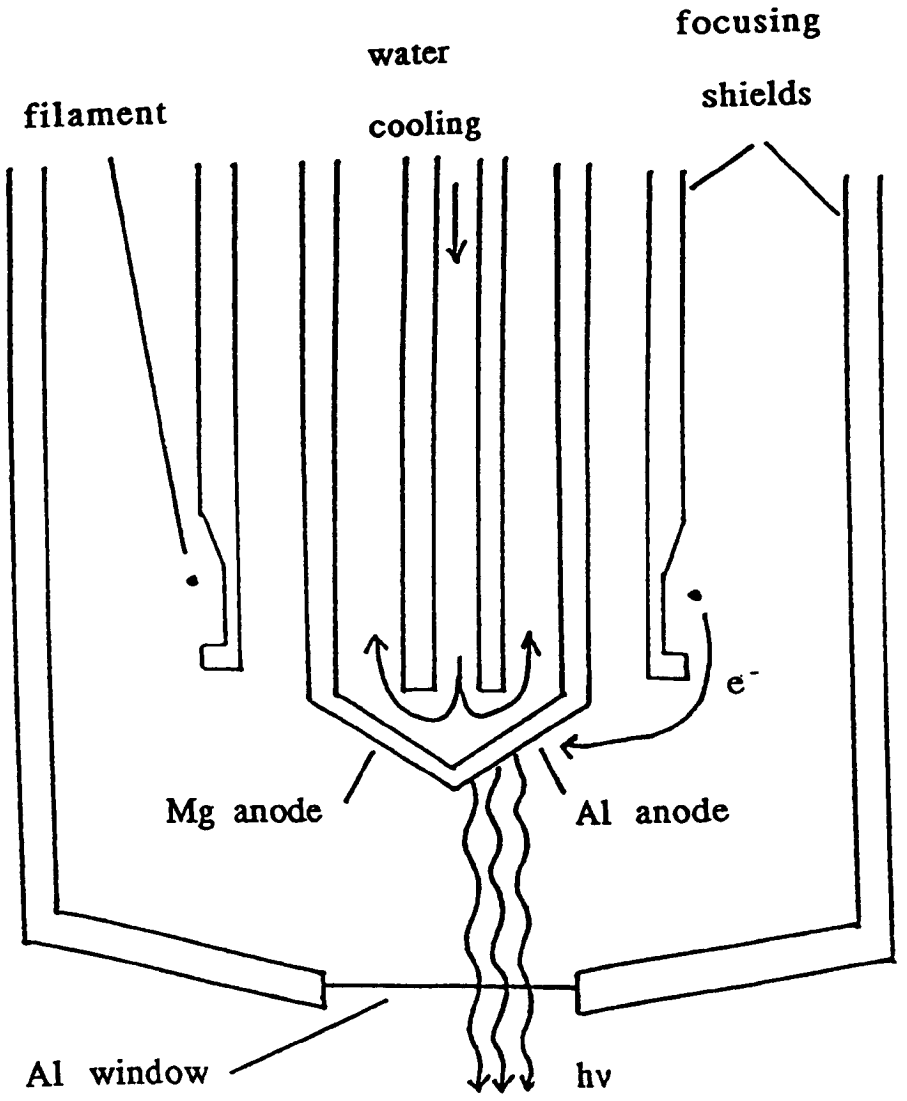

Fig. 2.7 Dual anode X-ray source.

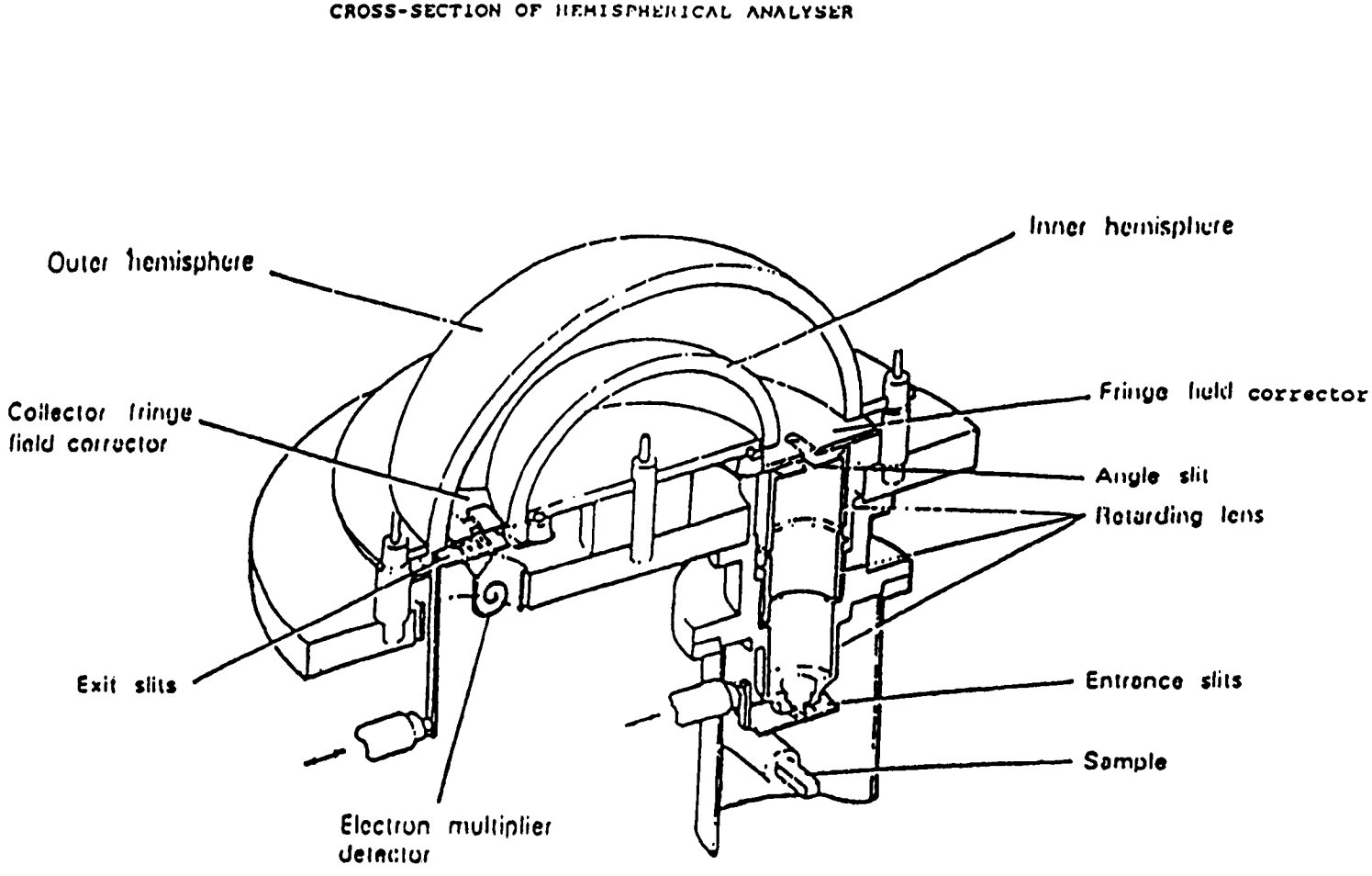

Fig. 2.8 Hemispherical electrostatic analyser.

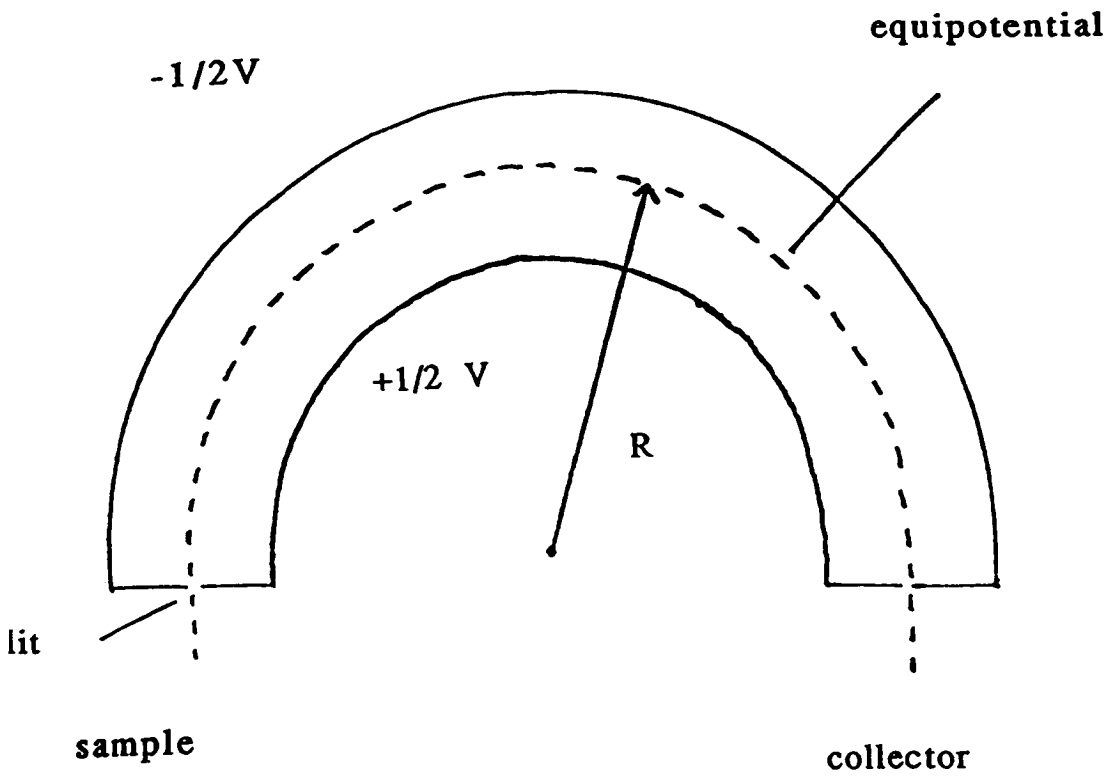

Fig. 2.9 An equipotential line within the hemispherical analyser.

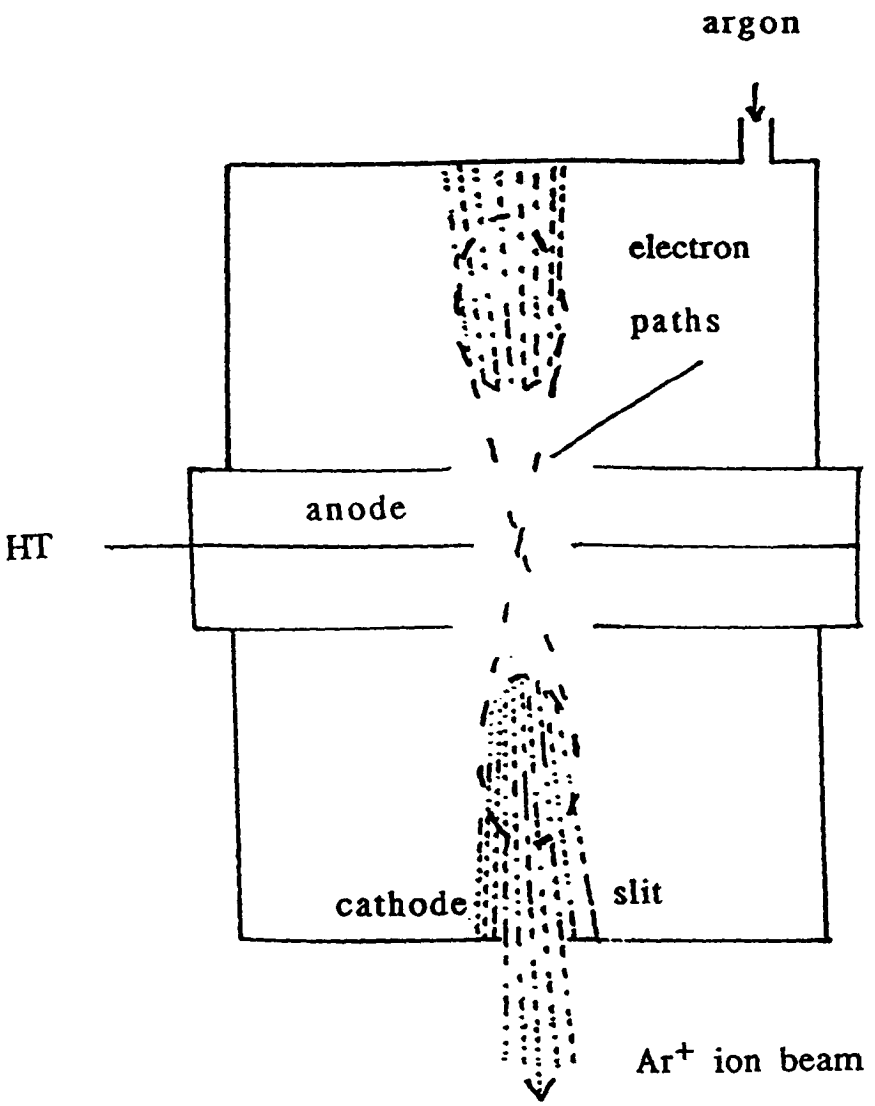

Fig. 2.10 Saddle field source ion gun.

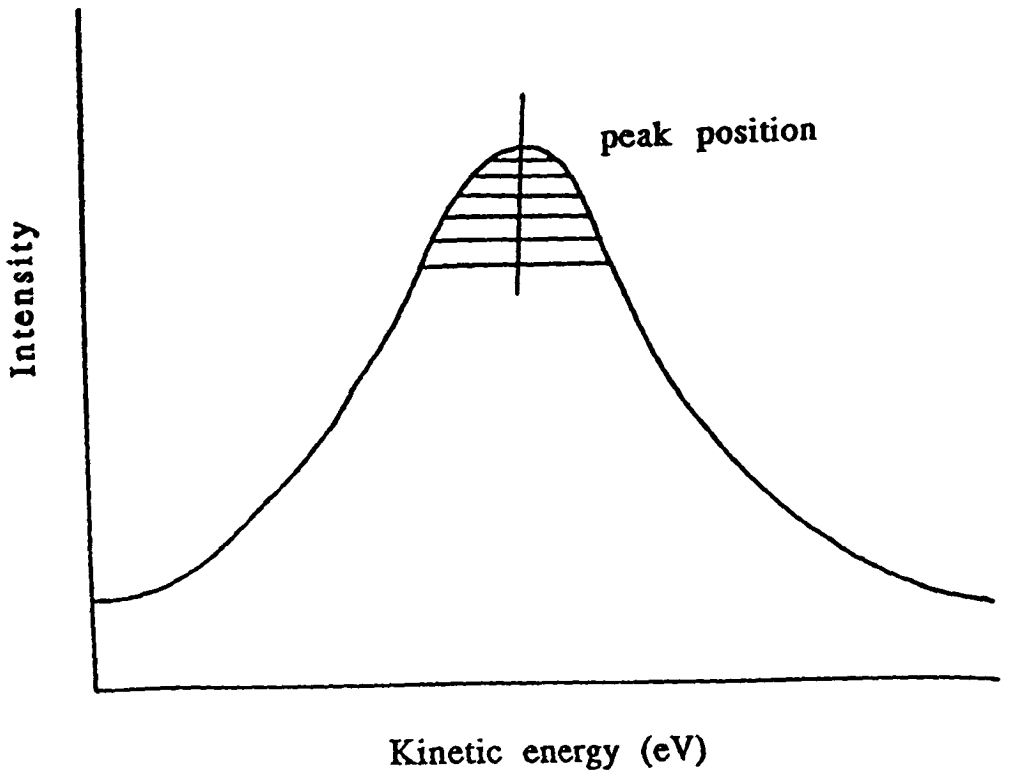

Fig. 2.11 Graphical method used to determine peak positions.

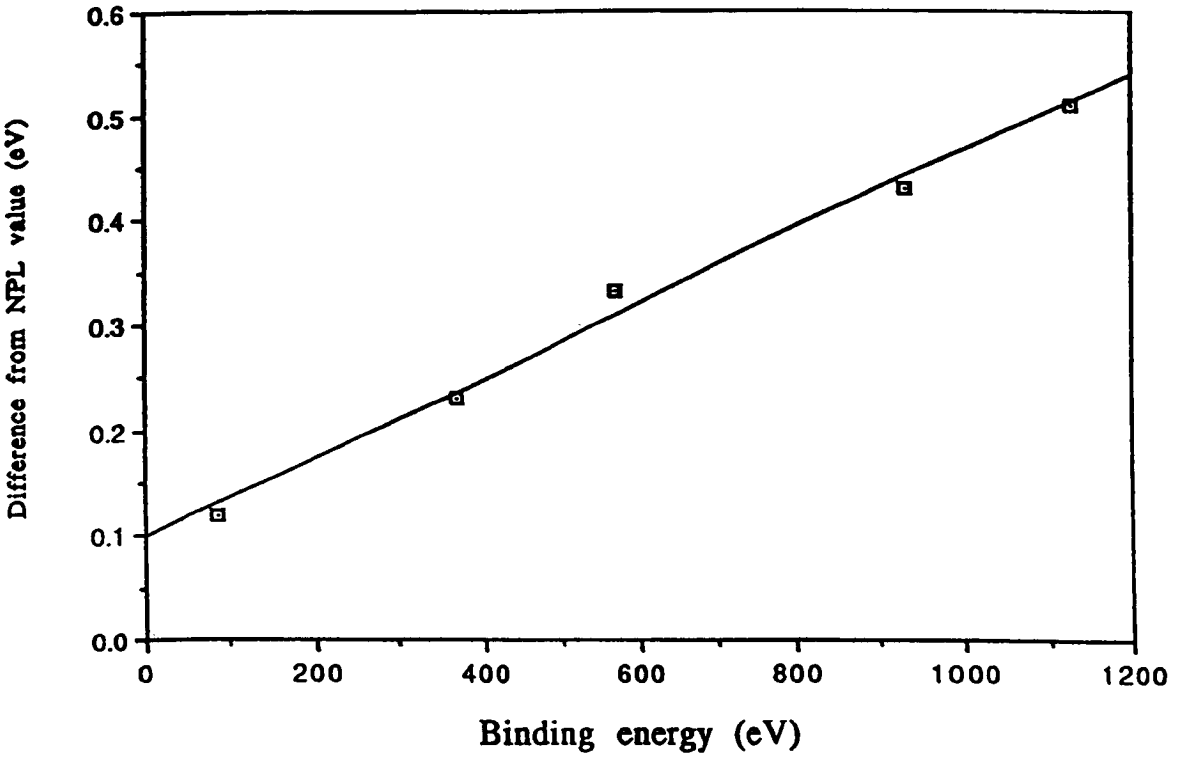

Fig 2.12 Difference of measured binding energies from NPL values versus binding energy for the reference peaks.

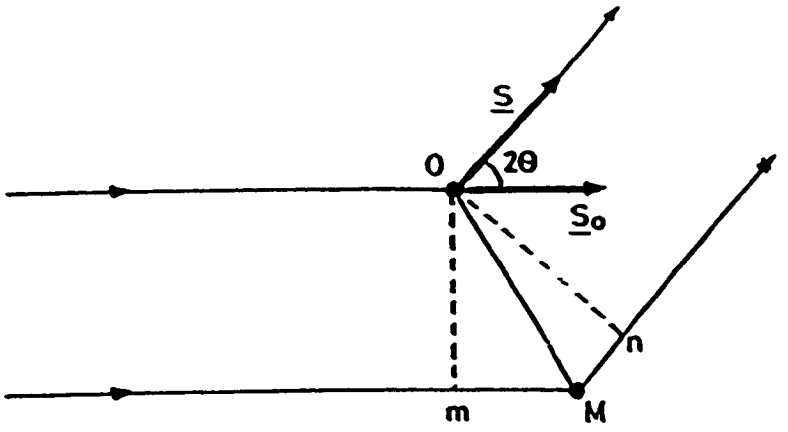

Fig 3.1 Interference between two waves from two scattering centres.

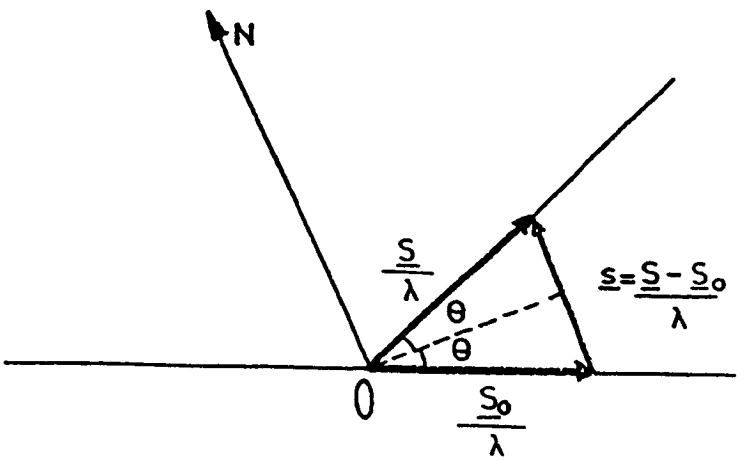

Fig. 3.2 Definition of the vector $\underline{s} = \underline{S} - \underline{S}_0/\lambda$.

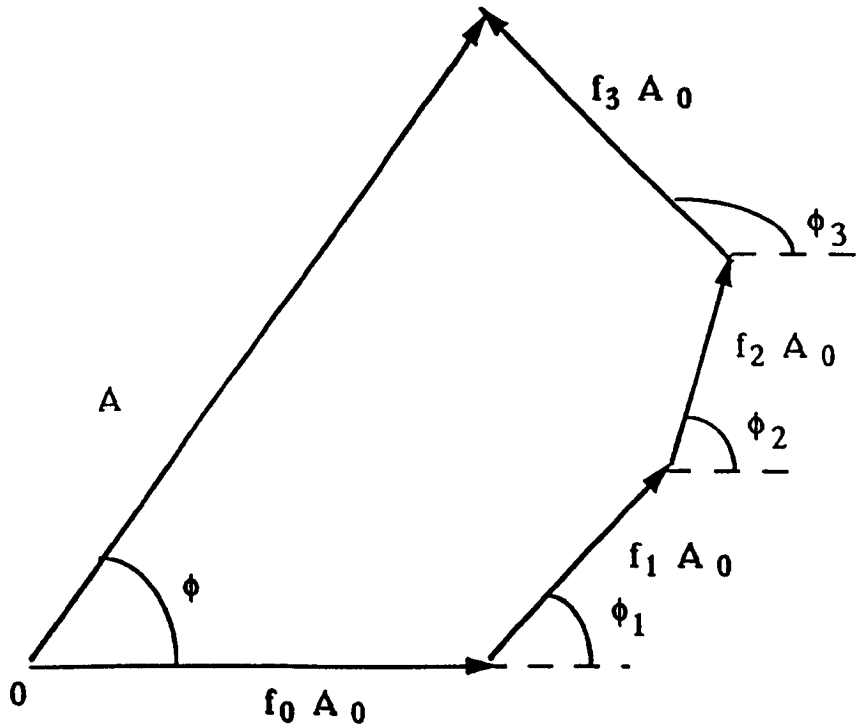

Fig. 3.3 Fresnel construction.

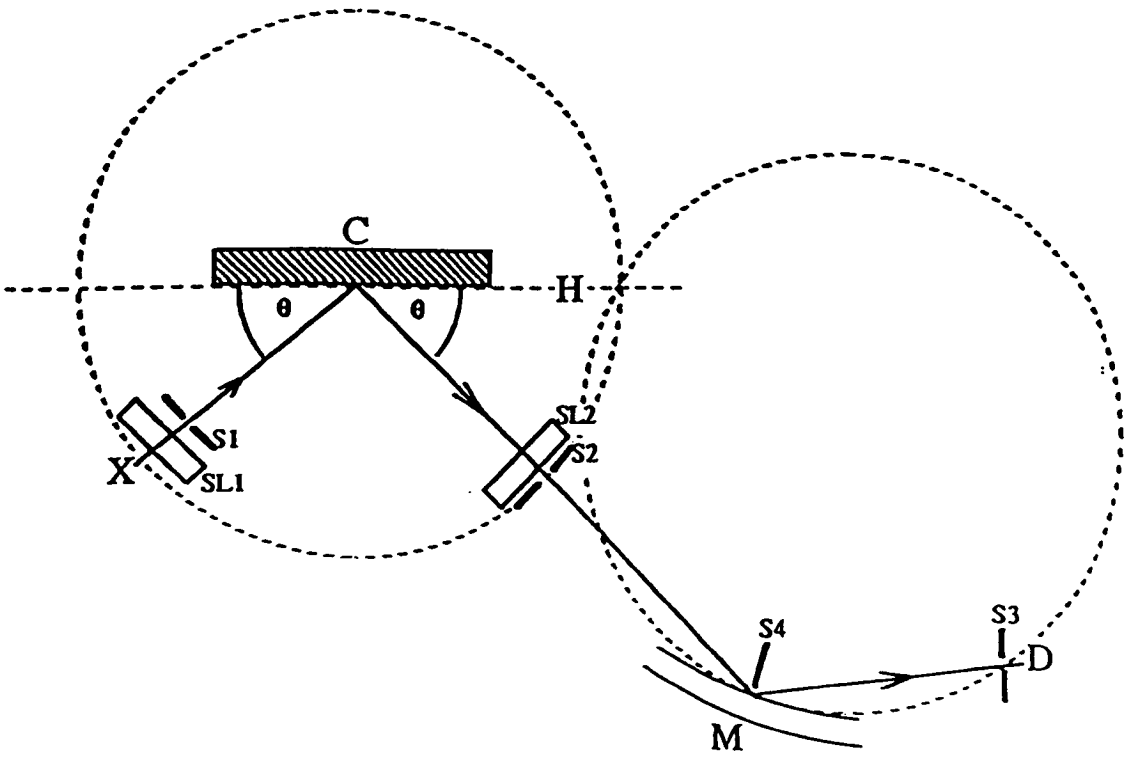

Fig. 3.4 Diffractometer geometry

X- X-ray source

SL- Soller slits

S- Collimating slits

C- sample

H- Horizontal plane

M- Monochromator

D- Detector.

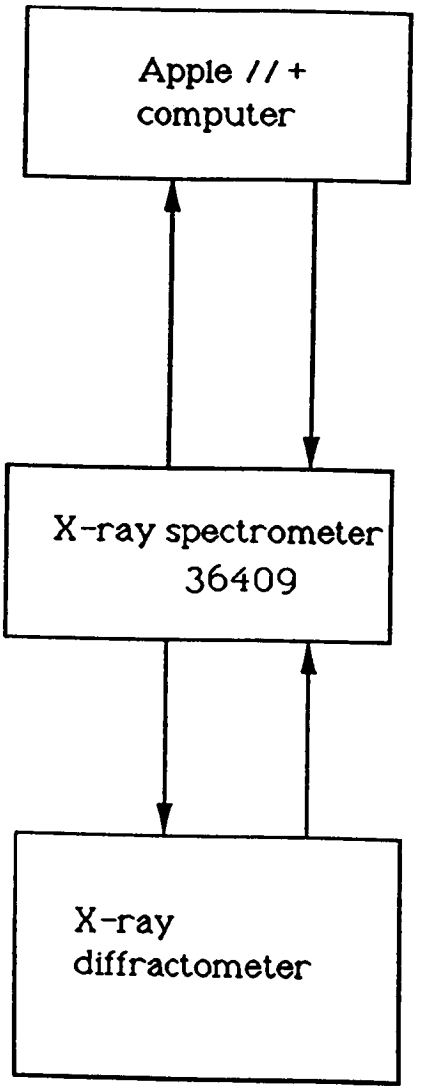

Fig. 3.5 Block diagram of the controlling unit for the diffractometer.

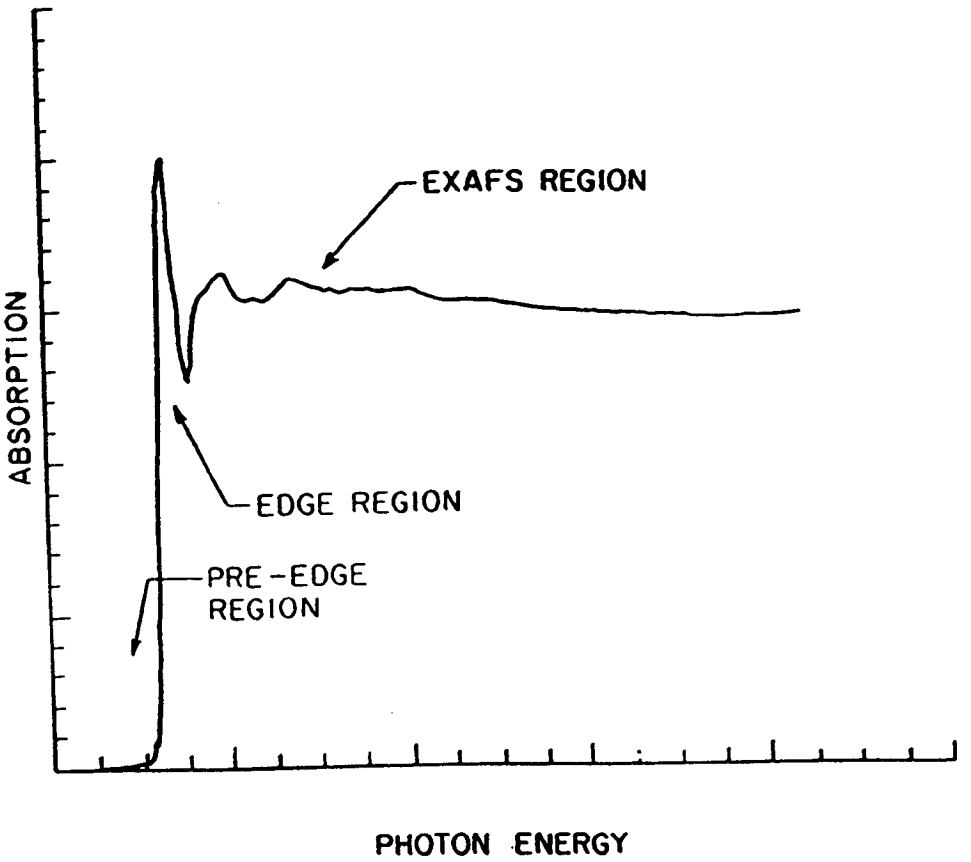

Fig. 4.1 Schematic of X-ray absorption spectrum showing the threshold region (including pre-edge and edge regions) and the EXAFS region.

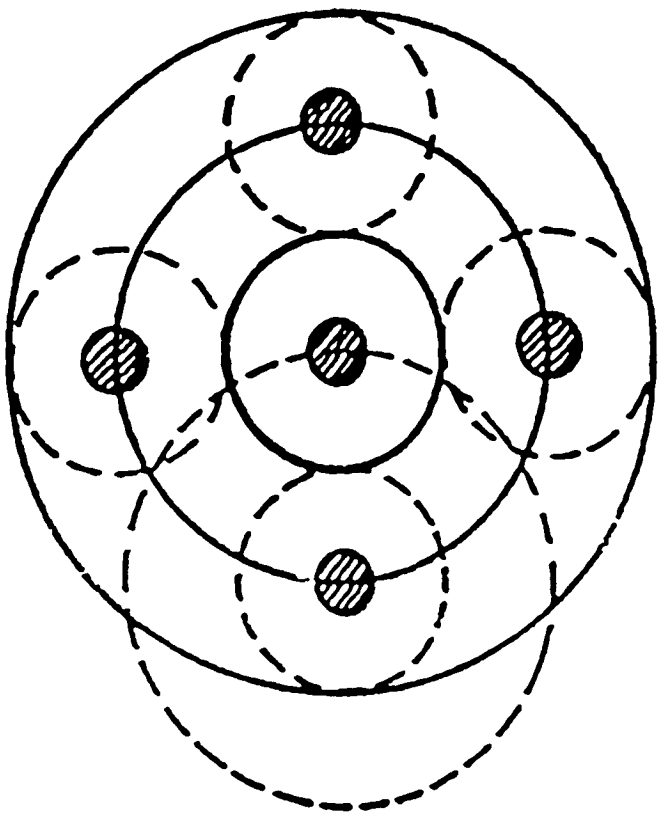

Fig. 4.2 Schematic representation of the excited electron wavefunction. The excited electronic state is centred about the centre atom. The solid circles represent the crests of the outgoing wave of the electronic state. The outgoing wave is scattered by surrounding atoms producing ingoing waves depicted by the dotted lines.

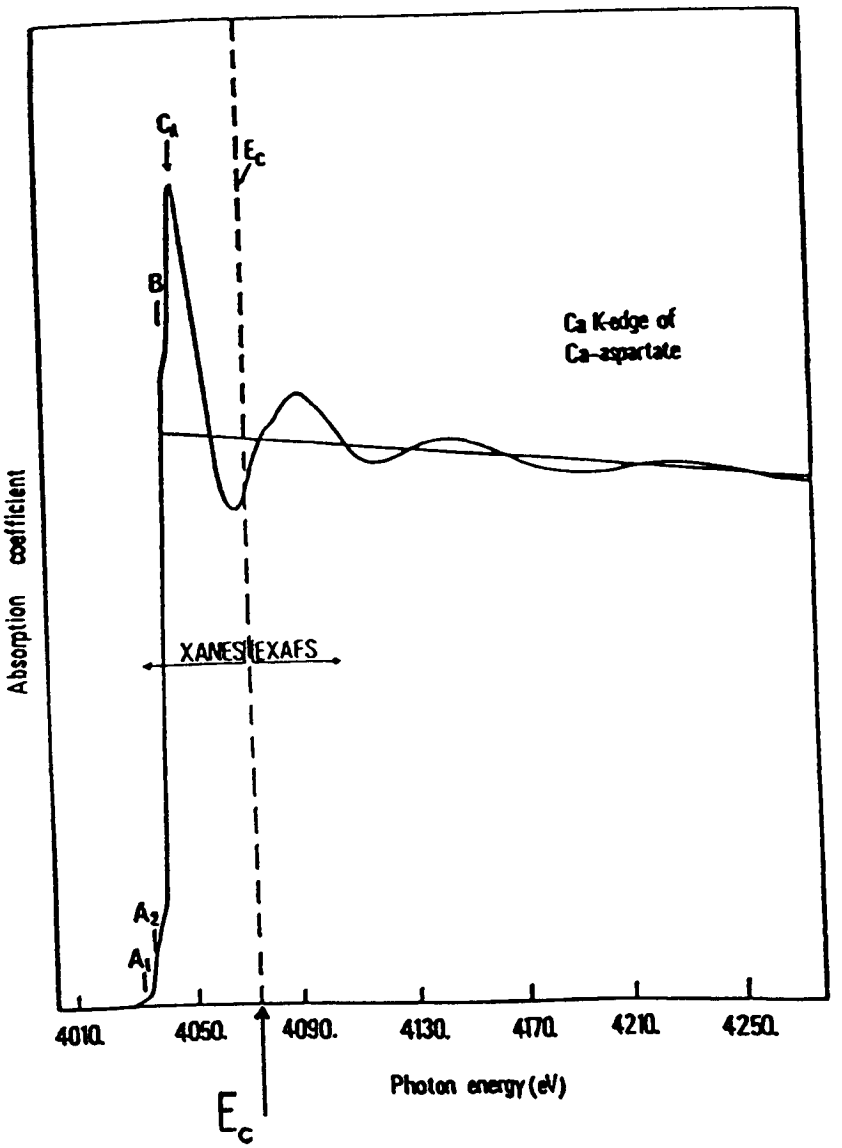

Fig. 4.3 X-ray absorption spectrum of a calcium complex showing the weak simple EXAFS and the strong near edge resonances (XANES).

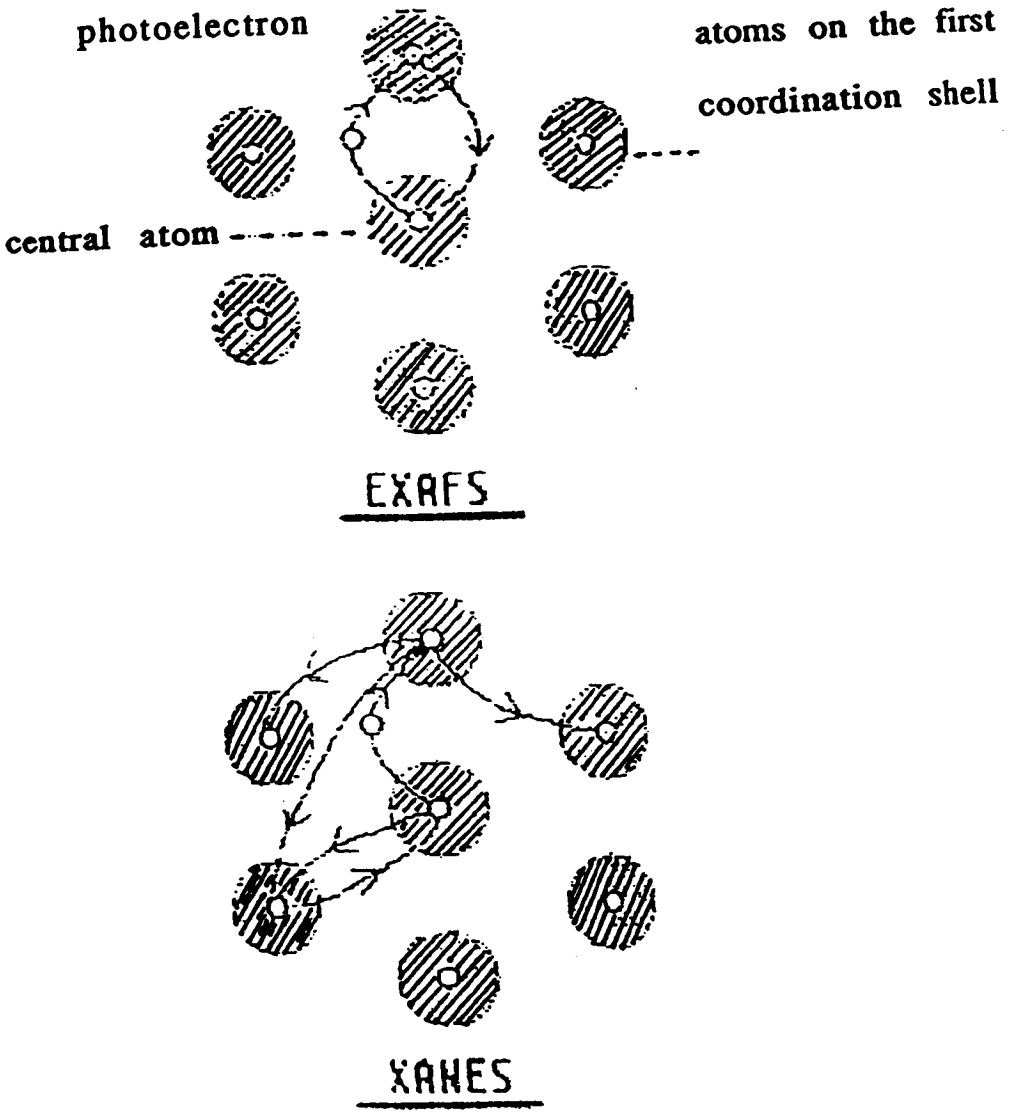

Fig. 4.4 Pictorial view of the scattering processes of the excited internal photoelectron determining the EXAFS (single scattering regime) and the XANES (multiple scattering regime) oscillations.

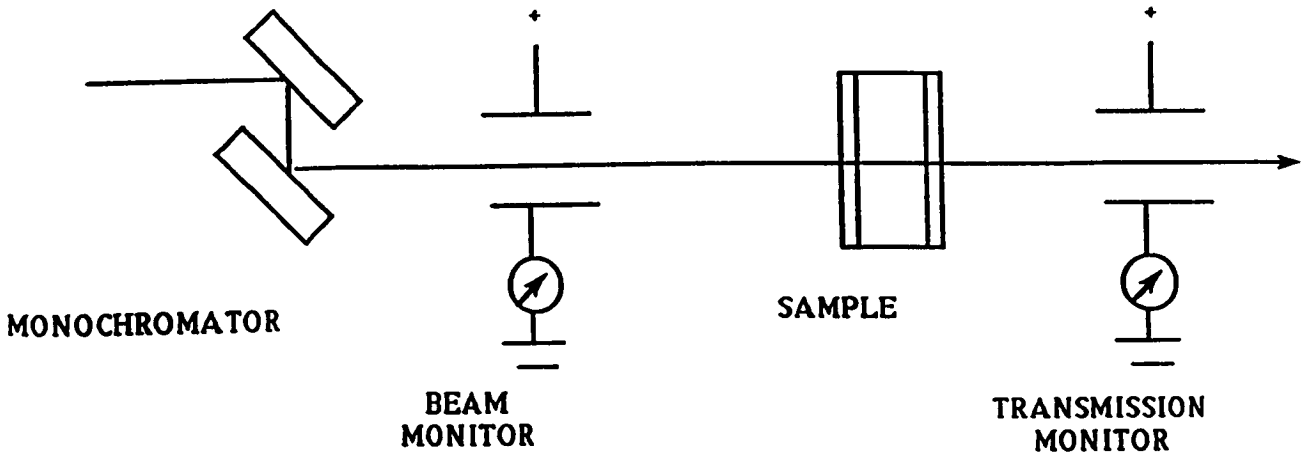

Fig. 4.5 Schematic for X-ray absorption measurement by transmission.

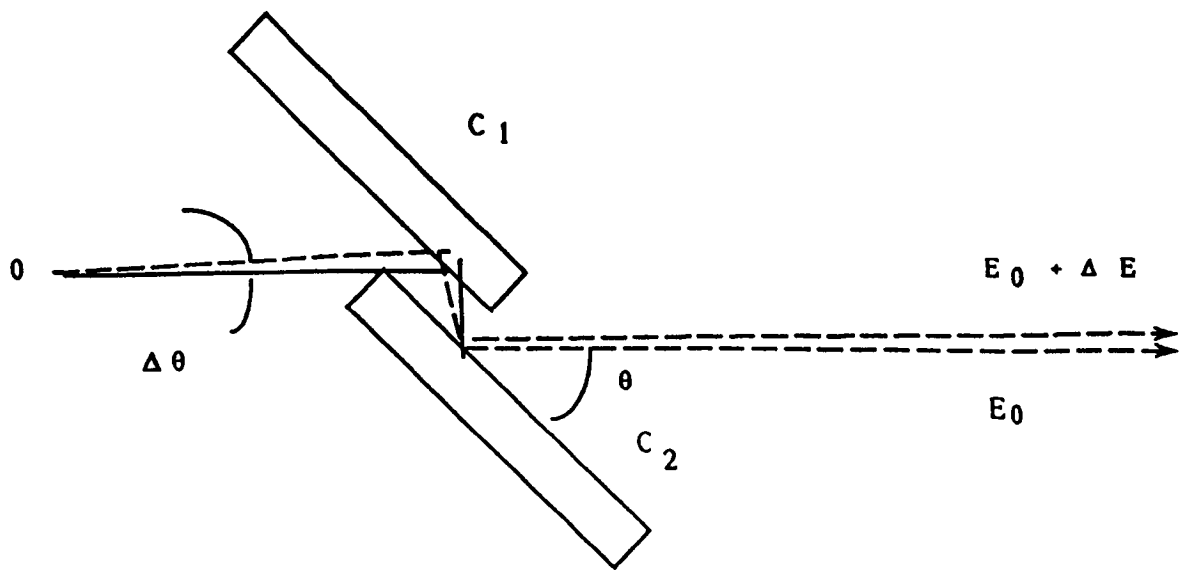

Fig. 4.7 Two-crystal X-ray monochromator in parallel configuration.

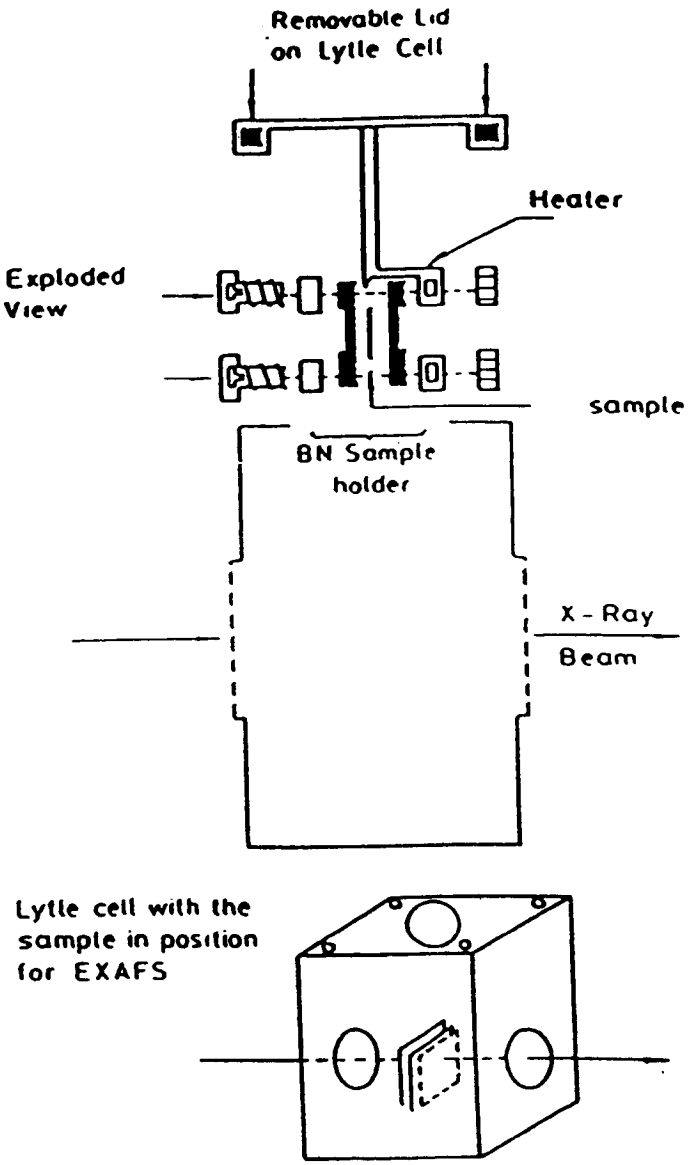

Fig. 4.6 Lytle cell used for high temperature EXAFS measurements.

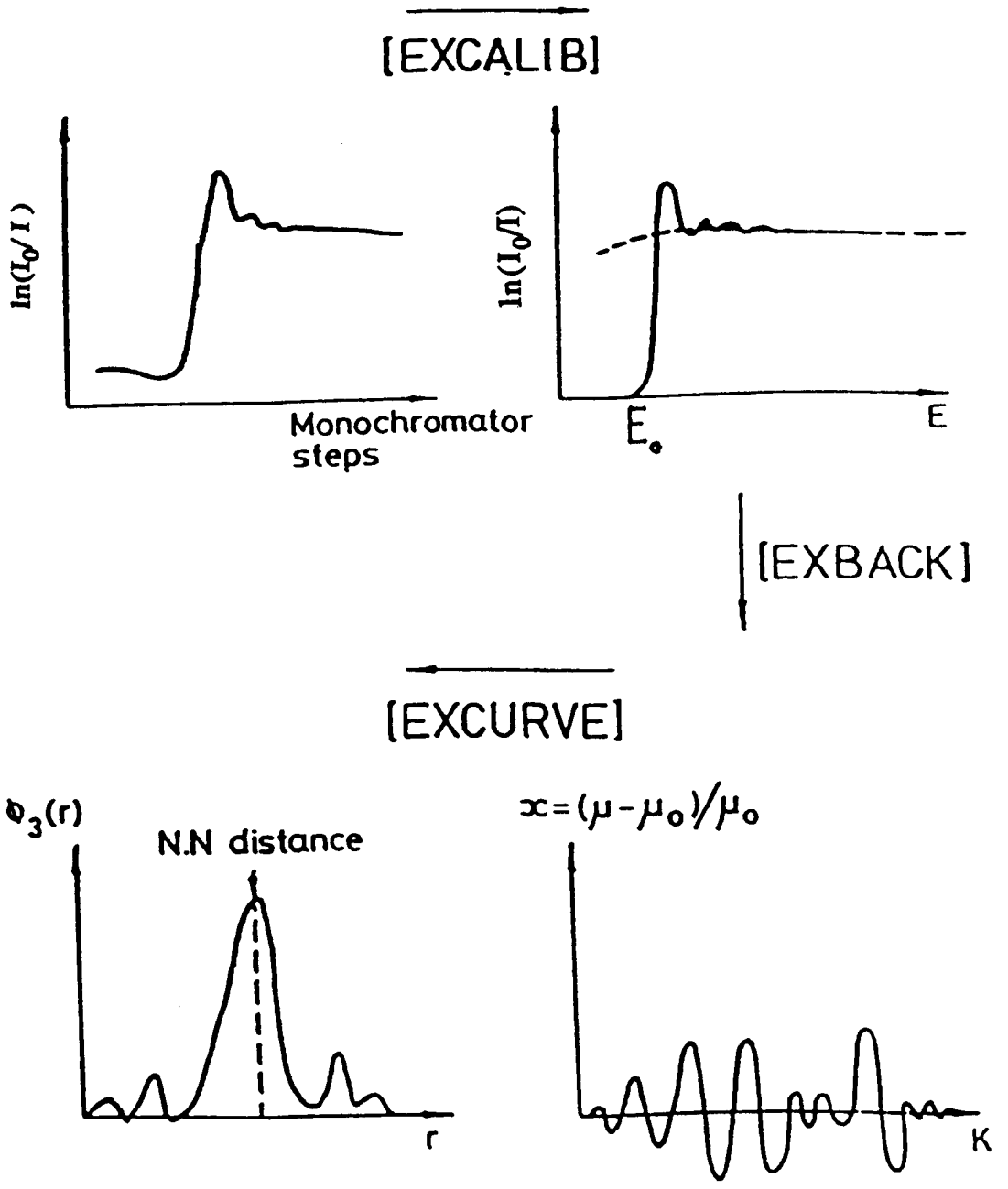

Fig. 4.8 Computer programms used for EXAFS data.

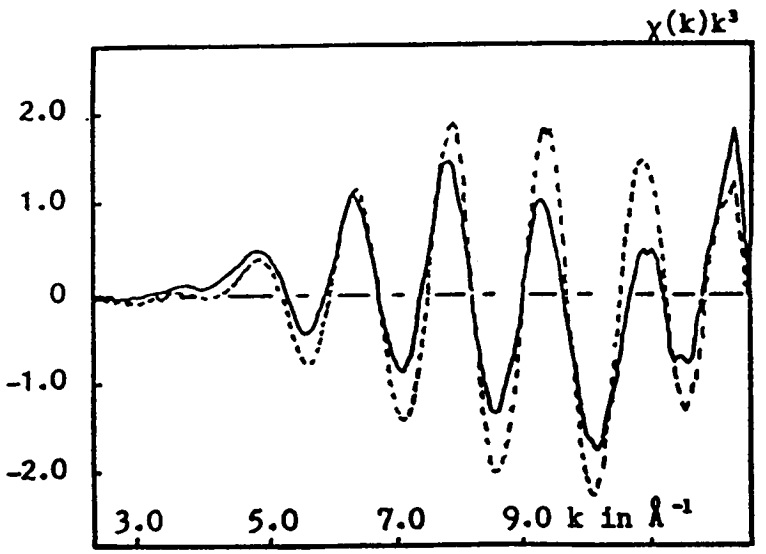

Fig. 4.9 Change with temperature of experimental Ge K edge EXAFS from $GeSe_2$ glass.

--- 22^0C; —— 350^0C.

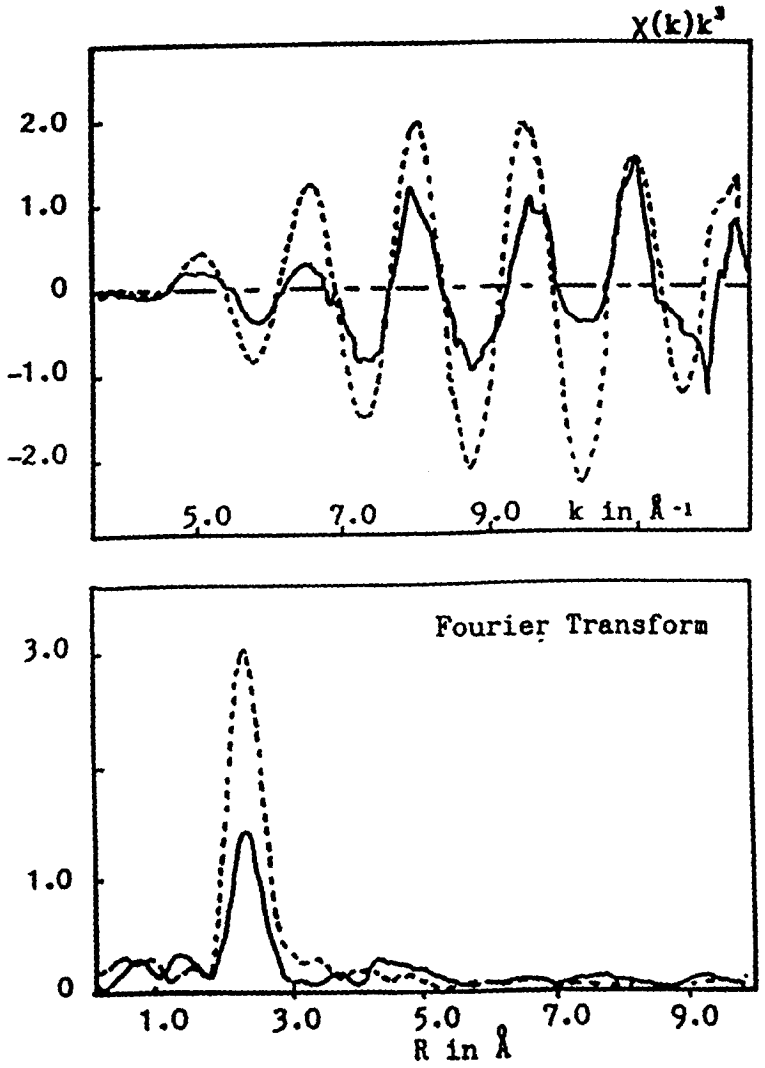

Fig. 4.10 Experimental Ge and Se K edge EXAFS from $GeSe_2$ glass.
– – – Ge; ——— Se

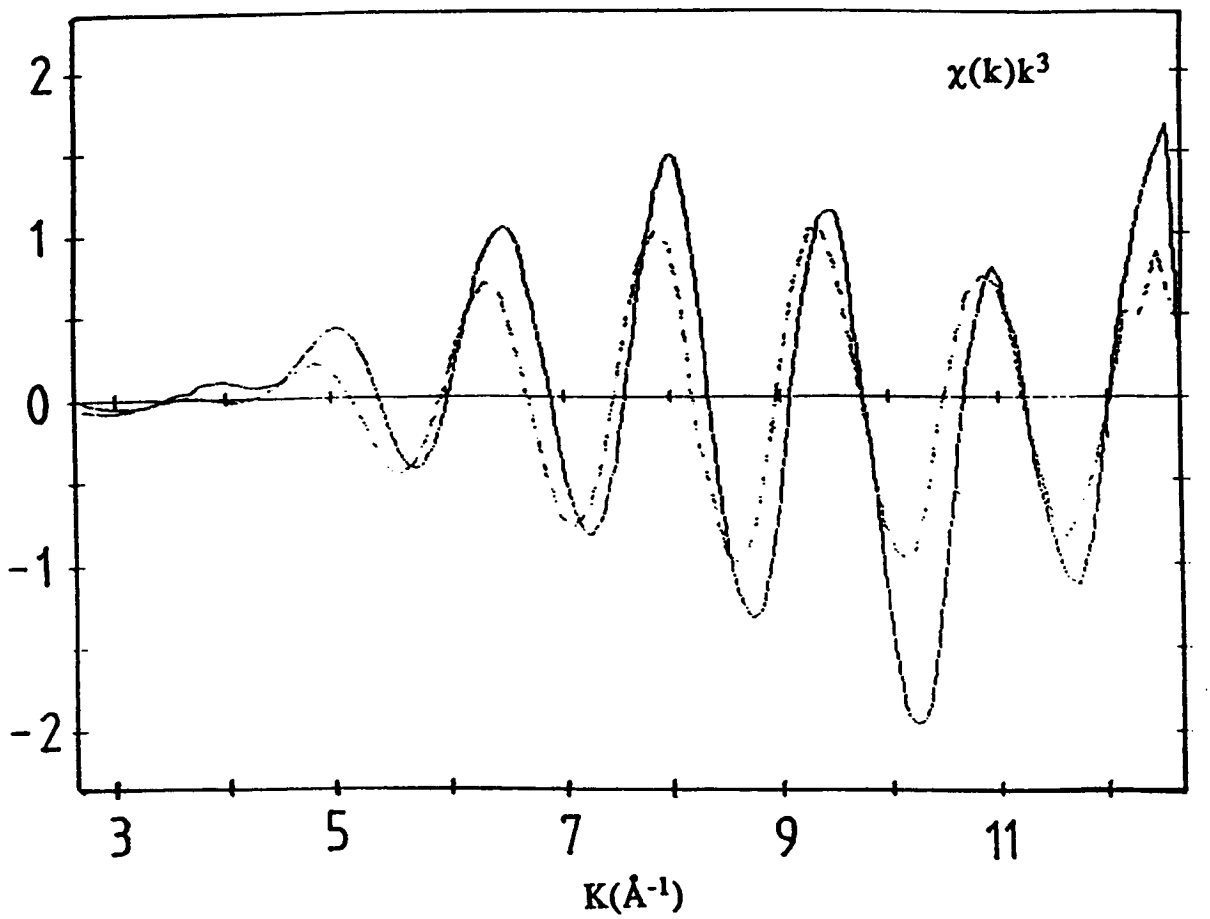

Fig. 4.11 Experimental room temperature (22^0C)

Ge K edge EXAFS from $GeSe_2$ and $(GeSe_2)_{92}Ga_8$ glaases.

—— $GeSe_2$; — — — $(GeSe_2)_{92}Ga_8$

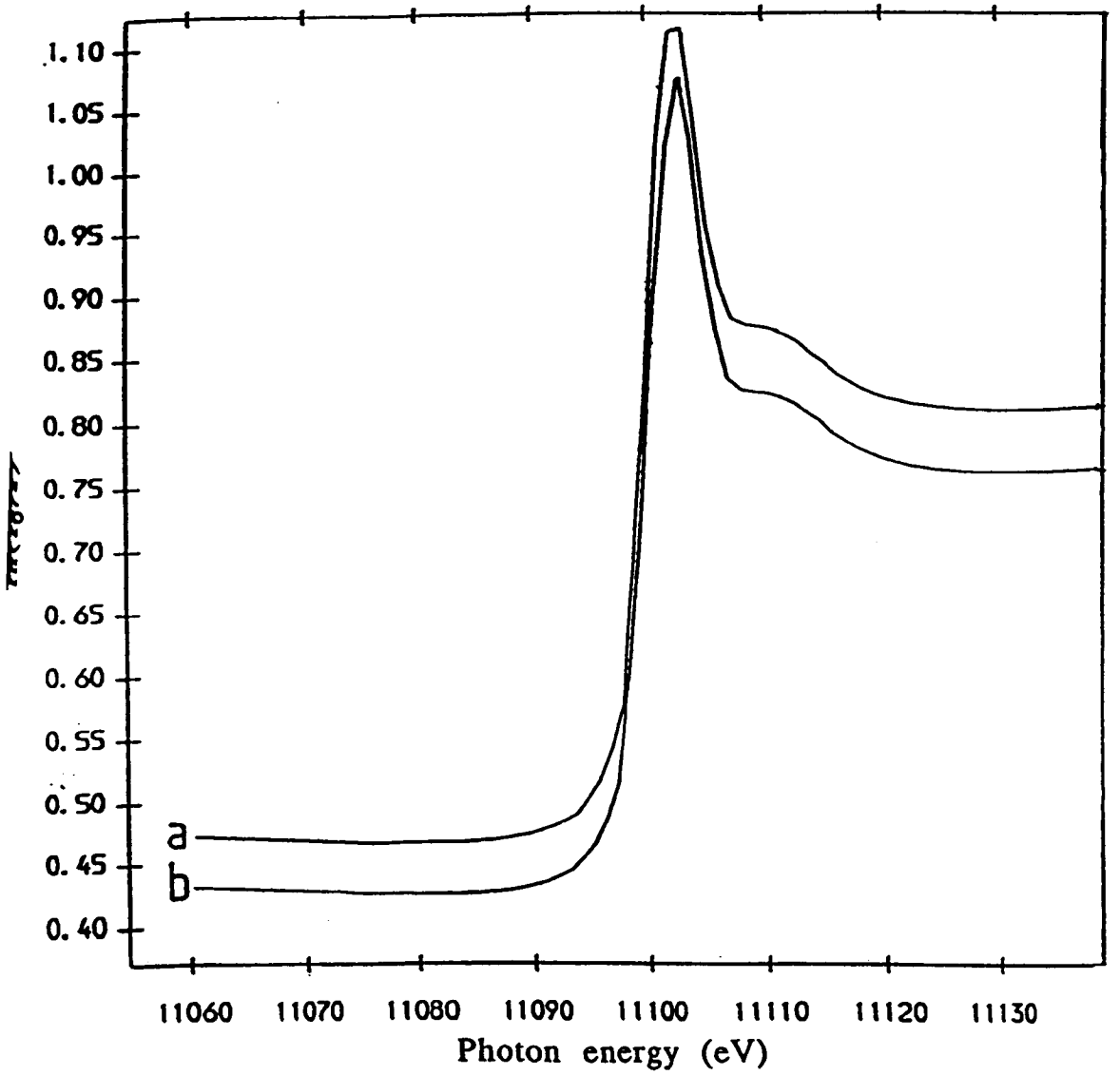

Fig. 4.12 XANES from $GeSe_2$ glass.

(a) 350^0C and (b) 22^0C .

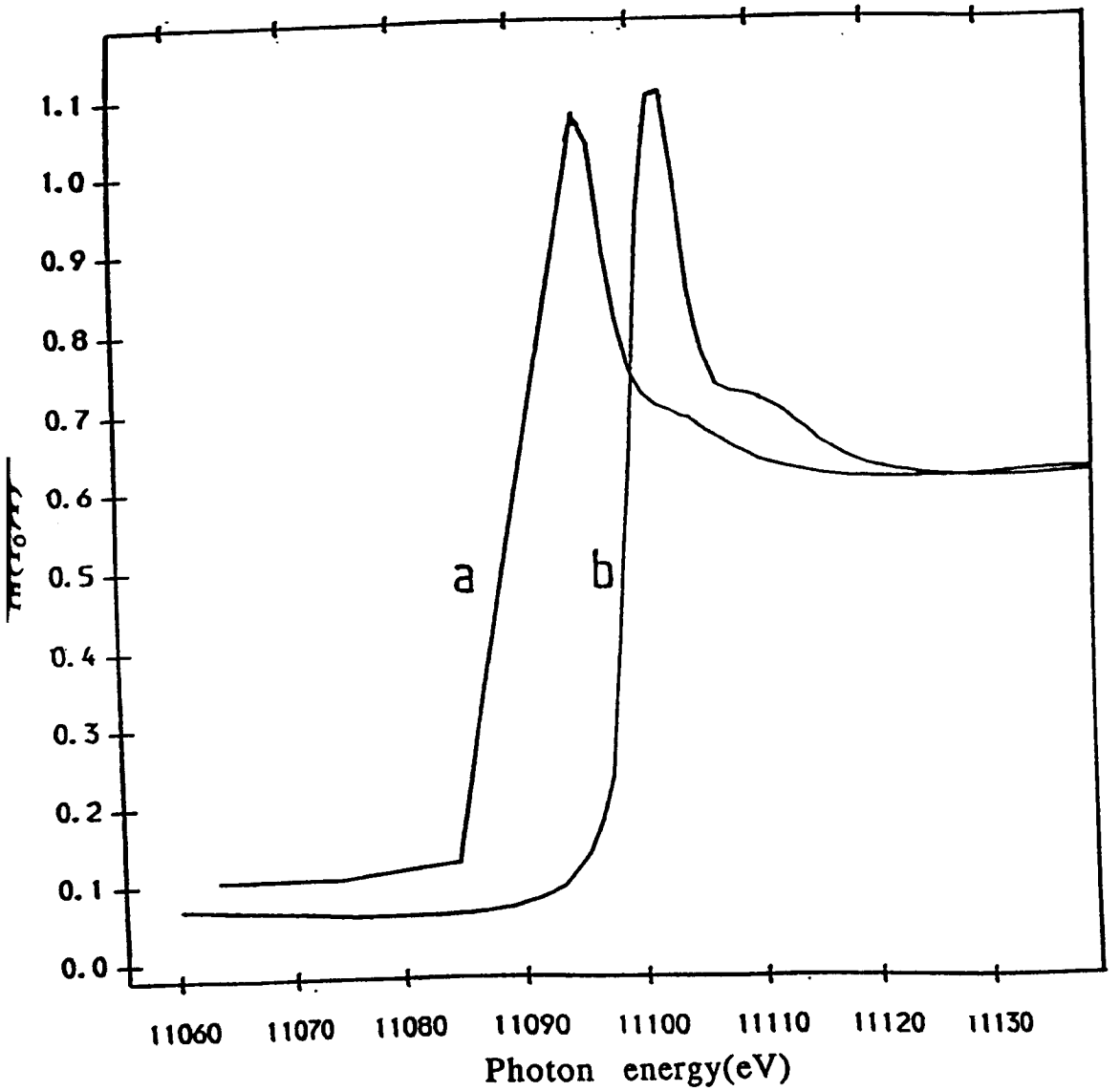

Fig. 4.13 XANES at room temperature (22^0C) from (a) $(GeSe_2)_{92}Ga_8$ glass and (b) $GeSe_2$ glass.

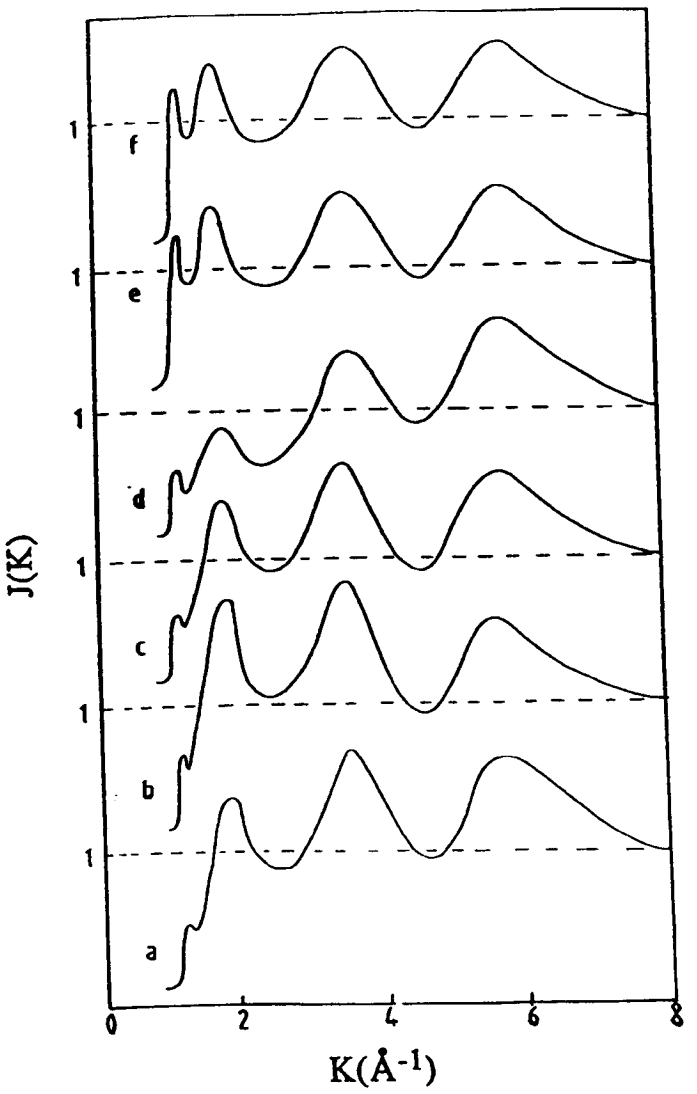

Fig. 5.1 X-ray interference functions for $Se_{1-x}S_x$ glasses

(a) x = 10 at %

(b) x = 15 at %

(c) x = 20 at %

(d) x = 25 at %

(e) x = 40 at %

and (f) x = 50 at %

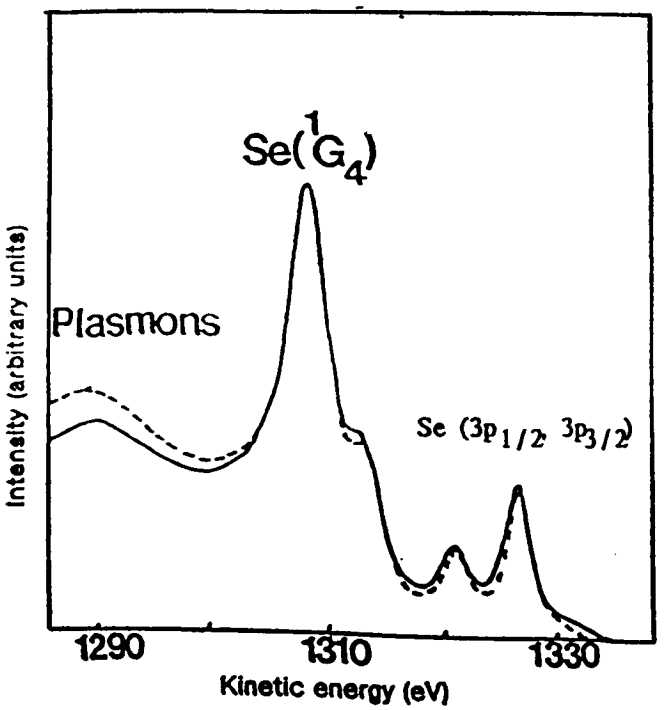

Fig. 5.2 Selenium Auger peaks in $Se_{90}S_{10}$ (full curve) and Se (broken curve) shifted so that $^1G_4$ peaks coincide.

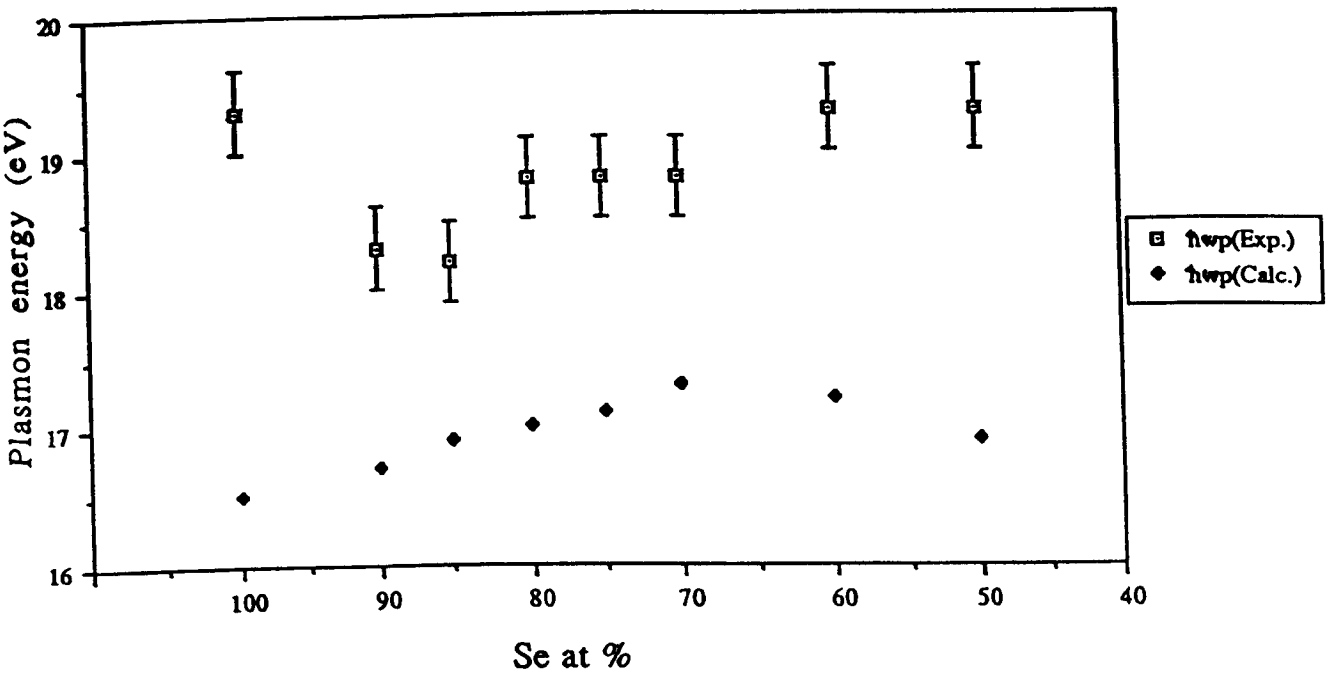

Fig 5.3 Change in plasmon energy with Se content in Se-S glasses both for calculated values and those determined experimentally from the $L_3M_{4,5}M_{4,5}$ Auger lines of Se.

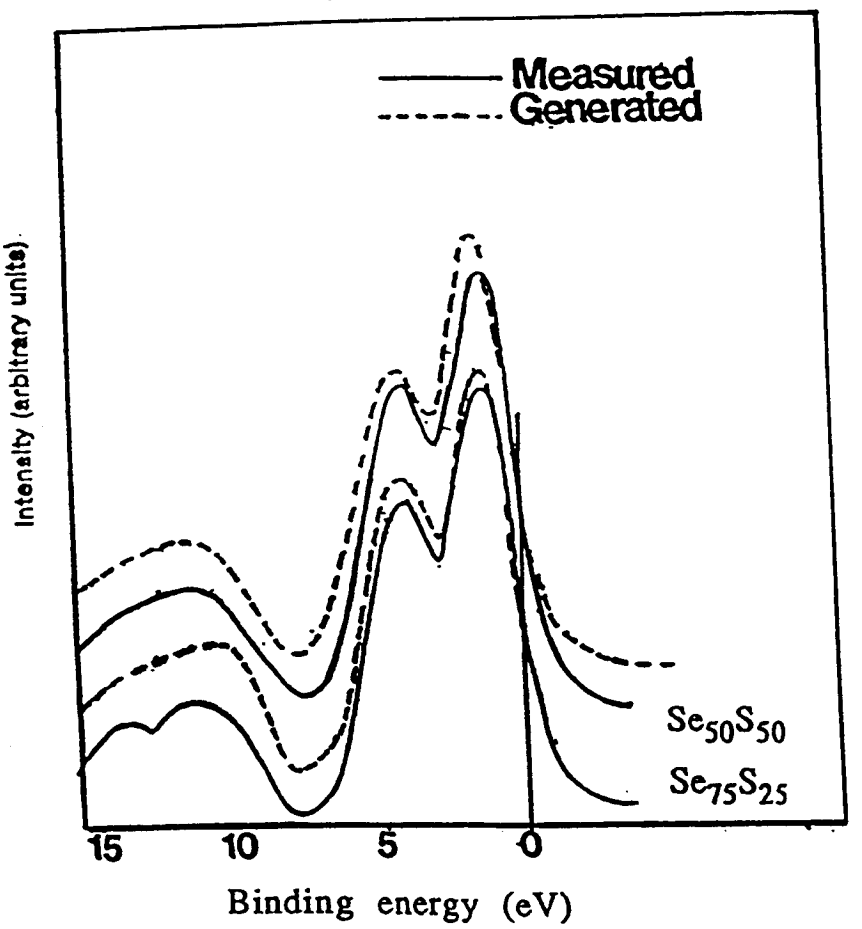

Fig. 5.4 Corrected valence band spectra, measured and generated, for $Se_{75}S_{25}$ and $Se_{50}S_{50}$ glasses.

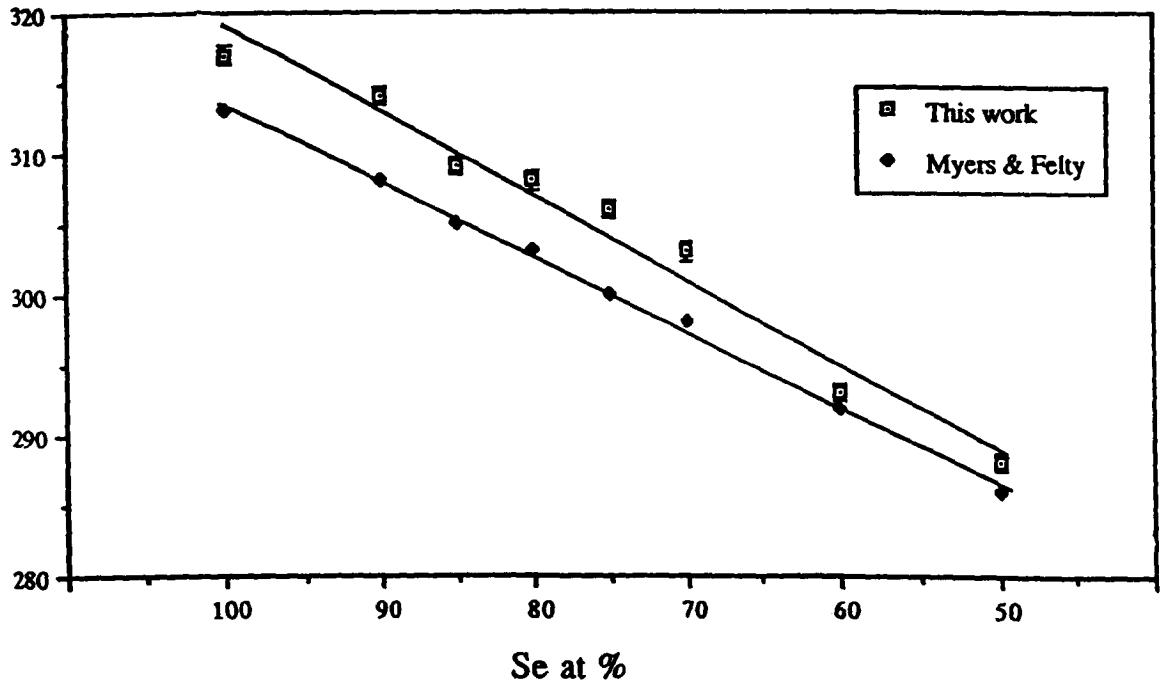

5.5 Change in glass transition temperature with Se content in Se-S glasses.

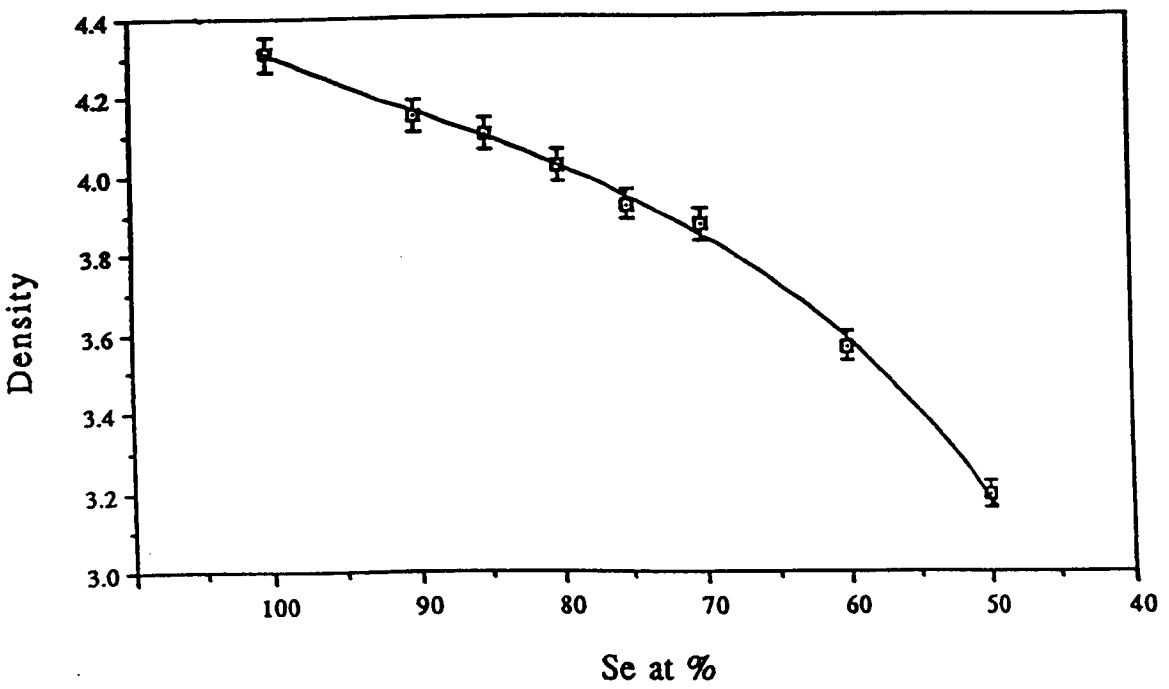

Fig. 5.6 Change in relative density with Se content in Se-S glasses.

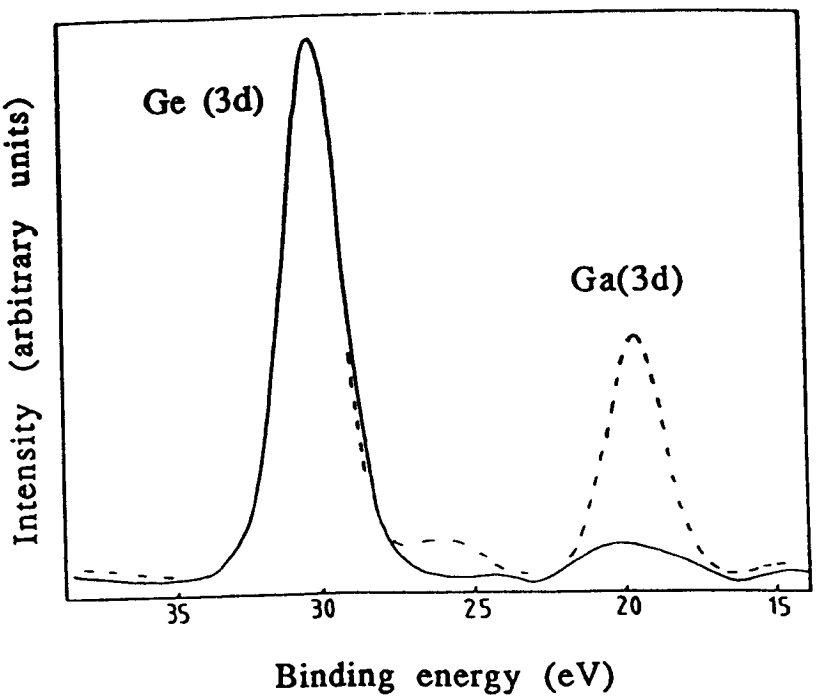

Fig. 5.7 Ge(3d) peak in $GeSe_2$ (full curve) and Ge(3d) and Ga(3d) peaks in $(GeSe_2)_{92}Ga_8$ (broken curve).

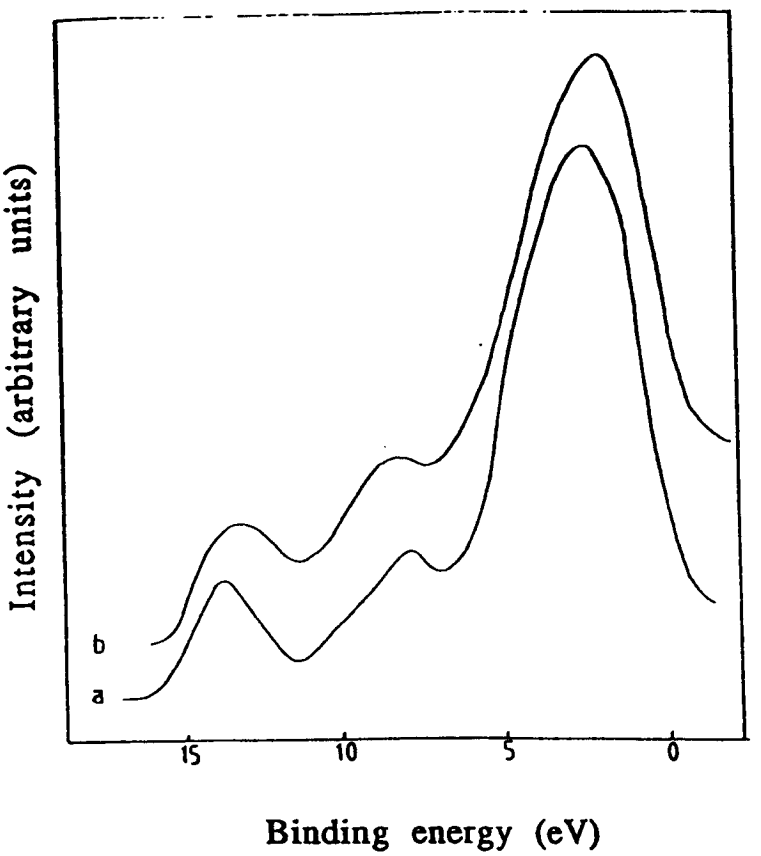

Fig. 5.8 Corrected valence band spectra for (a) $GeSe_2$ and (b) $(GeSe_2)_{96}Ga_4$.

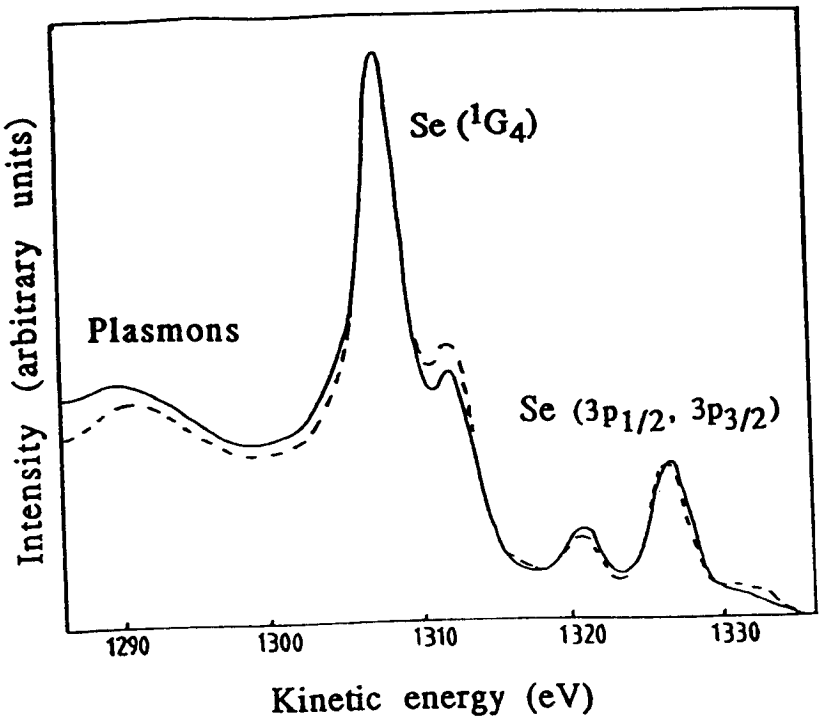

Fig. 5.9 Selenium Auger peaks in $(GeSe_2)_{96}Ga_4$ (full curve) and $(GeSe_2)_{92}Ga_8$ (broken curve) shifted so that $^1G_4$ peaks coincide.

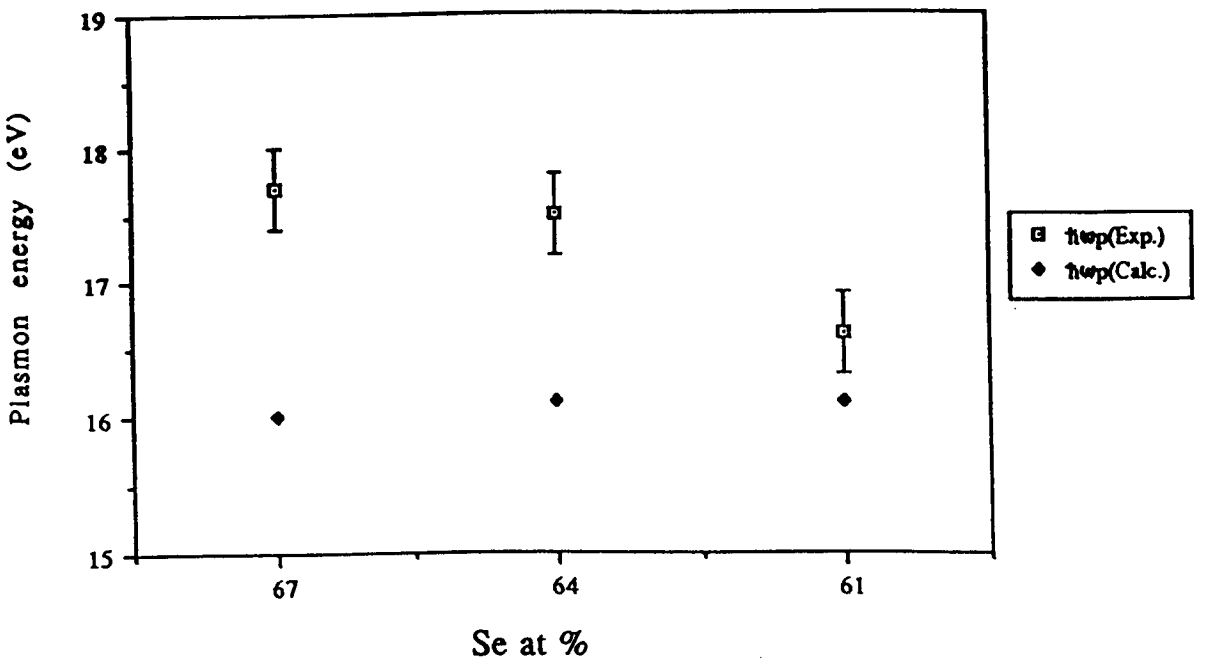

Fig. 5.10 Change in plasmon energy with Se content in Ge-Se-Ga glasses both for calculated values and those determined experimentally from the $L_3M_{4,5}M_{4,5}$ Auger lines of Se.

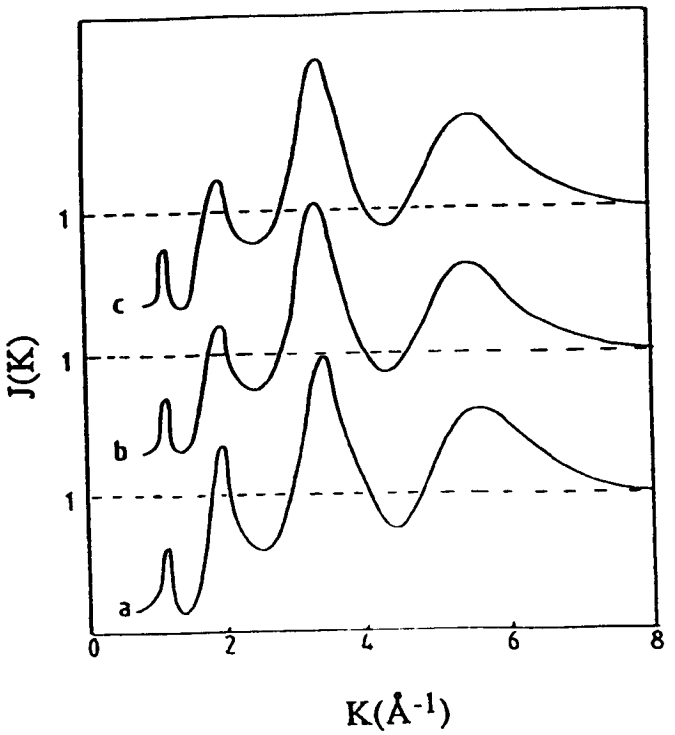

Fig. 5.11 X-ray interference functions for (a) $GeSe_2$ (b) $(GeSe_2)_{96}Ga_4$ and (c) $(GeSe_2)_{92}Ga_8$.

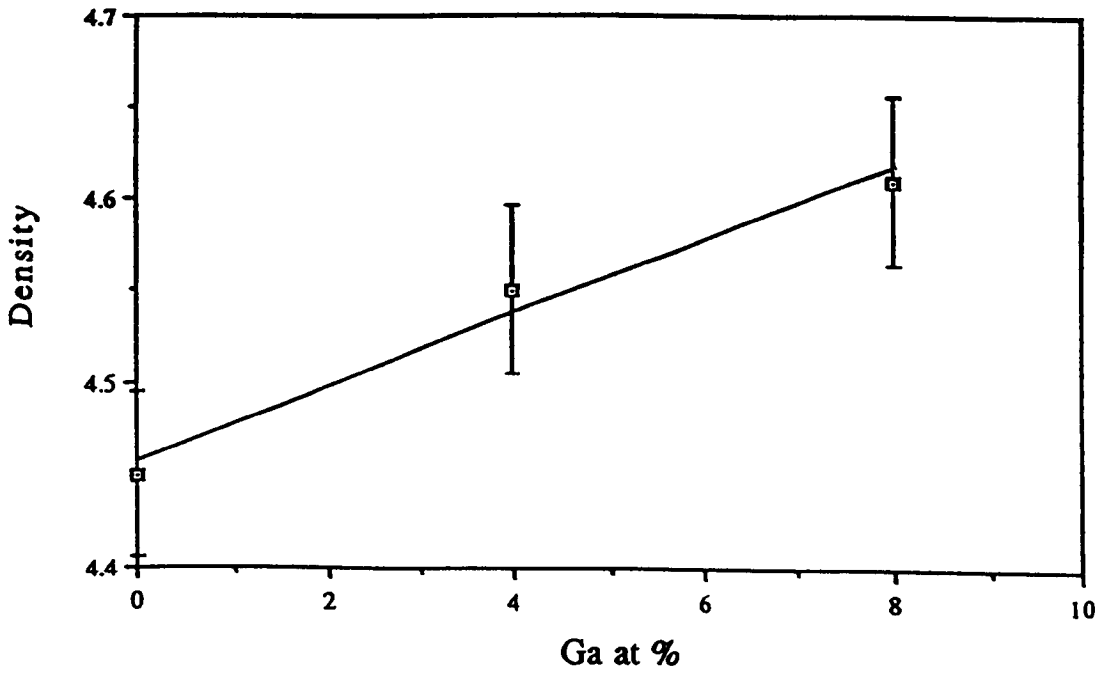

Fig. 5.12 Change in relative density with Ga content in Ge-Se-Ga glasses.

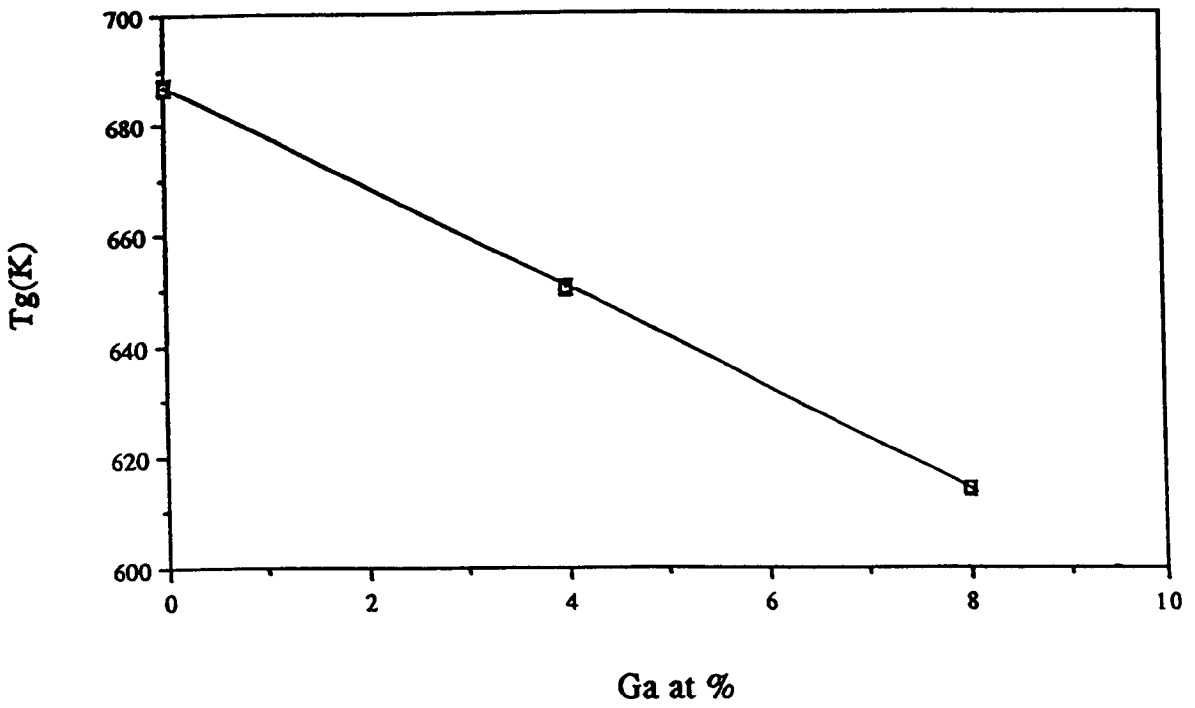

Fig. 5.13 Change in glass transition temperature with Ga content in Ge-Se-Ga glasses.

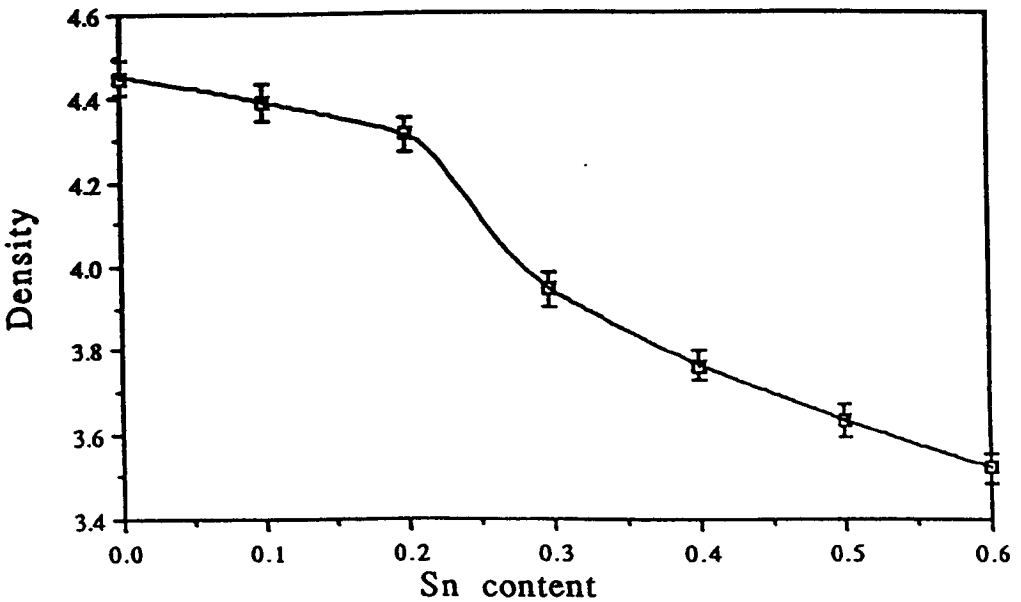

Fig. 5.14 Change in relative density with Sn content in Ge-Se-Sn glasses.

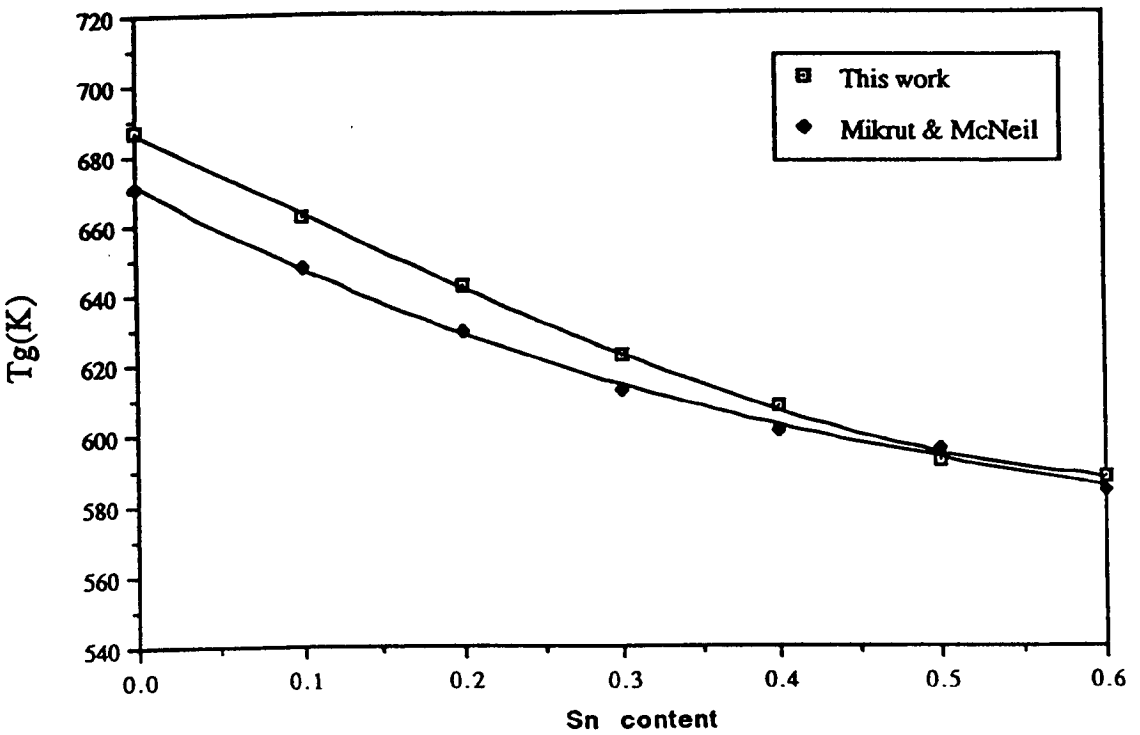

Fig. 5.15 Change in glass transition temperature with Sn content in Ge-Se-Sn glasses.

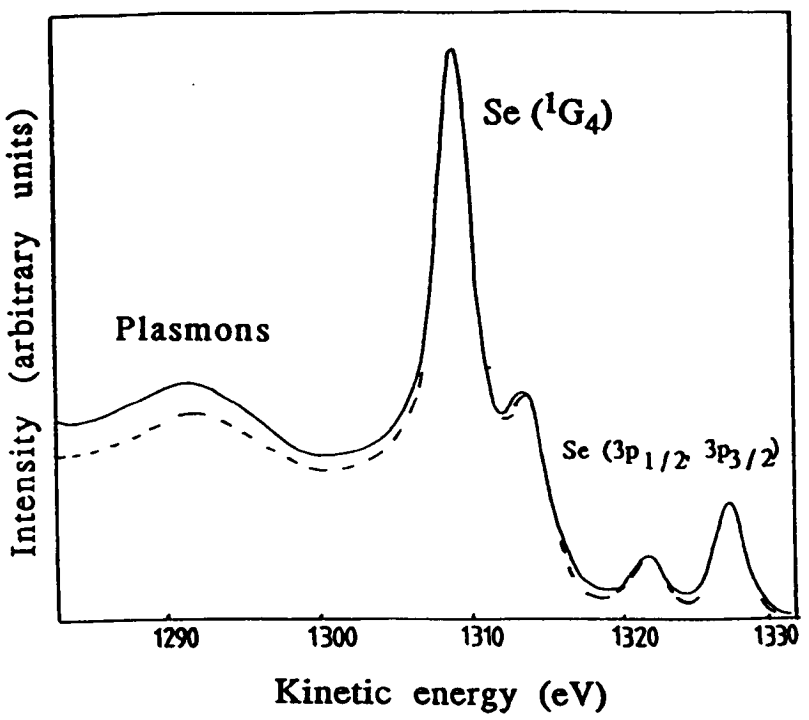

Fig. 5.16 Selenium Auger peaks in $Ge_{0.7}Sn_{0.3}Se_2$ (full curve) and $Ge_{0.5}Sn_{0.5}Se_2$ (broken curve) shifted so that $^1G_4$ peaks coincide.

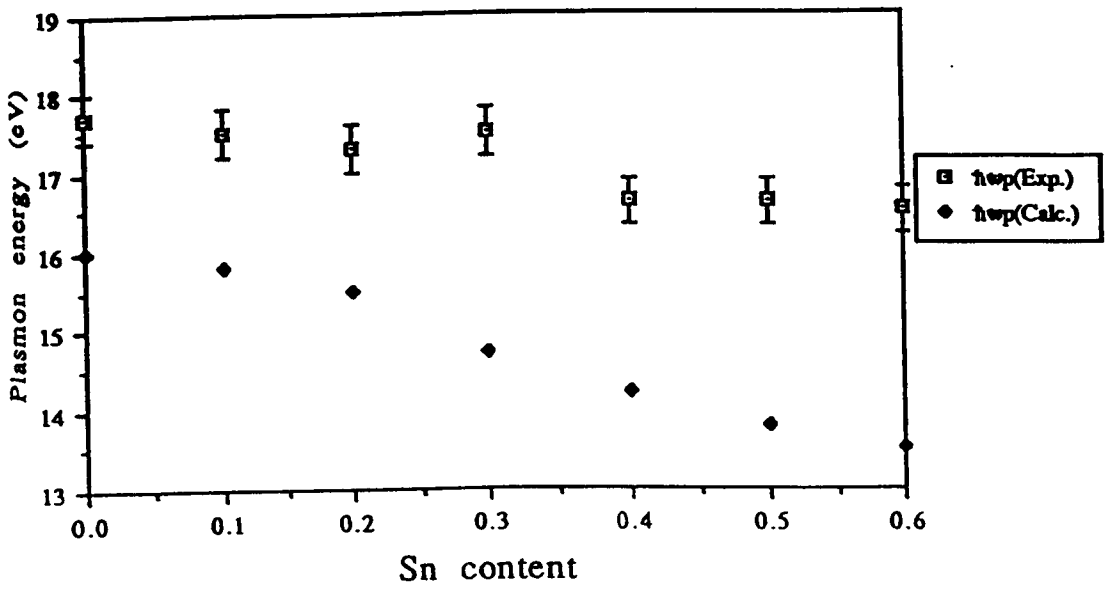

Fig. 5.17 Change in plasmon energy with Sn content in Ge-Se-Sn glasses both for calculated values and those determined experimentally from the $L_3M_{4,5}M_{4,5}$ Auger lines of Se.

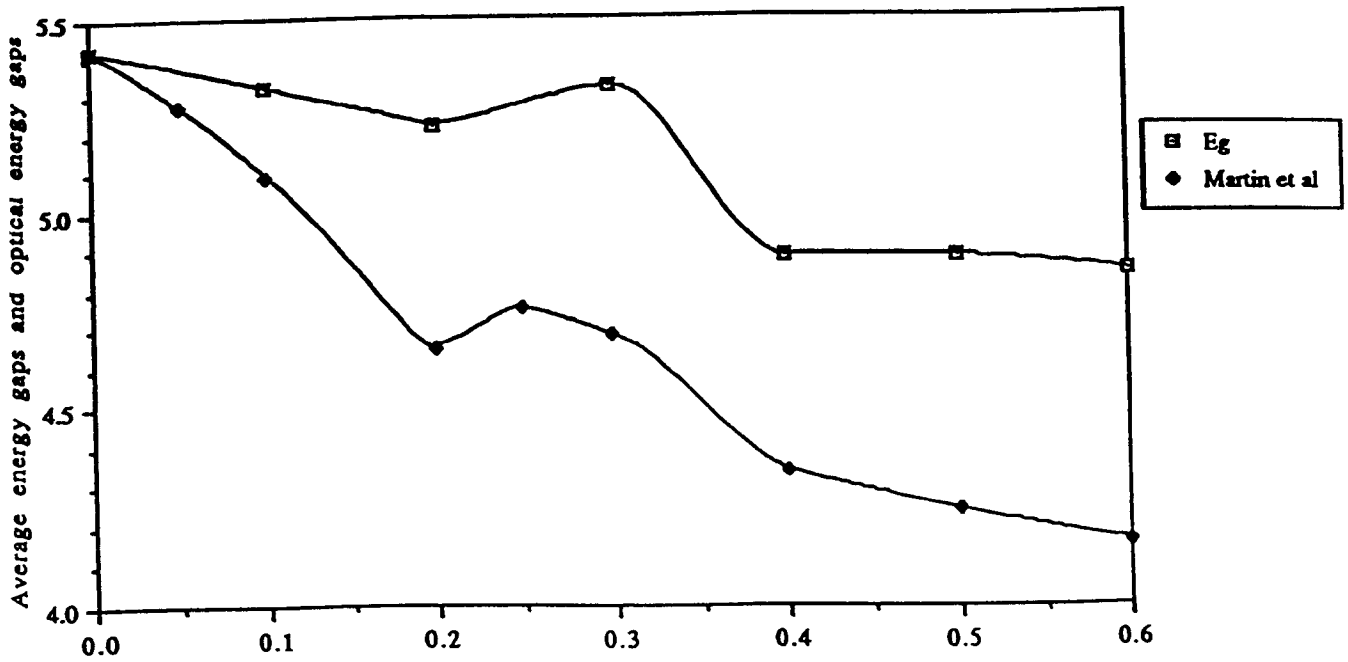

Fig. 5.18 Change in calculated values of the average energy gaps and measured optical energy gaps (Martin et al 1990) with Sn content in Ge-Se-Sn glasses. The values of the optical energy gaps were normalised to the value of the average energy gap of $GeSe_2$.

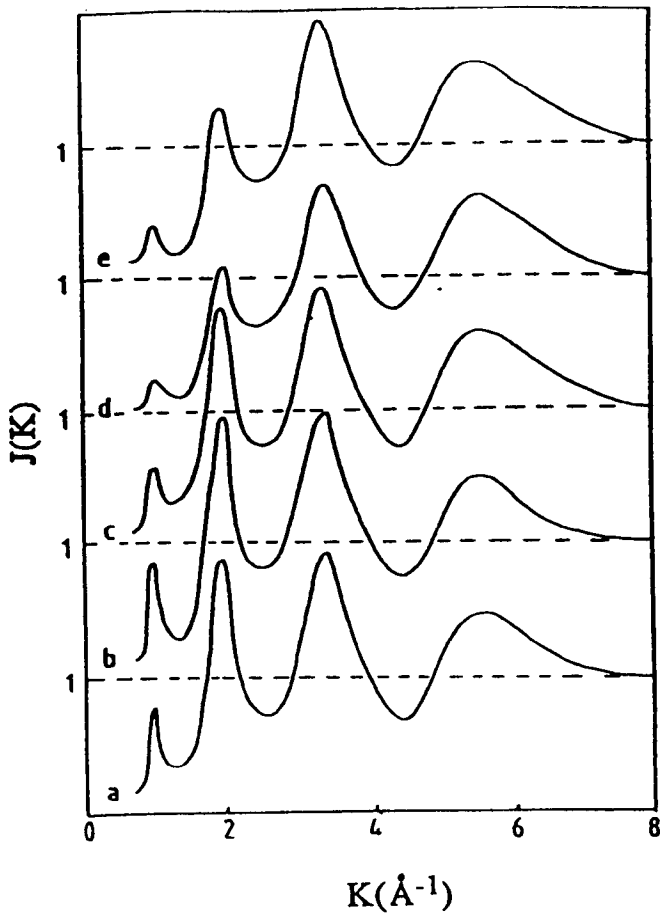

Fig. 5.19 X-ray interference functions for $Ge_{1-x}Sn_xSe_2$

(a) x = 0.1

(b) x = 0.2

(c) x = 0.3

(d) x = 0.4

and (e) x = 0.5

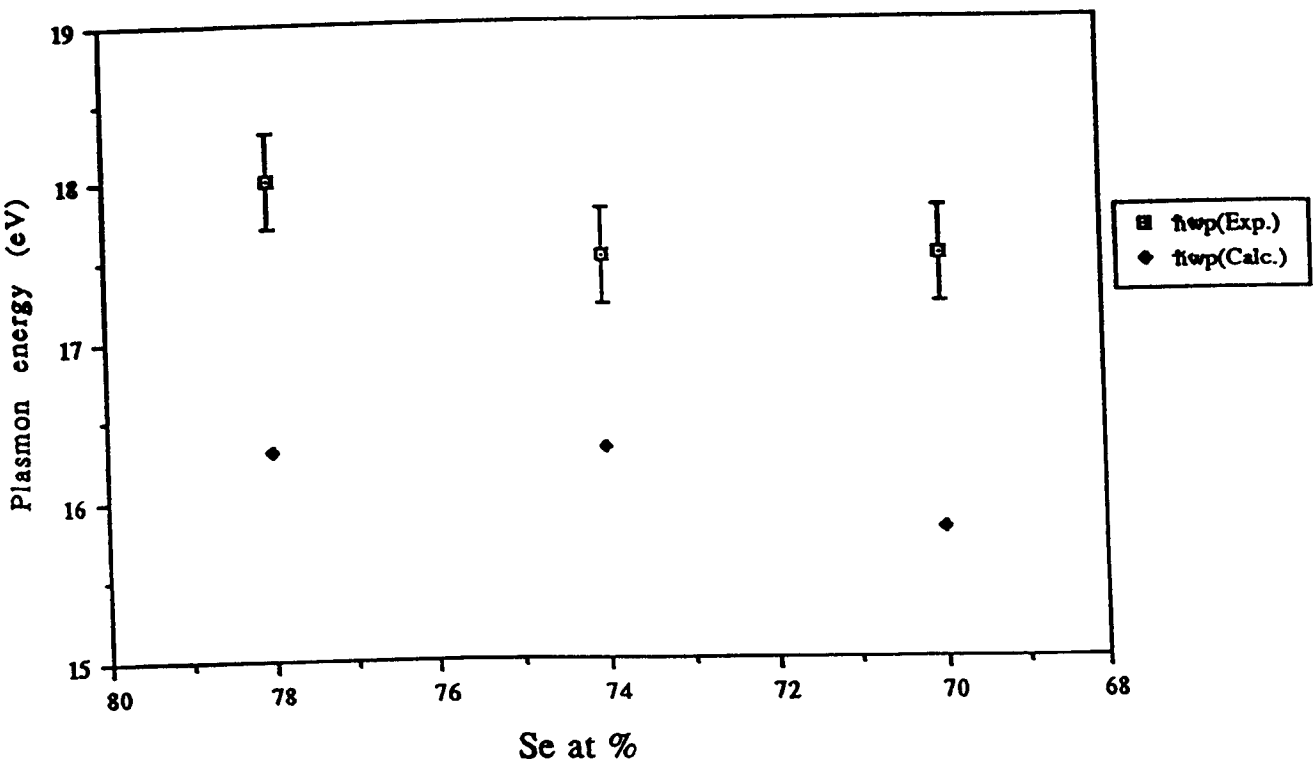

Fig. 5.20 Change in plasmon energy with Se content in Ge-Se-Bi glasses both for calculated values and those determined experimentally from the $L_3M_{4,5}M_{4,5}$ Auger lines of Se.

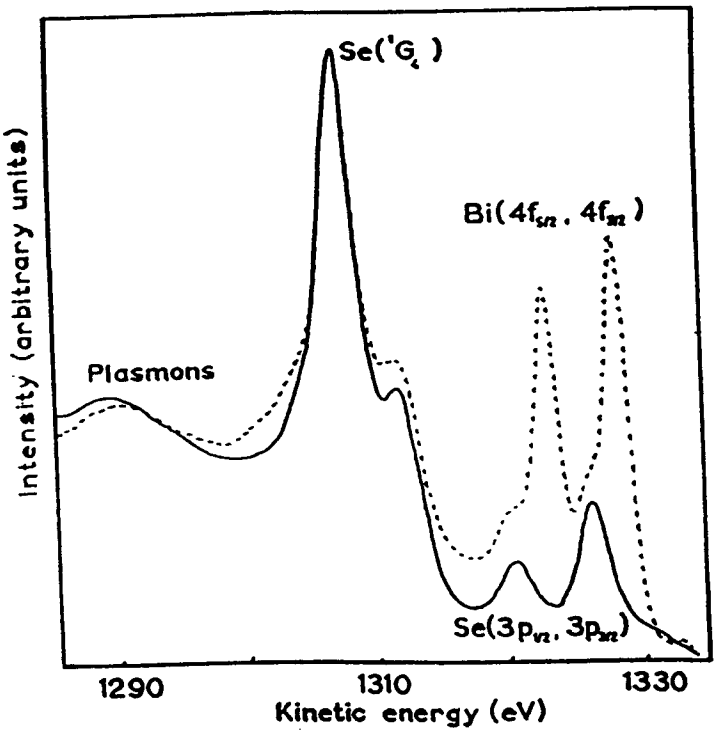

Fig. 5.21 Selenium Auger peaks in $GeSe_{3.5}$ (full curve) and $(GeSe_{3.5})_{90}Bi_{10}$ (broken curve) shifted so that $^1G_4$ peaks coincide.

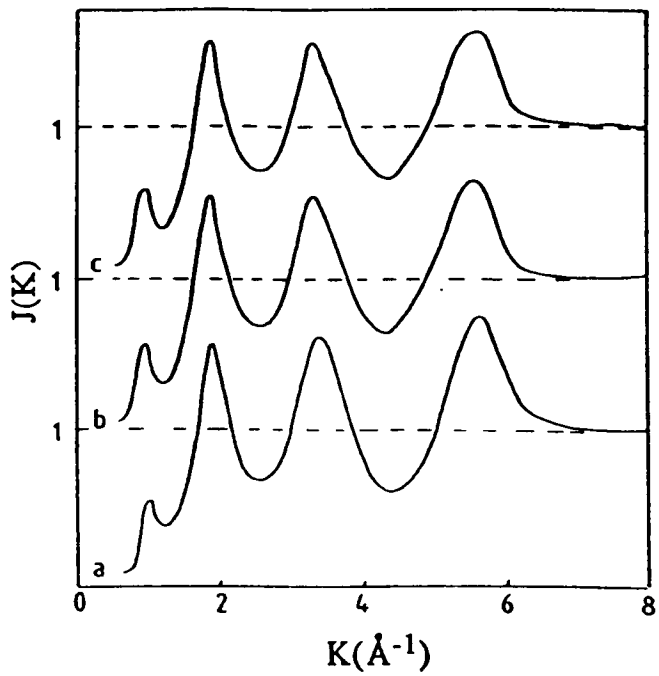

Fig. 5.22 X-ray interference functions for (a) $GeSe_{3.5}$ (b) $(GeSe_{3.5})_{95}Bi_5$ and (c) $(GeSe_{3.5})_{90}Bi_{10}$.

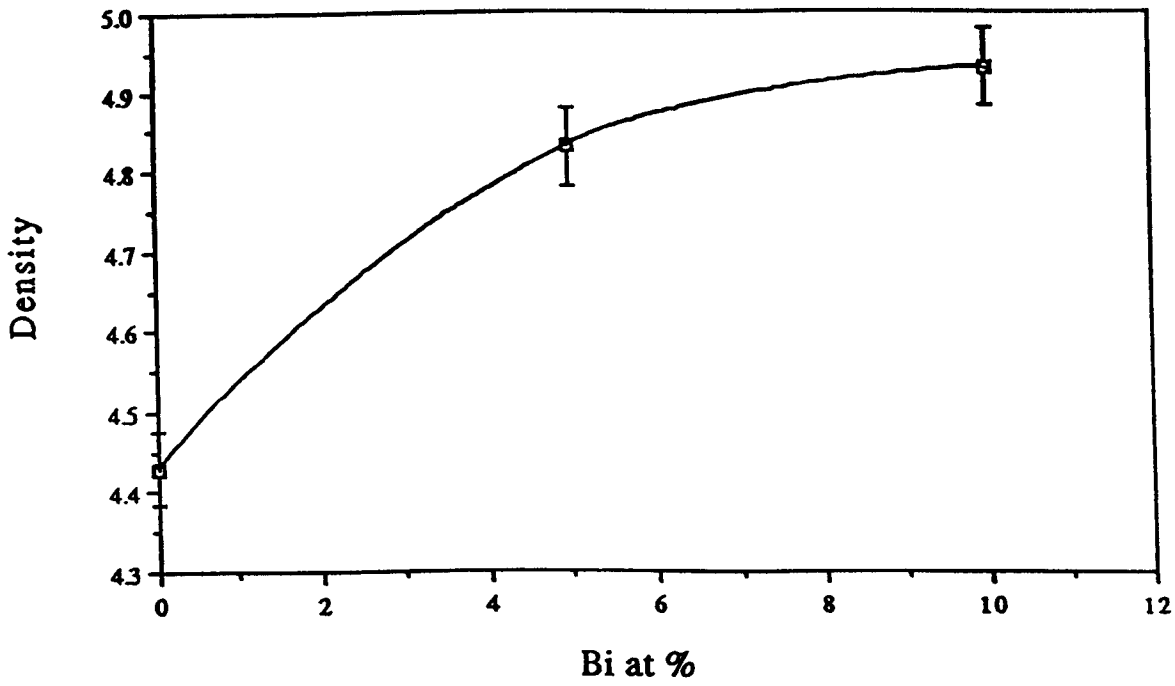

Fig. 5.23 Change in relative density with Bi content in Ge-Se-Bi glasses.

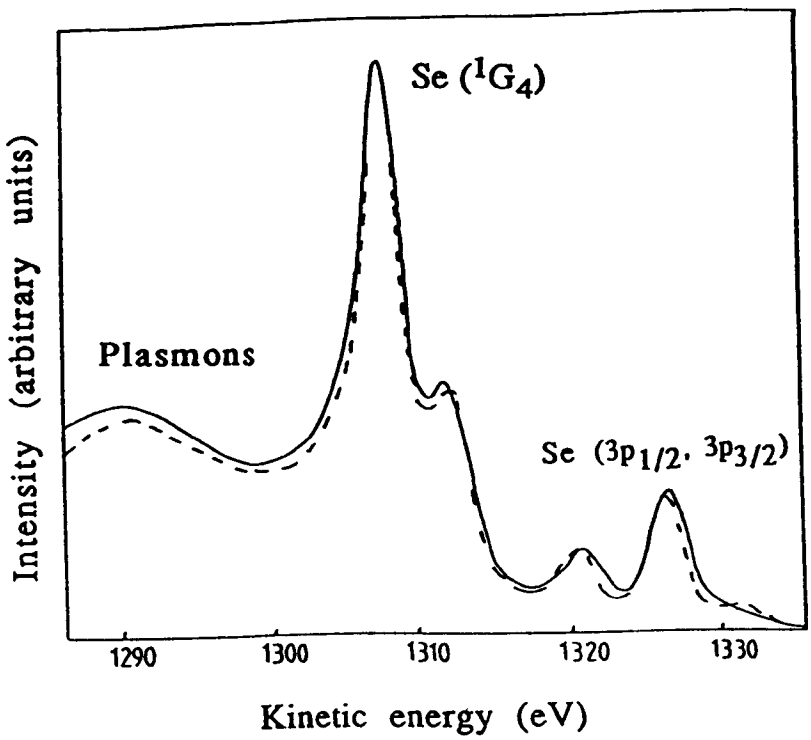

Fig. 5.24 Selenium Auger peaks in $GeSe_2$ (full curve) and $(GeSe_3)_{80}Sb_{20}$ (broken curve) shifted so that $^1G_4$ peaks coincude.

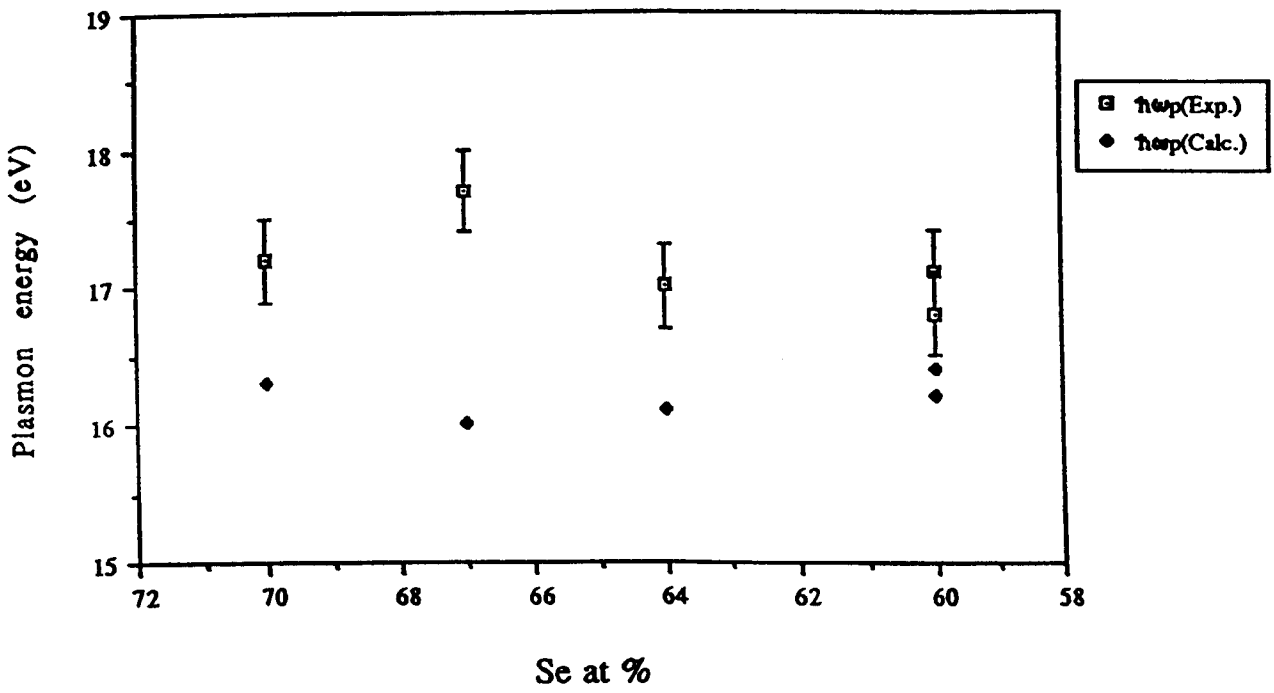

Fig. 5.25 Change in plasmon energy with Se content in Ge-Se-Sb glasses both for calculated values and those determined experimentally from the $L_3M_{4,5}M_{4,5}$ Auger lines of Se.

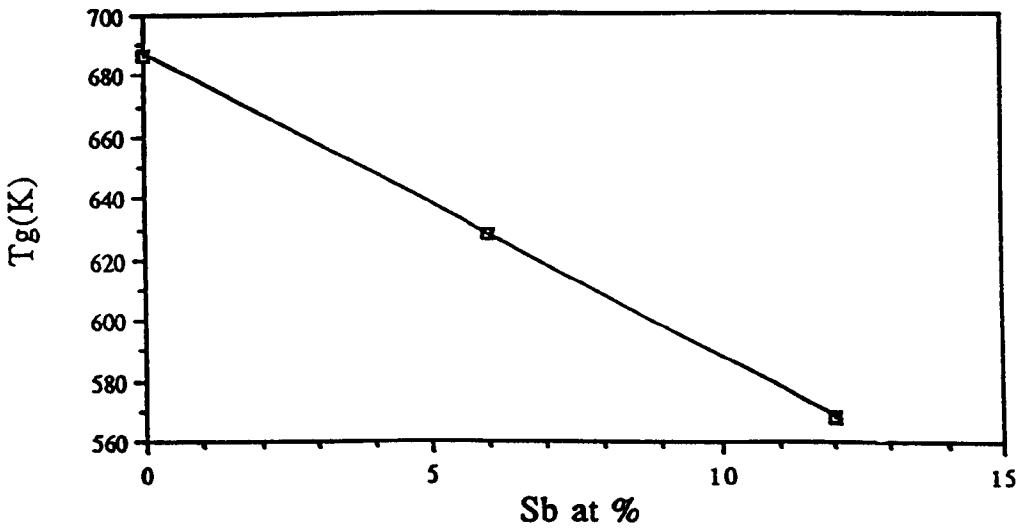

Fig. 5.26 Change in glass transition temperature with Sb content in Ge-Se-Sb glasses.

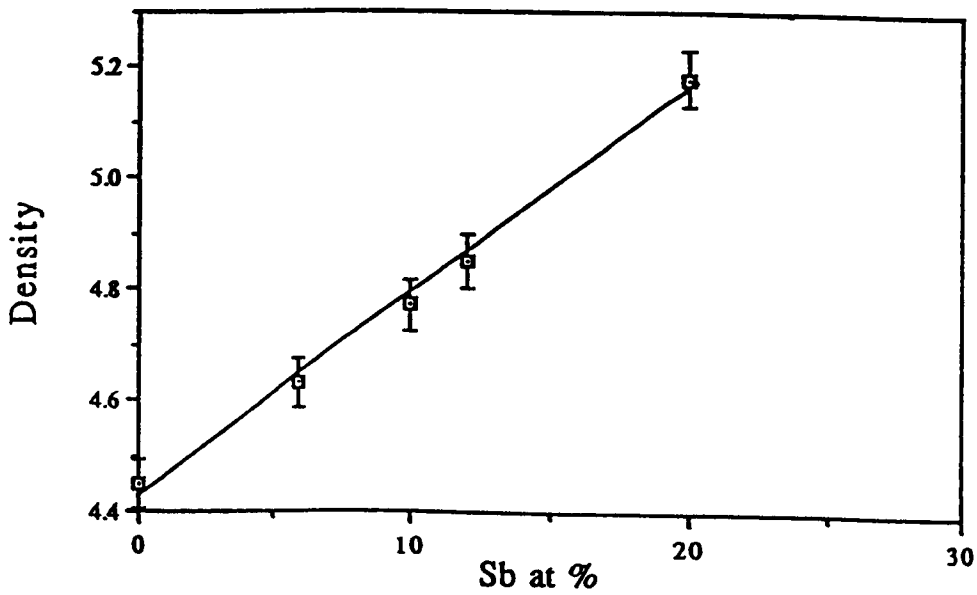

Fig. 5.27 Change in relative density with Sb content in Ge-Se-Sb glasses.

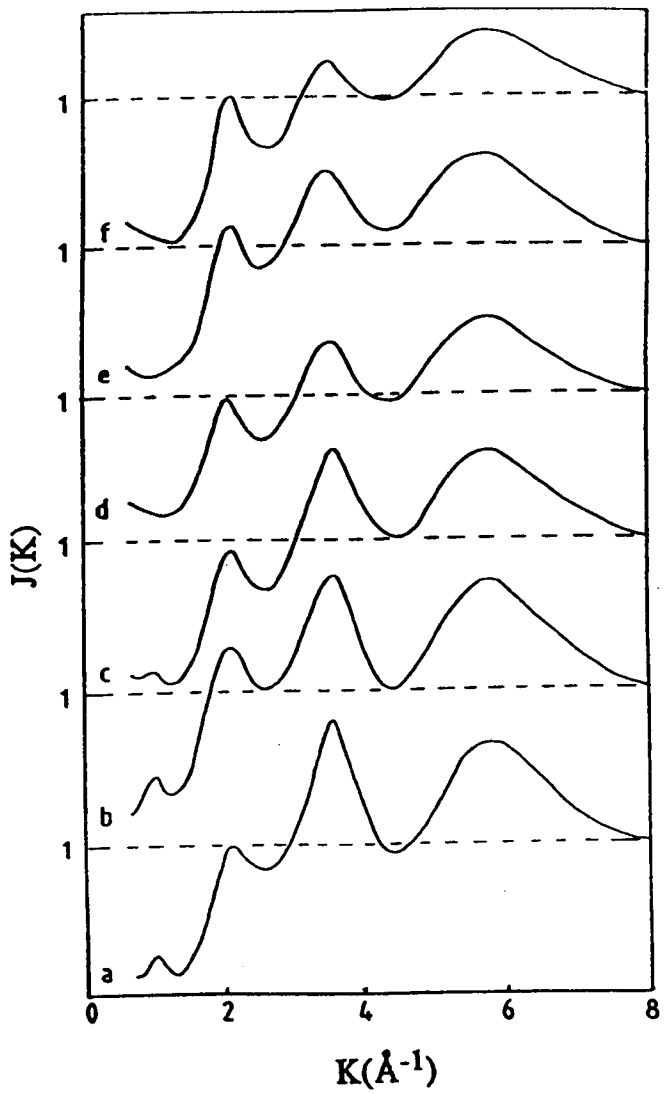

Fig. 5.28 X-ray interference functions for Ge-S-Ag glasses

(a) $Ge_{39.9}S_{55.1}Ag_5$

(b) $Ge_{36}S_{54}Ag_{10}$

(c) $Ge_{30}S_{55}Ag_{15}$

(d) $Ge_{28}S_{52}Ag_{20}$

(e) $Ge_{25}S_{50}Ag_{25}$

and (f) $Ge_{20}S_{50}Ag_{30}$

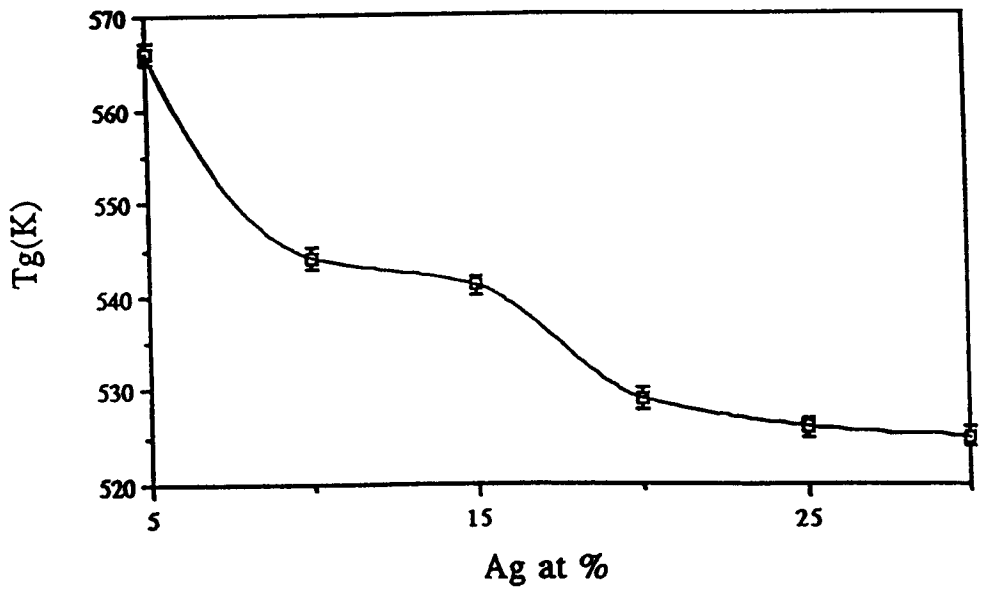

Fig. 5.29 Change in glass transition temperature with Ag content in Ge-S-Ag glasses.

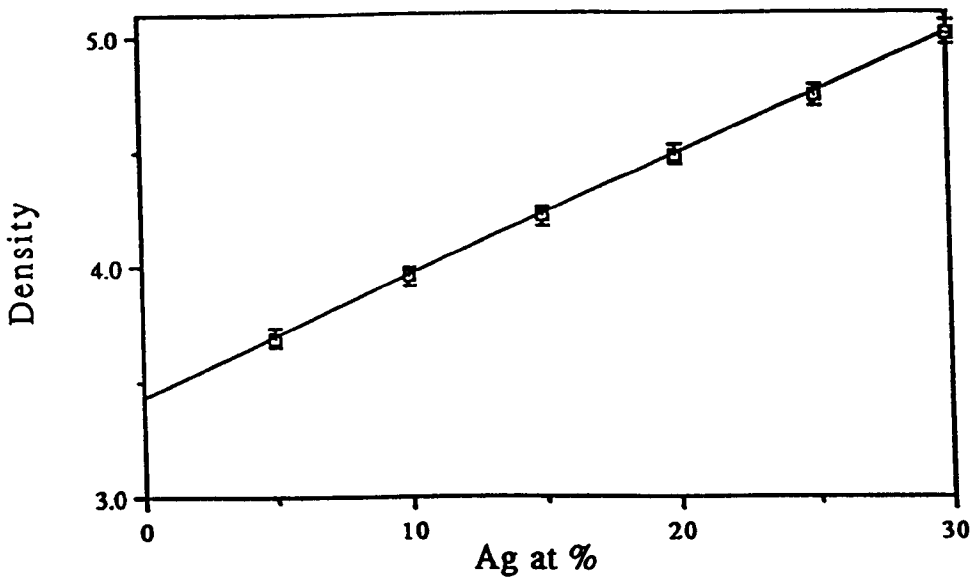

Fig. 5.30 Change in relative density with Ag content in Ge-S-Ag glasses.

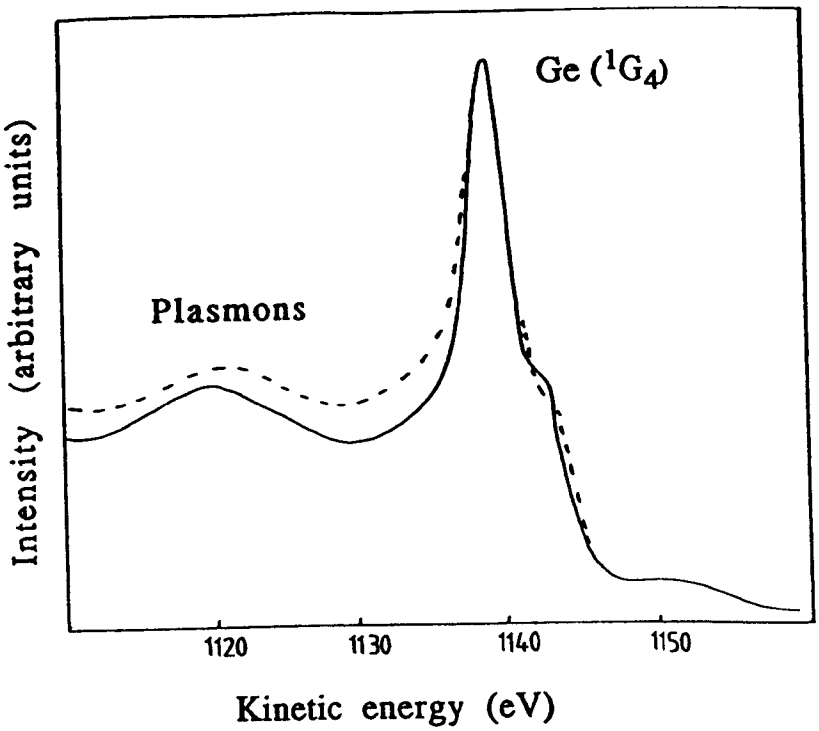

Fig. 5.31 Germanium Auger peaks in GeS_2 (full curve) and $(GeS_2)_{90}Ga_{10}$ (broken curve) shifted so that $^1G_4$ peaks coincide.

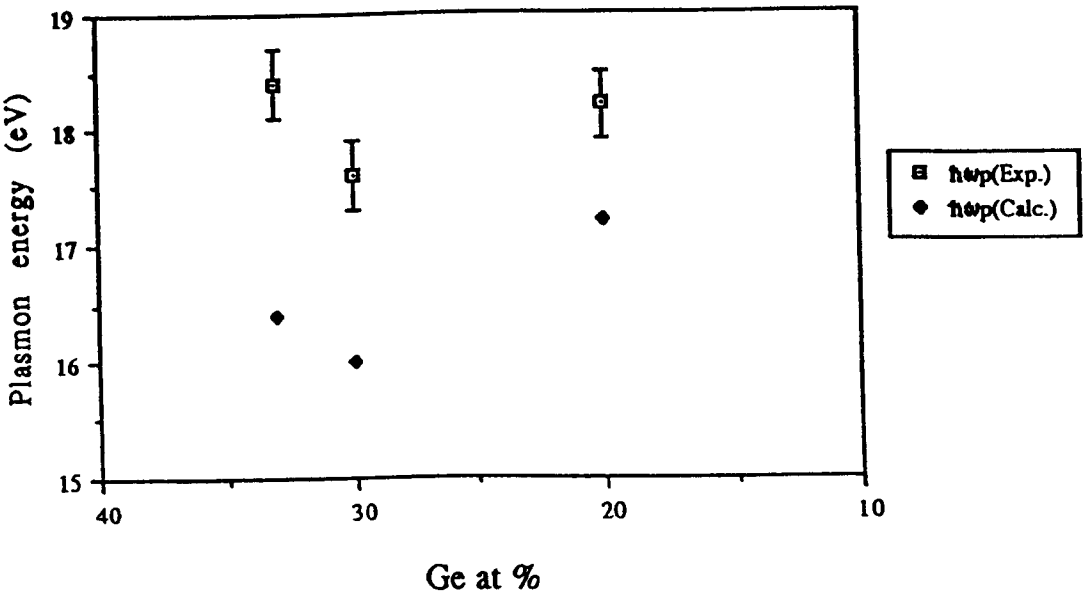

Fig. 5.32 Change in plasmon energy with Ge content in Ge-S-Ga glasses both for calculated values and those determined experimentally from the $L_3M_{4,5}M_{4,5}$ Auger lines of Ge.

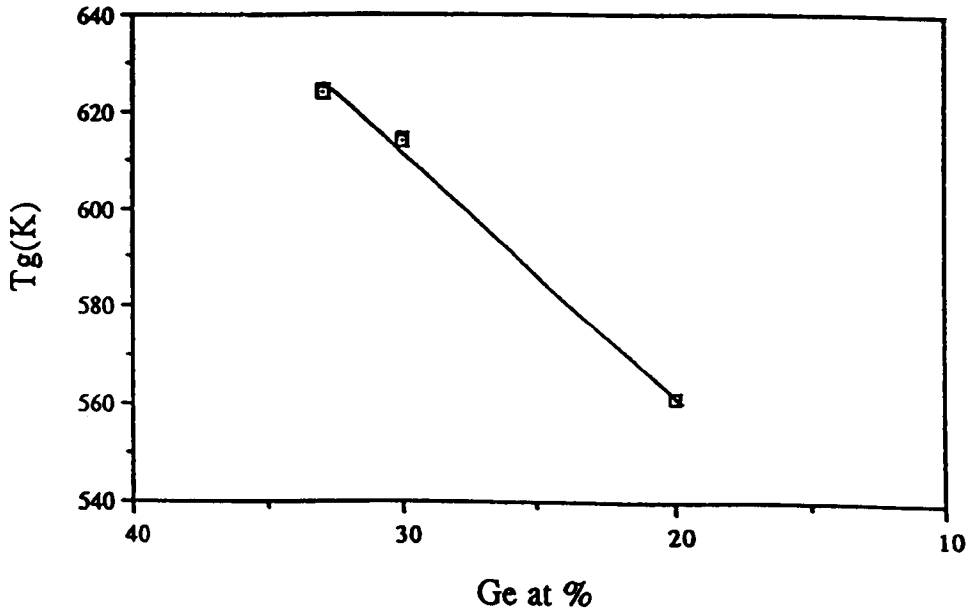

Fig. 5.33 Change in glass transition temperature with Ge content in Ge-S-Ga glasses.

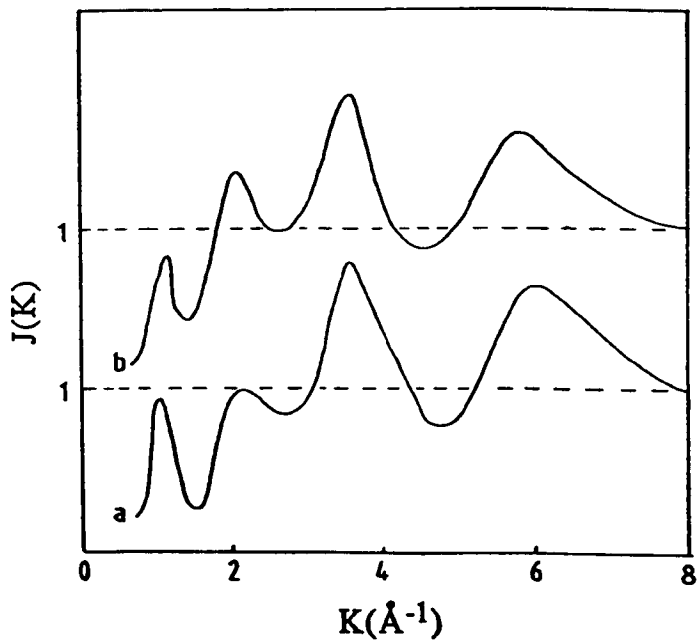

Fig. 5.34 X-ray interference functions for (a) GeS_2 and (b) $(GeS_2)_{90}Ga_{10}$.

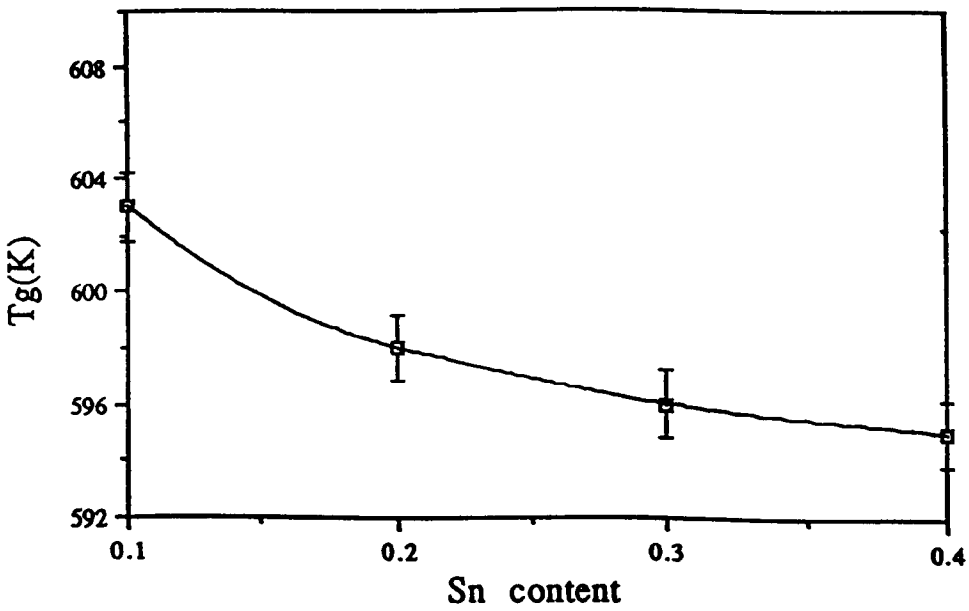

Fig. 5.35 Change in glass transition temperature with Sn content in Ge-S-Sn glasses.

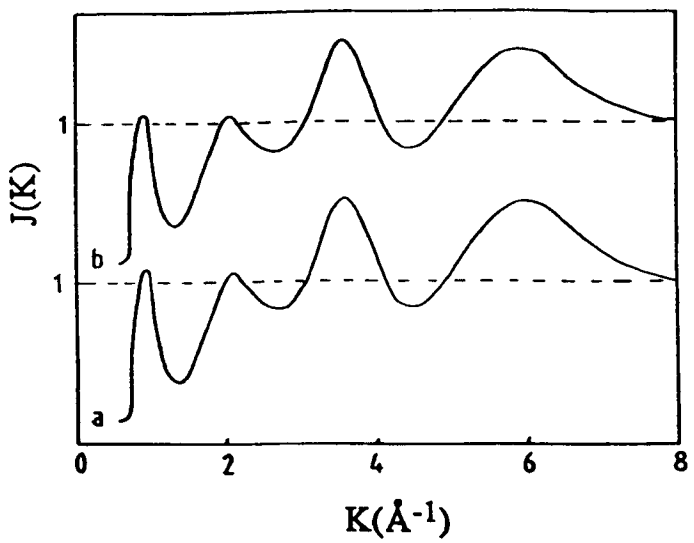

Fig. 5.36 X-ray interference functions for (a) $Ge_{0.9}Sn_{0.1}S_3$ and (b) $Ge_{0.8}Sn_{0.2}S_3$.

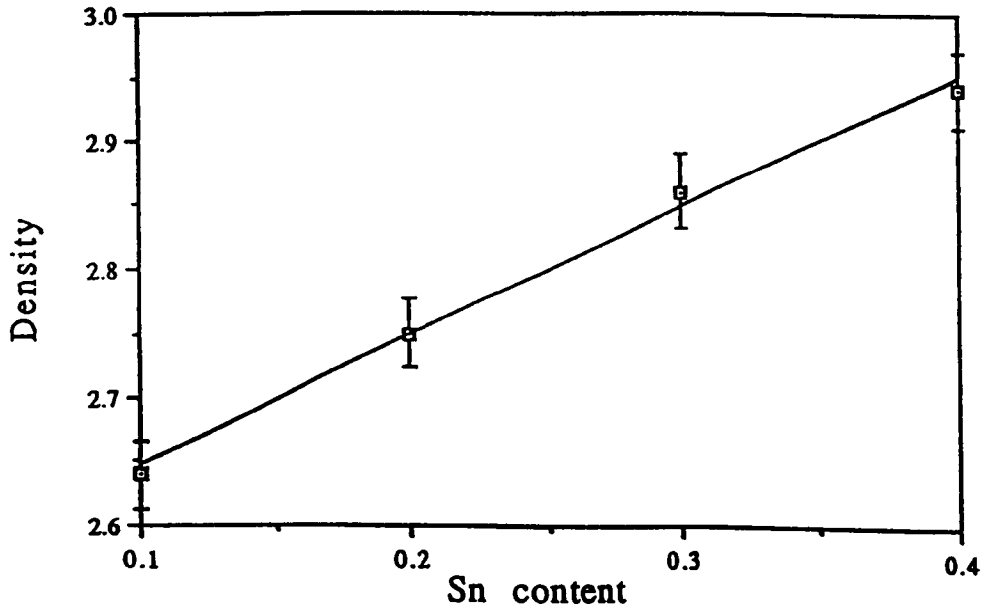

Fig. 5.37 Change in relative density with Sn content in Ge-S-Sn glasses.

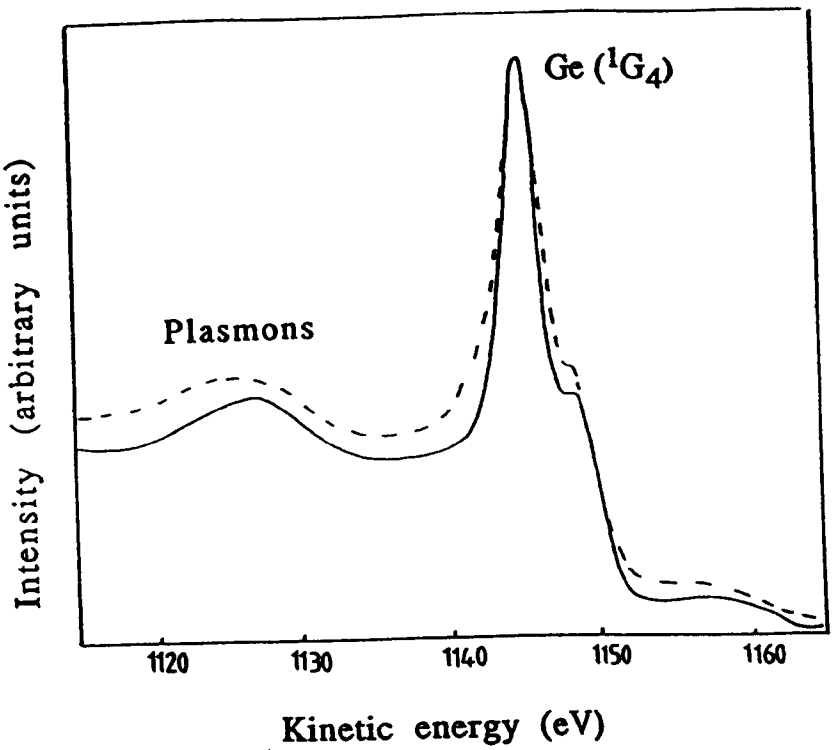

Fig. 5.38 Germanium Auger peaks in $Ge_{0.9}Sn_{0.1}S_3$ (full curve) and $Ge_{0.8}Sn_{0.2}S_3$ (broken curve) shifted so that $^1G_4$ peaks coincide.

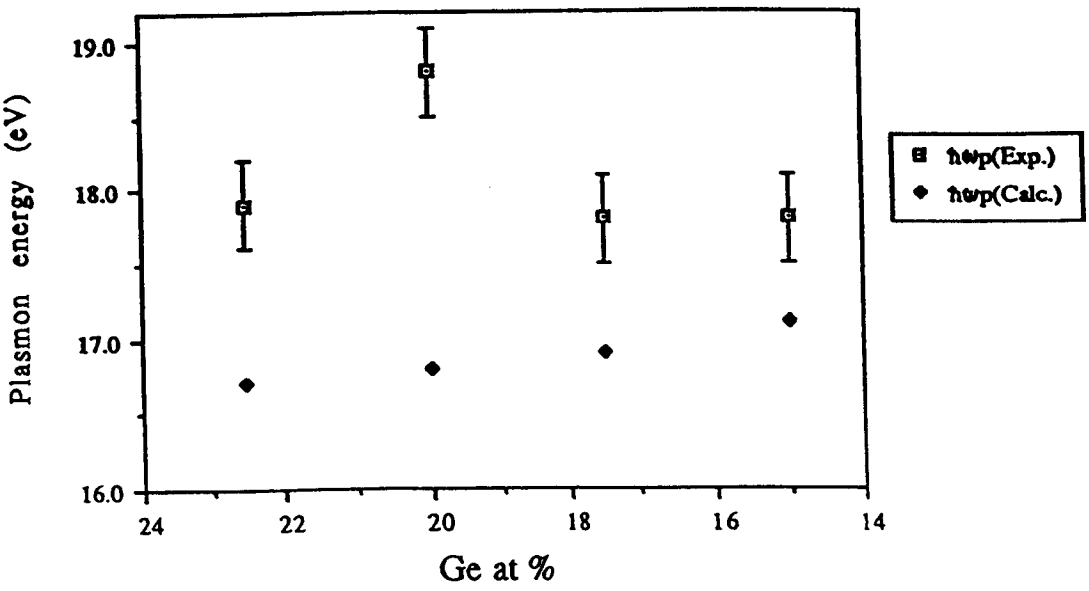

Fig. 5.39 Change in plasmon energy with Ge content in Ge-S-Sn glasses both for calculated values and those determined experimentally from the $L_3M_{4,5}M_{4,5}$ Auger lines of Ge.

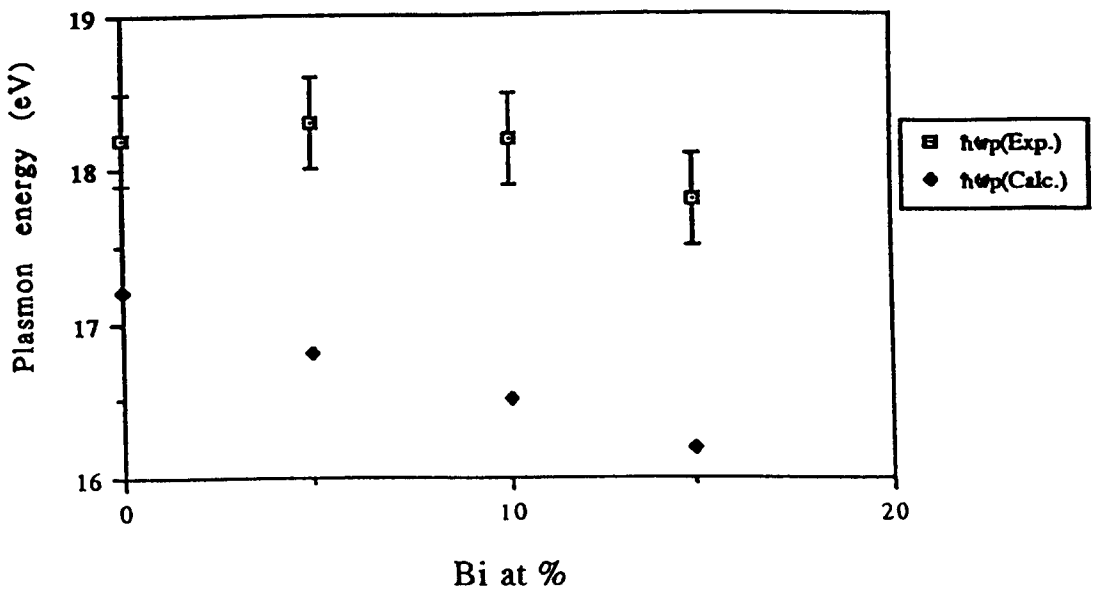

Fig. 5.40 Change in plasmon energy with Bi content in Ge-S-Bi glasses both for calculated values and those determined experimentally from the $L_3M_{4,5}M_{4,5}$ Auger lines of Ge.

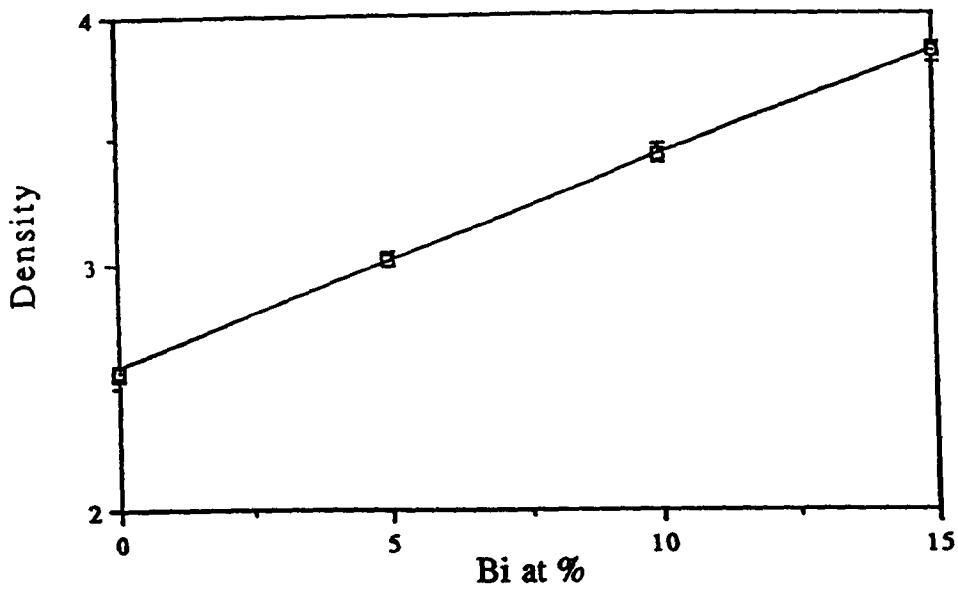

Fig. 5.41 Change in relative density with Bi content in Ge-S-Bi glasses.

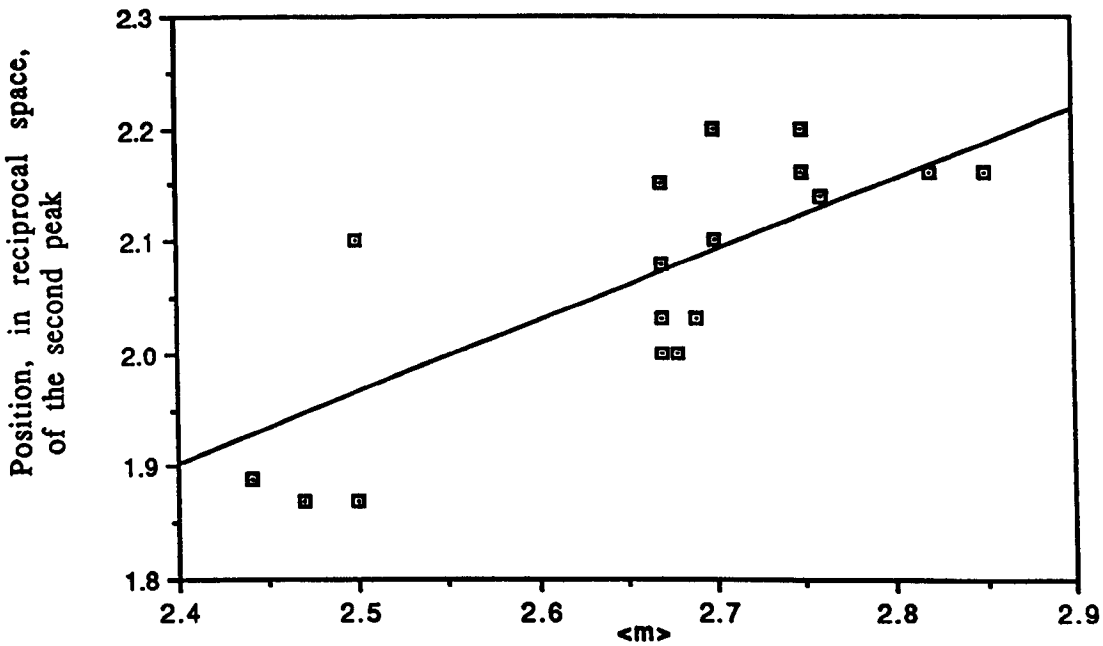

Fig. 5.42 Variation of the position, in reciprocal space, of the second peak of the X-ray interference function with the average coordination number < m >.

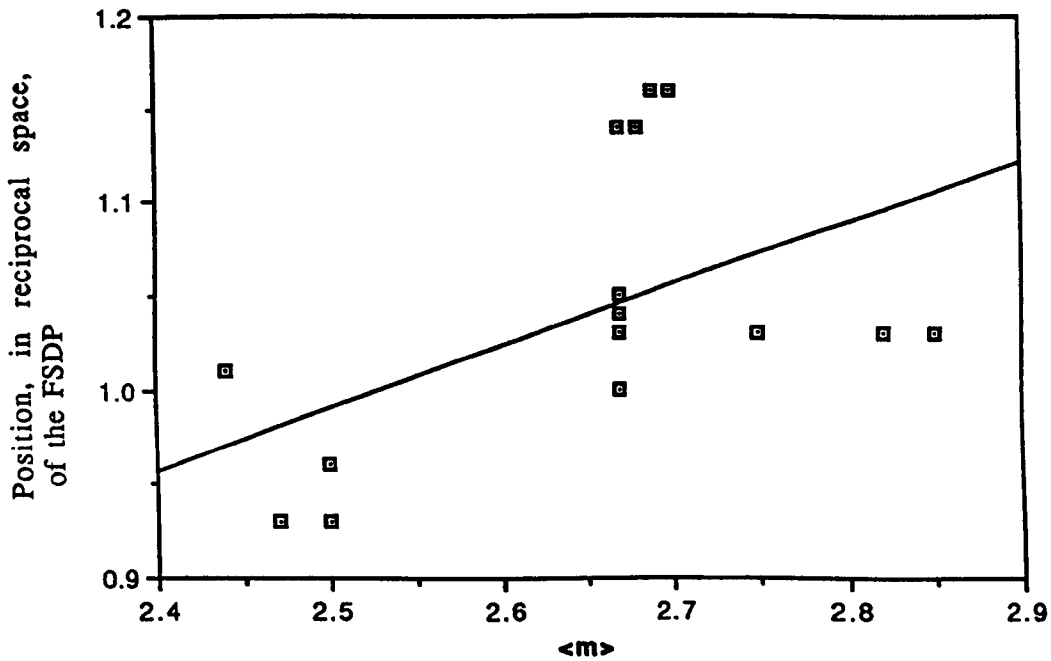

Fig. 5.43 Variation of the position, in reciprocal space, of the FSDP of the X-ray interference function with the average coordination number < m >.

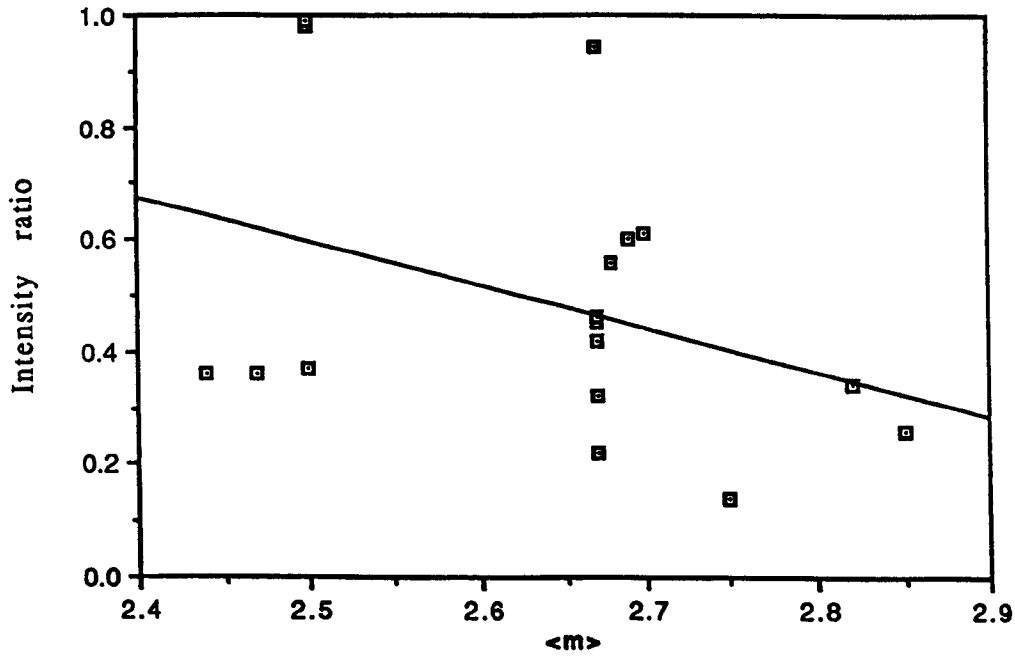

Fig. 5.44 Variation of the intensity ratio of the FSDP to the second peak with the average coordination number < m >.

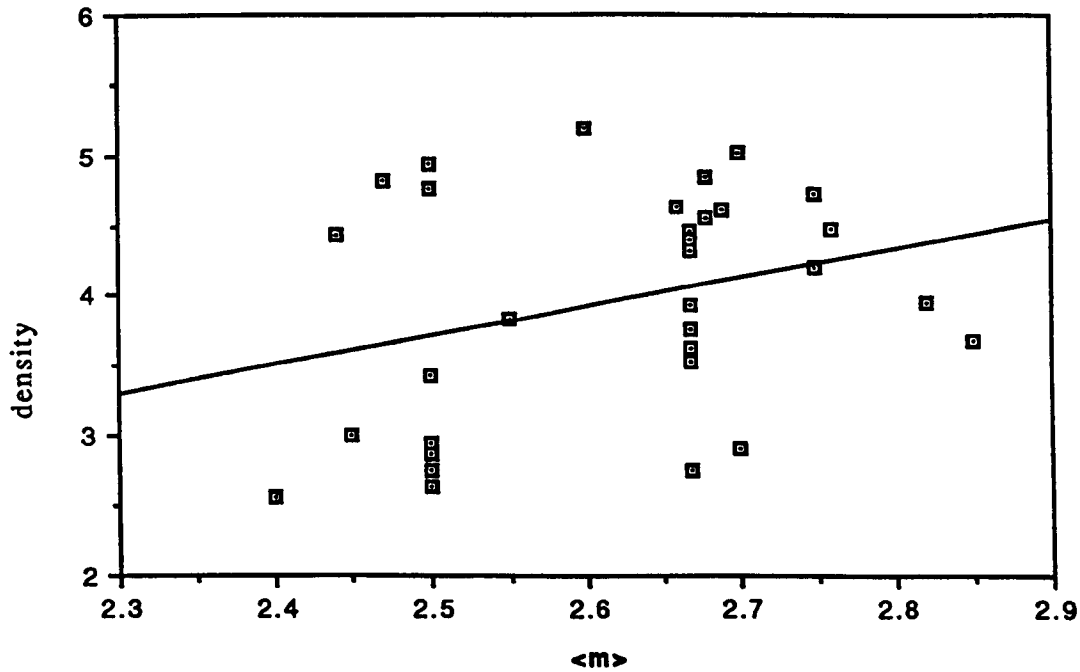

Fig. 5.45 Variation of the measured relative density with the average coordination number < m >.

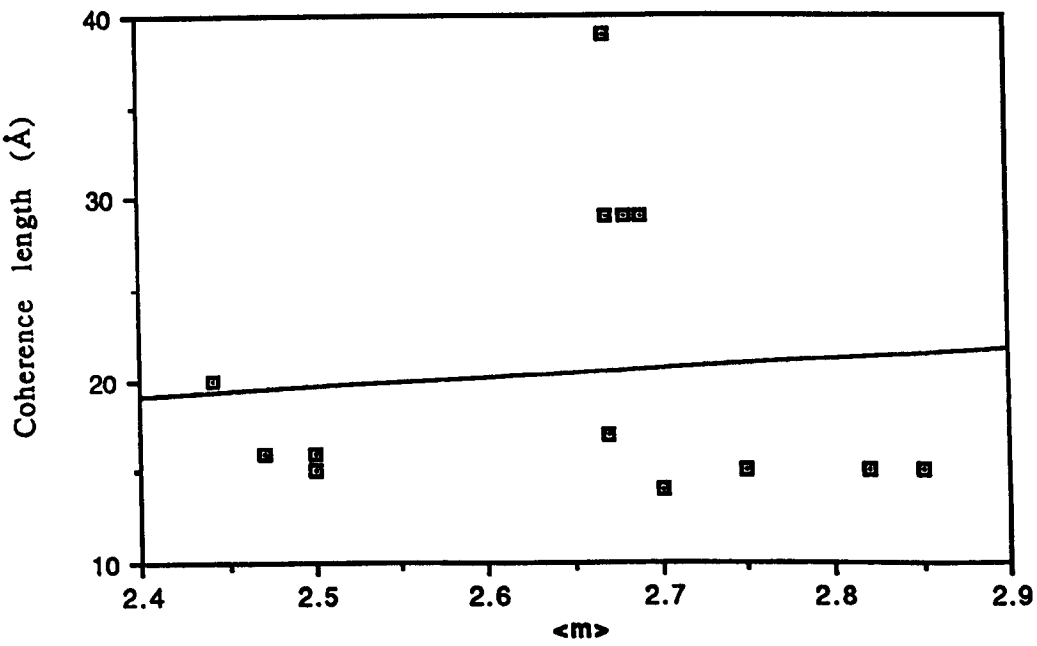

Fig. 5.46 Variation of the coherence length with the average coordination number < m >.

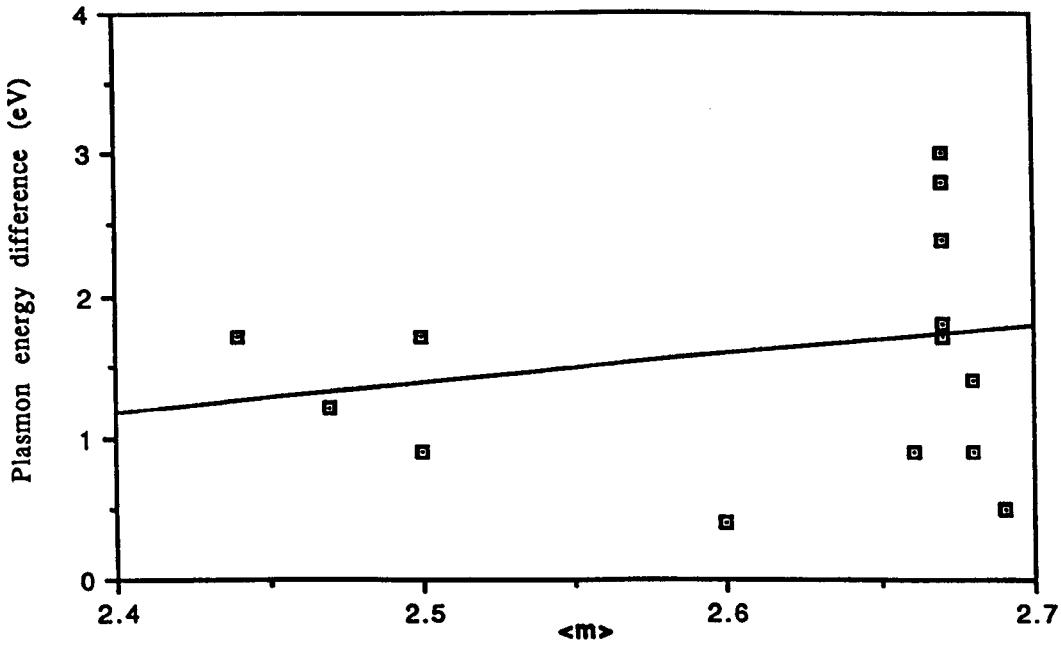

Fig. 5.47 Variation of the difference between the measured plasmon energy -loss from Se Auger and the calculated value with the average coordination number < m >.

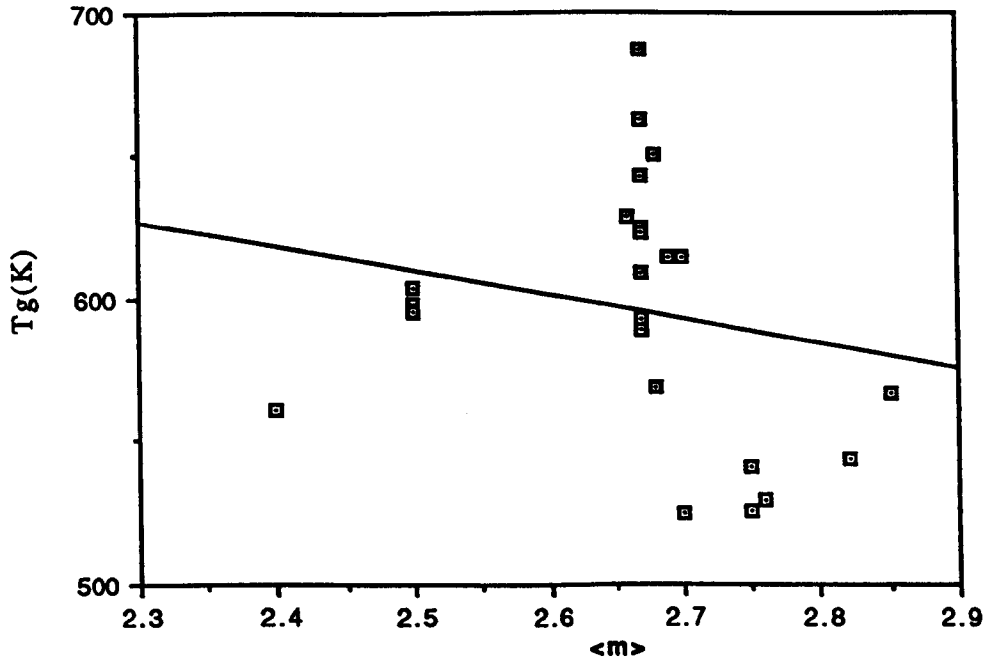

Fig. 5.48 Variation of the measured glass transition temperatures with the average coordination number < m >.

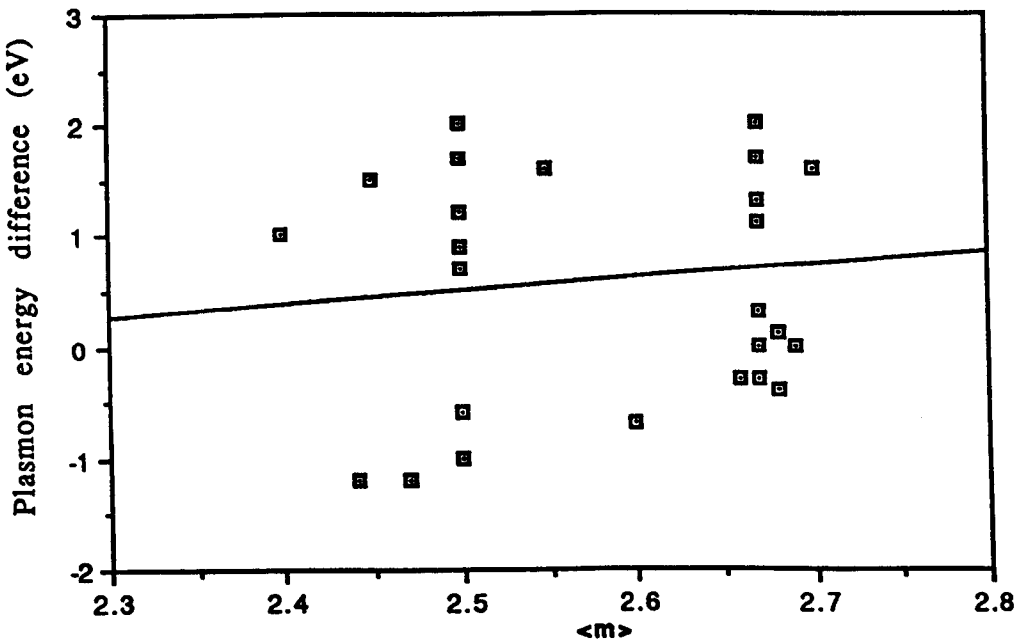

Fig. 5.49 Variation of the difference between
the measured plasmon energy-loss from Ge Auger and the calculated value, with the average coordination number < m >.

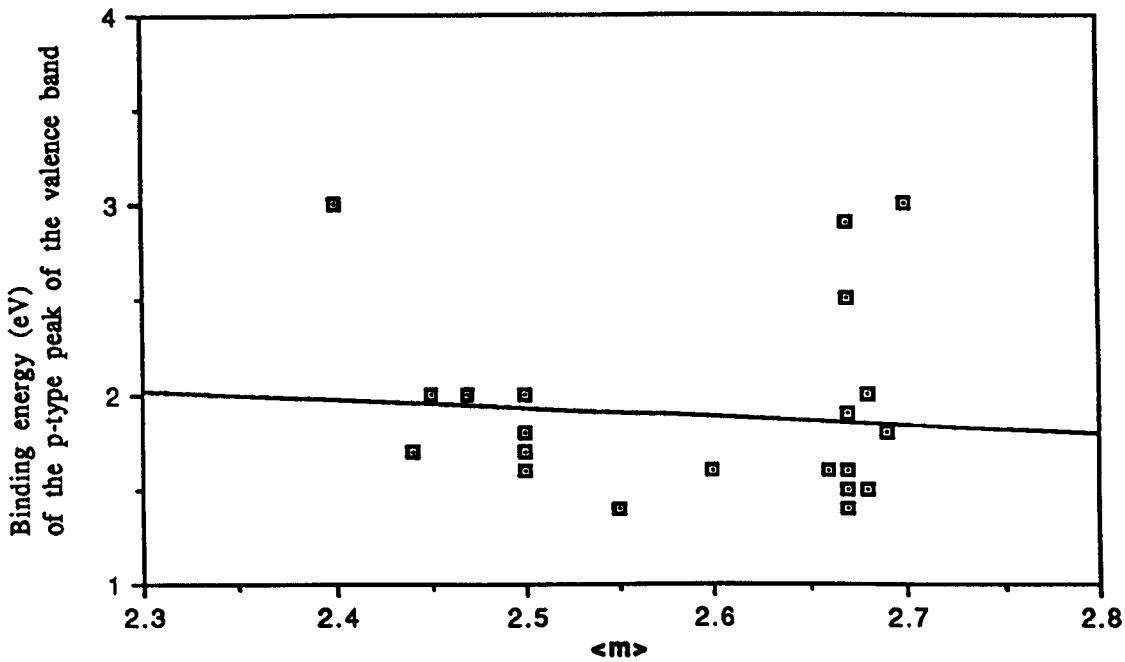

Fig. 5.50 Variation of the binding energy (eV), of the p-type peak of the valence band, with the average coordination number < m >.

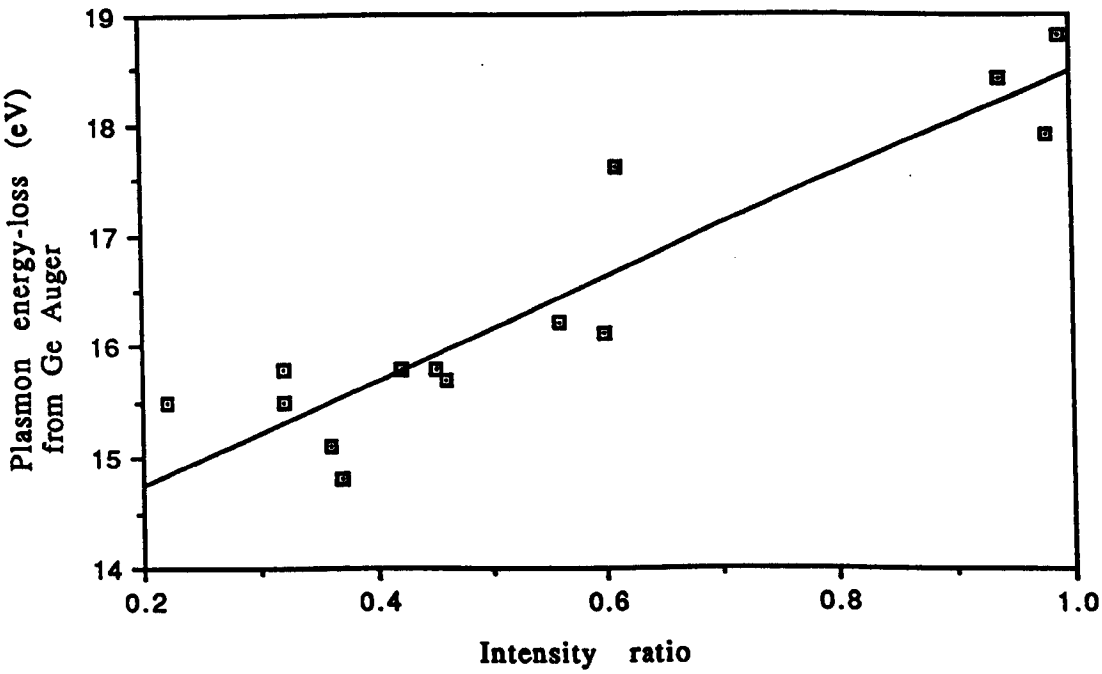

Fig. 5.51 Variation of the measured plasmon energy-loss (eV) from Ge Auger, with the intensity ratio of the FSDP to the second peak.

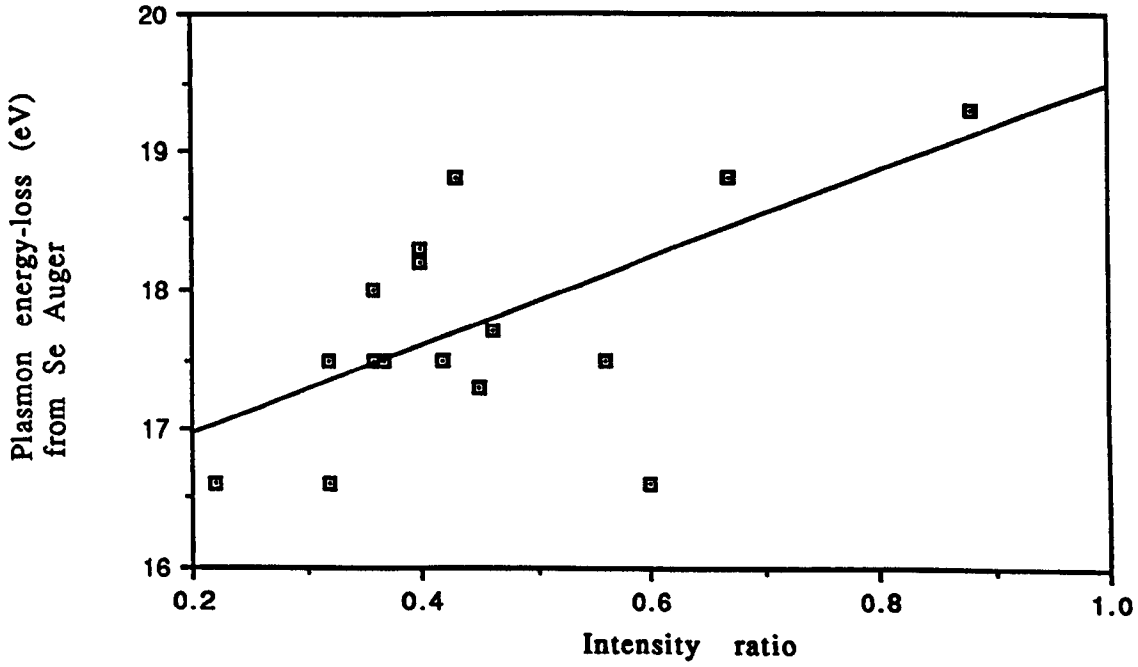

Fig. 5.52 Variation of the measured plasmon energy-loss (eV) from Se Auger, with the intensity ratio of the FSDP to the second peak.